EXPERIMENTAL AND THEORETICAL CHARACTERISATION OF TUNABLE FIBRE GRATINGS

DOMENICO GIANNONE

Doctor of Philosophy

ASTON UNIVERSITY
February 2003

ASTON UNIVERSITY

EXPERIMENTAL AND THEORETICAL CHARACTERISATION OF TUNABLE FIBRE GRATINGS

DOMENICO GIANNONE

Doctor of Philosophy

February 2003

ABSTRACT

This thesis presents details on both theoretical and experimental aspects of UV written fibre gratings. The main body of the thesis deals with the design, fabrication and testing of telecommunication optical fibre grating devices, but also an accurate theoretical analysis of intra-core fibre gratings is presented.

Since more than a decade, fibre gratings have been extensively used in the telecommunication field (as filters, dispersion compensators, and add/drop multiplexers for instance). Gratings for telecommunication should conform to very high fabrication standards as the presence of any imperfection raises the noise level in the transmission system compromising its ability of transmitting intelligible sequence of bits to the receiver. Strong side lobes suppression and high and sharp reflection profile are then necessary characteristics. A fundamental part of the theoretical and experimental work reported in this thesis is about apodisation. The physical principle of apodisation is introduced and a number of apodisation techniques, experimental results and numerical optimisation of the shading functions and all the practical parameters involved in the fabrication are detailed.

The measurement of chromatic dispersion in fibres and FBGs is detailed and an estimation of its accuracy is given. An overview on the possible methods that can be implemented for the fabrication of tunable fibre gratings is given before detailing a new dispersion compensator device based on the action of a distributed strain onto a linearly chirped FBG. It is shown that tuning of second and third order dispersion of the grating can be obtained by the use of a specially designed multipoint bending rig. Experiments on the recompression of optical pulses travelling long distances are detailed for 10 Gb/s and 40 Gb/s.

The characterisation of a new kind of double section LPG fabricated on a metal-clad coated fibre is reported. The fabrication of the device is made easier by directly writing the grating through the metal coating. This device may be used to overcome the recoating problems associated with standard LPGs written in step-index fibre. Also, it can be used as a sensor for simultaneous measurements of temperature and surrounding medium refractive index.

KEY WORDS
Optical Fibre, Fibre Bragg Gratings, Chirped Gratings, Dispersion Compensation, Long Period Gratings.

2

To the lovely memory of Roberta
who was able to perceive the funny side of any situation ...

To my parents, my sister and my brother
who believed the unbelievable.

ACKNOWLEDGEMENTS

CONTENTS

LIST OF FIGURES

Chapter 1

THE ROLE OF FIBRE GRATINGS IN PHOTONICS

1.1 An Historical Overview

We could define photonics as the branch of optical sciences and technology dealing with the way to generate and handle a very special kind of light. This light has a very high degree of monochromaticity, coherence and directionality and it is produced by stimulated emission, a quantum mechanical process described for the first time by Einstein in 1917, using machines that behave like "light amplifiers": the lasers. Actually, the advent of photonics dates back to the invention of the laser itself when Gordon Gould, a doctoral student under Charles Townes at Columbia University, built the first ruby laser in 1958. A second, but not less important, advancement in the field was the fabrication of the first optical fibre with loss under ~ 20 dB/Km, in the early seventies by Kapron *et al.* [1], from Corning. By 1979 further advances in the fabrication technology resulted in a gradual reduction of the fibre loss to only 0.2 dB/km at 1550 nm [2]. This inaugurated the birth of the optical fibres communication era. The loss characteristics of the single mode optical fibres determined also the choice of 1550 nm as the most suitable wavelength to operate optical communication links: the low loss occurring at 1550 nm allows optical signals to

propagate through very long distances without need of any regeneration. In recent times, photonics has advanced to the point that lasers are being used in many consumer electronic products, optical communication links have been installed on the most part of the surface of the planet and optical fibre cables cross the oceans to connect four continents. Highly efficient optical fibres have already largely replaced coaxial cables for long-haul communications applications, marking the first step of a technological revolution experts believe will ultimately results in all-optical communications. In a not so far future, photonics will be able to do exactly the same things as electronics (as to amplify, to switch and to process optical signals, for instance) with the only difference that photonics devices work with optical signals in place of the electrical ones. In the research stage it has been shown that optical fibres combined with Dispersion Management (DM) and Wavelength Division Multiplexing (WDM) techniques can be used to transmit information at rates beyond 1 THz [3]. The transmission of dozens of channel at 10Gbit/s in submarine cables through thousands of kilometres is already a commercial reality. The real limit to the speed transmission is today represented by the fact that, at some stage it is necessary to electronically manipulate the optical bit stream. As the electrons move in an electrical circuit comparatively much slower than the photons in a optical fibre, the more the data transmission speed grows, the less electronic devices are able to adapt to the performances of optical components (this is true, for instance, in the case of electronic light detectors). The strategic importance of photonics for modern telecommunications is evident if we consider the exponential growth of Internet related technologies (as in the case of real time audio and video conferences, for instance). The Internet "revolution" put the global communication systems under very high pressure and as a result, the demand for faster and more reliable optical components (if possible, also at low cost) is now higher than ten years ago and increases continuously. Between the many available technological options, fibre gratings are maybe the most versatile and potentially offer a solution to some of the many technical problems encountered for the implementation of the next generation of optical transmission systems. The successful commercial acceptance of fibre gratings probably depends on the easiness of fabrication and low cost. Moreover, fibre gratings are ideal because of their small size facilitating the fabrication of less bulky devices.

1.2 The Discovery of Doped Fibre Photosensitivity

Fibre grating technology derives directly from the quite accidental discovery that optical fibres are sensitive to some kind of laser light. This phenomenon is today known as "photosensitivity" of doped optical fibre. Photosensitivity is a non-linear effect which

enables an index grating, i.e. a periodic perturbation of the refractive index, to be written directly in the fibre core. The interest in fabrication of fibre grating based devices has started immediately after the phenomenon was observed for the first time in germano-silicate fibres in 1978, at the Communication Research Centre of Ottawa (Canada) by Hill *et al.* [4], [5], and this field has advanced today at the point that very complicated structures can be written in optical fibre. In the first experiment by Hill and co-authors, the blue laser radiation at 488 nm was back-reflected by the fibre end then producing a stationary wave pattern (by interference between the incident light and the 4% back-reflected) which is responsible for the formation of the grating. The more the strength of the grating increases, the stronger becomes the intensity of the back-reflected light, until a point where saturation is reached and nearly 100% of the incident light is reflected back. The underlying mechanism for optical inscription of the grating in the core fibre remained something of a mystery for about a decade. It is now clear that a two-photon absorption mechanism of the blue (488 nm) or green (514.5 nm) laser light, i.e. the absorption of two photons to higher-lying energy level, initiates the ionisation of oxygen-deficient bonds (so called "defects") whose absorption band is centred at 254 nm. The electrons released in this process are re-trapped at other sites. The final result of the process is a refractive index change in the silica that is permanent also after that the laser used to write the grating is switched off [6-8].

1.3 Fibre Gratings Fabrication and Their Applications

A decade after Hill's experiment, Meltz *et al.* [9] proved that ultraviolet radiation at 244 nm could be used to form gratings at any reflecting wavelength by illuminating the fibre through the side of the cladding making use of two intersecting beams of UV light (holographic method). By using this method, the period of the interference maxima and the index change can be set by the angle between the two beams and the UV wavelength. They also made clear that the strength of the grating obtained was proportional to the square of the light intensity of the laser used to write it. At the same time, different techniques, like hydrogen loading and flame brushing, were developed to enhance the magnitude of the photosensitivity in standard telecommunication fibres [10], [11]. But the most significant technical achievement is probably represented by the introduction of the phase-mask as a means to write fibre gratings. The phase-mask is a flat slab of silica glass which is transparent to UV light and contains a one-dimensional periodic surface relief etched on one face. The relief is made by the use of photolithographic techniques [12-15]. Still today, the phase-mask is one of the most used methods to fabricate fibre gratings: this is because

it is very easy to use and offers a reliable way for fabricating gratings at commercial scale. The fibre is irradiated from the side with two coherent UV beams that interfere producing a periodic interference pattern that writes a corresponding periodic refractive index grating in the core of the optical fibre, as schematically shown in Fig. 1.1.
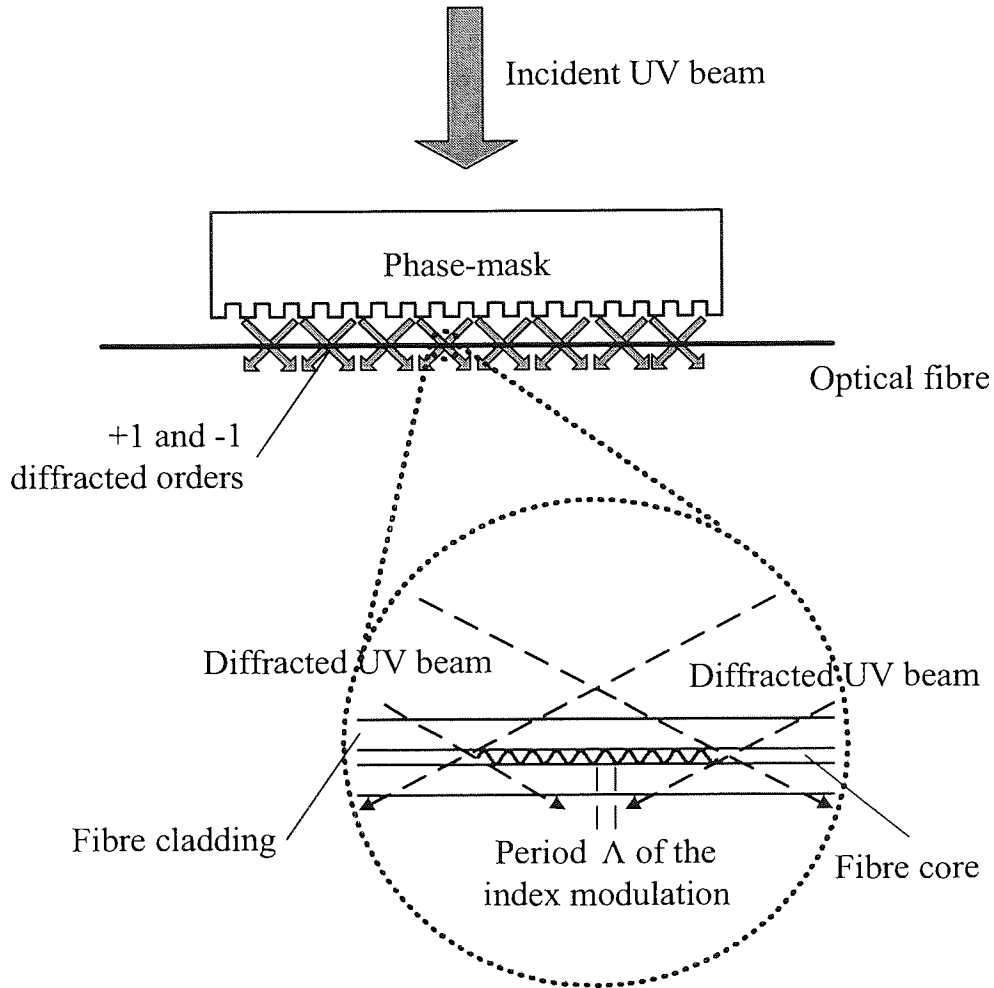
Figure 1.1 Schematic of the technique used for writing fibre gratings inside the core of a Ge-SiO$_2$ optical fibre by a phase-mask irradiated by a 244nm laser UV beam.

Ultraviolet light which is incident normal to the phase-mask passes through it and is then diffracted by the periodic corrugation of the phase-mask. Most of the diffracted light is contained in the 0, +1 and −1 diffracted orders. Ideally, the zero order is nearly totally suppressed and approximately 40% of the total light intensity is equally divided between +1 and −1 diffracted order. The growth of the grating with time is usually monitored using a broadband source and an optical spectrum analyser. The combination of beam characteristics and power necessary for fibre gratings production is usually delivered by an excimer or a frequency-doubled argon ion laser (even if it has been shown that fibre gratings could be also written using other sources or a different writing mechanism, as for

instance in the case of a CO_2 pulsed laser, without exposure to UV light, where the grating is obtained by the periodical defects created by a periodical "burning" of the fibre core) [16]. Argon laser offers excellent spatial and temporal coherence, stable output power, and good beam uniformity then it is usually preferred to the excimer laser. Nevertheless, the magnitude of the refractive index change depends on several different factors as the irradiation conditions (wavelength, intensity, and total dosage of irradiating light), as well as on the composition of the glassy material forming the core and/or any process on the fibre prior the exposure to UV light. Typically, an exposure to UV laser light at intensities ranging between 100 to 1000 mJ/cm^2 accounts of an increase of the core refractive index in a Ge-SiO_2 optical fibre with a magnitude ranging between 10^{-6} to 10^{-3}.
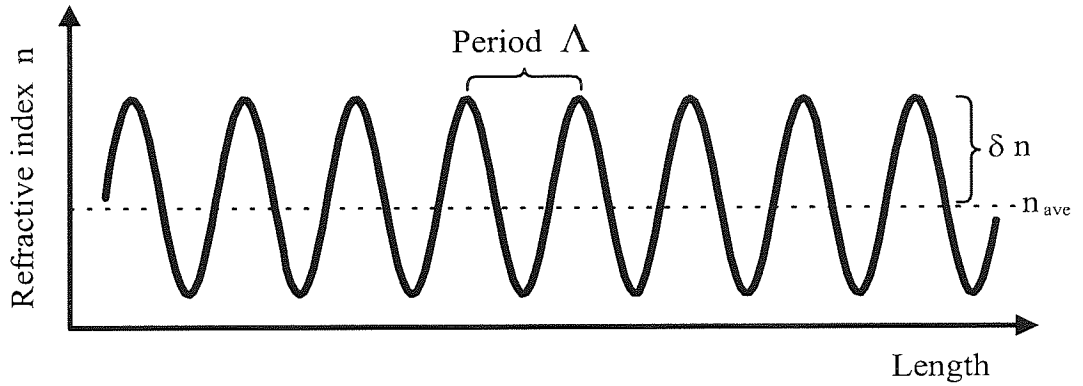
Figure 1.2 *Schematic linear periodic optical medium simulating a one-dimensional refractive index structure of a (Bragg) fibre grating.*

A first qualitative idea on how a fibre grating works can be obtained when we consider a linear period medium as the one shown in Fig. 1.2. In such a periodic structure the modulation amplitude is assumed to be small ($\delta n \ll n_{ave}$). If the modulation is not sinusoidal, δn represents the amplitude of the lowest Fourier component. When light propagating through such a medium has a wavelength $\lambda_B \approx 2 n_{ave} \Lambda$ (Bragg condition), Λ being the period of the modulation, exactly half a wavelength fits inside each period. As a consequence, the light Fresnel-reflected off interfaces which are an integer number of periods apart, is all in phase, leading to a strong reflected wave. Clearly, at wavelengths far from the Bragg condition, the light reflected off the various interfaces is mutually out of phase then it can propagate through the structure essentially unperturbed.

Actually, we could consider fibre gratings as directional couplers and group them in two different categories: Bragg Gratings (FBG's) and Long Period Gratings (LPG's). The two classes are determined by the different behaviour of each device. Fibre Bragg gratings have period shorter then 1μm and couple forward and backward propagating modes inside the

19

core fibre opening up a photonic band gap: while frequencies inside the gap are reflected, frequencies outside the gap can travel nearly unaffected. Unlike FBG's, long period gratings have a period of few hundreds of micrometers and behave in a totally different way. Figure 1.3 schematically shows the difference between the two classes. In the case a) the light incident on the grating is back-reflected by the periodic structure in the core. In the case b) instead the grating diverts the light from the core into the fibre cladding, where it can travel for many meters before being lost to scattering or absorption, or to be coupled back to the core again. The relation between the period Λ of the fibre grating and the wavelength λ of the incident light determines which of the two cases will occur.

a)

b)
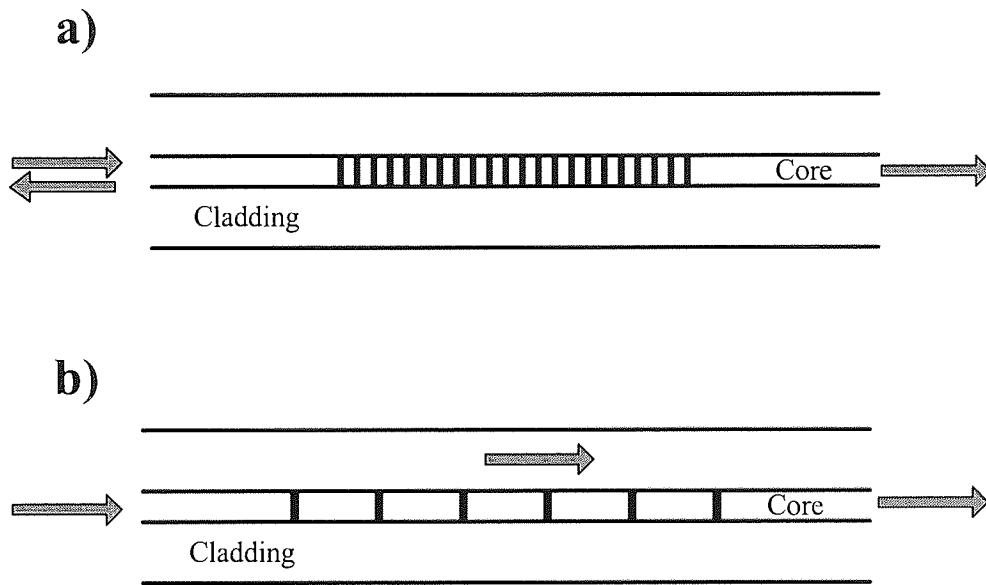
Figure 1.3 *Different behaviour shown by Bragg and Long Period Fibre Gratings: a) a FBG behaves as a counter-directional coupler working in reflection and coupling the back-propagating fundamental mode to the forward-propagating one in the core of a single mode fibre, b) a LPG is a co-directional coupler working in transmission and coupling the fundamental mode travelling in the core of a single mode fibre to multiple cladding modes.*

To back reflect a light beam at a wavelength around 1550 nm, the grating must have a period $\Lambda \sim 0.5$ µm. To couple the light from the core fibre into the cladding, the grating period Λ is much longer (generally in a range between 400 and 600 µm) and it is for that reason that we refer to such gratings as "Long Period". The fundamental guided mode propagating in the core of a single mode fibre is coupled to forward-propagating cladding modes by the optical grating. Because the cladding of a single-mode fibre can support many cladding modes, the spectrum of the LPG has many resonance peaks. As the spectral resonance peaks can be shifted by the refractive index change of the surrounding medium

20

around the fibre cladding itself [17], LPG's have found many applications as very accurate sensors. Actually, in nearly 25 years since they were discovered, fibre gratings have found application in many different fields: optical communications, lasers and amplifiers as well as a range of optical-based sensors have all benefited from the techniques allowing inscription of the grating directly into the fibre. Among the many applications of fibre gratings we mention the following:

- **Optical filters**: As fibre gratings can be fabricated with a very sharp reflection profile and high reflectivity, one of their most obvious applications has been, since the very beginning, the use as a narrow-band reflection filter. A full variety of optical filters has been realised so far: bandwidths between 6 GHz and 2 THz at 1550 nm, and reflectivity up to 100% are made possible just varying the length of the grating and/or the induced refractive index change. Filters with a more or less sophisticated degree of complexity (from apodized FBG's to Fabry-Perot filter with finesse up to ∼ 1000, to bandpass filters) are today commercially available [18-23].

- **Fibre lasers**: Another quite direct derivation of fibre grating technology is the all-fibre laser. In the case of fibre lasers the gratings are used in place of the mirrors in the laser cavity, forcing the laser to operate in a single longitudinal mode. This kind of laser offers also the advantage that it can be tuned by temperature or strain [24-26].

- **Distributed Bragg Reflector (DBR) lasers**: A laser can be directly modulated by coupling a fibre grating to the light generated from an anti-reflection coated facet. This can provide a source of short optical pulses without recurring to an external modulator [27], [28].

- **Add/Drop (MUX/DEMUX) devices:** Fibre gratings have proved to be critical components in lightwave applications. Actually their wavelength selective nature make them ideal for implementation of devices such as optical taps, wavelength switching add/drop nodes or channel selectors/couplers in WDM systems [29-33].

- **Dispersion compensation :** As chirped fibre gratings exhibit a large dispersion in reflection, they represent a valuable option for the in fibre compensation of chromatic and/or high order dispersion. Dispersion compensation can be achieved using short length of fibre with the advantage that the compensating element is compact but also introduces negligible loss penalty. Several significant experiments on dispersion compensation have been reported to date and new records on transmission length and bit rate are continuously established. Techniques to tune the grating dispersion/wavelength have been developed making these devices suitable for very

sophisticated WDM transmission systems. Recently, fibre gratings have also found application for the compensation of Polarization Mode Dispersion (PDM) [34-39].

- **Optical switching :** The study of nonlinear propagation of high intensity optical pulses in fibre gratings (generating grating or gap solitons by Kerr effect) [40-42] favourites the advancement of techniques for all optical switching of pulses in optical fibres. The nonlinear phenomena occurring inside the grating, when high intensity laser beam interacts with it, can also be used for generating fast pulses from a CW beam [43], [44].

- **Optical signal processing :** Fibre gratings offer a convenient way to spectrally shape optical pulse [45]. Today it is possible to fabricate super-structured fibre gratings with very complex amplitude and phase response. These new kind of gratings can be used to perform fundamental Optical Code Division Multiple Access (OCDMA) functions, as coding and encoding of chip patterns [46-48]. Chirped fibre Bragg gratings have been used to generate high frequency pulse streams or, with an appropriate design, to realize a real-time optical Fourier transformer [49], [50].

- **Optical based sensors:** Because of the high sensitivity to strain and temperature, fibre gratings are excellent for sensing applications [51], [52]. Sensors have been realized to detect temperature, strain and even the presence of chemicals around the fibre cladding. These sensors are very attractive also because they are insensitive to the electromagnetic fields and, unlike electrochemical sensors, do not need a reference electrode.

- **Microwave photonics:** In the last decade a growing interest has been shown in the emerging field of microwave photonics. Microwave fibre-optic links have several advantages when compared to conventional coaxial or waveguide links including reduced size and weight, low and constant attenuation over the entire modulation frequency range, imperviousness to electromagnetic interference, wide bandwidth, low dispersion and high information transfer capacity. These advantages mean that they are currently being considered for a number of applications including personal communications networks, millimetre-wave radio LANs antenna remote broadband video distribution networks and signal distribution for phased array antennas [53-55].

1.4 Overview on the Following Chapters

This thesis deals with both experimental and theoretical aspects on UV written fibre gratings. Even if the most relevant part of the work is about design, fabrication, measurement and testing of optical fibre grating based devices for telecommunications

purposes, some issues more related to the field of optical fibre sensors have been equally taken in consideration. A detailed theoretical background has been provided in the attempt to give the most general and clear description of the phenomena under investigation. Numerical modelling has also been implemented (whenever possible) and the results obtained from theory compared with the experimental data.

Chapter 2 is the starting point of the thesis and gives a complete theoretical background on fibre gratings. Coupled-mode theory, an essential instrument for understanding the behaviour of fibre grating, is introduced. The basic equations used for calculating the spectral response of FBG's (counter-propagating modes) and LPG's (co-propagating modes) is developed and analytical solution for uniform gratings is given. The Transfer Matrix Method (TMM), also called "piecewise uniform", is introduced for all the calculation to be made on non uniform gratings.

Chapter 3 deals with the apodisation of optical fibre gratings. We show that apodisation techniques represent a very important step in the control of the spectral response of a fibre grating, as well as in the reduction of the amplitude of group delay ripples (source of noise for all the telecommunication applications) in chirped gratings. The methodology used for the fabrication of apodized gratings is detailed and the underlying physical principles are investigated. A numerical model, based on TM method, is implemented and the results obtained by the simulation are compared to the experimental spectra. The implemented numerical model is a valuable tool for the experimental optimisation of all the practical parameters (such as the strength of the grating or the type and width of the apodisation function) used for the fabrication of apodised structures.

Chapter 4 investigates the origin of dispersion in single mode fibre (SMF) and the possibility of its control by the use of fibre gratings. A study on the accuracy and optimisation of the measurement of chromatic dispersion (based on the estimation of the group delay ripples), using the modulation phase-shift method, is carried on. The dependence of results on the modulation frequency is investigated. In a final section of the chapter, the study on the spectral (short wavelength losses) and temporal (time delay) characteristics of chirped gratings is presented and a comparison is made between apodised and unapodised grating case. An experimental demonstration of temporal Talbot effect, i.e. the generation of high-repetition-rate streams of optical pulses, by the use of linearly chirped FBG's is also given.

Chapter 5 is an investigation on the possible methods that can be implemented to fabricate tunable fibre gratings: thermal and mechanical tuning are considered with respect to advantages and disadvantages of each method. The principle of tuning second and third order dispersion by using a distributed strain applied on a chirped fibre grating is illustrated and mechanical tuning of the dispersion and slope for the case of a linearly chirped grating by a multipoint bending rig is demonstrated. An analytical model is developed enabling to calculate the amount of dispersion and slope delivered by the fibre grating for a given applied strain (direct problem) or, in alternative to derive the bending profile to be used to get a given dispersion (inverse problem). An experimental investigation on the transmission of optical pulses (in linear regime) at 10 Gb/s and 40 Gb/s is performed. Numerical modelling of the implemented tunable dispersion device is performed and the results obtained are compared to the experimental data.

Chapter 6 is about metal-clad coated fibre gratings. We used both FBG's and LPG's for our measurements. FBG's sensors coated with a large thermal expansion coefficient metal show an higher temperature sensitivity than the ones in bare fibre. In the case of LPG's coated with a metal, the devices behave as loss filters ideal for gain flattening of erbium-doped amplifiers or applications requiring the spectral control in general. The metal coating of the fibre has been obtained by using a sputtering machine (method that guarantee the maximal accuracy in the control of the thickness of the metal coating and of the cylindrical geometry as well). We investigate the case of silver coating and we show that, because of the very thin skin dept of the silver in the UV light region, it is possible to write a grating in the core of the fibre trough the silver coating. We proves that the grating written inside a three layers structure (made by fibre core, cladding and metal coating) is a very sensitive device for the detection of strain, bending, temperature and surrounding refractive index medium. An extension of the theory presented in chapter two to the case of metal coated fibres is also given. An extensive experimental investigation on sensing characteristics of a new LPG double-section silver coated device is performed.

Chapter 7 is the final chapter. It presents the conclusions of the thesis and summarise the most essential finding of this work with special attention to the possible future developments.

We end this introductory chapter by providing a summary of the principal achievements and novelty characters that have been reported in the present thesis:

- The coupled-mode theory formulated in chapter two, represents a generalisation of the usual more basic theory (see [56] for instance) and has the advantage of being a more flexible calculation tool, as it enables to calculate the coupling coefficient on the base of the real fibre parameters (the real core and cladding size, the core-cladding refractive index difference or the used envelope of the index perturbation, for instance). By using such a generalisation the theory results more easily adaptable to the real case and predicts in accurate way how the experimental parameters must be varied to get an experimental spectrum matching at the best the calculated one.

- A novel grating apodisation technique based on a variable speed double exposure method and the use of a unapodised phase mask is detailed in chapter 3.

- A new comparative numerical study on the five most common apodisation functions is carried on without the use of any commercial packages for the simulation of fibre gratings (the code has been written on the base of the theory developed in chapter two by using Matlab).

- A novel experimental characterisation of the modulation phase-shift method, used for the measurement of chromatic dispersion in both fibre and FBG's, has been performed. The estimation of the errors and effect of the modulation frequency on the measurement has been considered.

- A new attempt to characterise the group delay ripples in chirped FBG's by a statistical approach based on Fast Fourier Transform method has been developed.

- A novel interpretation of the physical mechanisms inducing abnormal spectral response in linearly chirped FBG's has been presented.

- An extensive theoretical and experimental characterisation of a totally new tunable dispersion compensator device, working on the application of a variable distributed strain to a chirped FBG by the use of a multipoint bending rig, is given in chapter five.

- A new tunable optical filter, working on the same principle than the tunable dispersion compensator, is experimentally characterised.

- A new two-section metal coated device, used as strain, bending and external refractive index sensor, is experimentally characterised in chapter six.

References

[1]   F.P. Kapron, D.B. Keck, R.D. Maurer, "Radiation losses in glass optical waveguides", *Appl. Phys. Lett.,* **17**, 1970, pp. 423-425.

[2]   T. Miya, Y. Terunuma, T. Hosaka, T. Miyashita, "Ultimate low-loss single mode fibre at 1.55 µm", *Electron. Lett.,* **15**, 1979, pp.106-108.

[3]   C.G. Gyaneshvar, R.E. Tench, O. Mizuhara, L.L. Wang, N.N. Dang, N. Chand, B. Mason, A. Ougazzaden, C.W. Lentz, "3.2 Tbit/s (40×80 Gb/s) transmission over 1000 km with 100 km span (25 dB loss) and 0.8 bit/s/Hz of spectral efficiency", in proc. OFC 2002 (Anaheim, USA, 2002), *paper TuA5*.

[4]   K.O. Hill, Y. Fujii, D.C. Johnson, B.S. Kawasaki, "Photosensitivity in optical fiber waveguides: application to reflection filter fabrication", *Appl. Phys. Lett.,* **32**, 1978, pp. 647-649.

[5]   B.S. Kawasaki, K.O. Hill, D.C. Johnson, Y. Fujii, "Narrow-band Bragg reflectors in optical fibers", *Opt. Lett.,* **3**, 1978, pp. 66-68.

[6]   D.K.W. Lam, B.K. Garside, "Characterisation of single mode optical fibre filters", *Appl. Opt.,* **20**, 1981, pp. 440-445.

[7]   R.J. Campbell, R. Kashyap, "The properties and applications of photosensitive germanosilicate fiber", *Int. Journ. Optoelectr.,* **9**, 1994, pp. 33

[8]   T.E. Tsai, G.M. Williams, E.J. Friebele, "Index structure of fiber Bragg gratings in Ge-SiO$_2$ fibers", *Opt. Lett.,* **22**, 1997, pp.224-226.

[9]   G. Meltz, W.M. Morey, W.H. Glenn, "Formation of Bragg gratings in optical fibers by a transverse holographic method", *Opt. Lett.,* **14**, 1989, pp. 823-825.

[10]   P.J. Lemaire, A.M. Vengsarkar, W.A. Reed, V. Mizarhi, "Refractive index changes in optical fibers sensitised with molecular hydrogen", in proc. OFC'94, (San Jose, USA, 1994), pp. 47-48.

[11]   P.J. Lemaire, R.M. Atkins, V. Mizrahi, W.A. Reed, "High pressure H$_2$ loading as a technique for achieving ultrahigh UV photosensitivity and thermal sensitivity in GeO$_2$ doped optical fibres", *Electron. Lett.,* **29**, 1993, pp. 1191-1192.

[12]   C. Dix, P.F. Mckee, "High accuracy electron-beam grating lithography for optical and optoelectronic devices", *Journ. Vac. Sci. Technol.,* **10**, 1992, pp. 2667.

[13]   A. Swanton, D.J. Armes, K.J. Young-Smith, C. Dix, R. Kashyap, "Use of e-beam written, reactive ion etched, phase masks for the generation of novel photorefractive fibre gratings", *Special issue Journ. Micro. Electron. Eng.,* **30**, 1996, pp. 509-512.

[14]   J.E. Curran, "Production of surface patterns by chemical plasma etching", *Journ. Phys. E,* **14**, 1981, pp. 393-407.

[15]   R. Kashyap, "Photosensitive optical fibers: devices and applications", *Opt. Fiber Technol.,* **1**, 1994, pp.17-34.

[16] D.D. Davis, T.K. Gaylord, E.N. Glytsis, S.G. Kosinski, S.C. Mettler, A.M. Vengsarkar, "Long-period fibre grating fabrication with focused CO_2 laser pulses", *Electron. Lett.*, **34**, 1998, pp. 302-303.

[17] B.H. Lee, Y. Liu, S.B. Lee, S.S. Choi, J.N. Jang, "Displacements of the resonants peaks of a long-period fiber grating induced by a change of ambient refractive index", *Opt. Lett.*, **22**, 1997, pp.1769-1771.

[18] B.H. Lee, J. Nishii, "Notch filters on cascaded multiple long-period fibre gratings", *Electron. Lett.*, **34**, 1998, pp. 1872-1873.

[19] K.O. Hill, D.C. Johnson, F. Bilodeau, S. Faucher, "Narrow-bandwidth optical waveguide transmission filters", *Electron. Lett.*, **23**, 1987, pp. 465-466.

[20] D.M. Bird, J.R. Armitage, R. Kashyap, R.M.A. Fatah, K.H. Cameron, "Narrow line semiconductor laser using fibre grating", *Electron. Lett.*, **27**, 1991, pp. 1115-1116.

[21] K. Sugden, L. Zhang, J.A.R. Williams, R.A. Fallon, L.A. Everall, K.E. Khisholm, I. Bennion, "Fabrication and characterization of bandpass filters based on concatenated chirped fiber gratings", *IEEE J. Lightwave Technol.*, **15**, 1997, pp. 1424-1432.

[22] F. Bhakti, P. Sansonetti, "Design and realization of multiple quarter-wave phase-shift UV written bandpass filters in optical fibers", *IEEE J. Lightwave Technol.*, **15**, 1997, pp. 1433-1437.

[23] A.M. Vengsarkar, P.J. Lemaire, J.B. Judkins, V. Bhatia, T. Erdogan, J.E. Sipe, "Long-period fiber gratings as band-rejection filters", *J. Lightwave Technol.*, **14**, pp.58-65.

[24] I.M. Jauncey, L. Reekie, R.J. Mears, D.N. Payne, C.J. Rowe, D.C.J. Reid, L. Bennion, C. Edge, "Narrow-linewidth fiber laser with integral fiber grating", *Electron. Lett.*, **22**, 1986, pp. 987-988.

[25] R. Wyatt, "High power broadly tunable erbium-doped silica fiber laser", *Electron. Lett.*, **25**, 1989, pp.1498-1499.

[26] S.V. Chernikov, R. Kashyap, P.F. McKee, J.R. Taylor, "Dual frequency all fiber grating laser source", *Electron. Lett.*, **29**, 1993, pp.1089-1090.

[27] N.A. Olsson, C.H. Henry, R.F. Kazarinov, H.J. Lee, K.J. Orlowsky, "Performance characteristics of a $1.5\mu m$ single frequency semiconductor laser with an external waveguide Bragg reflector", *IEEE J. Quantum Electron.*, **QE-43**, 1988, pp.143-147.

[28] G.P. Agrawal, N.K. Dutta, *Semiconductor Lasers,* 2nd ed. (Van Nostrand Reinhold, 1993, New York).

[29] H. Okayama, Y. Ozeki, T. Kunii, "Dynamic wavelength selective add/drop node comprising tunable gratings", *Electron. Lett.*, **33**, 1997, pp.881-882.

[30] A. Carballar, M.A. Muriel, J. Azaña , "WDM channel selector based on transmissive chirped moiré fibre grating", *Electron. Lett.*, **35**, 1999, pp. 386-388.

[31] L.R. Chen, S.D. Benjamin, P.W.E. Smith, J.E. Sipe, "Applications of ultrashort pulse propagation in Bragg gratings for wavelength-division-multiplexing and code-

division multiple access", *IEEE Jour. of Quantum Electron.*, **34**, 1998, pp.2117-2129.

[32] X.J. Gu, "Wavelength-division multiplexing isolation fiber filter and light source using cascaded long-period fiber gratings", *Opt. Lett.*, **23**, 1998, pp.509-510.

[33] Y. Zhu, C. Lu, B.M. Lacquet, P.L. Swart, S.J. Spammer, "Wavelength-tunable add/drop multiplexer for dense wavelength division multiplexing using long-period gratings and fiber stretchers", *Opt. Commun.*, **208**, 2002, pp.337-344.

[34] K.O. Hill, S. Thériault, B. Malo, F. Bilodeau, T. Kitagawa, D.C. Johnson, J. Albert, K. Takiguchi, T. Kataoka, K. Hagimoto, "Chirped in-fibre Bragg grating dispersion compensator: linearisation of dispersion characteristic and demonstration of dispersion compensation in 100 km, 10 Gbit/s optical fibre link", *Electron. Lett.*, **30**, 1994, pp. 1755-1756.

[35] K.C. Byron, K. Sudgen, T. Bricheno, I. Bennion, "Fabrication of chirped Bragg gratings in photosensitive fibre", *Electron. Lett.*, **29**, 1993, pp. 1659-1660.

[36] R. Kashyap, "Design of step-chirped fibre Bragg gratings", *Opt. Commun.*, **136**, 1997, pp. 461-469.

[37] L. Quetel, L. Rivoallan, M. Morvan, M. Monerie, E. Delevaque, J.Y. Guilloux, J.F. Bayon, "Chromatic dispersion compensation by apodised Bragg gratings within controlled tapered fibers", *Opt. Fiber Techol.*, **3**, 1997, pp. 267-271.

[38] X. Kun, F. Jia, X. Chen, M. Jin, M. Chen, X. Li, S. Xie, "A novel adjustable PMD compensation using sampled Bragg gratings with uniform grating period", *Opt. Commun.*, **202**, 2002, pp. 297-302.

[39] T. Komukai, M. Nakazawa, "Fabrication of non-linearly chirped fiber Bragg gratings for high-order dispersion compensation", *Opt. Commun.*, **154**, 1998, pp. 5-8.

[40] C. Martijn de Sterke, J.E. Sipe, "Gap solitons", *Progress in Optics XXXIII*, E. Wolf, ed., Elsevier, Amsterdam, 1994, pp. 203-260.

[41] B.J. Eggleton, R.E. Slusher, J.B. Judkins, J.B. Stark, A.M. Vengsarkar, "All-optical switching in long-period fiber gratings", *Opt. Lett.*, **22**, 1997, pp. 883-885.

[42] S. Wabnitz, "Pulse self-switching in optical fiber Bragg gratings", *Opt. Commun.*, **114**, 1995, pp.170-180.

[43] L. Larochelle, Y. Hibino, V. Mizrahi, G.I. Stegeman, "All-optical switching of grating transmission using cross-phase modulation in optical fibres", *Electron. Lett.*, **26**, 1990, pp. 1459-1460.

[44] G. Lenz, B.J. Eggleton, N. Litchinitser, "A pulse compressor based on self-phase modulation in a fiber Bragg grating", in proc. *CLEO'98*, paper CtuM50.

[45] P.C. Chou, H.A. Haus, J.F. Brennan III, "Reconfigurable time-domain spectral shaping of an optical pulse stratched by a fiber Bragg grating", *Opt. Lett.*, **25**, 2000, pp. 524-526.

[46] P.C. Teh, P. Petropoulos, M. Ibsen, D.J. Richardson, "Generation, recognition and recoding of 64-chip bipolar optical code sequences using superstructured fibre Bragg gratings", *Electron. Lett.*, **37**, 2001, pp. 190-191.

[47] G.E. Town, K. Chan, G. Yoffe, "Design and performance of high-speed optical pulse-code generator using optical fiber Bragg gratings", *IEEE Journ. of Selected Topics in Quant. Electron.*, **5**, 1999, pp.1325-1331.

[48] M.C. Cardakli, S. Lee, A.E. Willner, V. Grubsky, D. Starodubov, J. Feinberg, "Reconfigurable optical packet header recognition and routing using time-to-wavelength mapping and tunable fiber Bragg gratings for correlation decoding", *IEEE Phot. Technol. Lett.*, **12**, 2000, pp. 552-554.

[49] S. Longhi, M. Marano, P. Laporta, O. Svelto, M. Belmonte, B. Agogliati, L. Arcangeli, V. Pruneri, M.N. Zervas, M. Ibsen, "40-GHz pulse train generation at 1.5 μm with a chirped fiber grating as a frequency multiplier", *Opt. Lett.*, **25**, 2000, pp. 1481-1483.

[50] M.A. Muriel, J. Azaña, A. Carballar, "Real-time Fourier transformer based on fibre gratings", *Opt. Lett.*, **24**, 1999, pp. 1-3.

[51] Y.J. Rao, "In-fibre Bragg grating sensors", *Meas. Sci. Technol.*, **8**, 1997, pp. 355-375.

[52] A.D. Kersey, M.A. Davis, H.J. Patrick, M. LeBlanc, K.P. Koo, C.G. Askins, M.A. Putnam, E.J. Friebele, "Fiber grating sensors", *J. Lightwave Technol.*, **15**, 1997, pp. 1442-1463.

[53] A. Seeds, "Optical technologies for phased arrays antennas", *IEEE Trans. Electron.*, **E76-c**, 1995, pp. 198-206.

[54] J. Marti, V. Polo, F. Ramos, D. Monodie, "Photonic tunable microwave filters employing electroabsorption modulators and wideband chirped fibre gratings", *Electron. Lett.*, **35**, 1999, pp. 305-306.

[55] G. Yu, W. Zhang, J.A.R. Williams, "Evaluation of RF power degradation in microwave photonic systems employing uniform period fibre Bragg gratings", *Opt. Commun.*, **177**, 2000, pp. 271-275.

[56] A. Yariv, "Coupled-mode theory for guided-wave optics", *IEEE Journ. of Quantum Electron.*, **QE-9**, 1973, pp. 919-933.

Chapter **2**

FIBRE GRATINGS THEORY

2.1 Chapter Overview

This chapter is an introduction to the essential theoretical background used for the description of a large number of distributed feedback waveguide devices, in-fibre gratings included. The first paragraph of the chapter is a detailed analysis of the Coupled-Mode equation method. Because of its simplicity and physical intuitiveness, this method has already been fruitfully used as a preferred approach in understanding the behaviour of fibre gratings but also as an helpful tool for the design of more sophisticated in-fibre structures. The literature on the subject is vast and many good quality books and papers have been published up to now. The paper of Haus *et al.* [1] is a good general review of the most important aspects of the theory. We establish the most general form of Coupled-Mode equations, then we use the method to find the exact expression for the reflectivity (contradirectional coupling) and transmittivity (codirectional coupling) of a uniform grating. Moreover, in the case in which the coupling coefficient is a function of the axial coordinate z, the Transfer Matrix Method (TMM) is introduced as a numerical complement for the solution of the equations.

2.2 Coupled-Mode Theory

Broadly speaking, fibre gratings are periodical refractive index perturbations written directly in the core of the fibre using the fringes produced by two interfering UV laser beams, or also by the diffracted pattern of the light obtained from a phase-mask. The behaviour of both Fibre Bragg Gratings (FBG) and Long Period Gratings (LPG) presents strong analogies with the behaviour of directional couplers: indeed fibre gratings "couple" back and forward travelling modes inside the core or between core and cladding of the fibre. Fibre Bragg gratings can be regarded as a special case (one-dimensional) of "photonic band-gap" devices [2]. When the light travelling in the fibre core meets the grating, the frequencies inside the band gap are back-reflected, while the frequencies that are outside of the band gap can propagate through the grating nearly unaffected (with just a slower speed than the speed of light in a normal silica waveguide in the absence of the grating [3], [4]). In the case of Long Period Gratings instead, the fundamental guided mode travelling in the core of the fibre is coupled to the forward-propagating cladding modes: light is diverted from the core to the fibre cladding, where the cladding-air interface forms a total reflection surface allowing the light to travel for many meters before being lost or be coupled again into the core.

Coupled-mode theory represents the theoretical foundation of fibre gratings (but it is also used for a large class of guided wave components in integrated optics). The theory, developed in the mid fifties to analyse the behaviour of microwave directional couplers [5-7], describes the evolution of the optical field under the influence of directional coupling and starting from quite general premises, it can make very accurate predictions about the spectral response of the grating.

We consider an optical medium in which the dielectric permittivity ε varies periodically along the wave-propagation direction z:

$$\varepsilon(x, y, z) = \varepsilon(x, y) + \Delta\varepsilon(x, y, z) \qquad (2.2.1)$$

Here $\varepsilon(x,y)$ represents the unperturbed part of the dielectric permittivity and $\Delta\varepsilon(x,y,z)$ is periodic along the z direction (fibre axis) and is the only periodically varying part of the dielectric permittivity. We consider $\Delta\varepsilon(x,y,z)$ as a small perturbation that couples the modes of the unperturbed waveguide (the implicit assumption of the theory is that the field of the coupled structure may be represented by a linear superposition of the modes of the unperturbed structure). The normal propagation modes inside the structure described by $\varepsilon(x,y)$ are known and can be written as:

$$\vec{\xi}_m(x, y)e^{i(\beta_m z - \omega t)} \qquad (2.2.2)$$

31

where the mode subscript "m" can be either continuous (unbound modes) or discrete (confined modes) [8-10]. The normal modes in (2.2.2) are solutions of the following wave equation:

$$\left[\nabla_t^2 + \omega^2 \mu_0 \, \varepsilon(x,y) - \beta_m^2\right]\vec{\xi}_m(x,y) = 0 \qquad (2.2.3)$$

The transverse component of the electric field vector in the unperturbed medium can always be expressed in terms of a linear combination of normal modes:

$$\vec{E}_t(x,y,z,t) = \frac{1}{2}\left[\sum_m A_m \, \vec{\xi}_{tm}(x,y) \, e^{i(\beta_m z - \omega t)} + \text{c.c.}\right] \qquad (2.2.4)$$

where the "A_m's" are constant coefficients. Such an expansion is a consequence of the fact that these modes constitute a complete set (normalized to a power flow of 1 W in the direction of propagation z).

The orthogonal relation of the modes can be written as follows [11]

$$\frac{1}{2}\int_{-\infty}^{+\infty}\int_{-\infty}^{+\infty} dx \, dy \left(\vec{\xi}_{t\nu} \times \vec{\zeta}_{t\mu}^*\right)_z = \delta_{\nu\mu} \qquad (2.2.5)$$

where $\vec{\zeta}_\mu$ is the magnetic field associated with the mode $\vec{\xi}_\mu$.

If the modes $\vec{\xi}_m$ satisfy (2.2.3), the orthogonal relation (2.2.5) becomes:

$$\int_{-\infty}^{+\infty}\int_{-\infty}^{+\infty} dx \, dy \, \vec{\xi}_{t\mu}^*(x,y) \cdot \vec{\xi}_{t\nu}(x,y) = \frac{2\omega\mu_0}{\beta_\mu}\delta_{\nu\mu} \qquad (2.2.6)$$

where $\delta_{\nu\mu}$ is the Kronecker delta symbol for confined modes and the Dirac delta function for unbound modes.

We want to analyse now the propagation of the unperturbed modes in a medium described by the perturbed dielectric permettivity (2.2.1). The mathematical approach consists in expressing the electric field as an expansion in the normal modes of the unperturbed dielectric structure, where the expansion coefficients clearly depend on z, as for $\Delta\varepsilon \neq 0$ the waves in (2.2.2) are not eigenmodes anymore [12-14].

Assuming that the field contains forward and backward propagating modes, we can write its transverse component as:

$$\vec{E}_t(x,y,z,t) = \frac{1}{2}\left\{\sum_m \left[A_m(z)e^{i\beta_m z} + B_m(z)e^{-i\beta_m z}\right]\vec{\xi}_{tm}(x,y)e^{-i\omega t} + \text{c.c.}\right\} \qquad (2.2.7)$$

By inserting equation (2.2.7) into the following perturbed wave equation:

$$\left\{\nabla^2 + \omega^2\mu_0\left[\varepsilon(x,y) + \Delta\varepsilon(x,y,z)\right]\right\}\vec{E} = 0 \qquad (2.2.8)$$

and using (2.2.3), we find:

$$\sum_{\mu} \left\{ \left[\frac{d^2 A_{\mu}}{dz^2} + 2i\beta_{\mu} \frac{dA_{\mu}}{dz} \right] e^{i\beta_{\mu}z} + \left[\frac{d^2 B_{\mu}}{dz^2} - 2i\beta_{\mu} \frac{dB_{\mu}}{dz} \right] e^{-i\beta_{\mu}z} \right\} \vec{\xi}_{t\mu}(x,y) =$$

$$-\omega^2 \mu_0 \sum_{\nu} \Delta\varepsilon(x,y,z) \left[A_{\nu} e^{+i\beta_{\nu}z} + B_{\nu} e^{-i\beta_{\nu}z} \right] \vec{\xi}_{t\nu}(x,y) \qquad (2.2.9)$$

We assume further that the perturbation of the dielectric medium is "weak", so that the variation of the mode amplitudes is "slow" i.e.

$$\left| \frac{d^2 A_{\mu}}{dz^2} \right| << \left| \beta_{\mu} \frac{dA_{\mu}}{dz} \right| \text{ and } \left| \frac{d^2 B_{\mu}}{dz^2} \right| << \left| \beta_{\mu} \frac{dB_{\mu}}{dz} \right| \qquad (2.2.10)$$

then neglecting the second derivative in (2.2.9) we have

$$2i \sum_{\mu} \beta_{\mu} \left[\frac{dA_{\mu}}{dz} e^{i\beta_{\mu}z} - \frac{dB_{\mu}}{dz} e^{-i\beta_{\mu}z} \right] \vec{\xi}_{t\mu}(x,y) =$$

$$-\omega^2 \mu_0 \sum_{\nu} \Delta\varepsilon(x,y,z) \left[A_{\nu} e^{i\beta_{\nu}z} + B_{\nu} e^{-i\beta_{\nu}z} \right] \vec{\xi}_{t\nu}(x,y) \qquad (2.2.11)$$

If we take the scalar product of equation (2.2.11) with $\vec{\xi}_{t\mu}^*(x,y)$, integrating over all x and y and using the orthogonal property of the normal modes (2.2.6), we finally obtain:

$$\frac{dA_{\mu}}{dz} e^{i\beta_{\mu}z} - \frac{dB_{\mu}}{dz} e^{-i\beta_{\mu}z} =$$

$$i \frac{\omega}{4} \int_{-\infty}^{+\infty} \int_{-\infty}^{+\infty} dx\, dy \sum_{\nu} \Delta\varepsilon(x,y,z) \left[A_{\nu} e^{i\beta_{\nu}z} + B_{\nu} e^{-i\beta_{\nu}z} \right] \vec{\xi}_{t\mu}^*(x,y) \cdot \vec{\xi}_{t\nu}(x,y) \qquad (2.2.12)$$

We introduce now the transverse coupling coefficient between the modes μ and ν defined as follow

$$\kappa_{\mu\nu}^t(z) = \frac{\omega}{4} \int_{-\infty}^{+\infty} \int_{-\infty}^{+\infty} dx\, dy\, \Delta\varepsilon(x,y,z) \vec{\xi}_{t\mu}^*(x,y) \cdot \vec{\xi}_{t\nu}(x,y) \qquad (2.2.13)$$

leading to real and positive quantity for a positive $\Delta\varepsilon$.

We can finally write the equations governing the evolution along the z-axis of the amplitudes A_{μ} and B_{μ} of the μ-th mode as follows:

$$\frac{dA_{\mu}}{dz} = i \sum_{\nu} A_{\nu} \left(\kappa_{\nu\mu}^t + \kappa_{\nu\mu}^z \right) e^{i(\beta_{\nu} - \beta_{\mu})z} + i \sum_{\nu} B_{\nu} \left(\kappa_{\nu\mu}^t - \kappa_{\nu\mu}^z \right) e^{-i(\beta_{\nu} + \beta_{\mu})z}$$

$$\frac{dB_{\mu}}{dz} = -i \sum_{\nu} A_{\nu} \left(\kappa_{\nu\mu}^t - \kappa_{\nu\mu}^z \right) e^{i(\beta_{\nu} + \beta_{\mu})z} - i \sum_{\nu} B_{\nu} \left(\kappa_{\nu\mu}^t + \kappa_{\nu\mu}^z \right) e^{-i(\beta_{\nu} - \beta_{\mu})z}$$

$$(2.2.14)$$

We notice that considering the longitudinal component of the field E_z results in an additional coupling coefficient $\kappa_{\nu\mu}^z$. Nevertheless, as in a standard optical fibre such a coupling coefficient is generally much smaller in comparison with the transverse one

$\kappa_{\nu\mu}^z(z) \ll \kappa_{\nu\mu}^t(z)$, we can neglect it as a first approximation. Equations (2.2.14) constitute a set of coupled linear differential equations showing the change in the amplitude of each mode μ as a function of the perturbation $\Delta\varepsilon$ to the permettivity, the modal transverse field distribution, and the amplitude of all other modes present in the waveguide.

The perturbation $\Delta\varepsilon$ is the result of the phase grating written by UV laser directly in the fibre core, and the index profile of the fibre can by expressed as follows [15], [16]

$$n(x,y,z) = \begin{cases} n_{co}(x,y,z) = n_{co}\left\{1 + \sigma(x,y,z)\left[1 + p\cos\left(\frac{2\pi}{\Lambda}z + \Phi(z)\right)\right]\right\}, & r \le r_{co} \\ n_{cl} & , & r_{co} < r \le r_{cl} \\ n & , & r > r_{cl} \end{cases}$$

where n_{co}, n_{cl} and n are the unperturbed refractive indexes of the core, the cladding and the surrounding medium (air), respectively, Λ is the period of the index modulation (grating period), p is the visibility of the fringes ($0 \le p \le 1$), $\Phi(z)$ describes the grating chirp and $\sigma(x,y,z)$ is the envelope of the index perturbation. For a small index perturbation ($\sigma \ll 1$) we can assume $\Delta\varepsilon = \varepsilon_0 \Delta(n^2) \cong 2\varepsilon_0 n \Delta n$, then:

$$\Delta\varepsilon(x,y,z) = \begin{cases} 2\varepsilon_0 n_{co} \sigma(x,y,z)\left[1 + p\cos\left(\frac{2\pi}{\Lambda}z + \Phi(z)\right)\right], & r \le r_{co} \\ 0 & , & r > r_{co} \end{cases}$$

We could also distinguish between two different contributions to the coupling of the modes in the structure, a dc (period-averaged) and an ac coupling leading to the following coupling coefficients:

$$\kappa_{dc,\nu\mu}(z) = \frac{\omega}{2}\varepsilon_0 n_{co} \iint_{core} dx\, dy\, \sigma(x,y,z)\, \vec{\xi}_{\nu t}(x,y) \cdot \vec{\xi}_{\mu t}^*(x,y)$$

$$\kappa_{ac,\nu\mu}(z) = \frac{p}{2}\kappa_{dc,\nu\mu}(z)$$

(2.2.15)

This allows us to write the coupling coefficient as

$$\kappa_{\nu\mu}^t(z) = \kappa_{dc,\nu\mu}(z) + 2\kappa_{ac,\nu\mu}(z)\cos\left[\frac{2\pi}{\Lambda}z + \Phi(z)\right]$$

(2.2.16)

2.3 Solution of Coupled-Mode Equations for Uniform Gratings

2.3.1 Counter-directional Coupling

The behaviour of fibre Bragg gratings presents many analogies with the behaviour of other periodic dielectric structures that couple counter-propagating modes [17-19] and it can be fully described and understood using the coupled-mode theory. In the special case of

FBG's, the coupling occurs between the forward-propagating and the grating back-reflected part of the same fundamental guided mode travelling in the core of the fibre. As the difference Δn in the core-cladding refractive index of a standard single mode telecommunications fibre is usually less than 1%, we can use the weakly guiding approximation in our analysis (the modes inside the structure are supposed to be Linearly Polarized (LP)).

Inside the grating and around the wavelength at which the reflection of LP_{01} core mode occurs, the dominant interaction is between the amplitude $A^{co}(z)$ of the forward-propagating part of the mode with an identical counter-propagating part of amplitude $B^{co}(z)$. Retaining only the terms that involve A^{co} and B^{co} and making use of the synchronous approximation [20], we can write the coupled-mode equation for the fibre Bragg grating as follows:

$$\frac{d A^{co}}{dz} = i \; \kappa_{01-01}^{co-co} \; A^{co} + i \frac{p}{2} \; \kappa_{01-01}^{co-co} \; B^{co} \; e^{-i\left[\delta_{01-01}^{co-co} \, z - \Phi(z)\right]}$$

$$\frac{d B^{co}}{dz} = -i \; \kappa_{01-01}^{co-co} \; B^{co} - i \frac{p}{2} \; \kappa_{01-01}^{co-co} \; A^{co} \; e^{i\left[\delta_{01-01}^{co-co} \, z - \Phi(z)\right]}$$

(2.3.1)

where, by definition, $\delta_{01-01}^{co-co} = 2 \, \beta_{01}^{co} - \dfrac{2\pi}{\Lambda}$ is the detuning parameter.

The coupling coefficient can be calculated as

$$\kappa_{01-01}^{co-co} = \frac{\pi \, n_{co}}{\lambda \, Z_0} \iint\limits_{core} dx \; dy \; \sigma(x,y,z) \left| \xi_{01_t}^{co}(x,y) \right|^2$$

(2.3.2)

where $Z_0 = \sqrt{\mu_0 / \varepsilon_0}$ is the vacuum impedance and $\xi_{01_t}^{co}(x,y)$ is the transverse vector component of the LP_{01} core mode field inside the core region [21]

$$\xi_{01_t}^{co}(x,y) = \Gamma \, J_0\left(\frac{v \sqrt{1-b}}{r_{co}} r\right) \qquad r < r_{co}$$

(2.3.3)

Here Γ is a normalization constant based on a total power carried by the mode of 1 W:

$$\Gamma = \left[\frac{2 \, Z_0 \, b}{\pi \, n_{cl} \, (1 + b\Delta)}\right]^{\frac{1}{2}} \frac{1}{r_{co} \, J_1\left(v - \sqrt{1-b}\right)}$$

(2.3.4)

and v is the normalized frequency

$$v = \frac{2\pi}{\lambda} r_{co} \, n_{co} \, \sqrt{2\Delta}$$

(2.3.5)

$\Delta = (n_{co} - n_{cl})/n_{co}$ is the relative index difference and b is the normalized propagation constant of the fundamental mode:

$$b = \frac{\dfrac{\beta^2}{k_0^2} - n_{cl}^2}{n_{co}^2 - n_{cl}^2} \cong \frac{\dfrac{\beta_{01}^{co}}{k_0} - n_{cl}}{n_{co} - n_{cl}}, \quad k_0 = \frac{2\pi}{\lambda}, \quad \text{from which} \quad \beta_{01}^{co} = k_0\, n_{eff,01}^{co} = \frac{2\pi}{\lambda}\, n_{cl}\!\left(1 + b\,\Delta\right).$$

For each allowed mode, the dependence of the normalised propagation constant b from the normalised frequency v is known as dispersion relation and, for the modes propagating in the fibre core, is obtained by solving the transcendental equation [17]

$$v\sqrt{1-b}\,\frac{J_{\ell+1}(v\sqrt{1-b})}{J_\ell(v\sqrt{1-b})} = v\sqrt{b}\,\frac{K_{\ell+1}(v\sqrt{b})}{K_\ell(v\sqrt{b})} \tag{2.3.6}$$

or the mathematically equivalent one

$$v\sqrt{1-b}\,\frac{J_{\ell-1}(v\sqrt{1-b})}{J_\ell(v\sqrt{1-b})} = -v\sqrt{b}\,\frac{K_{\ell-1}(v\sqrt{b})}{K_\ell(v\sqrt{b})} \tag{2.3.7}$$

A plot of the dispersion relation of the core mode LP_{01} in a step index single mode fibre at 1550 nm is shown in Fig. 2.1.
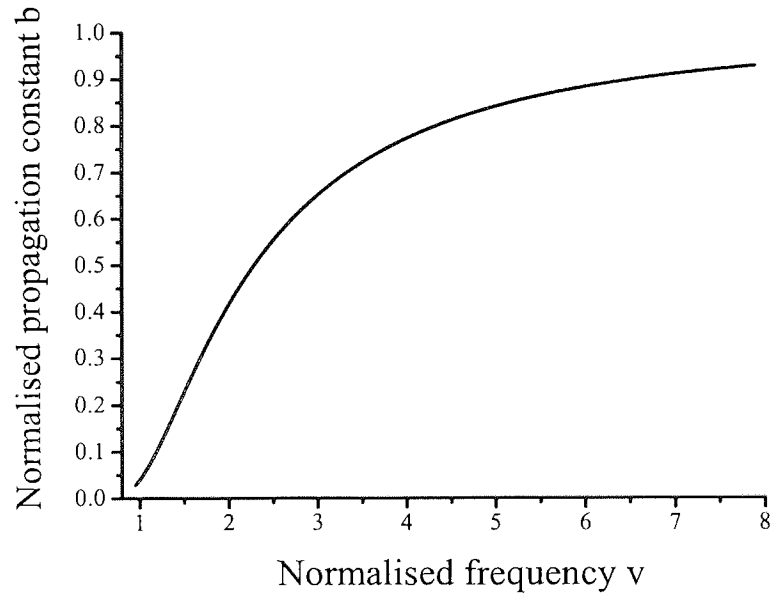
Figure 2.1 Dispersion relation for the fundamental core mode LP_{01} numerically calculated (using the weakly guiding approximation) at 1550 nm in a single mode step index fibre having a core-cladding refractive index difference $\Delta = 0.0028$, a core radius $r_{co} = 6$ μm, and a cladding radius $r_{cl} = 80$ μm.

As the LP_{01} mode is the only mode allowed in the core of a single mode fibre we can simplify the notation without any risk of misunderstanding:

$$A^{co} \equiv A \qquad B^{co} \equiv B \qquad \kappa_{01-01}^{co-co} \equiv 2\kappa \qquad \delta_{01-01}^{co-co} \equiv \delta \quad \text{and} \quad p = 1.$$

If we introduce, by definition, the two amplitudes R(z) and S(z) as follows:

$$R(z) = A(z) e^{\frac{i}{2}[\delta z - \Phi(z)]}$$

$$S(z) = B(z) e^{-\frac{i}{2}[\delta z - \Phi(z)]}$$

we can rewrite the coupled-mode equations (2.3.1) in the following very simple form:

$$\frac{dR}{dz} = i\varepsilon R + i\kappa S$$

$$\frac{dS}{dz} = -i\kappa R - i\varepsilon S \qquad (2.3.8)$$

where $\varepsilon = 2\kappa + \frac{1}{2}\left(\delta - \frac{d\Phi}{dz}\right)$.

The physical meaning of ε is as follows: $\frac{1}{2}\delta$ is the detuning and indicates how rapidly the power is exchanged between forward and backward travelling modes, κ influences the propagation due to the refractive index changes and the term $\frac{1}{2}\frac{d\Phi}{dz}$ takes in account a possible chirp of the grating period Λ.
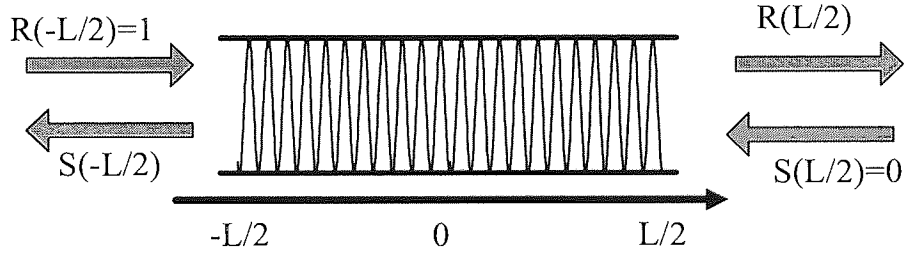
Figure 2.2 *Boundary conditions used for the solution of coupled-mode equations (2.3.8) in the counter-propagative case.*

For a uniform grating along the propagation axis z we have that $\sigma(x,y,z) = \sigma(x,y)$ and $d\Phi/dz = 0$, i.e. both ε and κ are constant coefficients. Then Eqs. (1.3.6) are a couple of first order ordinary differential equations with constant coefficients. A close-form solution for these equations can be found when appropriate boundary conditions are specified. We suppose that our dielectric medium is not dissipating power and that there is not backward going wave for $z \geq L/2$ so that $S(L/2) = 0$. Finally, the condition $R(-L/2) = 1$ corresponds to a forward going wave coming from $z = -\infty$. The solution of the coupled-mode equations gives the following expression for the amplitude reflection coefficient of the grating:

$$\rho = \frac{S(-L/2)}{R(-L/2)} = \frac{-\kappa \sinh(\alpha L)}{\varepsilon \sinh(\alpha L) + i\alpha \cosh(\alpha L)} \qquad (2.3.9)$$

37

where $\alpha = \sqrt{\kappa^2 - \varepsilon^2}$.

The reflectivity of the FBG, i.e. the power reflection coefficient, is then:

$$R = |\rho|^2 = \frac{\kappa^2 \sinh^2(\alpha L)}{\kappa^2 \cosh^2(\alpha L) - \varepsilon^2} \qquad (2.3.10)$$

The maximum reflectivity, that occurs when $\varepsilon = 2\kappa + \dfrac{\delta}{2} = 0$, is $R = \tanh^2(\kappa L)$ and it occurs at the wavelength

$$\lambda_{max} = \frac{\lambda_B}{1 - 2\kappa\dfrac{\Lambda}{\pi}} \qquad (2.3.11)$$

A useful measure of the bandwidth of a FBG is the separation between the first zeros on either side of the spectral peak that can be calculated equating the numerator in (2.3.10) to zero, which results in:

$$\varepsilon = \kappa \sqrt{1 + \left(\frac{\pi}{\kappa L}\right)^2} \qquad (2.3.12)$$

Assuming $\kappa = 0$, we have:

$$\varepsilon = 2\pi n_{eff,01}\left(\frac{1}{\lambda} - \frac{1}{\lambda_{max}}\right) \approx 2\pi n_{eff,01}\frac{\lambda_{max} - \lambda}{\lambda_{max}^2} \qquad (2.3.13)$$

Combining equations (2.3.12) and (2.3.13), we find that the bandwidth $\Delta\lambda = 2(\lambda_{max} - \lambda)$ between the first zeros is given by:

$$\Delta\lambda = \frac{\lambda_{max}^2}{n_{eff,01} L}\sqrt{1 + \left(\frac{\kappa L}{\pi}\right)^2} \qquad (2.3.14)$$

For the case of a uniform Bragg grating written in a step index fibre the envelope of the index perturbation $\sigma(x,y)$ is a constant:

$$\sigma(x,y) = \begin{cases} \sigma & \text{for } r \leq r_{co} \\ 0 & \text{for } r > r_{co} \end{cases} \qquad (2.3.15)$$

Using (2.3.3) and inserting (2.3.15), the coupling coefficient in (2.3.2) becomes:

$$\kappa = \frac{\pi n_{co}\,\sigma}{2\lambda Z_0}\Gamma^2 \int_0^{2\pi} d\varphi \int_0^{r_{co}} r\, dr\ J_0^2\left(\frac{v\sqrt{1-b}}{r_{co}}r\right) \qquad (2.3.16)$$

Then from (2.3.4) and using the Bessel function property [22]

$$\int z\, dz\ J_0^2(\eta z) = \frac{z^2}{2}\left[J_0^2(\eta z) + J_1^2(\eta z)\right]$$

38
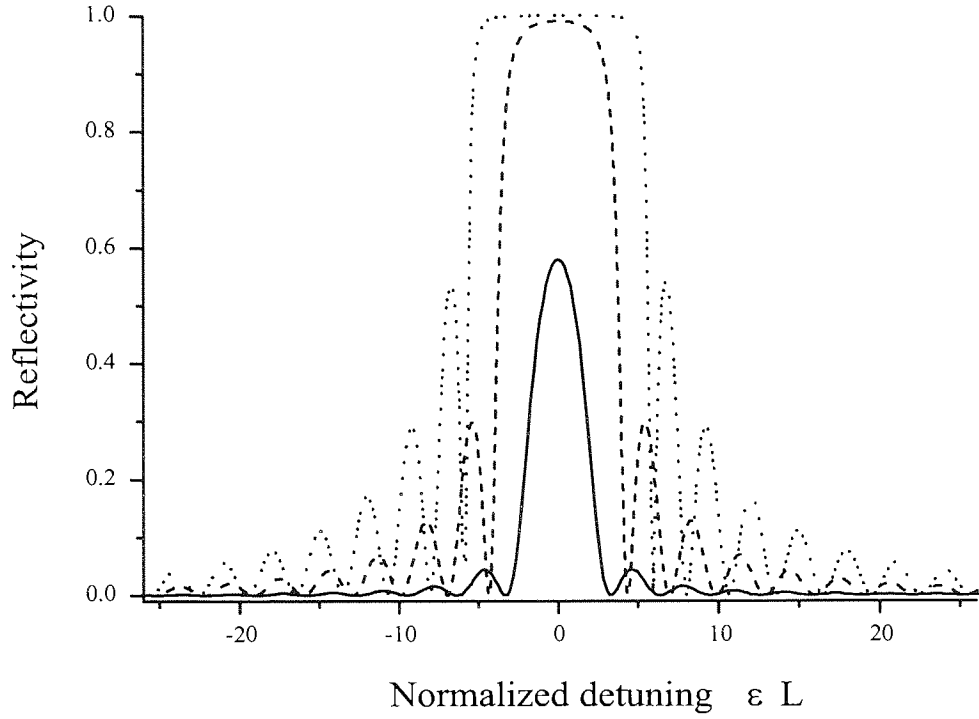
Figure 2.3 *Reflection spectra, calculated from Eq. (2.3.10), for a uniform Bragg grating with a physical length L=2 cm and strength* $\kappa L = 1$ *(solid line),* $\kappa L = 3$ *(dashed line),* $\kappa L = 5$ *(dotted line) respectively.*
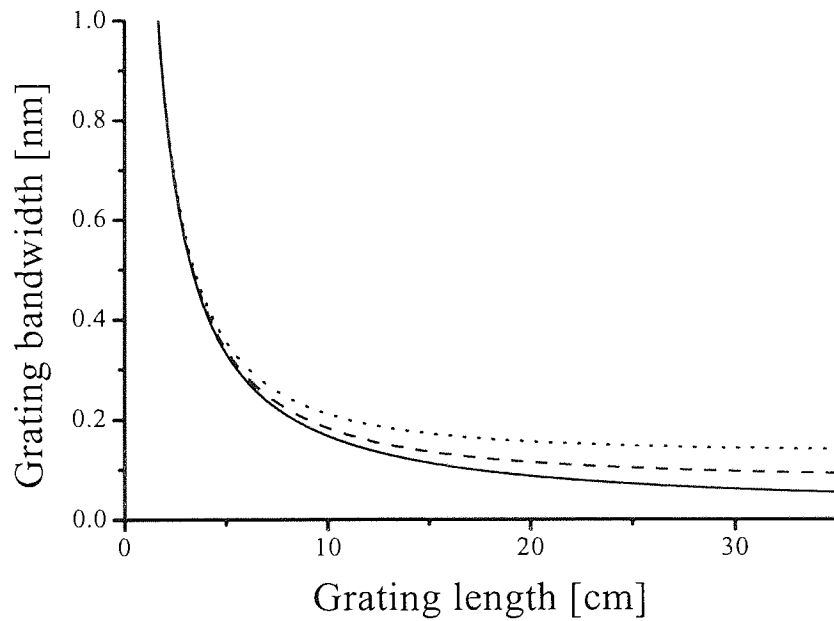
Figure 2.4 *Dependence of the grating bandwidth on physical length for a uniform Bragg grating, as calculated from (2.3.14), for three different values of the coupling coefficient:* $\kappa = 5 \times 10^{-5}$ μm^{-1} *(solid line),* $\kappa = 1.5 \times 10^{-4}$ μm^{-1} *(dashed line) and* $\kappa = 2.5 \times 10^{-4}$ μm^{-1} *(dotted line) .*

we obtain then the explicit expression for the coupling coefficient:

$$\kappa = \frac{\pi b\, n_{co}\, \sigma}{\lambda\, n_{cl}\, (1 + b\Delta)} \left[1 + \frac{J_0^2 \left(v\sqrt{1-b} \right)}{J_1^2 \left(v\sqrt{1-b} \right)} \right] \tag{2.3.17}$$

2.3.2 Codirectional Coupling

We consider the coupling between the fundamental core mode and the forward-propagating inner cladding modes. Using an identical procedure and making the same assumptions as in the case of counter-directional coupling, we can write the general form of the coupled-mode equations case as follows:

$$\frac{d\,A^{co}}{dz} = i\,\kappa_{01-01}^{co-co}\, A^{co} + i\,\kappa_{01-\ell m}^{co-cl}\, B^{cl}\, e^{-i\left[\delta_{01-\ell m}^{co-cl}\, z - \Phi(z) \right]}$$

$$\frac{d\,B^{cl}}{dz} = i\,\kappa_{\ell m - \ell m}^{cl-cl}\, B^{cl} + i\,\kappa_{01-\ell m}^{co-cl}\, A^{co}\, e^{i\left[\delta_{01-\ell m}^{co-cl}\, z - \Phi(z) \right]} \tag{2.3.18}$$

where A^{co} and B^{cl} are the amplitudes of the LP_{01} core mode and the $LP_{\ell m}$ cladding mode respectively, $\delta_{01-\ell m}^{co-cl} = \beta_{01}^{co} - \beta_{\ell m}^{cl} - \frac{2\pi}{\Lambda}$ is the detuning parameter and the coupling coefficients are given by (2.3.2) and

$$\kappa_{\ell m - \ell m}^{cl-cl} = \frac{\pi\, n_{co}}{\lambda\, Z_0} \iint\limits_{core} dx\, dy\; \sigma(x, y, z) \left| \xi_{\ell m_t}^{cl}(x, y) \right|^2 \tag{2.3.19}$$

$$\kappa_{01-\ell m}^{co-cl} = \frac{\pi\, n_{co}\, p}{2\lambda\, Z_0} \iint\limits_{core} dx\, dy\; \sigma(x, y, z)\; \xi_{01_t}^{co\,*}(x, y) \cdot \xi_{\ell m_t}^{cl}(x, y) \tag{2.3.20}$$

The transverse vector component of the electric field of a $LP_{\ell m}$ cladding mode in the fibre core is given by [21]

$$\xi_{\ell m_t}^{cl}(x, y) = \Psi\, J_\ell \left(\frac{V\sqrt{1-B}}{r_{co}}\, r \right) \cos(\ell\varphi) \quad , \quad r < r_{co} \tag{2.3.21}$$

where Ψ is a normalization constant based on a total power of 1 W carried by the mode (see [23] for details on calculations), V is the normalized frequency

$$V = \frac{2\pi}{\lambda}\, r_{co}\, \sqrt{2n\, (n_{co} - n)} \tag{2.3.22}$$

and B is the normalised propagation constant of the mode

$$B \approx \frac{\dfrac{\beta_{\ell m}^{cl}}{k_0} - n}{n_{co} - n} \quad \text{from which} \quad \beta_{\ell m}^{cl} = k_0\, n_{eff,\ell m}^{cl} = \frac{2\pi}{\lambda}\left[n + B\left(n_{co} - n \right) \right]$$

The dispersion relation for the modes allowed in the fibre cladding can be obtained, in analogy to the case of the core mode, by solving a transcendental equation including Bessel function [23].
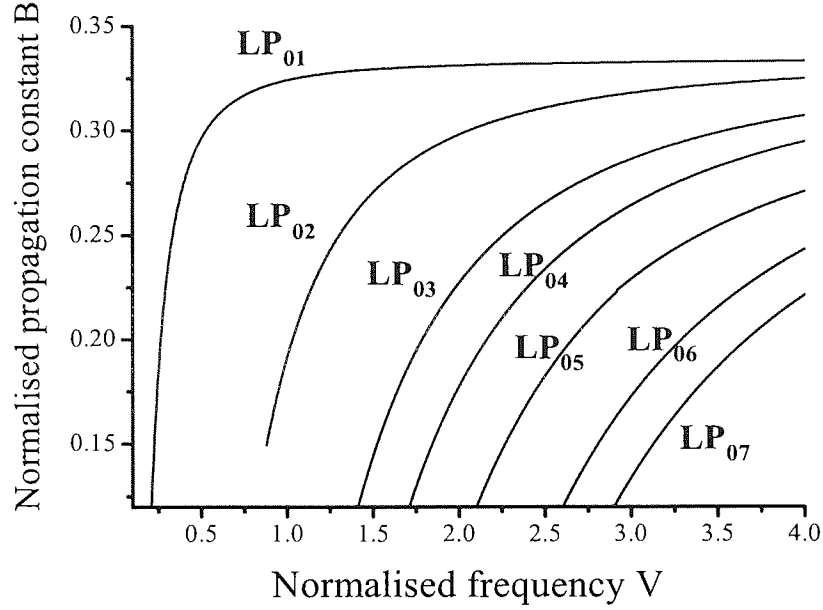
Figure 2.5 *Dispersion relation for the cladding modes of order LP$_{0m}$ (calculated at 1550 nm by using the weakly guiding approximation) in a step index fibre with a core-cladding refractive index difference Δ=0.0028, core radius r_{co}= 6 μm, and cladding radius r_{cl}=80 μm.*

If we now introduce the amplitudes

$$R(z) = A^{co}(z)\, e^{-\frac{i}{2}\left(\kappa_{01-01}^{co-co}+\kappa_{\ell m-\ell m}^{cl-cl}\right)z}\, e^{\frac{i}{2}\left[\delta_{01-\ell m}^{co-cl}\, z-\Phi(z)\right]}$$

$$S(z) = B^{cl}(z)\, e^{-\frac{i}{2}\left(\kappa_{01-01}^{co-co}+\kappa_{\ell m-\ell m}^{cl-cl}\right)z}\, e^{-\frac{i}{2}\left[\delta_{01-\ell m}^{co-cl}\, z-\Phi(z)\right]}$$

the coupled-mode equations (2.3.18) can be rewritten as

$$\frac{dR}{dz} = i\,\varepsilon_{\ell m}R + i\,\kappa_{01-\ell m}^{co-cl}\, S$$

$$\frac{dS}{dz} = -i\,\varepsilon_{\ell m}S + i\,\kappa_{01-\ell m}^{co-cl}\, R$$

(2.3.23)

where we have introduced the dc self-coupling coefficient

$$\varepsilon_{\ell m} = \frac{1}{2}\left(\delta_{01-\ell m}^{co-cl} + \kappa_{01-01}^{co-co} + \kappa_{\ell m-\ell m}^{cl-cl} - \frac{d\Phi(z)}{dz}\right)$$

(2.3.24)

41

We consider the case of a uniform grating along z: $\sigma = \sigma(x,y)$ and $\dfrac{d\Phi}{dz} = 0$. A closed-

form solution of (2.3.23) can be found using the boundary conditions $R(0) = 1$ and $S(0) = 0$ at the beginning of the interaction region.
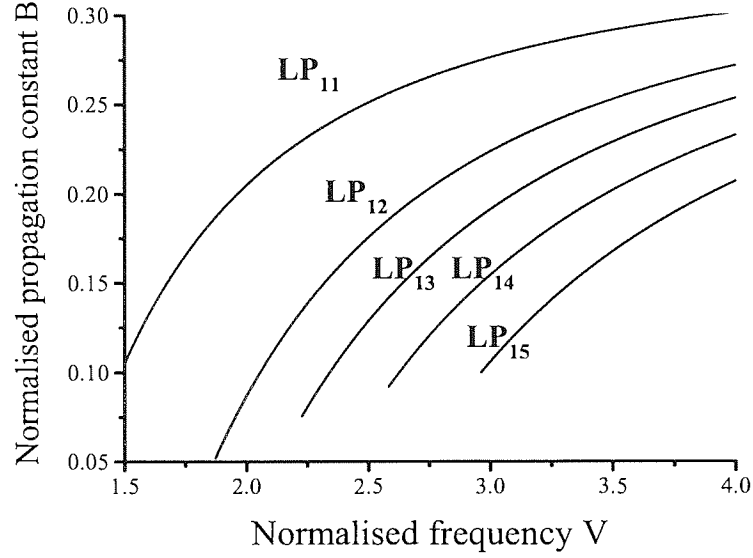
Figure 2.6 *Dispersion relation for the cladding modes of order LP_{1m} (calculated at 1550 nm by using the weakly guiding approximation) in a step index fibre with a core-cladding refractive index difference $\Delta=0.0028$, core radius $r_{co}=6$ μm, and cladding radius $r_{cl}=80$ μm.*

The transmittivity in the coupled state (or cross-transmission) for the coupling of the LP_{01} core mode to the $LP_{\ell m}$ cladding mode is given by

$$T_{\ell m} = \frac{|S(L)|^2}{|R(0)|^2} = \frac{1}{1 + \left(\dfrac{\varepsilon_{\ell m}}{\kappa^{co-cl}_{01-\ell m}}\right)^2} \sin^2\left(\alpha_{\ell m} L\right) \qquad (2.3.25)$$

where $\alpha_{\ell m} = \sqrt{\left(\kappa^{co-cl}_{01-\ell m}\right)^2 - \left(\varepsilon_{\ell m}\right)^2}$.

In analogy with the counter-propagative case, we find that the bandwidth (defined as the distance between the first zeros on either side of the spectral peak) can be written as

$$\Delta\lambda = \frac{2\lambda_{max}}{L\,\Delta n^{co-cl}_{eff}}\sqrt{1 - \left(\frac{L\,\kappa^{co-cl}_{01-\ell m}}{\pi}\right)^2} \qquad (2.3.26)$$

where $\Delta n^{co-cl}_{eff} = n^{co}_{eff,01} - n^{cl}_{eff,\ell m}$.

a)

b)
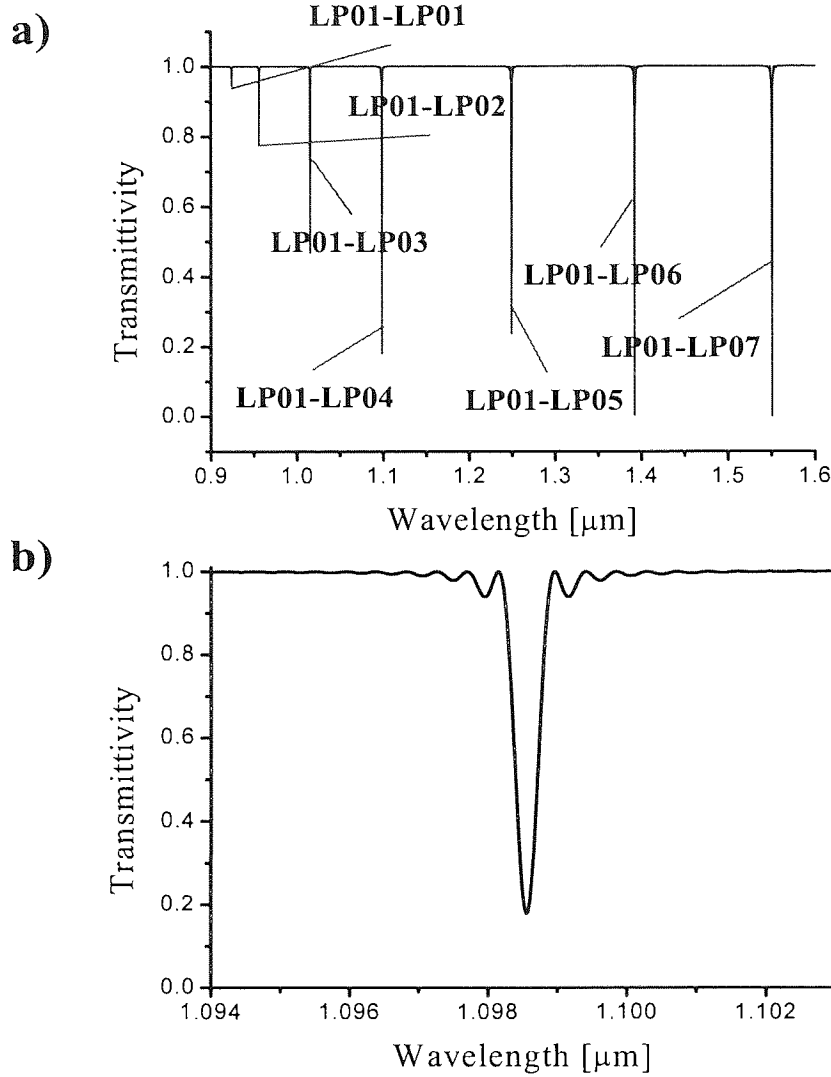
Figure 2.7 *a) Representative Long Period Grating transmission spectrum (in the coupled-state) as calculated from (2.3.27). The maximum coupling occurs between the LP_{01} core mode and the LP_{07} cladding mode at 1550 nm (the grating is supposed to be 18 cm long with a period Λ=400 μm. The condition $\kappa_{01-07}^{co-cl}\,L = \pi/2$ gives a value of the index modulation $\sigma = 4.36 \times 10^{-5}$), b) high resolution enlargement of the peak generated by the coupling LP_{01}-LP_{04}.*

The total cross transmission for coupling to cladding modes of the same order ℓ is

$$T_\ell = \sum_m T_{\ell m} \tag{2.3.27}$$

We notice that for a constant grating profile (2.3.15), the azimuthal integral in (2.3.20) becomes

$$\int_0^{2\pi} d\varphi \ \cos(\ell\varphi) = 2\pi\delta_{\ell 0}$$

43

Therefore the only non zero cross-coupling coefficients are those between the LP_{01} core mode and the LP_{0m} cladding modes. The self coupling constant for the core mode is given by (2.3.17). Using (2.3.21), the self-coupling constants for the cladding modes can be written as

$$\kappa_{0m-0m}^{cl-cl} = \frac{\pi\, n_{co}\, \sigma}{\lambda\, Z_0}\, \Psi^2 \int_0^{2\pi} d\varphi \int_0^{r_{co}} r\, dr\, J_0^2\left(\frac{V\sqrt{1-B}}{r_{co}}r\right) =$$

$$= \frac{\pi^2\, r_{co}^2\, n_{co}\, \sigma}{\lambda\, Z_0}\, \Psi^2 \left[J_0^2(V\sqrt{1-B}) + J_1^2(V\sqrt{1-B})\right] \qquad (2.3.28)$$

Finally, we write the cross coupling constant as

$$\kappa_{01-0m}^{co-cl} = \frac{\pi\, n_{co}\, \sigma}{2\lambda\, Z_0}\, \Gamma\, \Psi^2 \int_0^{2\pi} d\varphi \int_0^{r_{co}} r\, dr\, J_0\left(\frac{v\sqrt{1-b}}{r_{co}}r\right) J_0\left(\frac{V\sqrt{1-B}}{r_{co}}r\right) \qquad (2.3.29)$$

Using Eq. (2.3.4) and the property

$$\int z\, dz\, J_0(\eta z) J_0(\vartheta z) = \frac{z}{\eta^2 - \vartheta^2}\left[-\vartheta J_0(\eta z) J_1(\vartheta z) + \eta J_0(\vartheta z) J_1(\eta z)\right]$$

we obtain

$$\kappa_{01-0m}^{co-cl} = \frac{r_{co}\, n_{co}\, \sigma}{\lambda}\left[\frac{2\pi^3\, b}{Z_0\, n_{cl}\,(1+b\Delta)}\right]^{\frac{1}{2}} \Psi\, \frac{1}{v^2(1-b) - V^2(1-B)}$$

$$\times \left[-V\sqrt{1-B}\,\frac{J_0(v\sqrt{1-b})}{J_1(v\sqrt{1-b})}J_1(V\sqrt{1-B}) + v\sqrt{1-b}\, J_0(V\sqrt{1-B})\right] \qquad (2.3.30)$$

2.4 The Transfer Matrix (Piecewise-Uniform) Approach

There are practical cases (for instance in the case of apodized and chirped gratings) in which the grating structure is not uniform along the propagation axis z, which implies $\kappa = \kappa(z)$. In such a case the coupled-mode equations become a set of two coupled first-order ordinary differential equations with variable coefficients and a closed-form solution is not available anymore for these equations. Apart from direct numeric integration, a method that can be successfully applied is the piecewise-uniform approach. The idea is to model the non-uniform grating considering a certain number of slides within each the structure is assumed to be uniform, then associating a 2×2 matrix to each uniform section. The different contributions are multiplied to obtain a single 2×2 matrix describing the whole grating [24-28].

As an example of the application of the method, we consider the case of a bell-like function apodized grating: the envelope of the index modulation can be written as

$$\sigma(x,y,z) = \begin{cases} \sigma\ f(z) & \text{for } r \le r_{co} \\ 0 & \text{for } r > r_{co} \end{cases}$$

where f(z) is an apodization function as, for instance, a gaussian function or a one period of square cosine.

To apply the method of piecewise-uniform to the structure, we devide the grating in M uniform sections and we indicate with R_i and S_i the amplitudes of the field traversing the i-th section. For an apodized Bragg grating we start considering $R_0 = R(L/2) = 1$ and $S_0 = S(L/2) = 0$ and we want to calculate $R(-L/2) = R_M$ and $S(-L/2) = S_M$.
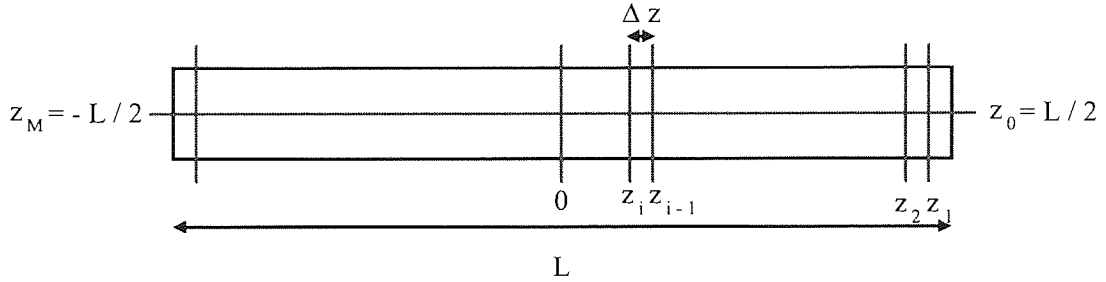
Figure 2.8 *Schematic diagram illustrating the application of piecewise-uniform method by dividing the non-uniform grating in M sections within each the grating is considered as uniform.*

The propagation through each uniform section is described by [29-31]

$$\begin{bmatrix} R_i \\ S_i \end{bmatrix} = F_i \cdot \begin{bmatrix} R_{i-1} \\ S_{i-1} \end{bmatrix} \tag{2.4.1}$$

where, for a Bragg grating, the F_i matrix is given by

$$F_i = \begin{bmatrix} \cosh(\alpha_i\ \Delta z) - i\ \dfrac{\varepsilon_i}{\alpha_i}\sinh(\alpha_i\ \Delta z) & -i\ \dfrac{\kappa_i}{\alpha_i}\sinh(\alpha_i\ \Delta z) \\ i\ \dfrac{\kappa_i}{\alpha_i}\sinh(\alpha_i\ \Delta z) & \cosh(\alpha_i\ \Delta z) + i\ \dfrac{\varepsilon_i}{\alpha_i}\sinh(\alpha_i\ \Delta z) \end{bmatrix} \tag{2.4.2}$$

and κ_i has a constant value calculated at the centre of each section:

$$\kappa_i = \kappa \cdot f\left(\frac{z_{i-1} + z_i}{2}\right)$$

Once that all of the matrices for the individual sections have been calculated, we calculate the output amplitude from

$$\begin{bmatrix} R_M \\ S_M \end{bmatrix} = F \cdot \begin{bmatrix} R_0 \\ S_0 \end{bmatrix}$$

45

where the matrix F describes the whole structure and is calculated as

$$F = F_M \cdot F_{M-1} \cdot \cdots \cdot F_i \cdot \cdots \cdot F_1$$

Then the total power reflection coefficient R of the grating can be calculated as

$$R = \left| \frac{S_M}{R_M} \right|^2 \qquad (2.4.3)$$

2.5 Chapter Conclusions

This chapter contains the theoretical background of the present thesis. Starting from very general premises, within the usual electromagnetic theory (i.e., considering the propagation of EM waves in a slightly perturbed periodical optical medium), we derived a detailed formulation of the coupled-mode equations. In their most general form these equations are expressed as in Eq. (2.2.14) and are the indispensable tool for the description of the evolution of the amplitudes of modes interacting along the propagation axis. We investigated the behaviour of two "coupled" modes in two distinct cases: when both modes propagate along the same direction (LPG's case), and the case where the modes propagate in the opposite direction with respect to each other (FBG's case). By using the weakly guiding approximation (i.e., by considering the difference of core-cladding refractive indexes comparatively smaller than 1), we can assume that the modes propagating through the waveguide are Linearly Polarized (LP). The weakly guiding approximation represents a considerable simplification of the calculations and can be used in a normal step index single mode optical telecommunication fibre (as the difference in the core-cladding fibre refractive index is usually less than 1%). The reflectivity (transmittivity) of the fibre grating can be calculated analytically in the uniform case, by solving the coupled-mode equations with appropriate boundary conditions. All the cases of nonuniform structures, are treated by using the Transfer Matrix method (a numeric extension of the theory, considering the contribution of each single piece of the grating as "locally" uniform, then multiplying between them the matrices associated with each section to get the total "transfer" matrix of the grating). We point out that, by using the above formulation, the value of the coupling coefficient between the transverse vector components of the core mode field and its counter-directional component (i.e., the one that is back-reflected from the grating), is calculated by using the real parameters of the fibre used (such as, the exact core and cladding radius, the refractive indexes and the resonant wavelength considered). In comparison with the most usual formulation of coupled-mode theory (see [8] for instance), our formulation presents the advantage of a greater flexibility, and for this

reason can be easily adapted to the real case, by just varying the fibre parameters. In turn this means that a bigger number of experimental features can be taken in account and explained by the model. The theory developed here has been used for all the simulations of fibre grating spectra, and especially in the case of chapter three where the theory has been used to write a code for the calculation of the theoretical spectral response of such gratings and the comparison with the experimental results. The three dimensional apodised grating spectra presented in the next chapter have been obtained using an algorithm based on Transfer Matrix method.

References

[1]   H.A Haus, W.P. Huang, "Coupled-mode theory", *Proc. IEEE*, **79**, 1991, pp.1505-1518.

[2]   J.D. Joannopoulos, R.D. Meade, J.N. Winn, "Photonic crystals", *Princeton University Press*, 1994.

[3]   C. Martijn de Sterke, N.G.R. Broderick, B.J. Eggleton, M.J. Steel, "Nonlinear optics in fiber gratings", *Opt. Fiber Technol.*, **2**, 1996, pp. 253-268.

[4]   H.G. Winful, R. Zamir, S. Feldman, "Modulational instability in nonlinear periodic structures: implications for gap solitons", *Appl. Phys. Lett.*, **58**, 1991, pp. 1001-1003.

[5]   J.R. Pierce, "Coupling of modes of propagation", *J. Appl. Phys.*, **25**, 1954, p. 179.

[6]   W.H. Louisell, "Coupled mode and parametric electronics", *John Wiley & Sons*, New York, 1960.

[7]   R. März, "Integrated optics: design and modeling", *Artech House*, London, 1995.

[8]   A. Yariv, "Coupled-mode theory for guided-wave optics", *IEEE Journ. of Quantum Electron.*, **QE-9**, 1973, pp. 919-933.

[9]   A. Yariv, P. Yeh, "Optical waves in crystals", *John Wiley & Sons*, New York, 1984.

[10]   A. Yariv, M. Nakamura, "Periodic structures for integrated optics", *IEEE Journ. of Quantum Electron.*, **QE-13**, 1977, pp. 233-253.

[11]   H. Kogelnik, "Theory of dielectric waveguides", Topics in Applied Physics: Integrated Optics, T. Tamir ed., *Springer Verlag*, New York, 1979.

[12]   R. Kashyap, "Fiber bragg gratings", *Academic Press*, London, 1999.

[13]   W-P. Huang, "Coupled-mode theory for optical waveguides: an overview", *J. Opt. Soc. Am. A*, **11**, 1994, pp. 963-983.

[14]   D. Marcuse, "Theory of dielectric optical waveguides", 2nd ed., *Academic Press*, New York, 1991.

[15] T. Erdogan, "Cladding-mode resonances in short- and long-period fiber grating filters", *J. Opt. Soc. Am. A*, **14**, 1997, pp. 1760-1773.

[16] V. Mizrahi, J.E. Sipe, "Optical properties of photosensitive fiber phase gratings", *J. Lightwave Technol.*, **11**, 1993, pp.1513-1517.

[17] A. Yariv, "Optical electronics in modern communications", 5th ed., *Oxford University Press*, New York, 1997.

[18]   S.S. Orlov, A. Yariv, S.Van Essen, "Coupled-mode analysis of fiber-optic add-drop filters for dense wavelength-division multiplexing", *Opt. Lett.*, **22**, 1997, pp.688-690.

[19] T. Erdogan, J.E. Sipe, "Tilted fiber phase gratings", *J. Opt. Soc. Am. A*, **13**, 1996, pp. 296-313.

[20] R.W. Boyd, "Nonlinear optics", *Academic Press*, London, 1992.

[21] D. Gloge, "Weakly guiding fibers", *Appl. Opt.*, **10**, 1971, pp. 2252-2258.

[22] A.W. Snyder, J.D. Love, "Optical waveguide theory", *Chapman and Hall*, London, 1983.

[23] M. Monerie, "Propagation in doubly clad single-mode fibers", *IEEE Trans. Microwave Theory and Techniq.*, **MTT-30**, 1982, pp.381-388.

[24] M. Yamada, K. Sakuda, "Analysis of almost-periodic distributed feedback slab waveguides via a fundamental matrix approach", *Appl. Opt.*, **26**, 1987, pp. 3474-3478.

[25] S. Radic, N. George, G.P. Agrawal, "Analysis of nonuniform nonlinear distributed feedback structures: generalized transfer matrix method", *IEEE J. Quantum Electron.*, **31**, 1995, pp. 1326-1336.

[26] T. Erdogan, "Fiber grating spectra", *J. Lightwave Technol.*, **15**, 1997, pp. 1277-1294.

[27] J. Hong, W. Huang, T. Makino, "On the transfer matrix method for distributed-feedback waveguide devices", *J. Lightwave Technol.*, **10**, 1992, pp. 1860-1868.

[28] B.G. Kim, E. Garmire, "Comparison between the matrix method and the coupled-wave method in the analysis of Bragg reflector structures", *J. Opt. Soc. Am. A*, **9**, 1992, pp. 132-136.

[29] M.A. Muriel, A. Carballar, J. Azaña , "Field distribution inside fiber gratings", *IEEE J. Quantum Electron.*, **35**, 1999, pp.548-558.

[30] H. Ke, K.S. Chiang, J.H. Peng, "Analysis of phase-shifted long-period fiber gratings", *IEEE Photon. Technol. Lett.*, **10**, 1998, pp. 1596-1598.

[31] M.A. Rodriguez, M.S. Malcuit, J.J. Butler, "Transmission properties of refractive index-shifted Bragg gratings", *Opt. Communic.*, **177**, 2000, pp. 251-257.

Chapter 3

APODISED FIBRE GRATINGS

3.1 Chapter Overview

This chapter deals with a very important issue of fibre grating technology: the apodisation. The practical importance of this technique is not only related to the possibility of giving the right shape to the reflection spectrum of a FBG, but also to the ability of improving the grating dispersion characteristics (time delay ripple smoothing) [1]. The first paragraph explains the working principle of the technique and the practical reasons why standard FBGs are unsuitable for some specific applications. Then an overview of the most commonly used apodisation techniques is given, with special attention on two apodisation methods: the double exposure variable speed method and the phase-mask dither method. A comparison between the experimental spectra and the theoretical predictions from the TM method is also made. In the last section, numerical optimisation of all the practical parameters used in the apodised grating fabrication is performed. A comparative analysis of shape, reflectivity and side lobes suppression capability is made using different apodising functions.

3.2 Working Principle of Fibre Grating Apodisation

As already mentioned in Chapter 1, FBGs are excellent devices, when used in reflection, for all the applications requiring to distinguish between different wavelengths (channels selection or filtering). This is because of their wavelength selective nature as, at least in principle, only the resonant wavelength is reflected back from the grating, while the other wavelengths are transmitted through the fibre. Nevertheless, for some applications, especially in the field of optical communications, it is necessary for the FBG to conform to very high fabrication standards because the presence of any imperfection in the grating could compromise the ability of the system of transmitting intelligible sequence of bits to the receiver. Usually, desirable characteristics for the design of FBGs are: a flat top reflection spectrum with a sharp skirt, a high reflection in a narrow wavelength range and a high transmission elsewhere. The recent advances in WDM systems have reduced the channel spacing below 0.4 nm (50 GHz) at 1550 nm. Unfortunately, as shown in Fig. 3.1, the reflection spectrum of a uniform FBG (i.e. a grating where the modulation of the refractive index is uniform along the length) exhibits a series of secondary maxima (also called "side lobes") in addition to the central reflection peak. The side lobes are generated by Fabry-Perot reflection due to the finite extent of the grating itself and to the index step at the boundaries of the grating.
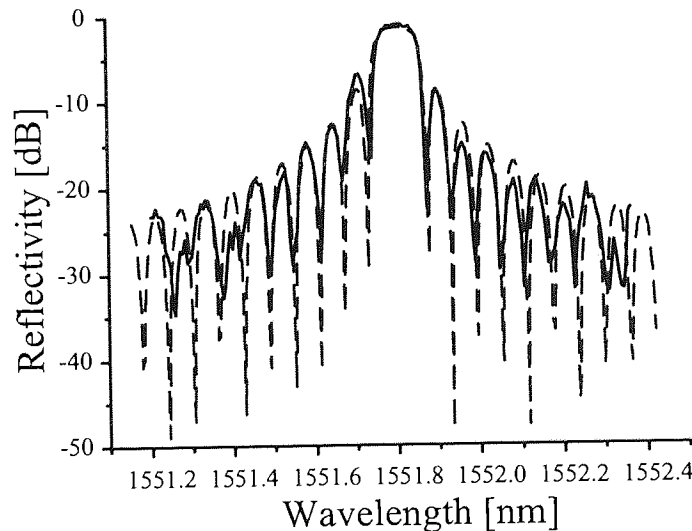
Figure 3.1 *Experimental (solid line) and theoretical (dashed line) spectra of a 2 cm long uniform FBG. The grating has been fabricated in a standard hydrogenated Ge-doped fibre, using an electron beam etched phase mask (QPS Technology). The theoretical curve has been calculated using (2.3.8), and (2.3.15) with $n_{eff}=1.447$, $\beta_{01}^{co} = 5.86 \times 10^{-3}$ nm^{-1} and $\kappa L = 2$.*

Such an unfavourable spectral response is not suitable for WDM systems because of two main reasons: first, the presence of side lobes forces to operate the optical link with an increased separation in frequency between the different channels in the attempt to keep under control the interference (cross-talk) between adjacent channels. Second, the presence of side lobes generates intra-channel noise that degrades the quality of the optical bit pattern sent to the receiver. We call "apodised" a non uniform grating where the secondary maxima have been suppressed or lowered (at least 20 dB under the level of the Bragg reflection peak) compared to the case of a uniform grating. A few different approaches to achieve this result have been reported, all of them having a common feature: the introduction of a gradual and "suitably shaped" variation in the refractive index modulation of the grating. Hill et al. [2], [3] firstly demonstrated that the side lobes in the frequency response of a periodically perturbed optical waveguide can be suppressed by designing filters with a grating coupling coefficient that varies spatially along the grating length. This effect could be easily achieved by irradiating the optical fibre with a non uniform UV exposure where the intensity is proportional to amplitude of a predetermined "bell-like" shading function (such as a gaussian or $\cos^2$ function).
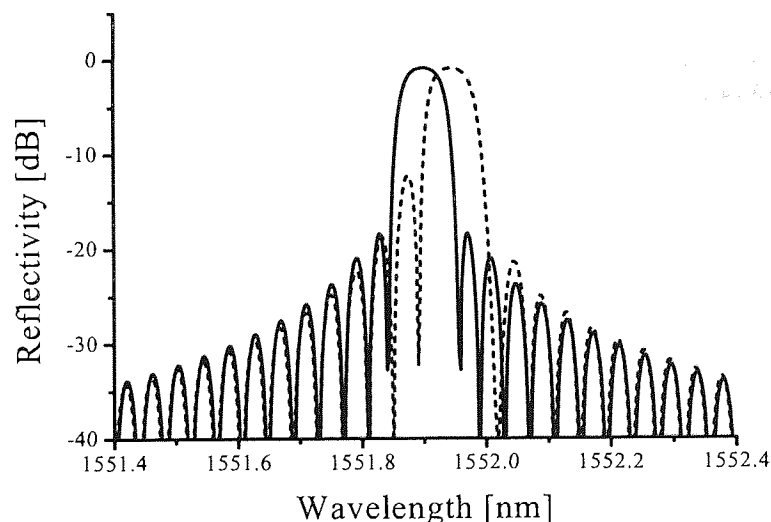
Figure 3.2 Numerical calculation results showing the difference between the spectrum of an apodised grating where the average refractive index is constant (solid line) and the spectrum of the same grating in the case where the background refractive index varies along z (dashed line). The 2 cm long FBG is gaussian apodised and it has a strength $\kappa L = 2$ (the parameters used for the simulation are the same as in Fig. 3.1). The change in the refractive index produces a broadening of the resonant peak and the appearance of an asymmetric peak on the short wavelength side of the spectrum.

The final result of such a technique is that the two ends of the grating are exposed to a lower UV light intensity than the central part and this modifies the coupling coefficient

along the structure. The problem connected to this approach is that not only the coupling coefficient along the grating is changed but also a change in the fibre average refractive index is produced, due to the fact that some regions of the fibre are exposed to a more intense UV radiation than others. Unfortunately, the variation of the average refractive index leads to an undesirable chirp of the Bragg wavelength with a consequent broadening of the spectral response and the appearance of adjacent asymmetric structures on the reflection peak [4], [5].
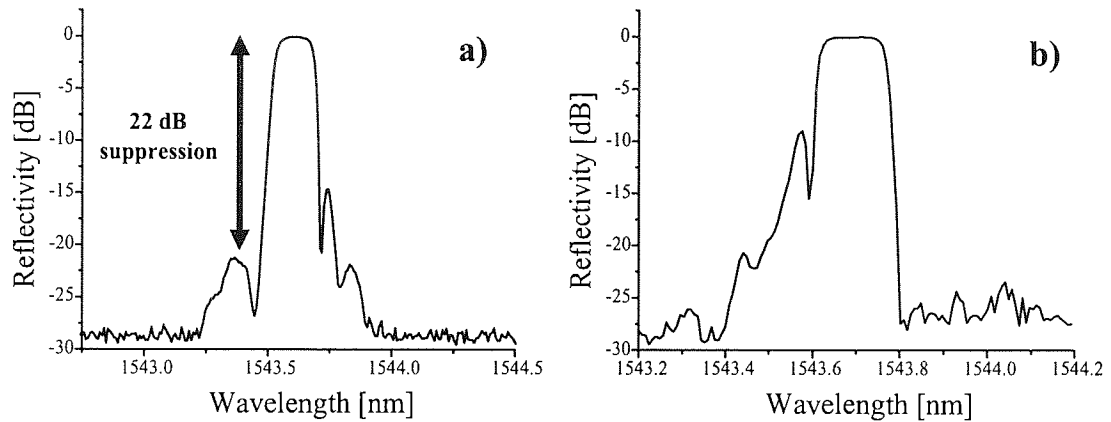
Figure 3.3 Two experimental spectra of a 3 cm long apodised FBG's (gaussian shading function, C=8) made in hydrogenated SMF by using an e-beam phase-mask (QPS Technologies), with a laser average output power of 118 mW and a scan speed of: a) 0.1 mm/s, b) 0.08 mm/s. The spectra show the effect of an imperfect apodisation due to a change in the fibre background refractive index.

Figure 3.2 shows the theoretical spectra of gaussian apodised gratings, obtained using the TM method, in the case where the average refractive index is kept constant (solid line) or is allowed to change along z (dashed line). A correct apodisation procedure should change $\kappa(z)$ along the grating length, keeping at the same time the average (background) refractive index at a constant value. From a practical point of view this means that the UV dose on each section of the grating should be the same and that the grating should be gradually "erased" in proximity of the boundaries to get the apodisation. Therefore only σ (index modulation envelope) is allowed to change as a function of z in (2.3.17), while the average refractive index n_{co} must remain to a constant value. The principle is schematically illustrated in Fig. 3.4.

3.3 Apodisation Techniques

From a practical point of view, apodising a FBG is a delicate job. In a standard uniform grating the first side lobes on both sides of the central peak are never more than 10 dB

52

down the reflection level of the central Bragg resonance and this means that their reflectivity is 10% of the reflectivity of the central peak. On the other hand, for an apodised FBG where the level of the first side lobes is at least 20 dB down the level of the central resonance, the side lobes reflectivity is only 1% of the reflectivity of the central peak.
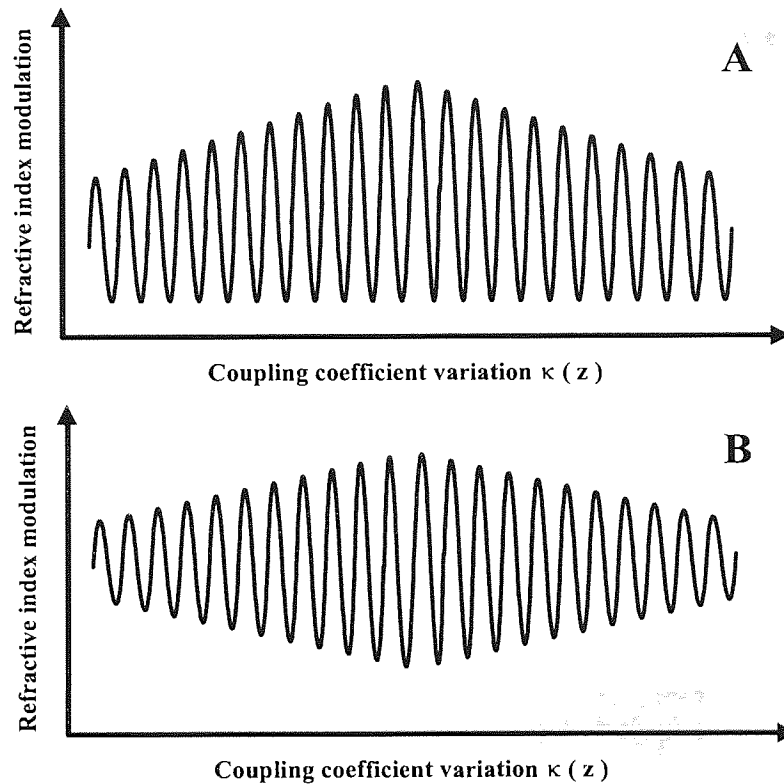
Figure 3.4 Schematic diagram showing the difference between: (A) a non uniform variation of the refractive index modulation obtained using a non uniform UV exposure and, (B) a non uniform variation of the refractive index modulation obtained by uniform irradiation. In both cases the reduction of the coupling coefficient strength at the two boundaries of the grating produces apodisation, but in the first case, as the background average refractive index is varying, also a chirp of the Bragg wavelength is introduced.

Writing apodised FBGs having 20 - 22 dB side lobes suppression is possible by standard techniques but requires already a special care. Beyond 25 dB the task is usually much more challenging. A side lobes suppression of 23 dB, for instance, means that the side lobes reflectivity should be only 5‰ of the central peak reflectivity. The reason why this is hard to achieve is that at this stage any small perturbation (such as dust on the fibre, tiny vibrations, or temperature variations) starts to compete with the apodisation process. On the other hand, at least in the vast majority of the practical cases, several micro-phase-shifts are introduced in the structure during the fabrication process. This means that the apodisation profile of the grating is perturbed and, as a consequence, the side lobes suppression is usually not exceeding 22 – 23 dB by the use of conventional apodisation

techniques. We wish to describe here the most important apodisation techniques that have been reported to date. Some of these methods are based on the principle of moving the phase-mask and/or the fibre during the scan with UV laser beam [6]. Other methods, regarding the apodisation of chirped FBGs, are instead based on the multiple gratings printing technique [7]. We shortly overview the most commonly used methods of apodisation before describing in more detail two techniques, that we used for the fabrication of all the apodised FBGs included in this thesis: the variable speed double exposure technique and the dither phase mask technique.
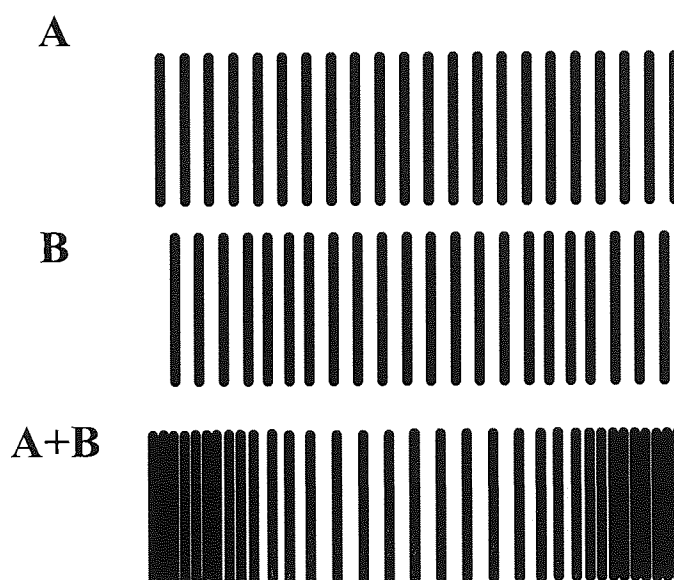
Figure 3.5 *Moiré groove pattern of an apodized phase-mask fabricated by electron beam lithography. The electron beam writes two gratings (A and B) on top of each other having a slightly different period and starting point (not to scale) generating the groove pattern (A+B). From Ref. [8].*

- *Apodised phase-mask:* The use of a phase-mask with variable diffraction efficiency represents in many respects the easiest way to fabricate apodised fibre gratings. Since the glassy material that composes the phase-mask is completely transparent to the UV radiation, the method guarantees a uniform UV beam exposure, which means that a constant average refractive index is kept inside the grating structure [8-10]. The phase-mask is designed in such a way that the perfect zero order suppression occurs in the centre and decreases towards the ends. The diffracted +1 and −1 orders will have then the required bell-like shape intensity distribution necessary to generate the modulated refractive index. The phase-mask is fabricated using a focused ion beam and direct etching the pattern in silica. A Moiré groove pattern is generated by a

double exposure of two 50% duty cycle gratings of slightly different periods. The phase and the period of the two gratings are adjusted in such a way that the grooves overlap perfectly in the centre and are out of phase by exactly half a period at the ends (see Fig. 3.5). This method has the advantage of being very reproducible as the envelope of the UV fringes is determined by the design of the phase mask alone, but also presents the disadvantage of not being flexible because it does not allow for instance to modify the shading function used for the apodisation process.

- *Interferometric techniques:* These techniques are used to "intrinsically" apodise the grating using a similar principle to the one used for the apodised phase-mask: two different gratings of slightly different period are written simultaneously in the core of the fibre (using the two beams coming from the two branches of the interferometer). The envelope of the obtained Moiré grating has the bell-like shape required for the apodisation and the total dose of UV light is kept constant along the grating [11]. Moreover, if the UV light is composed of two slightly different monochromatic frequencies the double set of fringes will produce a pattern that is the "beat" envelope of the two, with fringes vanishing at the position $\pm z$ from the centre (where the fringes from one frequency are out of phase with respect to the fringes of the other frequency). More sophisticate techniques making use of a phase-mask in addition to the interferometer have also been described [5], [12], [13]. These techniques have the advantage to be tunable but unfortunately are also difficult to control and thus do not offer too much reproducibility. Another usual limit is that only short length gratings (generally few millimetre long) can be written by the use of this technique.

- *Symmetric stretch method:* The technique consists of a repetitive, symmetric, longitudinal stretching of the fibre around the centre. The strain is applied using a piezoelectric stack controlled by a computer at the same time that the grating is being written. Stretching the fibre at the boundaries of the grating of exactly half a period will produce a cosine apodisation [14], [15].

- *Moving fibre/phase mask method:* The technique relies on the movement of the fibre along with the phase mask in front of a stationary UV beam, or alternatively on the scan of the UV beam across a fixed phase mask, with the fibre moving slowly relative to the phase mask. The fibre is mounted on a holder that can be moved using a precision piezoelectric translator [16], [17].

- *Polarization control method:* The technique relies on the controlled introduction of discrete π phase shifts between the refractive index modulation profiles produced by two polarizations of the UV beam. The coupling coefficient is directly affected the

ratio of the UV intensity of the two polarisation states, while keeping a constant background refractive index along the grating [18], [19].

3.3.1 The Variable Speed Double Exposure Apodisation Technique

We present here a novel apodisation technique working on the principle of double scan by a UV laser beam through the region of the fibre where the grating is written. The speed can be varied along the scanned length of fibre and is controlled by a computer. The first exposure is made with the only purpose of preconditioning the refractive index of the fibre core to compensate for any non uniform refractive index variation that is created by the second stage of the fabrication process. The first scan is made in the absence of the phase-mask, then a fibre grating can be written using a uniform phase-mask by the second scan. The scanning speed of the beam along the length of the fibre has to be proportional to the amplitude of the shading function used for the apodisation. The strength of the FBG will depend on the intensity of the UV light, that in turn depends on the exposure time to the beam. The second scan is used to write a grating in the fibre core with a coupling coefficient κ that depends on z.
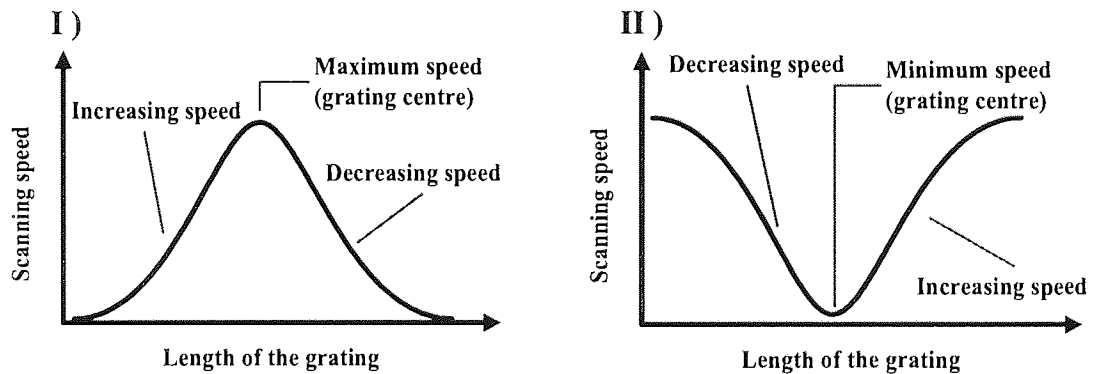
Figure 3.6 *Schematic speed distribution in double exposure apodisation technique: I) case where the fibre refractive index is preconditioned by the first scan; II) case where the actual FBG is written in the fibre core by a second scan through the phase-mask.*

The effect of changing the value of κ along the length of the grating is obtained by exposing the different sections of the fibre to UV light for a time proportional to the wished strength. The exposure time, and therefore the strength of the grating, is proportional to the reciprocal of the scanning speed in the section considered: the higher is the scanning speed, the weaker would be the grating written in fibre. During the first exposure the computer controls the movement of the translation stage used to scan the beam along the fibre, starting from a given initial speed, then accelerating up to the maximum speed is reached (in the middle of the irradiated span) and decelerating again

56

symmetrically toward the first half section of the grating. This results in a bigger increase of the refractive index of the fibre at the boundaries than in the centre of the irradiated span. When the grating is written by the second scan, the translation stage starts with the maximum speed, slowing down in the centre, then accelerating again toward the opposite end. This two-stage process is schematically shown in Fig. 3.6. The speed distribution for the case in exam follows a gaussian profile. The double exposure mechanism enables to keep the refractive index of the fibre at a constant value changing at the same time the strength of the FBG along its physical length. This technique represents a flexible approach to gratings apodisation because, in addition to the "classical" gaussian profile, a large class of bell-like functions (parabolic, truncated cosine or hypergaussian, for instance) can be used for the two exposures. The results obtained depend sensibly on the type of function used. In principle, the only requirements for the correct grating apodisation are an accurate computer control of the translation stage speed, according to the chosen shaping function, and a stable output optical power from the UV laser.
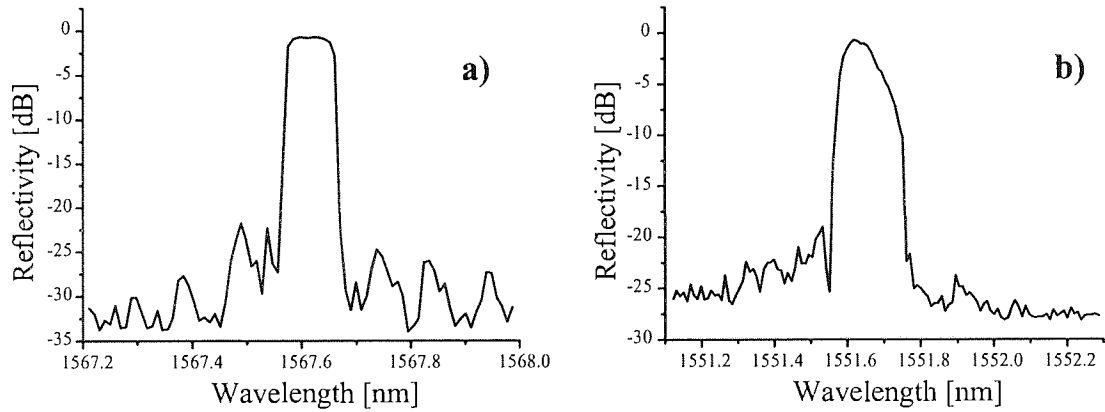
Figure 3.7 *Experimental spectra of 2 cm long apodised FBGs fabricated by variable speed double scan technique using a phase-mask (QPS Technology) and the gaussian shaping function (3.3.1): a) $v_0 = 0.05 \, mm \cdot s^{-1}$ and $C = 4$, b) $v_0 = 0.04 \, mm \cdot s^{-1}$ and $C = 5$.*

Figure 3.7 shows two experimental spectra of apodised FBGs obtained with variable speed double exposure technique using the following gaussian shading function

$$v(z) = v_0 \, e^{-C\left(\frac{z}{L}\right)^2}$$

where v(z) represents the translation stage speed as a function of the position along the grating, v_0 is the initial speed, L is the physical length of the grating, and C is a control parameter used to vary the width of the gaussian function. Unfortunately the technique does not give very reproducible results (only a 20% of the cases result in a good apodised grating). The typical spectrum is often showing an asymmetric profile (due to a chirp

induced by a non perfectly compensated refractive index difference). As the argon doubled frequency laser offers an excellent stability of the output power, the principal source of the asymmetry is most likely the translation stage. Actually, the used translation stage has been designed to work at a constant speed and not below $0.05 \, \text{mm} \cdot \text{s}^{-1}$. The set-up shows its limits especially for the second scan (when the translation stage is supposed to move at higher speed at the boundaries of the grating). Figure 3.8 shows the effect of a not exactly compensated refractive index at the boundaries of the grating, by comparing the central peak of the experimental spectrum to the theoretically calculated one. The asymmetric broadening shown at the two sides of the central resonant peak is typically produced by a not exact compensation of the chirp induced by a differential UV exposure. Actually, another practical limit of the technique is about the optical alignment, that is supposed to change slightly in the two exposures (with and without phase mask). The change in the optical alignment in turn affects the total dose of UV radiation at which the fibre is subjected in a way that is quite difficult to predict a priory with the highest accuracy.
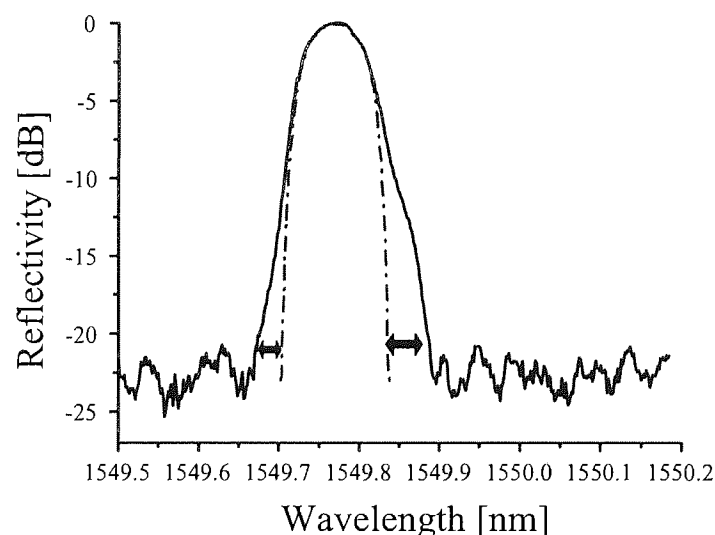
Figure 3.8 *Effect of an imperfect gaussian ($C = 1$, $L = 1.5 \, cm$, $\kappa \, L = 2$, $n_{eff} = 1.447$) apodisation due to the unbalanced chirp produced from the variable speed double exposure. The two left-right arrows show the deviations of the experimental spectrum from the theoretically calculated symmetric profile of the central Bragg resonance.*

3.3.2 The Phase-Mask Dither Apodisation Technique

The phase-mask dither technique is probably the method offering the highest reproducibility rate for the fabrication of apodised FBGs (with the exception of the apodised phase-mask technique) and it offers also the advantage of an higher flexibility if

compared to other techniques, as the grating reflectivity can be shaped according to the profile of the chosen apodisation function. From the experimental results we obtained on a large number of apodised gratings can be seen that this technique, when correctly used, guarantees a success of 60% (critical factors are the stability of the translation stage and the long term reliability of the piezoelectric oscillator used for the fabrication). The technique enables the fabrication of good quality apodised gratings once that all the "sensitive" parameters (such as the voltage applied to the piezo, the translation stage scan speed and/or the output laser power) have been optimised.
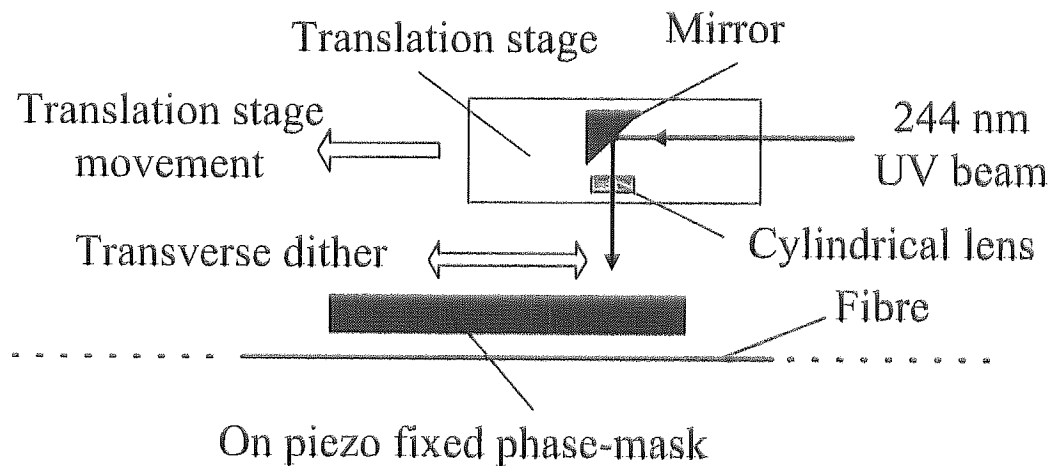
Figure 3.9 *Schema of the experimental set-up used for the fabrication of apodised gratings by phase-mask dither technique.*

Figure 3.9 shows a simplified diagram of the experimental set-up used to write apodised gratings by phase-mask dither method. Contrary to the previously described variable speed double exposure method, the apodisation process by using this technique is based on a single exposure: the laser beam is scanned with constant speed along the full length of the phase-mask using a 45° tilted mirror mounted on the top of a computer controlled translation stage. A cylindrical lens is used to focus the laser beam on the fibre and the spot size of the beam is reduced to approximately 0.5 mm before reaching the fibre. If the laser power is not varying with time, the uniform exposure to the UV light guarantees that the background refractive index has a constant value in the region of the fibre where the grating is written. The phase-mask is fixed onto a piezoelectric oscillator that is driven by a triangular function generator at 25 Hz. The computer controls, via a feedback mechanism, the amplitude of the transverse dither applied to the phase-mask by varying the applied voltage to the piezoelectric oscillator. The amplitude of the dither applied to the phase-mask is proportional to the amplitude of a predefined shaping function, as shown in Fig.

3.10. For a correct apodisation of the grating it is necessary to calibrate in advance the dither of the piezoelectric oscillator, because the movement of the phase-mask should correspond to exactly half period of the phase-mask to "wash out" the fringes. Therefore, before starting the fabrication process it is essential to find out the appropriate voltage to apply to the piezoelectric oscillator in order to make it moving of exactly half-period of the phase-mask. This can be achieved by writing some "testing" uniform grating on a dummy fibre, with the phase-mask oscillating at different constant amplitudes, i.e. by applying different voltages to the piezoelectric oscillator: for a given voltage the UV beam will not be (nearly) able to write any grating on the fibre through the phase-mask. The voltage at which the grating is erased generally ranges between -0.27 and -0.33 Volts, depending on the period of the pattern chosen and weight of the phase mask. Another preliminary calibration has to be done for the constant speed of the translation stage, according to the length of the grating that should be written, the laser power and the kind of fibre used. This has to be done because, if the translation stage moves too slowly, the fibre will be exposed to a high dose of UV light, and this will saturate the induced refractive index change before the scan is completed. As a result the grating spectrum will present an asymmetric shape.
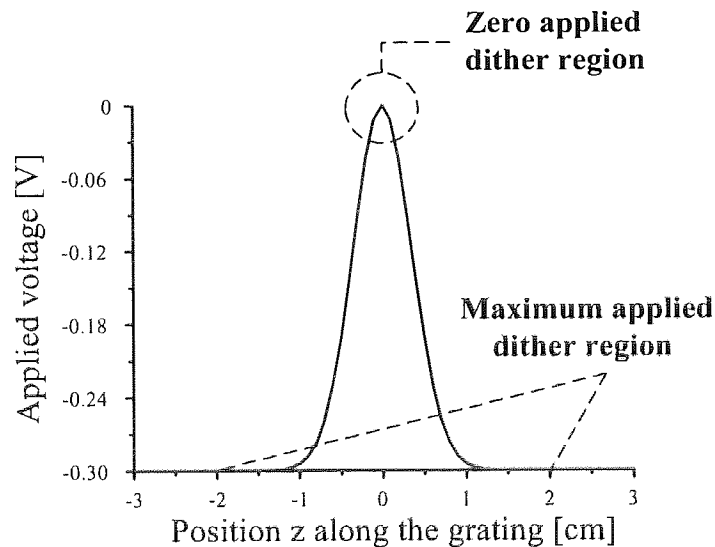
Figure 3.10 Diagram showing the amplitude of the dither as a function of the applied voltage to the piezoelectric oscillator in the case where a gaussian apodisation function is used.

Figure 3.11 shows the spectrum of an apodised grating made by using the dither phase mask technique. The theoretical spectrum calculated using the piecewise uniform method is also shown. The grating was fabricated using a translation stage speed of 0.07 mm/s and a value of the gaussian width control parameter of $C = 3$. The strength of the grating in the theoretical curve is $\kappa L = 7.4$. It can be easily observed that the agreement between the

theoretical curve and the experimental results is very good for what concerns the central peak. However, the experimental spectrum differs from the simulation for what concerns the structure of the side lobes: irregular side lobes are clearly visible in the experimental spectrum in contrast with the regular periodical behaviour predicted by the theory. Actually this is a quite usual case, as the majority of the apodised experimental spectra presents an irregular structure at both sides of the central reflection peak. On the contrary, the side lobes of a uniform grating are generally quite regular and they usually fit well with the simulation (see Fig. 3.1).
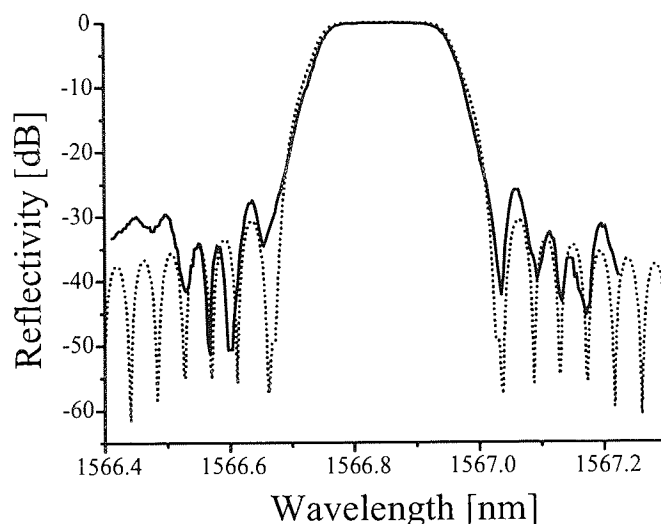
Figure 3.11 Experimental spectrum (solid line) of a 2 cm long gaussian apodised FBG fabricated using the phase-mask (Ibsen Technology) dither method. A comparison with the theoretical response calculated by piecewise uniform method (dotted line) is also shown.

We want to give an explanation about the reasons for which the simulation predict a much higher side lobes suppression than we can get in reality and also, we want to investigate why the structure of side lobes is different in the simulation and in the real case. To do so, we have a look of the spectra of apodised gratings in Fig. 3.12. In all the cases shown in Fig. 3.12, the length of the grating is L=1.5 cm and a value of C = 3 is used in the gaussian apodisation function. The scanning speed is set to 0.05 mm s^{-1} and the output power from the laser (244 nm FreD Argon-ion doubled frequency laser) is 100 mW. It can be seen from the spectra that, compared to the uniform case, the side lobes of an apodised grating are far "weaker" (the purpose of the apodisation is, in fact, to reduce the reflectivity of the undesired secondary maxima). Because of their weakness, the side lobes of an apodised grating are much more sensitive to any perturbation present in the environment at the time of the fabrication. Any irregular vibration of the translation stage during its movement, or presence of dust on the fibre and/or on the phase-mask, or tiny aperiodicity in the

oscillation of the piezoelectric, or laser power fluctuation would directly affect the structure of these side lobes by introducing a small randomly varying phase shift in the grating structure. The effect of this "noise" is more visible on the side lobes because of their weakness. In the attempt to validate this conjecture, we have inserted a randomly varying phase term in the simulation of apodised gratings by TM method [20-22]. The results are reported in Fig. 3.13.
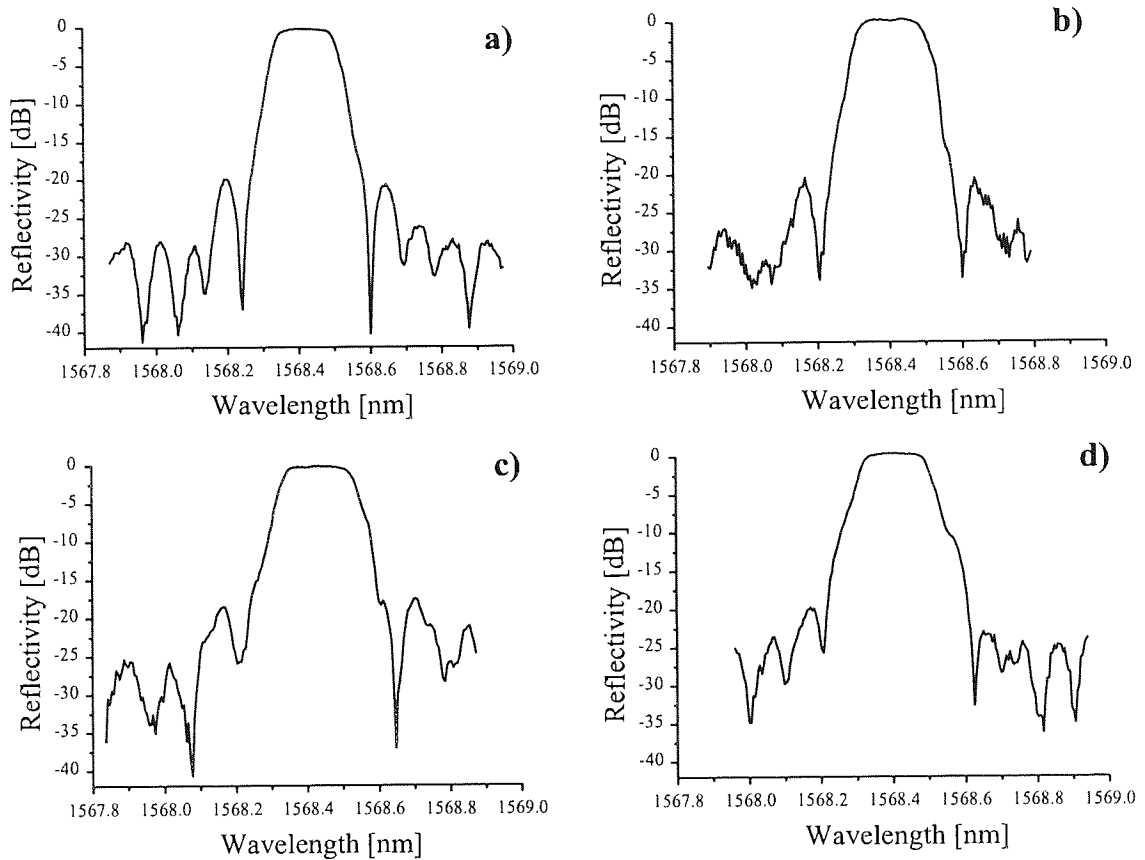
Figure 3.12 Experimental spectra of gaussian apodised FBGs. The pictures show the effect of a non calibrated voltage applied to the piezoelectric oscillator (the dithering has an amplitude slightly higher or lower than half of the period of the phase-mask): a) spectrum obtained using an optimised voltage of -0.33 V, b), c) and d) spectra written for three slightly different voltages around the optimised one (-0.30 V, -0.35 V, and -0.40 V respectively).

Both curves in Fig. 3.13 represent the same apodised grating and are numerically generated. The solid curve has been obtained by inserting a 1% randomly variable phase-shift term that simulates the effect of several small perturbations interfering with the grating writing process (noise). The obtained spectrum seems to be more realistic when compared to the experimental cases. We notice that a fluctuation of 1% in the phase of the grating is already able to compromise the ability of the technique of suppressing the side

lobes. A result of such an investigation is that side lobes suppression is never higher than 20 dB if the randomly varying phase term is not smaller than 1‰. This also explains why a side lobes suppression higher than 30 dB, even if predicted from the theory, is never found in reality by using this apodisation technique.
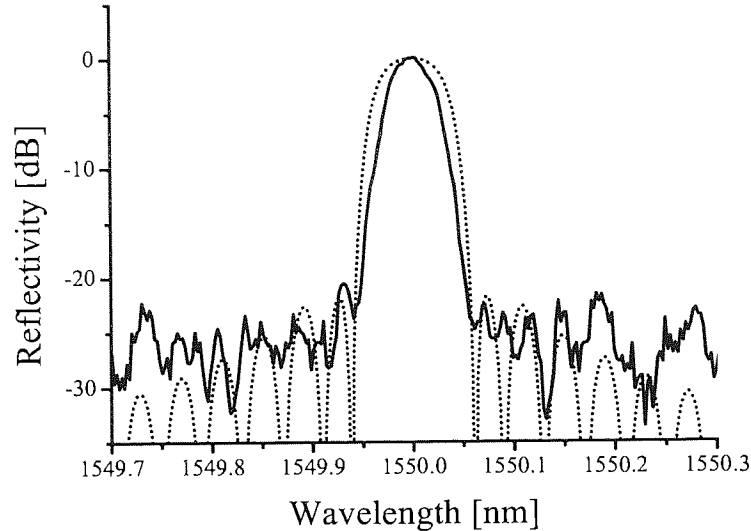
Figure 3.13 *Theoretical spectra of a 2 cm long gaussian apodised (C=1.3 and kL=2) FBGs without a random phase-shift term (dotted line) and with a random phase-shift term (solid line).*

Apodised gratings with side lobes suppression around 20 dB are still useful in practice, but for some special applications (such as in the optical communications field) this suppression value could not be enough. An active control on all the possible noise sources should be implemented to achieve side lobes suppression higher than 30 dB.
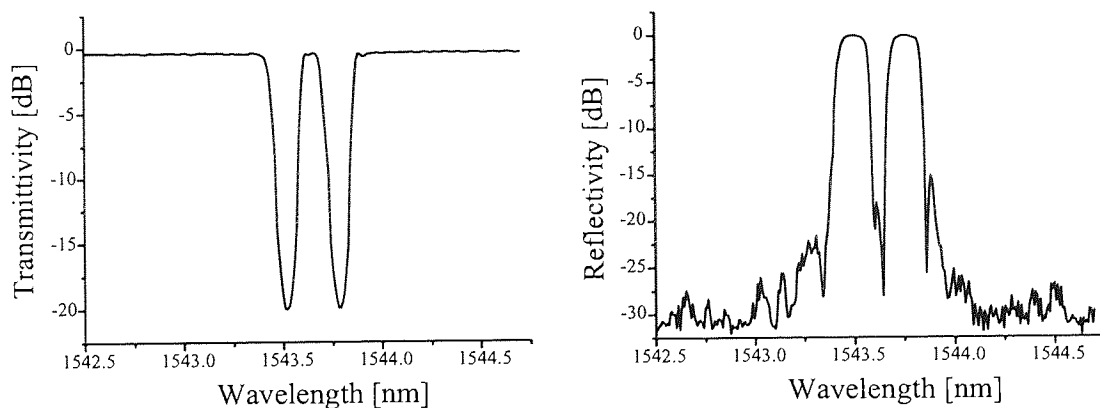
Figure 3.14 *Experimental example of apodised double peak FBG's photoimprinted with a double scan on the same section of a SMF by using phase mask dither technique.*

A special care should be addressed to the control of the voltage applied to the phase-mask (to eliminate possible mechanical hysteresis and nonlinearities in the feedback control

63

system), because any deviation from the half-period oscillation amplitude would introduce noise, thus limiting the degree of apodisation that can be achieved. We conclude this section on grating apodisation by phase mask dither technique, by giving an example of application of the technique to multi grating printing. The idea was to write two identical (same strength and reflectivity) apodised FBG's at just a fraction of nanometre apart from each other. These gratings were required to fabricate an actively mode-locked tunable dual-wavelength fibre laser [23] and were fabricated by physical superposition of the two gratings on the same span of fibre, the second written after stretching the fibre (to shift the resonant peak of approximately 0.3 nm). The gratings obtained are shown in Fig. 3.14. The quality of the couple is reasonably good if we consider that a double scan process was used to produce it.

3.4 Numerical Optimisation of Apodisation Functions

The bandwidth of an apodised grating is always larger than that of a uniform grating of the same length. This is because the apodisation process shortens the effective length of the FBG by gradually reducing the grating strength toward the two ends of the structure. It is also true that, for gratings having the same strength and length, the bandwidth of the central peak and the suppression of side lobes depend sensibly on the used apodisation function. Other characteristics of the reflection spectrum, like the flat top and square-like shape also depend on the apodisation function (the apodisation function affects also the time delay ripples of a chirped FBG, but this aspect will be considered in chapter four) [24-27]. Numerical modelling of apodised gratings is a useful way to determine the effect of each apodisation function on the grating spectrum [28]. Indeed it gives us a hint on the apodisation function that is more suitable for the specific purpose of interest (such as minimising the bandwidth, lowering the side lobes, or obtaining the flattest top in the reflection spectrum) and on the control parameter C (i.e. the width of the apodisation function) or on the grating strength that is more suitable for each case. We consider here the following set of six very common apodisation functions and we compare them for the case of a two centimetres long grating (considering both a weak and a strong coupling):

$$\text{Gaussian:} \qquad f(z) = e^{-C\left(\frac{z}{L}\right)^2} \qquad\qquad (3.5.1)$$

$$\text{Super-gaussian:} \qquad f(z) = e^{-C\left(\frac{z}{L}\right)^4} \qquad\qquad (3.5.2)$$

64

$$\text{Parabolic:} \quad f(z) = 1 - \left(\frac{z}{C \cdot L}\right)^2 \tag{3.5.3}$$

$$\text{Truncated Cosine:} \quad f(z) = \cos^n\left(\frac{C \pi z}{L}\right) \quad , \quad n = 2, 13 \tag{3.5.4}$$

$$\text{Blackman:} \quad f(z) = \frac{1 + (1+C) \cos\left(\frac{\pi z}{L}\right) + C \cos\left(\frac{2 \pi z}{L}\right)}{2 + 2C} \tag{3.5.5}$$

a) Weak grating case ($\kappa L = 1$)
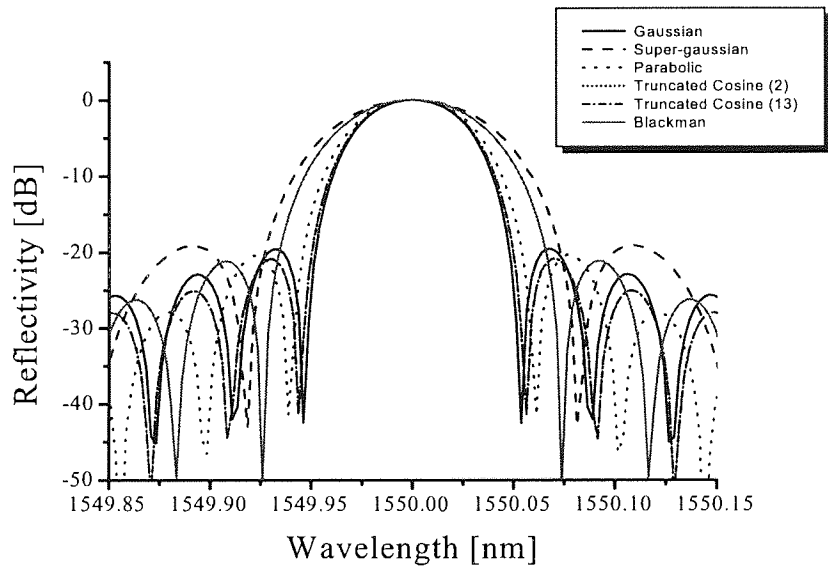
Figure 3.15 *Theoretical reflectivity of a differently apodised 2 cm long FBG (for $\kappa L = 1$).*

Figure 3.15 shows the theoretical spectra calculated using the piecewise uniform method for each of the above apodisation functions in the case $\kappa L = 1$. The characteristics of these spectra are summarised in Table 3.1. The curves in Fig. 3.15 have been obtained by optimising the value of the control parameter C for each function in such a way to get a side lobes suppression of approximately 20 dB. This is because the reflection profiles of similarly apodised FBGs can be compared without ambiguity. For what concerns the bandwidths of the apodised gratings, three of the apodisation functions give approximately the same result: Gaussian, Truncated Cosine (with n=13) and Parabolic.

$\kappa L = 1$	C	Side lobes suppression (dB)	$\Delta \lambda_0$ (nm)	$\Delta \lambda_{3dB}$ (nm)	$\Delta \lambda_0 - \Delta \lambda_{3dB}$ (nm)
Gaussian	1	20.00	0.107	0.050	0.057
Super-gaussian	10	19.05	0.162	0.063	0.099
Parabolic	0.5	20.49	0.122	0.047	0.075
Truncated Cosine (2)	0.65	21.18	0.110	0.050	0.060
Truncated Cosine (13)	0.25	19.84	0.108	0.050	0.058
Blackman	0.25	21.22	0.149	0.063	0.086

Table 3.1 *Apodised grating characteristics for different shaping functions.*

These three functions minimise the 3dB bandwidth of the grating approximately in the same way, but they differ with respect to the distance $\Delta \lambda_0$ between the two side lobes adjacent to the central peak. The parabolic function tends to broad the peak width more than the other two. The narrowest value $\Delta \lambda_0$ of the bandwidth is obtained when a Gaussian apodisation function is used. No one of these spectra has a flat top, as this is because of weak strength of the grating. If we compares Figs. 3.17, 3.21 and 3.25 we can also see that the parabolic apodisation is generally less effective in suppressing the side lobes than the gaussian and the truncated cosine. We can then conclude that, in the case of weak gratings, the most suitable apodisation function is the gaussian as it minimises the bandwidth and allows at the same time a good level of side lobes suppression. The worst case is when a super-gaussian apodisation function is used: from Fig. 3.19 we can see that this function is not very effective in suppressing the side lobes and from Fig. 3.15 we can observe that the bandwidth is the largest one.

b) Strong grating case ($\kappa L = 7$)

Also in this case the comparison is made between functions having a control parameter C such as the side lobes suppression is around 20 dB. But this time the situation is quite different as the apodised grating is strong. Figure 3.16 clearly shows that the Blackman function gives the best compromise among side lobes suppression, narrow bandwidth of the central peak, and smooth shape.
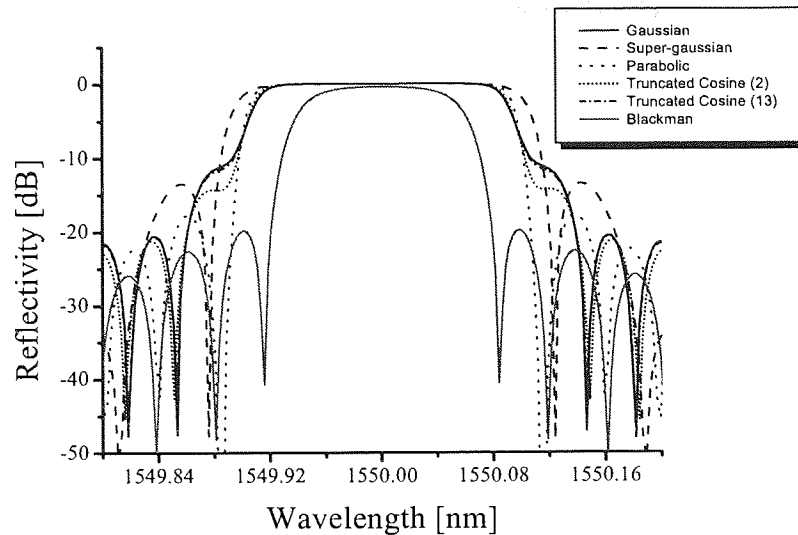
Figure 3.16 *Theoretical reflectivity of a differently apodised 2 cm long FBG (for κ L = 7)*

The super-gaussian and the parabolic functions have a better "squared" shape but, apart from the bandwidth that is larger, they show a reduced capability of suppressing the side lobes (this can be seen from Fig. 3.20 and Fig. 3.22). The truncated cosine and gaussian functions show a higher capability of suppressing the side lobes but the shape of the central peak is less regular and the bandwidth is larger than in the case of the Blackman function. Even if the latter does not guarantee a perfectly flat top of the reflection spectrum, the top flatness is sufficient for most part of the applications.

κ L = 7	C	Side lobes suppression (dB)	$\Delta \lambda_0$ (nm)	$\Delta \lambda_{3dB}$ (nm)	$\Delta \lambda_0 - \Delta \lambda_{3dB}$ (nm)
Gaussian	1.7	20.72	0.290	0.183	0.107
Super-gaussian	10	13.87	0.248	0.208	0.040
Parabolic	0.5	17.59	0.224	0.189	0.035
Truncated Cosine (2)	0.74	21.08	0.290	0.183	0.107
Truncated Cosine (13)	0.32	20.61	0.294	0.183	0.111
Blackman	0.20	19.80	0.170	0.110	0.060

Table 3.2 *Apodised grating characteristics for different shaping functions.*

Gaussian Apodisation (k L = 1)
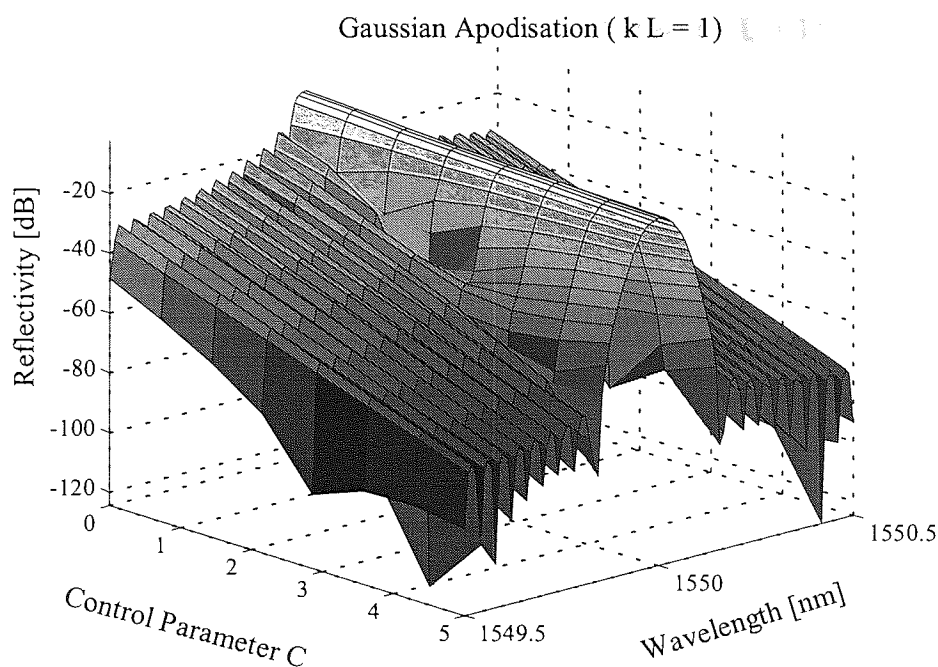
Figure 3.17 *Numerical computation of side lobes suppression as a function of the width control parameter C of a gaussian apodisation function for the case of a weak grating.*

Gaussian Apodisation (k L = 7)
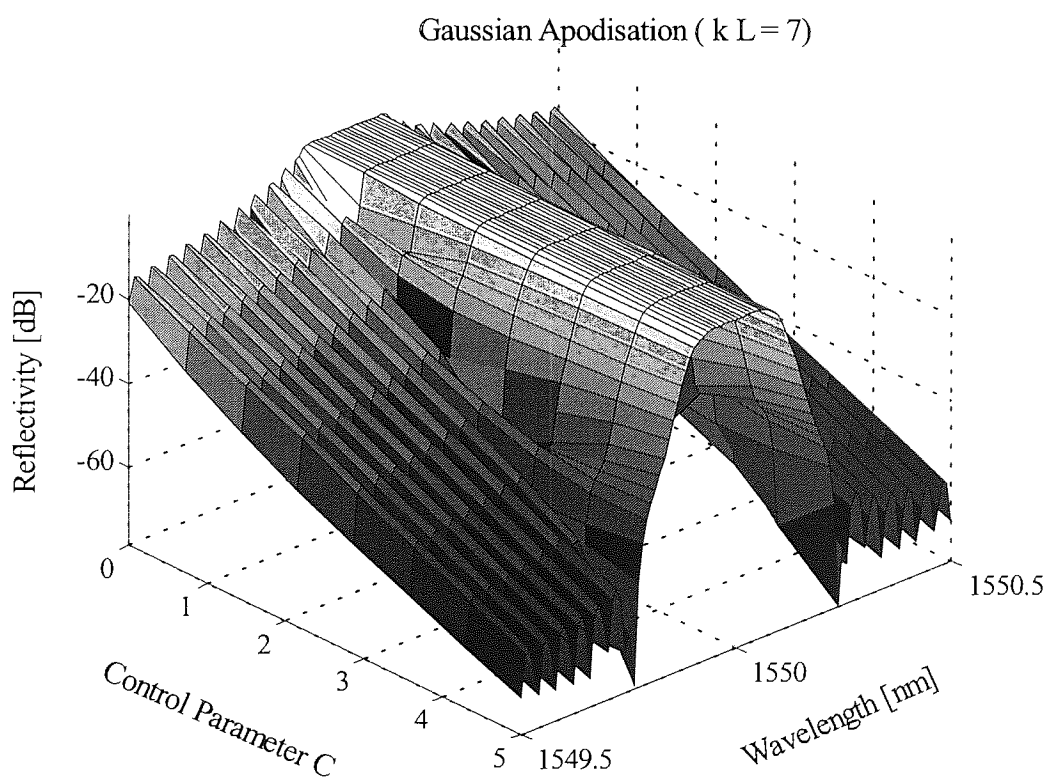
Figure 3.18 *Numerical computation of side lobes suppression as a function of the width control parameter C of a gaussian apodisation function for the case of a strong grating.*

Super-gaussian Apodisation (k L = 1)
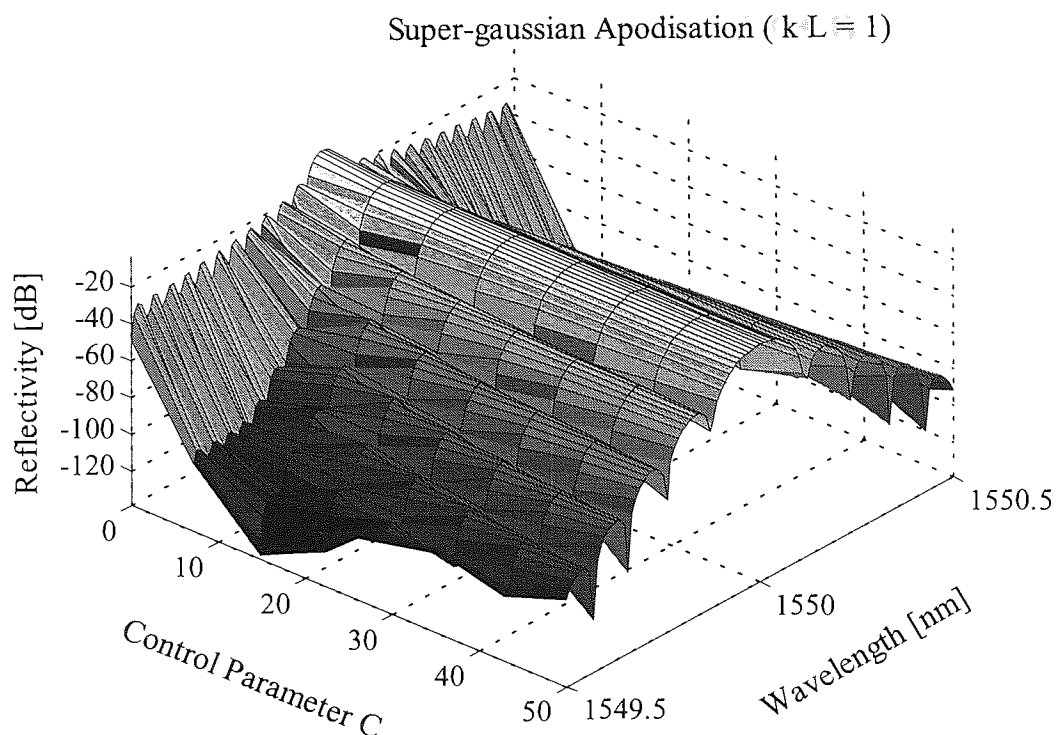
Figure 3.19 *Numerical computation of side lobes suppression as a function of the width control parameter C of a super-gaussian apodisation function for the case of a weak grating.*

Super-gaussian Apodisation (k L = 7)
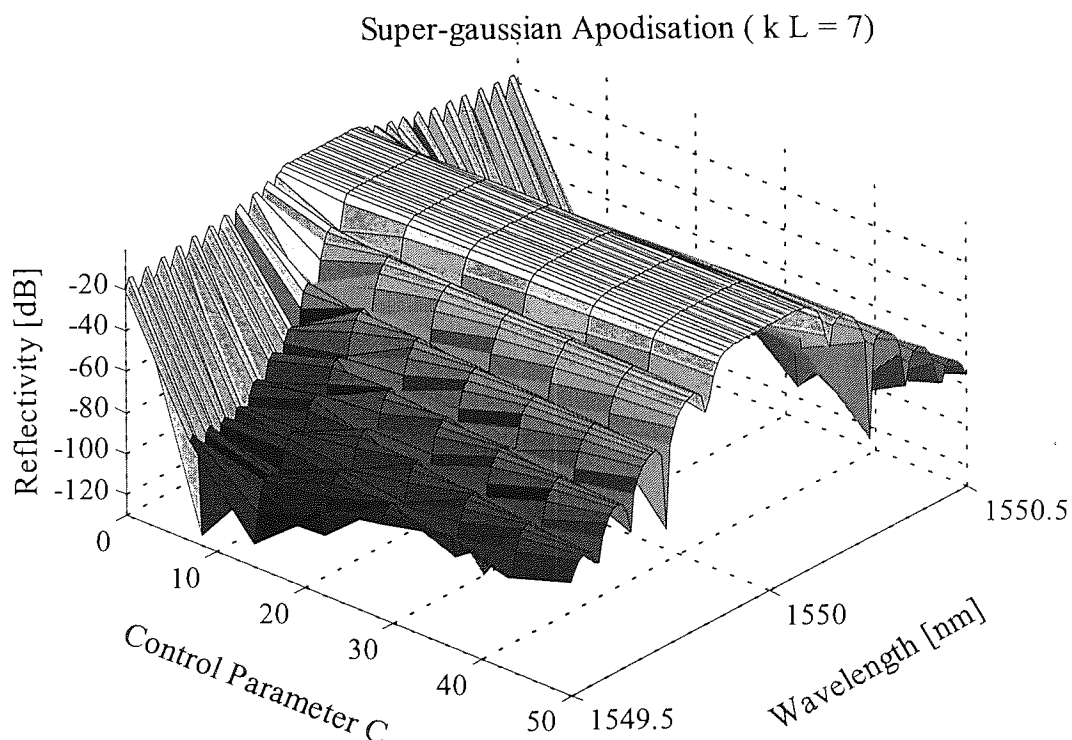
Figure 3.20 *Numerical computation of side lobes suppression as a function of the width control parameter C of a super-gaussian apodisation function for the case of a strong grating.*

Parabolic Apodisation (k L = 1)
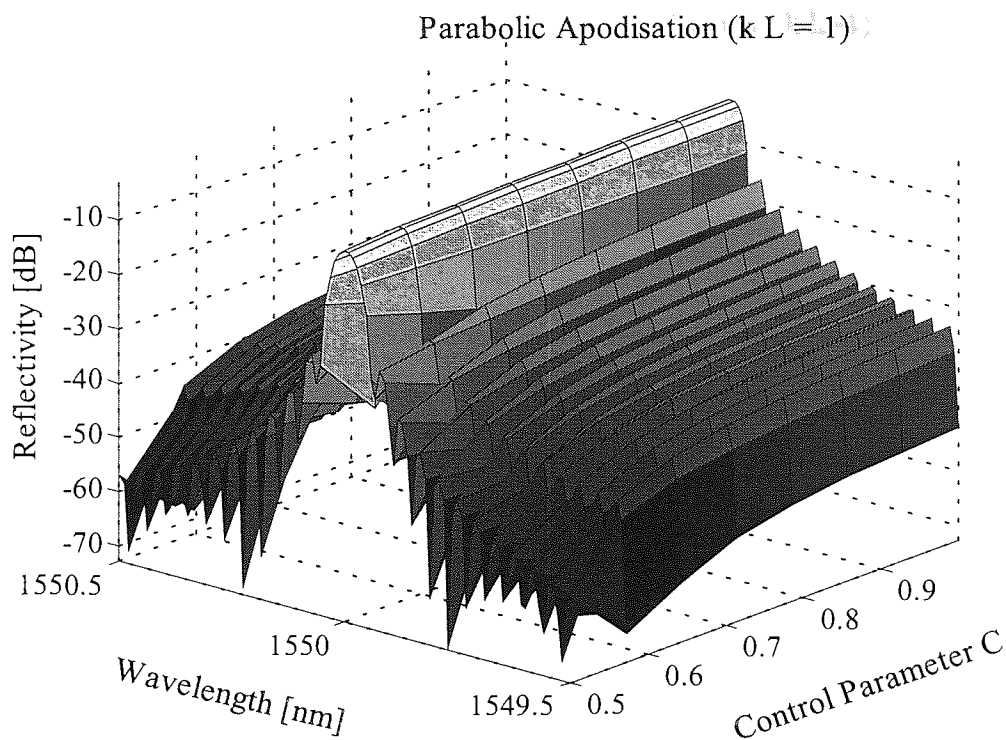
Figure 3.21 *Numerical computation of side lobes suppression as a function of the width control parameter C of a parabolic apodisation function for the case of a weak grating.*

Parabolic Apodisation (k L = 7)
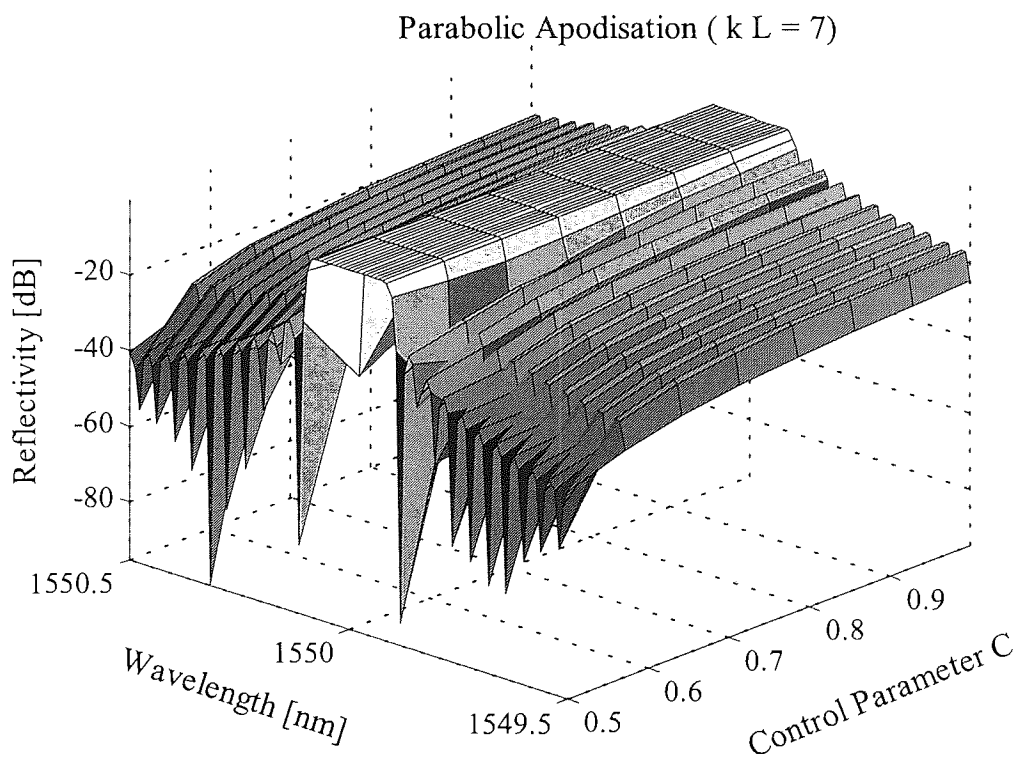
Figure 3.22 *Numerical computation of side lobes suppression as a function of the width control parameter of a parabolic apodisation function for the case of a strong grating.*
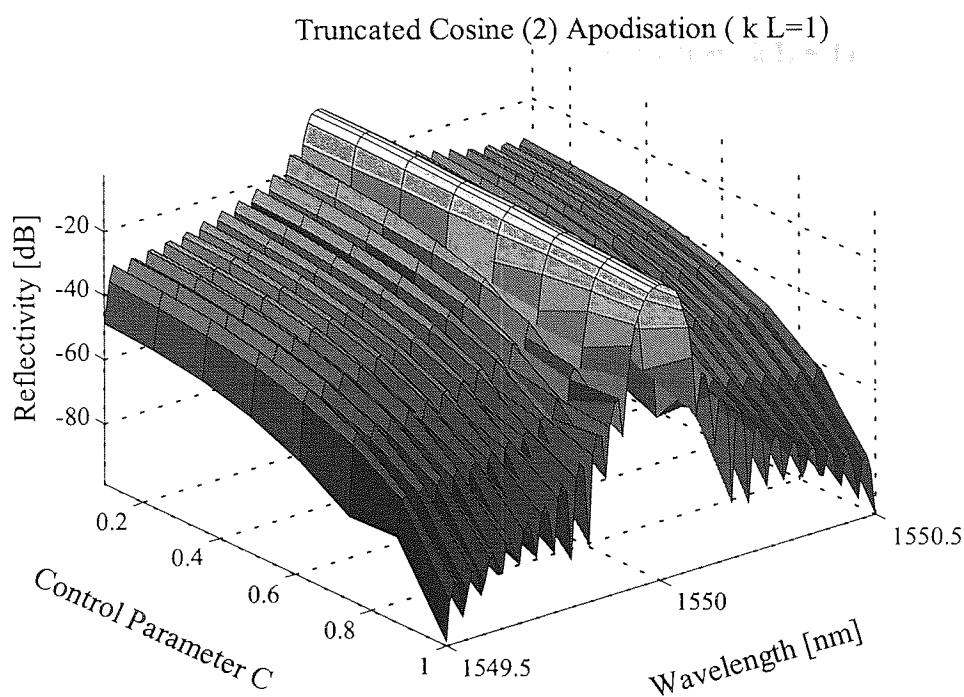
Figure 3.23 *Numerical computation of side lobes suppression as a function of the width control parameter of a truncated cosine (n=2) apodisation function for the case of a weak grating.*
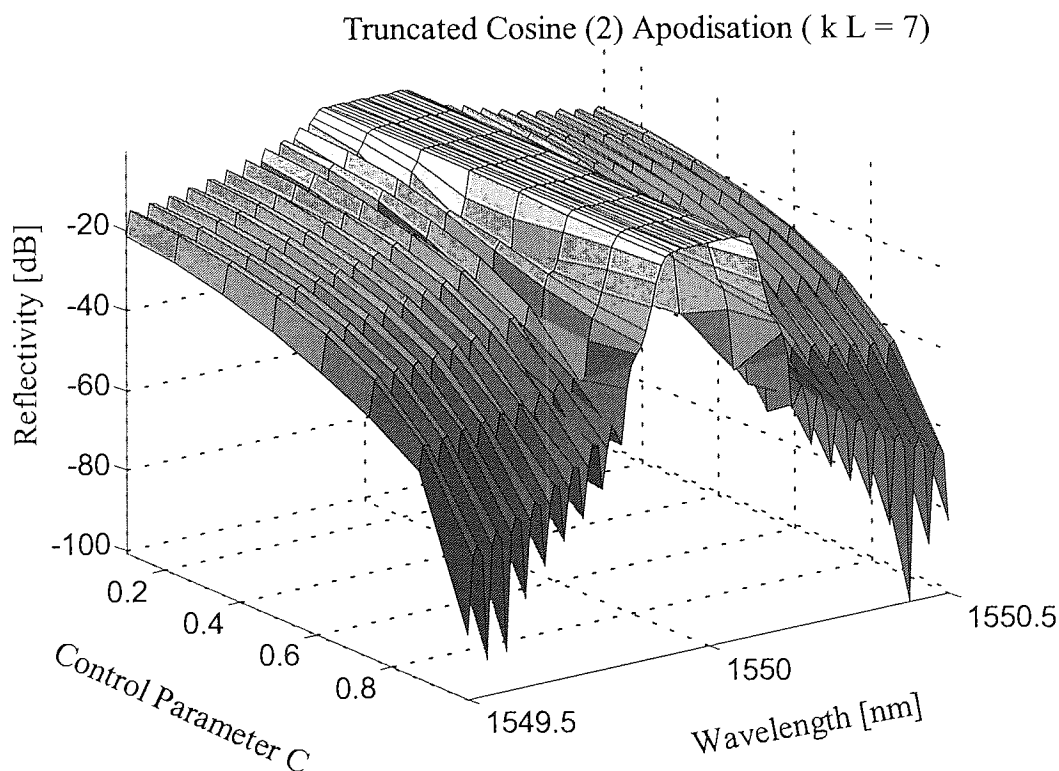
Figure 3.24 *Numerical computation of side lobes suppression as a function of the width control parameter of a truncated cosine (n=2) apodisation function for the case of a strong grating.*

Truncated Cosine (13) Apodisation (k L = 1)
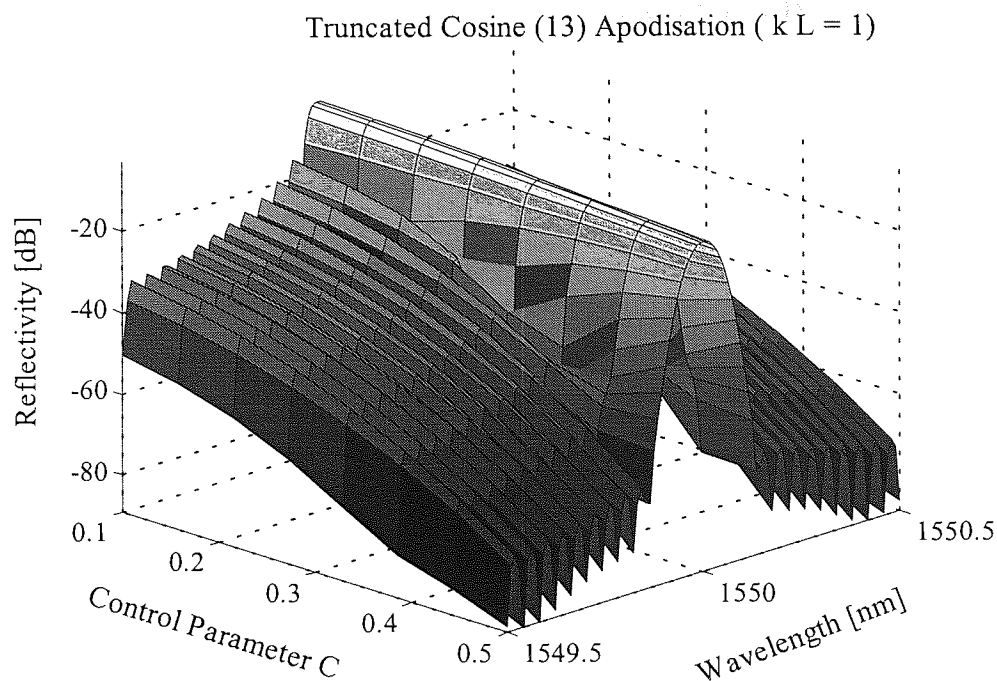
Figure 3.25 *Numerical computation of side lobes suppression as a function of the width control parameter C of a truncated cosine (n=13) apodisation function for the case of a weak grating.*

Truncated Cosine (13) Apodisation (k L = 7)
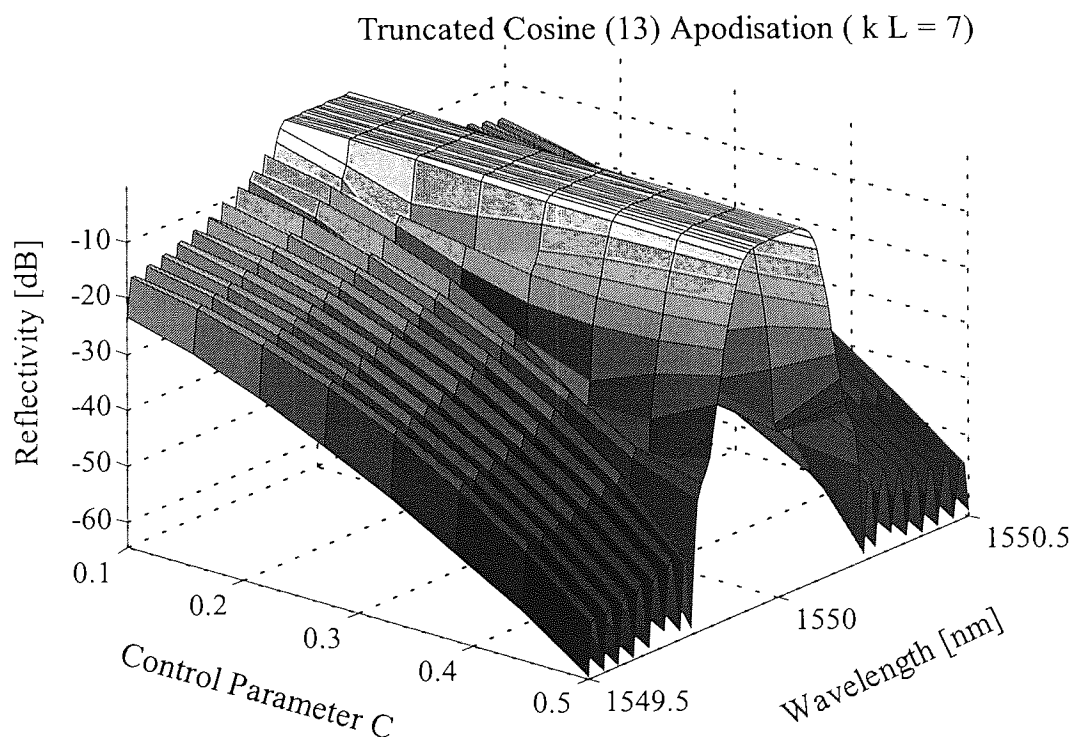
Figure 3.26 *Numerical computation of side lobes suppression as a function of the width control parameter of a truncated cosine (n=13) function for the case of a strong grating.*
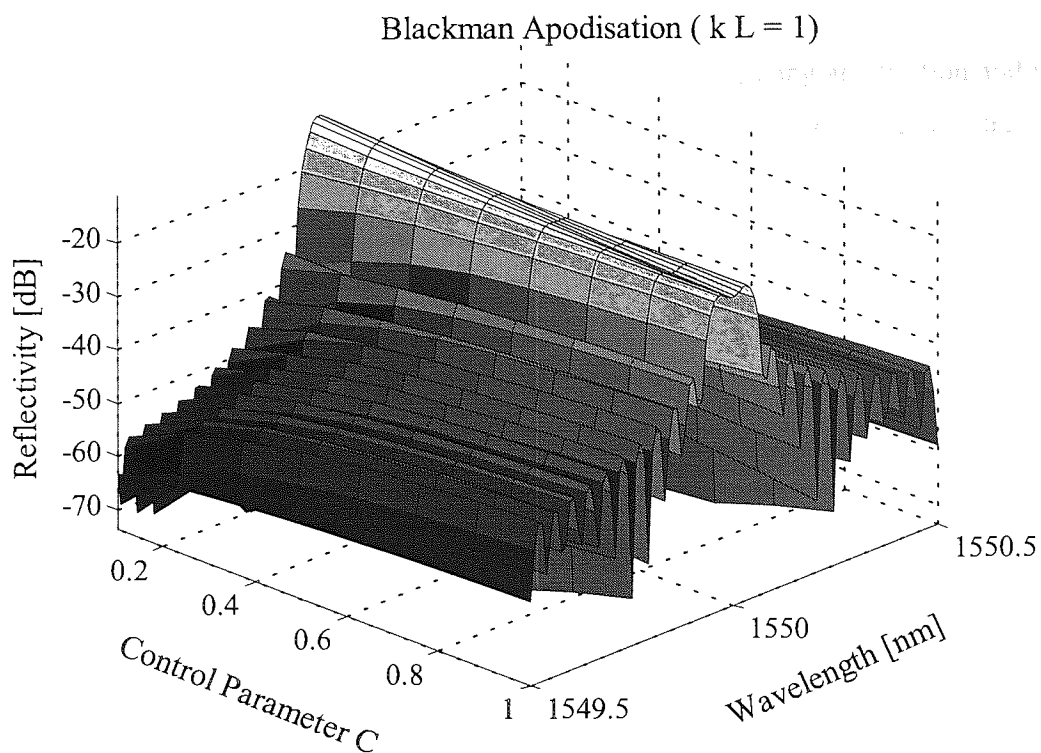
Figure 3.27 *Numerical computation of side lobes suppression as a function of the width control parameter C of a Blackman apodisation function for the case of a weak grating.*
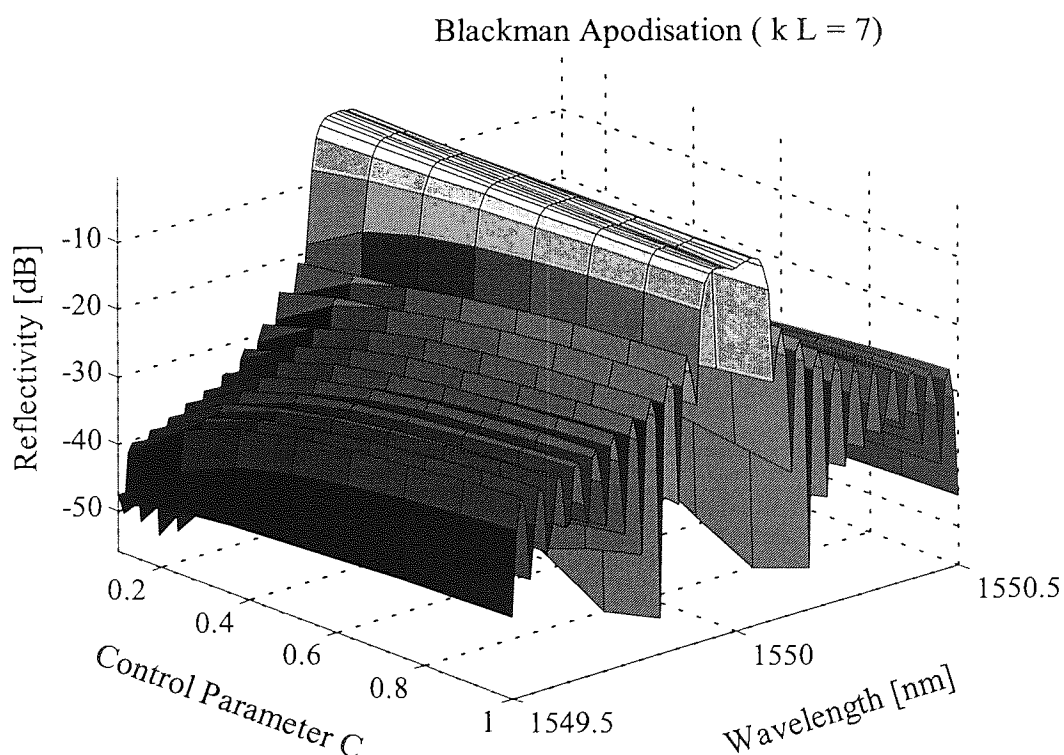
Figure 3.28 *Numerical computation of side lobes suppression as a function of the width control parameter of a Blackman apodisation function for the case of a strong grating.*

3.5 Chapter Conclusions

In this chapter we investigated the physical principles of fibre grating apodisation and we gave details on the most common experimental techniques used for reducing the strength of the unwanted lateral side-lobes in the spectrum of an ordinary FBG. Special attention was given to the description of two apodisation techniques: the variable speed double scan technique and the phase mask dither technique. The first one is a novel technique based on a variant of the usual double exposure technique (where an amplitude mask is used for the first scan used for preconditioning the fibre background refractive index, and the grating is written through another amplitude mask in conjunction with a phase mask in the second scan [29]). In comparison with the most general method, the double scan variable speed technique is more simple as only a phase mask is required for the apodisation of the grating. We also investigated the advantages and the disadvantages of each technique proving that, even if the variable speed technique is in principle the easiest method to implement, it is a more difficult one to control. On the contrary, the phase mask dither technique allows the fabrication of a better quality gratings (with a more symmetric shape of the Bragg reflection peak) and guaranties a higher success rate. To find the dependence of apodisation on the used parameters (such as the width of the apodisation function and the strength of the grating), we performed a full numeric investigation on six different shaping function. The numerical model, based on the theory developed in chapter two, shows that the used apodisation function should depend on the strength of the grating. More precisely, a Gaussian shaping function should be used in the case of a weak grating, where a Blackman function is more convenient for a strong grating. The numerical analysis enables to compare the different apodisation function and can also be used to predict the result obtained on real gratings for a given value of the parameter C (width of the apodisation function) and strength of the grating to be written.

References

[1]   K. Ennser, M.N. Zervas, R.I. Laming, "Optimization of apodized linearly chirped fiber gratings for optical communications", *IEEE J. Quantum Electron.,* **34**, 1998 pp.770-778.

[2]   M. Matsuhara, K.O. Hill, "Optical-waveguide band-rejection filters: design", *Appl. Opt.,* **13**, 1974, pp. 2886-2888.

[3]   K.O. Hill, "Aperiodic distributed-parameter waveguides for integrated optics", *Appl. Opt.,* **13**, 1974, pp. 1853-1856.

[4]   T. Erdogan, "Fiber Bragg spectra", *J. Lightwave Technol.*, **15**, 1997, pp. 1277-1294.

[5]   R. Kashyap, "Fiber bragg gratings", *Academic Press*, London, 1999.

[6]   H. Storøy, H.E. Engan, B. Sahlgren, R. Stubbe, "Position weighting of fibre Bragg gratings for bandpass filtering", *Opt. Lett.*, **22**, 1997, pp. 784-786.

[7]   R. Stubbe, B. Sahlgren, S. Sandgren, A. Asseh, "Novel technique for writing long superstructured fiber Bragg gratings" in proc. Photosensitivity and Quadratic Nonlinearity in Glass Waveguides 1995 (Washington DC, USA, 1995), *paper PD1*.

[8]   J. Albert, K.O. Hill, B. Malo, S.T. Thériault, F. Bilodeau, D.C. Johnson, L.E. Erickson, "Apodisation of the spectral response of fibre Bragg gratings using a phase mask with variable diffraction efficiency", *Electron. Lett.*, **31**, 1995, pp. 222-223.

[9]   J. Albert, K.O. Hill, D.C. Johnson, F. Bilodeau, M.J. Rooks, "Moiré phase masks for automatic pure apodisation of fibre Bragg gratings", *Electron. Lett.*, **32**, 1996, pp. 2260-2261.

[10]   J.J. Pan, Y. Shi, "Steep skirt fibre Bragg grating fabrication using a new apodised phase mask", *Electron. Lett.*, **33**, 1997, pp. 1895-1896.

[11]   H.G. Fröhlich, R. Kashyap, "Two methods of apodisation of fibre-Bragg-gratings", *Opt. Commun.*, **157**, 1998, pp. 273-281.

[12]   P.-Y. Cortès, F. Ouellette, S. LaRochelle, "Intrinsic apodisation of Bragg gratings written using UV-pulse interferometry", *Electron. Lett.*, **34**, 1998, pp. 396-397.

[13]   T. Komukai, K. Tamura, M. Nakazawa, "An efficient 0.04 nm apodized fibre Bragg grating and its application to narrow-band spectral filtering", *IEEE Photonics Technol. Lett.*, **9**, 1997, pp. 934-936.

[14]   R. Kashyap, A. Swanton, D.J. Armes, "Simple technique for apodising chirped and unchirped fibre Bragg gratings", *Electron. Lett.*, **32**, 1996, pp. 1226-1228.

[15]   R. Kashyap, M.H. Reeve, "Single-ended fibre strain and length measurement in the frequency domain", *Electron. Lett.*, **16**, 1980, pp. 689-691.

[16]   M.J. Cole, W.H. Loh, R.I. Laming, M.N. Zervas, S. Barcelos, "Moving fibre/phase mask-scanning beam technique for enhanced flexibility in producing fibre gratings with a uniform phase mask", *Electron. Lett.*, **31**, 1995, pp. 92-94.

[17]   W.H. Loh, M.J. Cole, M.N. Zervas, S. Barcelo, R.I. Laming, "Complex grating structures with uniform phase mask based on the moving fiber-scanning beam technique", *Opt. Lett.*, **20**, 1995, pp. 2051-2053.

[18]   J.B. Jensen, N. Plougmann, H.-J. Deyerl, P. Varming, J. Hübner, M. Kristensen, "Polarization control method for ultraviolet writing of advanced Bragg gratings", *Opt. Lett.*, **27**, 2002, pp.1004-1006.

[19]   P. Varming, J.B. Jensen, N. Plougmann, M. Kristensen, J. Hübner, in *Bragg Gratings, Photosensitivity, and Poling in Glass Waveguides,* Vol. 61 of OSA Trends in Optics and Photonics (Optical Society of America, Washington D.C., 2001), paper BWA5-1.

[20] R. Feced, M.N. Zervas, "Effect of random phase and amplitude errors in optical fiber Bragg gratings", *J. Lightwave Technol.*, **18**, 2000, pp. 90-101.

[21] M. Ibsen, R.I. Laming, "Fibre non-uniformity caused Bragg grating imperfections", in proc. OFC 1999 (San Diego, USA, 1999), *paper 2/ FA1-1*.

[22] F. Ghiringhelli, C. Alegria, M.N. Zervas, "Effect of phase shift perturbations and complex local time delay in fiber Bragg gratings", BGPP 2001 (Stresa, Italy, 2001), paper BWA3.

[23] D. Pudo, L.R. Chen, D. Giannone, L. Zhan, I. Bennion, "Actively mode-locked tunable dual-wavelength erbium-doped fiber laser", *IEEE Photon. Technol. Lett.*, **14**, 2002, pp. 143-145.

[24] K. Ennser, M.N. Zervas, R.I. Laming, "Optimisation of apodised linearly chirped fiber gratings for optical communications", *IEEE J. Quantum Electron.*, **34**, 1998, pp. 770-778.

[25] D. Pastor, J. Capmany, D. Ortega, V. Tatay, J. Martì, "Design of apodised linearly chirped fiber gratings for dispersion compensation", *J. Lightwave Technol.*, **14**, 1996, pp. 2581-2588.

[26] C. Yang, Y. Lai, "Improving the spectral sharpness of an apodized fibre grating", *J. Opt. A: Pure Appl. Opt.*, **2**, 2000, pp. 422-425.

[27] M.N. Zervas, R. Feced, "Synthesis of fiber gratings", in proc. OFC 2000, (Baltimore, USA, 2000), paper TuH1.

[28] R. Feced, M.N. Zervas, M.A. Muriel, "An efficient inverse scattering algorithm for the design of nonuniform fiber Bragg gratings", *IEEE J. Quantum Electron.*, **35**, 1999, pp.1105-1111.

[29] B. Malo, S. Thériault, D.C. Johnson, F. Bilodeau, J. Albert, K.O. Hill, "Apodised in-fibre Bragg grating reflectors photoimprinted using a phase mask", *Electron. Lett.*, **31**, 1995, pp. 223-225.

Chapter 4

LINEARLY CHIRPED FBGs AND OPTICAL DISPERSION MEASUREMENTS

4.1 Chapter Overview

This chapter contains both a theoretical description and an experimental characterization of chirped FBGs used as dispersive elements. Firstly, the physical mechanism inducing pulse broadening in a optical fibre is analysed, then the use of dispersive elements to compensate for such a broadening, such as dispersion compensating fibre or linearly chirped FBGs, is illustrated. The definitions of chromatic dispersion and dispersion slope (high order dispersion) are also given. An important part of the chapter concerns the measurement of the dispersion of fibres and FBGs. The modulation phase shift measurement method is detailed: the optimisation of the experimental parameters involved in the measurement is discussed together with the limitations and measure errors analysis. Examples of dispersion measurements by the use of the above method are given for fibres and FBGs. Another important point is the analysis of the group delay ripples, as this aspect could affect the transmission capability of an optical link. Such an analysis is undertaken by a statistical and mathematical (Fourier Transform) approach. The study of the group delay ripples in

unapodised and apodised FBGs confirms the effectiveness of apodisation in reducing their amplitude. We consider then the spectral characterisation of linearly chirped FBGs, with a special attention to two main imperfections occurring in the reflectivity: the insertion loss and the short wavelength loss. A description of the experimental techniques used, during the grating's fabrication process, to compensate for such losses is also given. The last section deals with experimental results on the temporal Talbot effect. We prove that, under precise conditions on the period of the input signal, a multiplication of the bit rate of the pulse stream (up to ten times) is possible by simply using the dispersive properties of a linearly chirped FBG used in reflection.

4.2 Compensation of Optical Fibre Dispersion

The current choice of operating optical fibre communication links at a wavelength near 1550 nm is mainly due to two important reasons: the silica fibre loss curve characteristic and the advent of Erbium Doped Fibre Amplifiers (EDFAs). Standard Monomode Fibres (SMFs) are step-index waveguides with minimum loss point around 1550 nm. There is an intrinsic advantage in operating transmission links at this wavelength as the transmission distance can be maximized in such a way. On the other hand, EDFAs, that also operate at 1550 nm, provide a periodic analog amplification rather than digital regeneration with the advantage of higher signal power levels and a further increase of the distance that the signals can travel before detection and regeneration. The combination SMF-EDFA seems then perfect for the implementation of a lightwave signals system over very long transmission distances [1], [2]. However, as the zero dispersion wavelength of a SMF is around 1310 nm, the amount of chromatic dispersion at 1550 nm is rather significant (typically around $17 \, ps/nm/km$) and, even worse, the dispersion of the optical fibre generally varies over the EDFA gain bandwidth (the typical variation of dispersion with wavelength is $0.08 \, ps/nm^2/km$). Obviously, the presence of an unbalanced dispersion in the communication link is armful for the system, as it can seriously compromise the information-carrying capacity of the system. Broadly speaking, the chromatic dispersion produces a variation in the speed of propagation of a lightwave signal that depends on wavelength. Because of chromatic dispersion, each wavelength inside the optical pulse travels through the fibre at a slightly different speed and this results in a broadening of the optical pulse as shown in Fig. 4.1. In practice, chromatic dispersion places a limit on the maximum distance that an optical pulse can cover without regeneration. This maximum

propagation length can be estimated by determining the transmission distance at which the pulse has broadened by one bit interval and, for a signal of width $\Delta\lambda$ is given by [3]

$$L_{max} = \frac{1}{B \cdot D \cdot \Delta\lambda}$$ (4.2.1)

As an example, if we consider a commercial transmission system, with bit-rate $B = 10\,\text{Gbit/s}$, fibre dispersion $D = 17\,\text{ps/nm/km}$, and pulse spectral bandwidth $\Delta\lambda = 0.4\,\text{nm}$ (corresponding to a 3 ps gaussian pulse), we have that the maximum propagation length is ~ 14.7 km. For data rates higher of 10 Gbit/s, the maximum propagation distance is of the order of kilometres: beyond this distance the signal broadening causes overlap of neighbouring pulses then signal corruption.
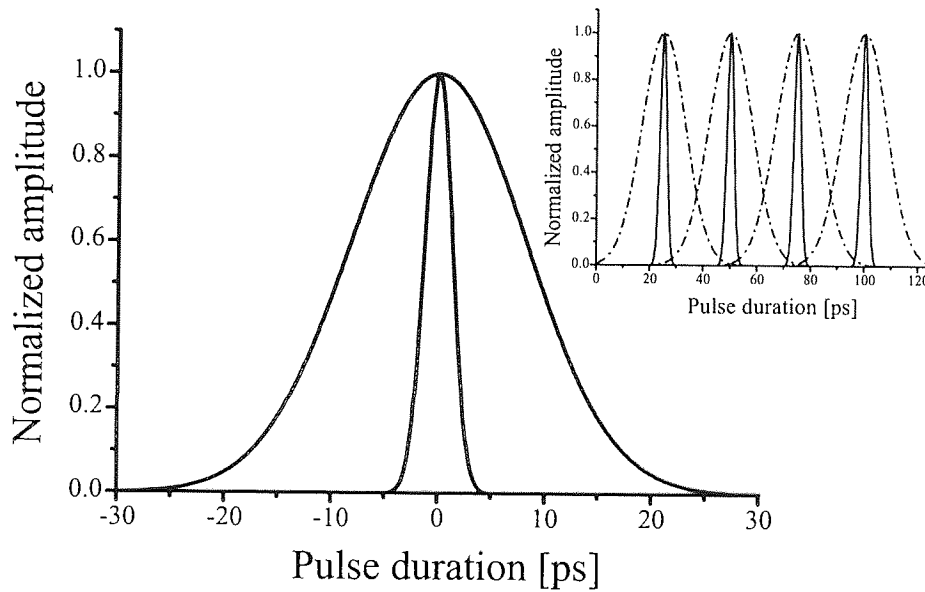
Figure 4.1 *Pulse broadening caused by chromatic dispersion on a single 3 ps FWHM pulse travelling through 1 km of standard telecommunication fibre. The inset shows the effect of chromatic dispersion on a 40 Gbit/s data stream after propagation through the same length of SMF.*

Clearly, an efficient lightwave transmission system including EDFAs, must employ some sort of dispersion compensation to accommodate the dispersion of hundreds or even thousands of kilometres of fibre. The problem of the dispersion compensation has been tackled using so many different approaches that it is practically impossible to mention all of them [4-10]. At the state of the art, the most popular and successfully utilised methods to compensate for the dispersion induced on the optical pulses by the propagation in SMF are based on the insertion, at some point of the optical link, of an element imposing a dispersion of opposite sign (i.e. negative or "normal" dispersion). This compensating element (generally, a span of special compensating fibre or a chirped fibre Bragg grating) is employed to nullify the effect of the anomalous dispersion produced by the SMF. The

use of a dispersion compensating fibre (DCF) was originally proposed by Lin *et al.* [11], and this is today the method of choice for compensation of the chromatic dispersion effect in optical links. The advantage of using DCF relies in its high figure of merit (the absolute value of the dispersion divided by the attenuation (in dB/km), usually expressed in units of ps/nm-dB) and the high negative dispersion (typically around -100 ps/nm-km). Nevertheless this fibre has also some disadvantages: a very high bending loss sensitivity, higher attenuation than SMF (generally around 0.35 dB/km) and the inability to compensate the higher order dispersion, apart from the problem of being quite expensive. So, even if compensation by DCF is still the most popular method, the use of chirped fibre gratings to deliver negative (normal) dispersion, is still actively investigated because of the many advantages that it offers. Like DCF, chirped fibre gratings are passive elements (they do not require any power supply) and moreover, they are compact, have low insertion loss, and can be fabricated to affect both a broad-band and a narrow-band of optical signals. Most importantly, there are techniques that can be used to make them tunable in dispersion (and this is the subject of the next chapter). The use of linearly chirped FBGs to cancel the effect of the chromatic dispersion induced by SMF was firstly proposed by Ouellette [12]. The working principle is easy to understand: the (anomalous) chromatic dispersion of SMF acts in such a way that the shorter wavelength components of an optical pulse travel faster than the longer wavelengths [13], [14].
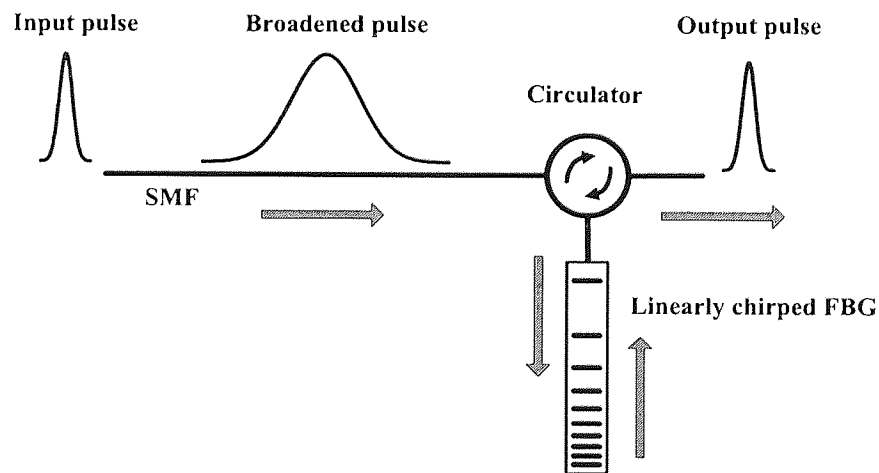
Figure 4.2 *Schematic of the optical pulse recompression by use of a linearly chirped FBG.*

A linearly chirped FBG introduces a time delay between the spectral components that are reflected around the beginning of the grating and those that are reflected at its end. It is straightforward to set the grating in such a way as to reflect the faster travelling spectral components of a dispersed optical pulse around its end, thus restoring the original pulse

shape. The use of a chirped FBG in reflection geometry requires an optical circulator (Faraday rotator) to allow the pulse to pass through the grating and to be reinserted in the transmission line, as it is shown in Fig. 4.2.
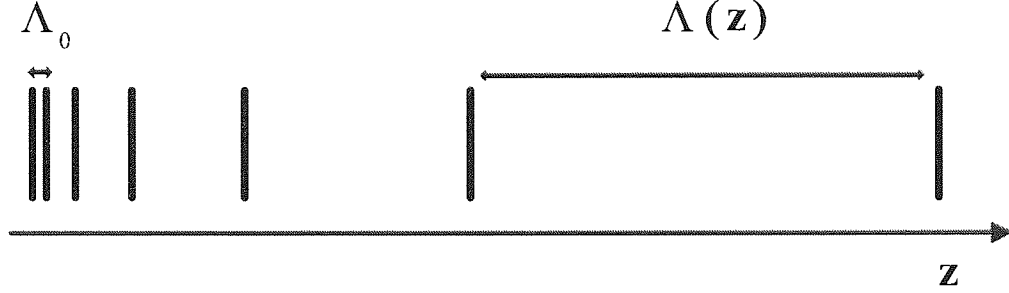
Figure 4.3 *Period dependency of a linearly chirped FBG on the axial coordinate z.*

Figure 4.3 is a representation of the dependency of the refractive index modulation on the position z along the fibre. In the case of a linearly chirped FBG, the Bragg condition, i.e. the condition linking the grating period Λ to the resonant wavelength λ_B, is satisfied for different wavelengths at different positions along the grating length, according to

$$\lambda_B (z) = 2\, n_{\text{eff},01}^{co} \, \Lambda(z) = 2\, n_{\text{eff},01}^{co} \left(\Lambda_0 + \alpha_0\, z \right) \qquad (4.2.2)$$

where Λ_0 is the initial period of the grating, α_0 is the chirp rate (usually expressed in nm/cm) and z is the axial coordinate along the grating.

Each wavelength, that is included in the grating bandwidth and constitutes the optical pulse spectrum, is back-reflected by a different section of the grating, i.e. after travelling a different distance z from the grating beginning. Because of that, each wavelength experiences a different group delay τ given by

$$\tau = \frac{2\, z}{v_g} = 2\, z\, \beta_1 = 2\, z\, \frac{d\beta_{01}^{co}}{d\omega} = -\frac{4\pi c z}{\omega^2} \cdot \frac{d\beta_{01}^{co}}{d\lambda} \qquad (4.2.3)$$

where $v_g = 1/\beta_1$ is the group velocity (the pulse speed propagation), c is the vacuum speed of light and $\omega = 2\pi c/\lambda$ is the angular frequency. A plot of the group velocity as a function of the wavelength in a SMF is given in Fig. 4.4. The curve has been obtained by using

$$\beta_1 = \frac{1}{c}\left(n + \omega\, \frac{dn}{d\omega} \right) = \frac{n_g}{c} \qquad (4.2.4)$$

where the refractive index is approximated by the Sellmeier equation [1]

$$n^2(\omega) = 1 + \sum_{j=1}^{m} \frac{B_j\, \omega_j^2}{\omega_j^2 - \omega^2} \qquad (4.2.5)$$

with m=3 and $B_1 = 0.6961663$, $B_2 = 0.4079426$, $B_3 = 0.897794$, $\lambda_1 = 0.0684043$ μm, $\lambda_2 = 0.1162414$ μm and $\lambda_3 = 9.896161$ μm.
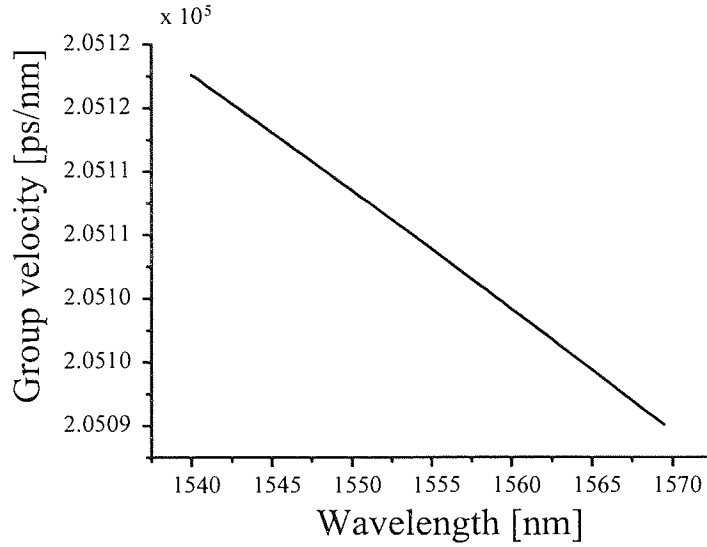
Figure 4.4 *Numerically calculated SMF group velocity as a function of the wavelength in the region of interest for a FBG.*

As the bandwidth of a chirped FBG is only few nanometers wide, and the wavelength dependence of the group velocity is very weak in such a small wavelength range, we can assume that the group velocity v_g is a constant in (4.2.3), then the group delay τ is a function only of z (physical length of the grating). This assumption is important for the derivation of a theory on tunable FBGs that will be presented in the next chapter.
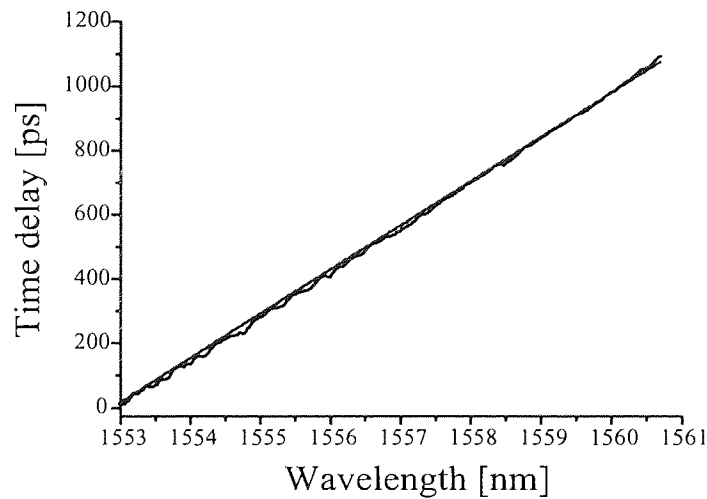
Figure 4.5 *Comparison between the experimental time delay of an 11 cm long linearly chirped FBG and the one calculated by inserting a chirp rate $\alpha_0 = 0.25$ nm / cm and a group velocity $v_g = 2.0511 \times 10^5$ nm / ps in (4.2.2) and (4.2.3).*

If a linearly chirped grating is used at the end of a span of SMF, in reflection and with the light injected from the long wavelength side, the time delay imposed to the "blue" part of the pulse spectrum will be proportional to the distance z that the pulse has to cover before

being reflected. This mechanism therefore compensates for the naturally occurring dispersion in SMF.

4.3 Some General Definitions

In a single mode fibre, chromatic dispersion results from the interplay of two different contributions: material dispersion and waveguide dispersion [15]. Material dispersion results from the nonlinear dependence upon wavelength of the refractive index and the corresponding group velocity of silica. Waveguide dispersion instead, arises from the geometry of the guided structure such as the core diameter, and depends on the difference in index between the core and the cladding. Provided that the guide dimensions are such that the mode is independent of wavelength, waveguide dispersion is usually much smaller than material dispersion and can be then neglected. The pulse broadening in SMF is due to the fact that the laser source radiates on a small but finite bandwidth (no laser is strictly monochromatic). Chromatic dispersion acts in such a way that simultaneously launched wavelengths propagate with different group velocities along the fibre and this leads to a broadened pulse beyond the initial time slot. The dispersion of an optical fibre around 1550 nm can be considered as the result of several order contributions in a Taylor series [16]. The dispersed pulse width Δt of an optical pulse of spectral width $\Delta\lambda$ can then be expressed as

$$\Delta t = \Delta\lambda \cdot \frac{d\tau(\lambda_0)}{d\lambda} + \frac{(\Delta\lambda)^2}{2} \cdot \frac{d^2\tau(\lambda_0)}{d\lambda^2} + \cdots \qquad (4.3.1)$$

where $\tau(\lambda_0) = L / v_g(\lambda_0)$ is the group delay and L is the fibre length.

Equation (4.3.1) can be rewritten as

$$\Delta t = \Delta\lambda \cdot L \cdot D(\lambda_0) + \frac{(\Delta\lambda)^2}{2} \cdot L \cdot D'(\lambda_0) + \cdots \qquad (4.3.2)$$

where we have introduced the fibre dispersion $D(\lambda_0)$ and the dispersion slope $S(\lambda_0)$, defined as

$$D(\lambda_0) = \frac{d}{d\lambda}\left[\frac{1}{v_g(\lambda)}\right]_{\lambda=\lambda_0} \quad \text{and} \quad S(\lambda_0) = D'(\lambda_0) = \frac{d}{d\lambda}[D(\lambda)]_{\lambda=\lambda_0} \qquad (4.3.3)$$

Typical values of D and S around 1550 nm for SMF (Corning SMF-28) are $D \approx 17\,ps/nm/km$ and $S \approx 0.08\,ps/nm^2/km$.

In the case of linearly chirped FBGs, a useful empiric relation to estimate the amount of chromatic dispersion that can be delivered by the grating is

83

$$D = \frac{2\,n_{eff}\,L}{c\,\Delta\lambda} \qquad\qquad (4.3.4)$$

where n_{eff} is the effective refractive index, L is the length of the grating, c is the vacuum speed of light and $\Delta\lambda$ is the grating bandwidth. As the amount of dispersion delivered by the grating is directly proportional to its physical length, it is clear the importance to develop writing technique that enable the fabrication of very long FBGs and minimise at the same time the stitching and phase errors inside the grating structure.

4.4 Chromatic Dispersion Measurements

The implementation of an accurate method for the measurement of the chromatic dispersion in optical components (such as SMF, DCF and FBGs) has become with time a more and more important issue, and this is primarily because of the increasingly growing transmission speed used to operate optical communication networks. The experimental estimation of the chromatic dispersion is generally obtained by measuring the time delay on the spectral components of light propagating through the optical device under investigation as a function of the wavelength. The time delay measurement is usually performed by interferometric methods [17-20], or alternatively via a phase shift technique [21-23]. Because of its simplicity and robustness, the latter is already an extensively used technique in most part of the commercially available measurement devices. The working principle of phase shift measurement is outlined in Fig. 4.6.
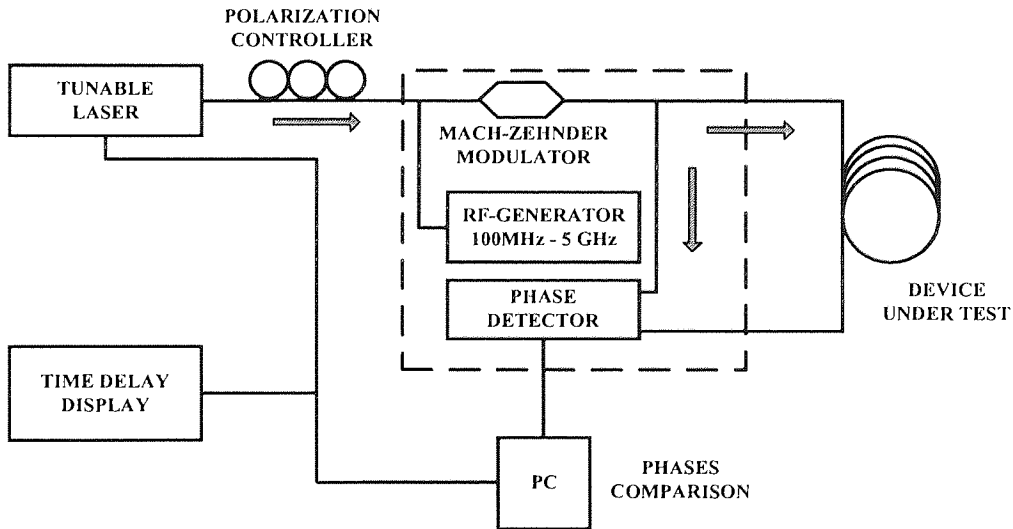
Figure 4.6 *Schematic diagram of the experimental set-up used for the measurement of chromatic dispersion by the phase-shift method.*

The input light source is a narrow bandwidth wavelength tunable laser (Photonetics TUNICS-PR) that is externally amplitude-modulated by a Mach-Zehnder modulator to

produce a waveform with a single, dominant Fourier component such as a sinusoidal, trapezoidal, or square wave modulation. The frequency tunability ranges between 100 MHz and 5 GHz and its stability is better than one part in 10^8. The polarization state of the light injected into the modulator can be modified by using a polarization controller. At the exit of the modulator the optical signal is split in two: the first branch is used as a reference signal (phase-locked to the modulating signal) and is sent directly to a phase detector (vector voltmeter). The second branch is sent to the phase detector after circulating through the device under test. A personal computer is used to control the wavelength scanning step of the tunable laser and to compare the two traces received from the phase detector. The time delay is obtained from the measured phase shift Φ between the two traces by using

$$\tau \ (\text{in ps}) = \frac{\Phi \ (\text{in degrees})}{360 \cdot \nu \ (\text{in Hz})} \tag{4.4.1}$$

and displayed on the computer screen. It is essential at this stage to prevent any ambiguity of $n \cdot 360$ degrees (n integer) during the measurement. For an unambiguous phase measurement, the wavelength step should be limited so that the produced phase change falls within the $\pm 180°$ range of the detector. Anyway, in our experimental set-up, this is not necessary as the tracking and adjustment of all $360°$ phase changes is automatically made by the computer. The accuracy of the time delay measurement depends primarily on the resolution of the phase measurement. Typically, vector voltmeters have a phase resolution of ≈ 0.1 degrees and most of the times this is enough to get an accuracy under 1ps on the time delay measurement. By the way, it is useful to note that, due to the wavelength discretization, the (4.4.1) represents an approximation that strictly provides an accurate result only if the time delay variation as function of wavelength is reasonably small. Wavelength accuracy is also important as the actual phase shift is proportional to the wavelength step. The method is not suitable for measuring the dispersion of short spans of fibre as the change in phase would be too small to be detected. At last, thermal transients in the measurement set-up and in the device under test can significantly contribute to the measurement errors. A given change in temperature produces a corresponding change in the fibre length, thus affecting the time delay measurement according to

$$\delta \tau = \frac{\delta L}{L} \tau \tag{4.4.2}$$

where L is the path length at a given temperature, and δL is the fibre elongation due to the temperature change. To minimize temperature effects, we allowed the device under test and the electronic equipments to stabilize in the ambient air before starting the measurements.

4.4.1 Modulation Frequency Calibration

It is well known that optical components, such as linearly chirped FBGs, exhibit substantial oscillations in the time delay response. These oscillations, usually referred to as group delay ripples, arise from a combination of factors: imperfections in the fabrication process and/or in the host optical fibre, as well as noise in the grating profile (period and/or refractive index modulation), may produce a multipath interference effect (Fabry-Perot micro-cavities) between adjacent sections of the grating. With some extent, apodisation can be used to minimize the amplitude of these ripples [24-27]. Nevertheless, even with the most sophisticated fabrication techniques, group delay ripples are unavoidable. These ripples have a direct impact on the performance of high speed optical transmission systems, as they produce dispersion errors and intersymbol interference [28-31]. There is still some debate on the extent to which the amplitude of these ripples produces distortion on the transmitted signal (in general it is not possible to make a prediction of the system performance on the bases of the ripple amplitude only). Nevertheless, in most part of the work published on the subject, the authors characterize the quality of the chirped grating by giving the value of the average amplitude of these group delay oscillations in picoseconds. The appropriate determination of the amplitude and periodicity of the group delay ripples is strictly connected to the resolution used in the measurement. In the case of the phase-shift technique, Fig. 4.7 clearly shows that the measured amplitude of delay ripples depends sensibly on the modulation frequency chosen for the measurement.
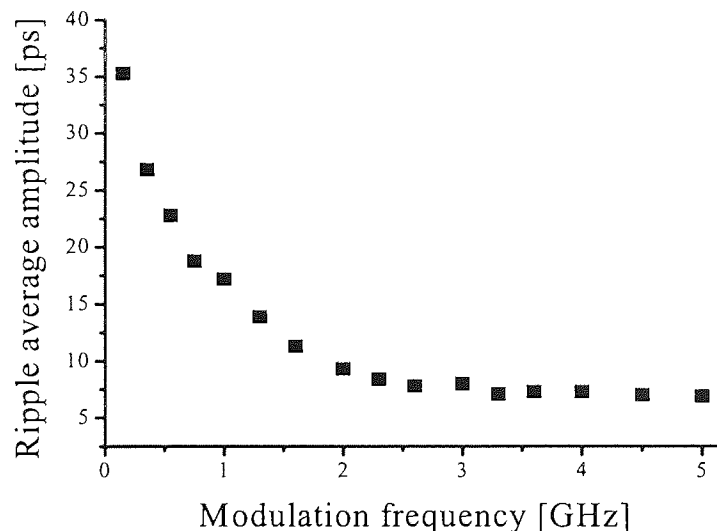
Figure 4.7 *Experimental average value of the amplitude of the group delay ripples (measured peak to peak) for a linearly chirped FBG (unapodised) as a function of the modulation frequency, in the phase-shift measurement technique.*

86

For a correct evaluation of the minute details in the time delay curve, it is essential to use an appropriate modulation frequency. In general a high modulation frequency provides a good temporal resolution but, at the same time, degrades the wavelength resolution, thus originating an improper group delay ripples characterisation. A modulation of 3 GHz, for instance, does not resolve properly the short period components of the group delay ripples due to the broadening of the source. On the other hand, a modulation frequency of 300 MHz and below adds noise to the group delay measurement due to the poor temporal accuracy. As a compromise between these two limiting cases, modulation frequencies around 1 GHz are generally accepted as the most suitable for an appropriate evaluation of the group delay ripples of a chirped FBG [32]. Where not stated otherwise, we intend that the dispersion measurements are made by setting the modulation frequency to 1 GHz.

4.4.2 Examples of Dispersion Measurements in Fibres and FBGs

We give here a few examples of the application of the phase shift method, and also we evaluate the magnitude of the incertitude associated with the dispersion measurement by using this method. We start by measuring the dispersion occurring in a span of SMF. Provided that the span of fibre under test is not too short, the method gives an accurate measurement of its chromatic dispersion. For instance, Fig. 4.8.a shows a measurement of the time delay in a 6.8 km long SMF.
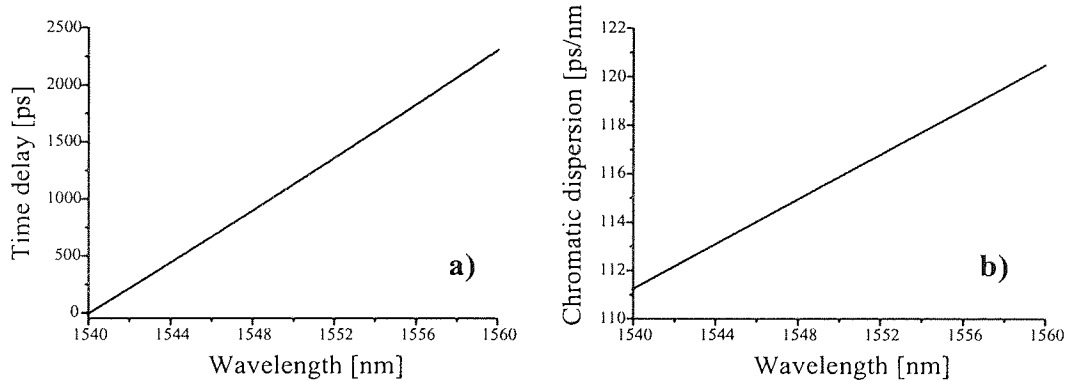
Figure 4.8 Phase shift method measurement on 6.8 km of SMF: a) time delay as a function of wavelength, b) calculated chromatic dispersion (derivative of time delay with respect to wavelength) as a function of wavelength.

The accuracy of the time delay measurement (see (4.4.1)) is estimated by using the following formula (to minimize the error on the phase measurement we choose 1 pμ that is the smallest step in wavelength allowed by the tunable laser) [33]

$$\frac{\delta \tau}{\tau} = \sqrt{\left(\frac{\delta \Phi}{\Phi}\right)^2 + \left(\frac{\delta \nu}{\nu}\right)^2} = 2\ \% \tag{4.4.3}$$

The experimental time delay at 1550 nm for the SMF under test is then:

$$\tau \pm \delta\tau = \left(1126 \pm 20\right) \text{ps}$$

The calculated value of chromatic dispersion delivered by the SMF at 1550 nm is

$$D \pm \delta D = (17.0 \pm 0.3) \text{ ps nm}^{-1}\text{km}^{-1}$$

where the incertitude on the dispersion measurement was estimated by using

$$\frac{\delta D}{D} = \sqrt{\left(\frac{\delta\tau}{\tau}\right)^2 + \left(\frac{\delta\lambda}{\lambda}\right)^2}$$

We want to measure now the dispersion delivered by a FBG. Figure 4.9 shows the experimental reflection spectrum and time delay of an unapodised linearly chirped FBG. The 11 cm long FBG was fabricated using a commercial chirped phase mask (Lasiris Technology) and a doubled frequency Argon laser (Coherent 300C FreD) with an output power of ~ 100 mW at 244 nm. The spectrum has been obtained using a tunable laser (Photonetics TUNICS-PR), with a step in wavelength of 1 pμ, and an optical spectrum analyser (HP 71451A), injecting the laser light from the short wavelength side of the grating (by the use of a three port circulator). The measurement of time delay was made using the phase shift method and the same step in wavelength of the tunable laser. Injecting the light from the short wavelength side of the grating corresponds to a bigger delay applied to the longer wavelengths than to the shorter ones. When used from this side, the grating delivers a constant anomalous chromatic dispersion whose measured value is

$$D \pm \delta D = (128.16 \pm 0.14) \text{ ps nm}^{-1}$$
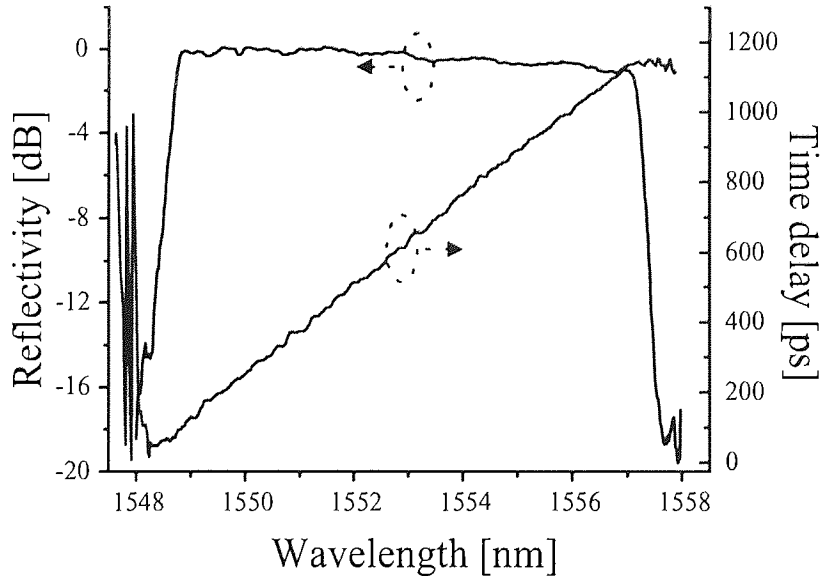
Figure 4.9 *Reflectivity and time delay measurements on a 11 cm long linearly chirped FBG fabricated using an holographic phase-mask (Lasiris Technology).*

88

4.4.3 Group Delay Ripples Characterisation

Figure 4.10.a shows the structure of typical group delay ripples (obtained by linearisation of the experimental curve) of an unapodised chirped FBG fabricated by using an holographic chirped phase-mask (Lasiris Technology). The histogram in Fig. 4.10.b represents the statistical distribution of these ripples.
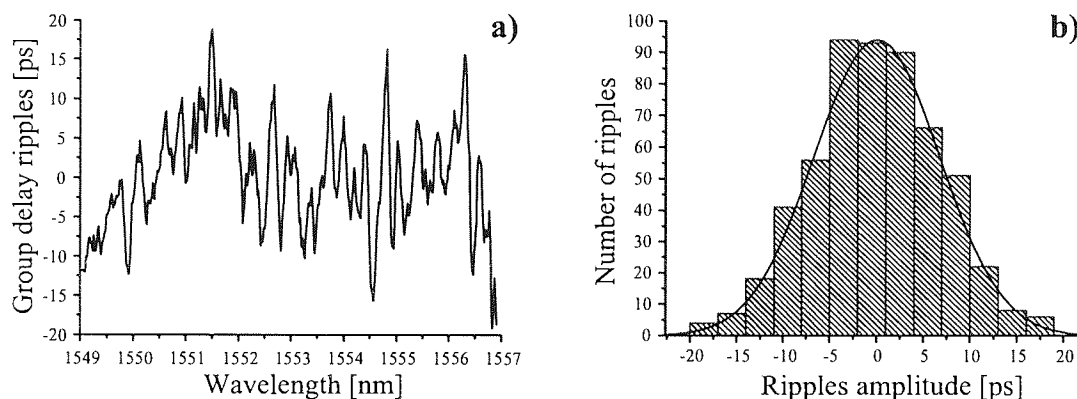
Figure 4.10 Analysis of ripples in the time delay response of a 11 cm long unapodised linearly chirped FBG made by using a chirped phase-mask (Lasiris Technology): a) group delay ripples as a function of wavelength, b) statistical distribution of the ripples amplitude.

As we already mentioned, the group delay ripples are produced by randomly distributed imperfections of the fibre and unpredictable fluctuations of the profile and phase of the grating. It is not surprising then that the amplitude of the group delay ripples can be described by a normal distribution. From Fig. 4.10.b, where the discrete plot is approximated by a continuous Gaussian distribution, it can be seen that more than 50% of the group delay ripples have an amplitude of ± 5 ps or less, while 68% have an amplitude of ± 7 ps or less. The average amplitude of the ripples, for the unapodised linearly chirped FBG (Fig. 4.9), is ± 5.5 ps. This low value is also an indirect proof of the very high manufacturing quality of the phase-mask (that seems to be nearly completely free from stitch errors). Figure 4.11 refers to a similar grating but this time apodised by using a Gaussian function (C=2). The apodised grating exhibits a substantial reduction of the amplitude of the ripples: 68% of the group delay ripples has an amplitude of ± 5 ps or less, and the average amplitude is estimated to be ± 4.4 ps, which means an average reduction of 20% with respect to the unapodised case. From the experimental data it can also be seen that the reduction of in-bandwidth ripples does not sensibly depend on the specific apodisation function used during the fabrication process.
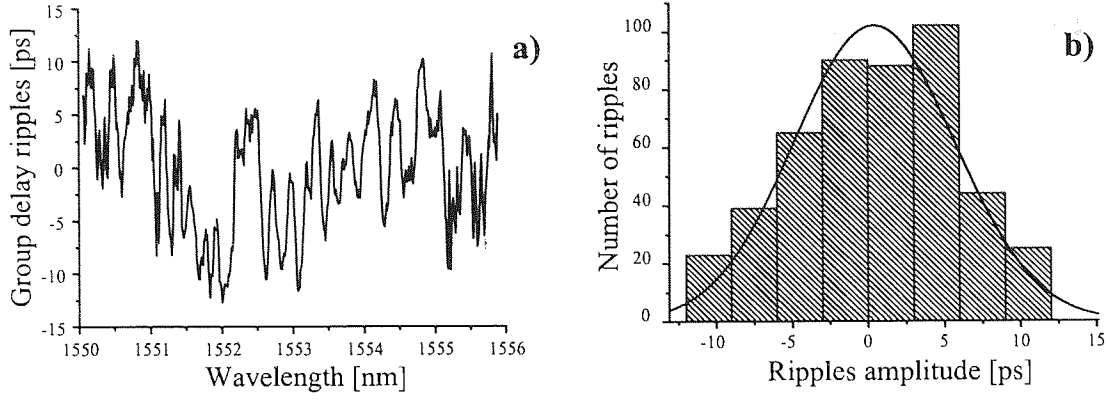
Figure 4.11 *Analysis of a 9 cm long gaussian apodised (C=2) linearly chirped FBG made by using Lasiris Technology phase-mask and dither phase-mask technique: a) group delay ripples as a function of wavelength, b) statistic distribution of the ripples.*

The fact that the group delay ripples data can be described by a normal distribution is a sign of their random origin. Nevertheless, it is still possible that some hidden periodicity, that is present in the group delay pattern, is not disclosed by a simple statistical analysis. For instance, some small defects of periodical nature, introduced by the stitching errors of the phase mask used in the fabrication of the FBG, could be hidden inside the group delay ripples distribution and thus not be revealed by statistics. A very useful mathematical tool that can be used on this subject is the Fourier transform. The ability of this tool of identifying periodical features inside the analysed data is well known. The numerical Discrete Fourier Transform (DFT) [34] (or the Fast Fourier Transform (FFT), that is a variant of the same algorithm, conceived to minimise the computation time), is easy to implement on any programming language. It is useful to recall here the basic definitions. For a dataset x[n] with n in the range $0 \leq n \leq N-1$, (where x[n] are complex numbers), the forward DFT is defined as

$$X[k] = \sum_{n=0}^{N-1} x[n] \exp(-i2\pi F_k n) \qquad 0 \leq n \leq N-1 \qquad (4.4.4)$$

where $F_k = k/N$. The DFT transforms N complex numbers x[n] into N complex numbers X[k]. Also it should be noted that DFT involves only the data values and their indices (other variables associated with the data, such as time, are not needed in the calculation). In practise, DFT is often performed on data collected at an equal (time) interval τ. It is easy to convert the index into "time" $t = n\tau$, and $F_k = k/N$ into "frequency" $f_k = \dfrac{k}{N\tau}$.

The inverse (backward) DFT is defined as

$$x[n] = \frac{1}{N} \sum_{k=0}^{N-1} X[k] \exp(i 2\pi F_k n) \qquad 0 \le k \le N-1 \qquad (4.4.5)$$

The FFT algorithm was originally proposed by Danielson and Lanczos [35] who demonstrated for the first time that if the total number of data points N is an integer power of 2, the DFT of these N numbers can be rewritten as the sum of two DFTs, each of length N/2, as follows

$$X[k] = \sum_{j=0}^{N/2-1} x[2j] \exp\left(-i\frac{2\pi k j}{(N/2)}\right) + W^k \sum_{j=0}^{N/2-1} x[2j+1] \exp\left(-i\frac{2\pi k j}{(N/2)}\right) \qquad (4.4.6)$$

where $W = \exp\left(-i\frac{2\pi}{N}\right)$. The recursive use of the Danielson-Lanczos lemma reduces the calculations to approximately $N \log_2 N$, compared to approximately N^2 required by DFT. To test the effectiveness of the method in spotting periodicities in a given set of data we generated pseudo-random group delay ripples by using

$$\sum_{n=1}^{m} A_n \sin\left(\omega \frac{2\pi}{\Omega_n}\right) \qquad (4.4.7)$$

where A_n is the peak amplitude of the sinusoidal variation, Ω_n is the period (in Hz) of the ripples and $\omega = \frac{2\pi c}{\lambda}$ is the angular frequency within the grating bandwidth.
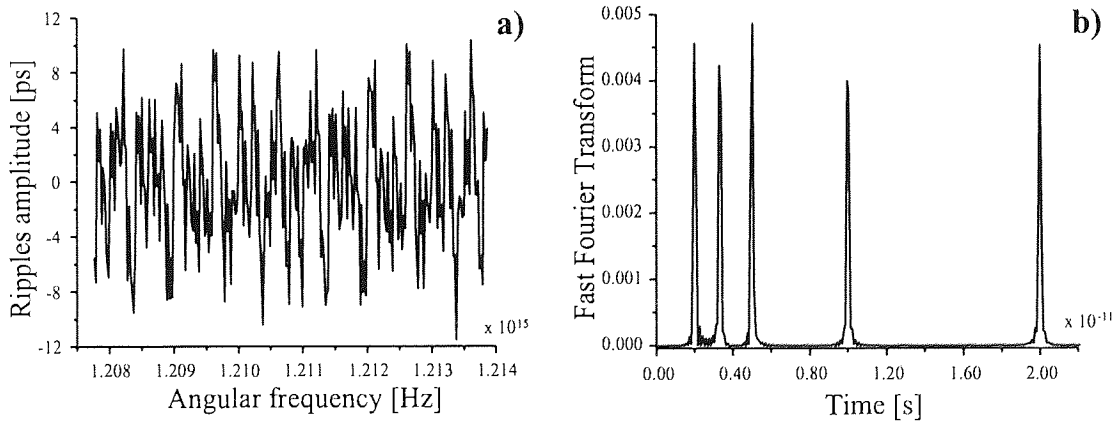
Figure 4.12 Demonstration of the FFT's ability of spotting hidden periodicities: a) pseudo-random group delay ripples generated by superposition of five different Ω_n in (4.4.7), b) FFT performed on the data, clearly showing the five periodicities contained in the pseudo-random pattern.

For the sake of simplicity, we took $A_n = 3$ ps for any n and chose five different periods: $\Omega_1 = 0.5 \times 10^{11}$ Hz, $\Omega_2 = 0.1 \times 10^{12}$ Hz, $\Omega_3 = 0.2 \times 10^{12}$ Hz, $\Omega_4 = 0.3 \times 10^{12}$ Hz, and $\Omega_5 = 0.5 \times 10^{12}$ Hz. The pseudo-random ripples generated as superposition of the five curves are shown in Fig. 4.12.a. The FFT performed on these data is shown in Fig. 4.12.b,

91

which is a clear proof of the validity of the method. Indeed all the five periods are precisely detected as $\Omega_n = 1/T_n$, where T_n are the values of the peaks in 4.12.b.

In the attempt to detect hidden periodicities, we performed the FFT on the experimental group delay ripples data of Fig. 4.10.a. The result is that the FFT is unable to identify any periodicity smaller than the full range of variability of the data. As a consequence, we deduce that there is no periodicity in such data, i.e. their nature is actually determined by random (not systematic) perturbations on the system when writing the grating.

4.5 Spectral Characteristics of Linearly Chirped FBGs

We analyse here the most commonly encountered imperfections of chirped FBGs, that occur because of the fabrication process or due to the intrinsic nature of the gratings. It is generally agreed that one important element in the fabrication of a FBG with high specifications, is a good quality phase-mask (for instance, there is no point in trying to write a good FBG by using a phase-mask with many stitch errors). Actually, this is only one aspect of the problem as the excellent quality of the phase-mask does not necessarily imply a good FBG. Many different issues contribute to the final result. For instance, a grating too strong in transmission or too long will have an higher loss compared to a weak or short one. Moreover if the beneficial effect of apodisation is to reduce the average value of group delay ripples, it also true that it affects the reflectivity of the grating not always in a desirable way.
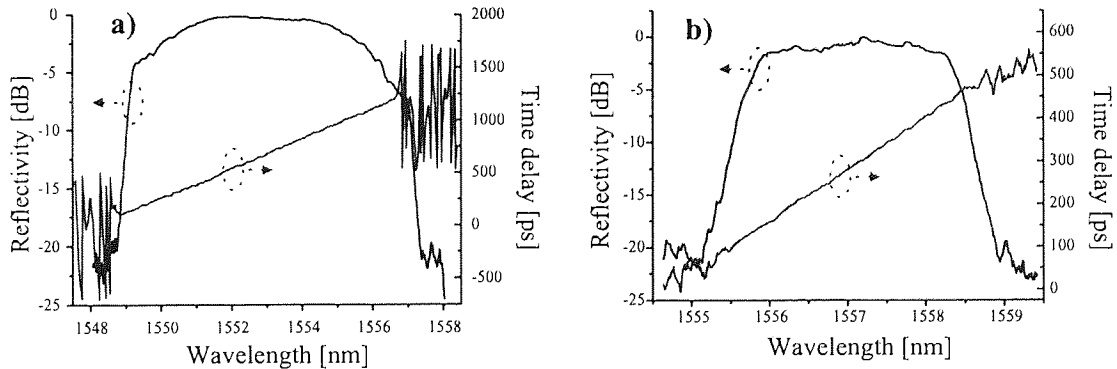
Figure 4.13 Experimental spectrum and time delay of two apodised linearly chirped FBGs: a) 11 cm long gaussian apodised (C=2), b) 6 cm long truncated cosine apodised (C=0.4 and n=2).

Therefore a good grating is the result of a compromise between all these variables, depending on the use for which it has been designed. Ideally, a good chirped FBG is a grating with a top as much flat as possible and, if used as a dispersion compensator, with a long physical length and a smooth time delay response (generally, in the case of long haul transmission systems, the average amplitude of the group delay ripples has to be below

92

±5 ps, even if dispersion-managed soliton transmission systems are quite immune to the perturbation effect produced by the group delay ripples [30]). Apart from the imperfections due to technical errors during the fabrication process, as for instance a misalignment of the laser beam with the phase-mask and the fibre, or a laser power fluctuation, some "intrinsic" imperfections (i.e. related to the nature of the grating) can be found in the spectrum of a chirped FBG. The first problem encountered is the insertion loss, that is due to the physical length of a chirped FBG. As we mentioned already, one reason for using SMFs in long haul transmission networks is the very low loss that these fibres exhibit around 1550 nm.
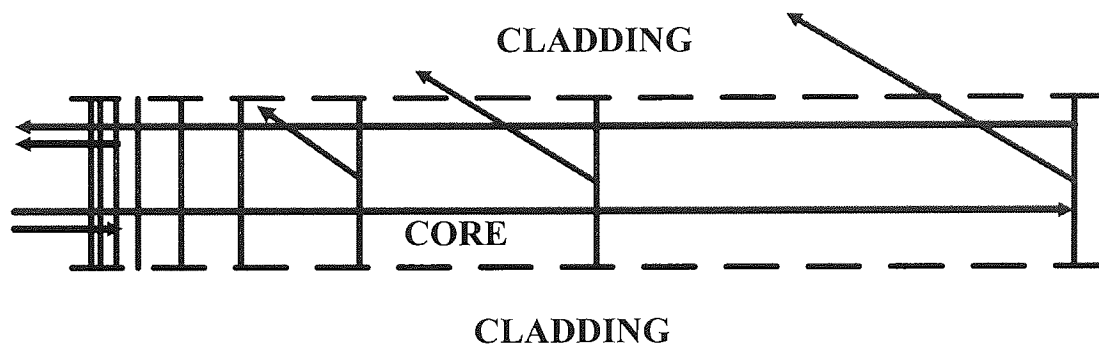
Figure 4.14 Schematic illustration of the insertion losses produced on the long wavelength side of a FBG spectrum. The loss increases proportionally to the length of the FBG.

Anyway, when a FBG is written inside the fibre core, the produced refractive index modulation will slightly increase the fibre loss. The loss increases with the strength of the grating, because a prolonged exposition to strong intensity UV light produces micro damages at the boundary between core and cladding, which contribute to the fibre loss. As schematically shown in Fig. 4.14, insertion loss affects the wavelengths travelling longer inside the fibre (as they interact for a longer time with the FBG structure). In the case of Fig. 4.14, as the long wavelengths follow a longer optical path, they are attenuated more than the short wavelengths (that are reflected back just at the beginning of the structure). The insertion loss depends also on the physical length of the grating. Figure 4.15 shows the measured insertion loss (approximately 1.5 dB at the longer wavelength side of the spectrum) for a 10 cm long chirped FBG (moderately strong). Most of the time, this small loss is armless for a transmission system and can be easily compensated by using an optical amplifier. An analysis of the effect of the insertion loss on the group delay ripples shows that the loss does not affect the ripple's average amplitude. If a flat top is needed for some specific application, an asymmetric apodisation function can be used to equalize the difference in reflectivity at the two opposite sides of the spectrum. Of a different nature are instead the losses shown in Fig. 4.16.a. These losses appear on the short wavelength region of the spectrum of a chirped FBG when observed from the long wavelength side (i.e. the

93

light is injected from the long wavelength side of the grating that thus generates a normal dispersion). Unfortunately, such short wavelength losses are always present in the spectrum of an ordinary FBG that has been written in SMF. Usually the amount of loss is proportional to the grating strength (losses up to 10 dB in the blue region of the spectrum have been observed for very strong gratings). The reason for such losses is the coupling with cladding modes [36].
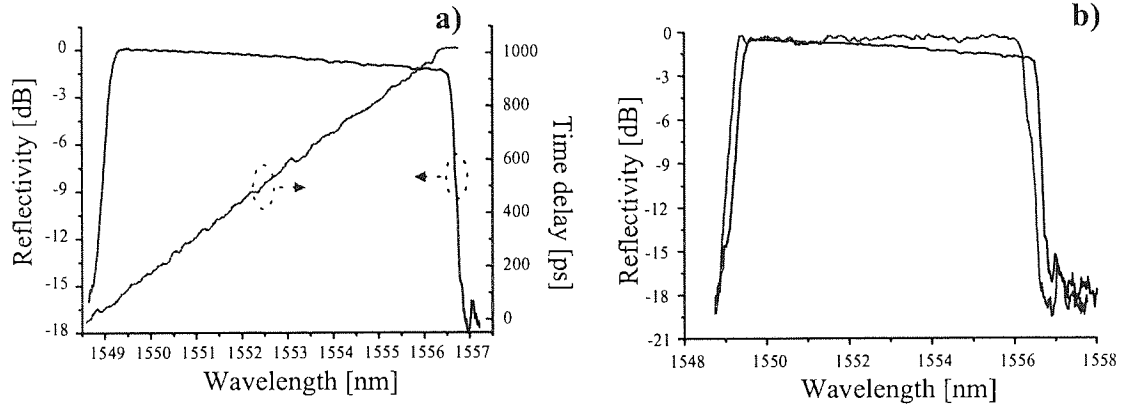
Figure 4.15 *Experimental demonstration of the compensation of insertion loss effect by a suitable asymmetric apodisation: a) measured spectrum and time delay of a 10 cm long linearly chirped FBG without apodisation, b) equalised spectrum.*

Although the structure has been designed to couple the co-propagating LP_{01} core mode with its counter-propagating part, the phase matching condition for coupling the forward propagating core mode to higher order cladding mode is also satisfied for shorter wavelengths. Part of the optical power is then transferred to the cladding producing a slope (lower reflectivity) from one side of the spectrum. Short wavelength losses, as they modify the reflection profile of the grating, also induce noise on the group delay ripples. Figure 4.16.b shows the average deviation from linearity of the measured time delay of the grating. The average oscillation value in the time delay curve has been measured as ± 8 ps (54% worse than when the grating is observed from the short wavelength side). Unfortunately, using the grating from the long wavelength side corresponds to a negative sign dispersion delivered by the grating, which is suitable for compensating the positive sign dispersion of the SMF. Clearly, further steps should be taken to improve the quality of the grating from this side because, as it is, the grating can not be used as a dispersion compensator due to the high asymmetric loss and the big group delay ripples. Some authors have proposed the use of a special depressed cladding fibre to minimise the losses [37].

94
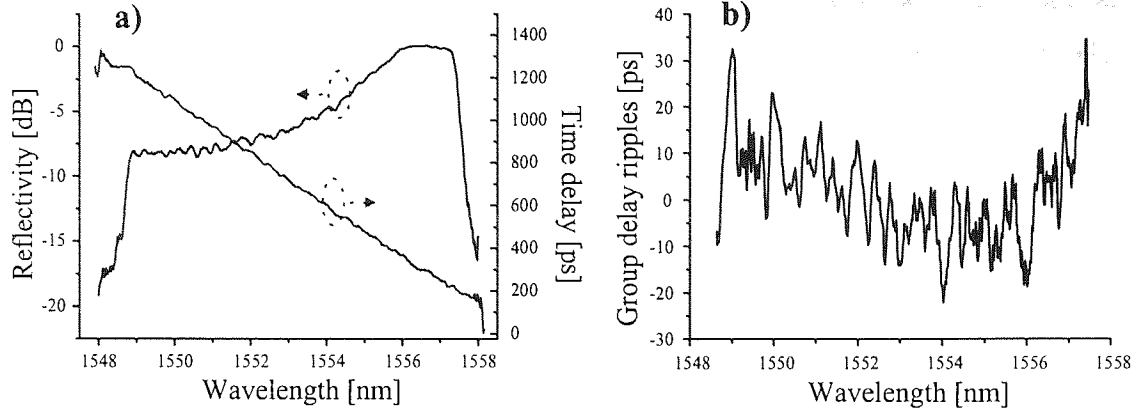
Figure 4.16 *a) Experimental spectrum and time delay of a chirped FBG as seen from long wavelength side, b) group delay ripples measurement.*

Because of the poor sensitivity of this fibre to UV light, however, a reasonably strong FBG is hard to achieve. Alternatively, it is possible to temper the coupling constant along the grating length by using the double exposures technique. The coupling coefficient along the grating is varied by the apodisation technique in such a way to be smaller in the short wavelength region than in the long wavelength one. The technique has proved to be effective for gratings with transmission strength between -15 and -20 dB, even if it seems to affect the amplitude of group delay ripples by producing an average increase of approximately 30%.

4.6 Temporal Talbot Effect by Linearly Chirped FBGs

Temporal Talbot effect is an analogous effect to the paraxial diffraction of optical beams in space but concerns the temporal distortion of narrow-band pulses in dispersive media. The spatial Talbot effect (or self-imaging effect) states that if a periodic object is illuminated with coherent light, exact images of the object are produced at a finite distance from the object [38]. Even if spatial Talbot effect is not new to the scientific community, only recently its temporal counterpart has been investigated and an interesting multiplication effect has proved to be possible by using linearly chirped FBGs in single mode fibres [39-41]. The generation of high-repetition-rate optical pulse trains in the wavelength region near 1550 nm is a topic of major importance for the realization of ultrahigh-speed optical communication systems. Active mode-locking methods have been used for the generation of short optical pulses synchronised with an external clock. However, the repetition rate of pulse trains obtained from a mode-locked laser is limited by the modulation frequency at which the intracavity modulator can operate (usually a few tens of GHz). Several techniques to increse the repetition rate of an optical pulse train have been proposed.

95

Among them, we mention: soliton compression of the beat signal between two optical carriers [42], rational harmonic mode locking [43], higher-order FM mode locking [44], and pulse-train multiplication by propagation in long fibre dispersion line [45]. The reflection from a linearly chirped FBG can be also used to multiply the repetition rate. The effect does not involve nonlinearities but is a direct consequence of the Talbot effect. The propagation of monochromatic light at a wavelength λ over a distance d, in Fresnel conditions, is described by an amplitude response $h_d(x)$ [46]

$$h_d(x) \propto \exp\left(-j\frac{\pi}{\lambda d}x^2\right)$$ (4.6.1)

where x is the Cartesian coordinate perpendicular to the propagation direction z. The reflection from a linearly chirped FBG is described by its reflection coefficient $r(\omega) = |r(\omega)| \exp[-j\Phi(\omega)]$. This reflection coefficient exhibits flat amplitude and quadratic phase response (i.e. linear time delay $\tau(\omega) = \partial\Phi(\omega)/\partial\omega$) over a limited spectral bandwidth $\Delta\omega$ centred on ω_0 (central Bragg frequency).
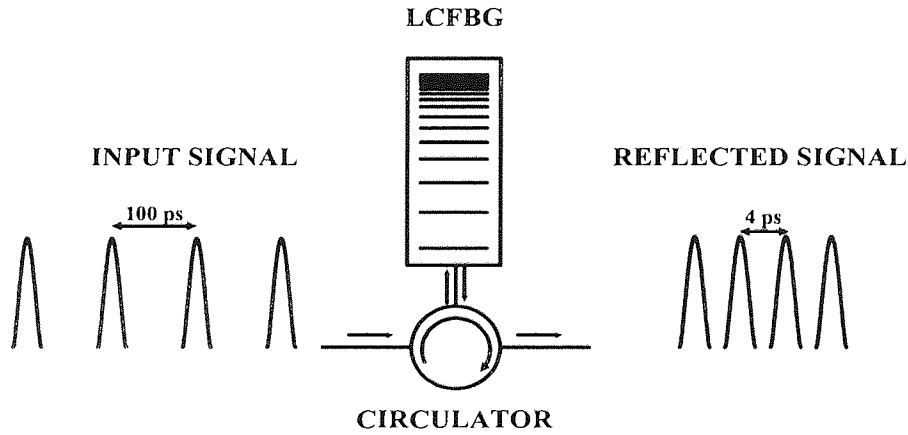
Figure 4.17 *Schematic of the technique for multiplying the repetition rate of a train of pulses by temporal Talbot effect.*

Therefore, the first-order dispersion coefficient $\ddot{\Phi} = \partial^2\Phi(\omega)/\partial\omega^2$ is nearly constant within this spectral bandwidth, and the complex envelope $\hat{h}_r(t)$ of the reflection impulse response can be written as

$$\hat{h}_r(t) \propto \exp\left(j\frac{1}{2\ddot{\Phi}}t^2\right)$$ (4.6.2)

where t is the time variable (without the pulse delay $\tau(\omega_0)$ taken into account). The space-time analogy for the Talbot effect is obtained by comparison of (4.6.1) and (4.6.2). The result from spatial diffraction can be transferred to temporal dispersion of the pulses reflected by a linearly chirped FBG just using the following transformations

96

$$x \leftrightarrow t \quad \text{and} \quad \lambda d \leftrightarrow 2\pi \ddot{\Phi} \tag{4.6.3}$$

We consider a train of short optical pulses with repetition rate T and arbitrary shape. Assuming that the signal is centred on the Bragg frequency ω_0 and has a bandwidth narrower than the grating bandwidth $\Delta\omega$, the input periodic signal is the temporal analog of the periodic field amplitude distribution in such a way that repetition time T corresponds to the spatial period Λ. If the period T of the input signal satisfies the Talbot condition:

$$T^2 = \frac{2\pi|\ddot{\Phi}|}{s} \quad \text{with } s = 1, 2, 3, \dots \tag{4.6.4}$$

we have that the reflected signal is, within a constant factor, an exact replica of the input signal (temporal counterpart of the Talbot images) as schematically shown in Fig. 4.17.
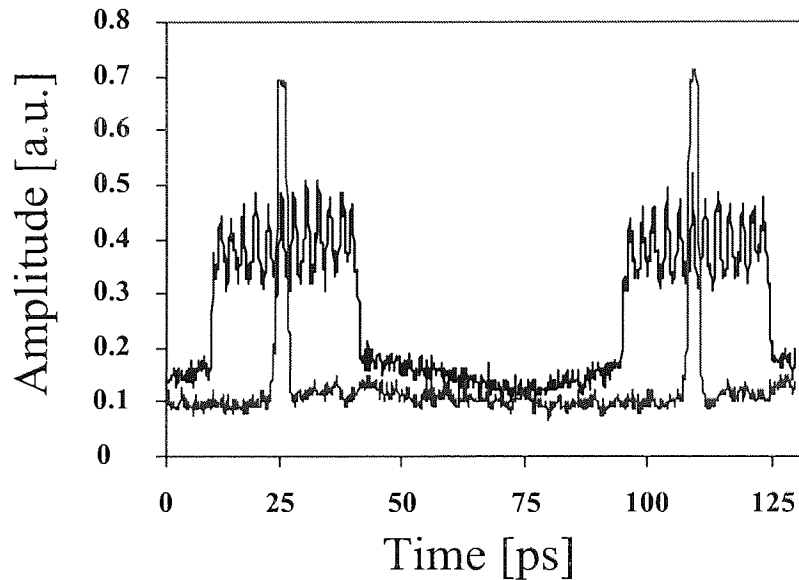
Figure 4.18 Experimental demonstration of the pulse rate multiplication by temporal Talbot effect in a linearly chirped FBG.

We performed an experiment using a fibre grating with the same characteristics as the one in Fig. 4.9. A circulator was used to retrieve the reflected signal. The pulse source was a mode-locked fibre laser (PriTel UOC-3) that provided 2.7 ps pulses at the operating wavelength of 1550 nm. The time-bandwidth product was ~0.34, showing that the laser output pulses were transform limited and *sech²(t)* in shape with a good approximation. As we had no way to modify the dispersion cofficient of the grating $\ddot{\Phi}$, we tried to tune the modulation frequency of the PriTel laser in such a way that the repetition period T of the pulse train satisfied the Talbot condition (4.6.4). After being reflected from the FBG the pulses were sent to an autocorrelator (FR-103, Femtochrome Research, Inc.) to be analysed. The output was displayed on the screen of an oscilloscope (Gould 1602) and is shown in Fig. 4.18. One may see that the pulses are not an exact replica of the input ones

97

because we were forced to operate at frequencies near the Talbot condition but not exactly satisfying it as the laser was instable for some modulation frequencies. Also, the pulses are not fully resolved because of the limited resolution of the autocorrelator. Nevertheless clear signs of multiplication of the repetition rate are visible.

4.7 Chapter Conclusions

This chapter introduced some important ideas and definitions on optical dispersion and its measurement. These concepts are essential for a proper understanding of the material presented in the next chapter. The first section of the present chapter deals with the concept of optical dispersion and basic definitions such as time delay and group velocity dispersion that are used for the characterisation of the dispersion in both single mode fibre and FBGs. We discussed the detrimental effect of an unbalanced dispersion, especially when high speed optical fibre links are considered, then we proved the necessity of an active dispersion compensation. The second part of the chapter has a more practical nature dealing with the methods used for the measurement of chromatic dispersion. An investigation on the experimental accuracy is carried on and all the possible causes of "error" in the measurement are identified and their magnitude estimated. We also tried a new statistical approach on the distribution of group delay ripples in the attempt of detecting hidden periodical regularities (that potentially could give useful information on the quality of the phase mask, such as the stitching errors, for instance). An investigation on the origin of two predominant imperfections in the spectrum of a linearly chirped FBG, insertion losses and short wavelength losses, is carried on and possible solutions, implemented at the time of the fabrication, are proposed. Key fabrication techniques to improve the quality of linearly chirped FBGs are described. The last section of the chapter illustrates a method for the generation of ultra high repetition rate optical pulses by spatial Talbot effect. An experiment was performed by using a linearly chirped FBG and a starting 10 Gb/s optical stream. A multiplication of the rate up to ten times is experimentally proved.

References

[1]   G.P. Agrawal, "Nonlinear fibre optics", 3rd edition, *Harcourt Publishers Ltd*, 2001.

[2]   E. Desurvire, "Erbium-doped fibre amplifiers", *Wiley*, New York, 1994.

[3]   I. Kaminov, T.L. Koch Ed., "Optical fiber telecommunications IIIA", *Academic Press*, 1997.

[4]   A.D. Ellis, M.C. Tatham, D.A.O. Davies, D. Nesset, D.G. Moodie, G. Sherlock, "40 Gbit/s transmission over 202 km of standard fiber using midspan spectral inversion", *Electron. Lett.*, **31**, 1995, pp. 299-301.

[5]   A.H. Gnauck, S.K. Korotky, J.J. Veselka, J. Nagel, C.T. Kemmerer, W.J. Minford, D.T. Moser, "Dispersion penalty reduction using an optical modulator with adjustable chirp", *IEEE Photon. Technol. Lett.*, **3**, 1991, pp. 916-918.

[6]   T.L. Koch, R.C. Alferness, "Dispersion compensation by active predistorted signal synthesis", *IEEE J. Lightwave Technol.*, **LT-3**, 1985, pp. 800-805.

[7]   A.M. Vengsarkar, W.A. Reed, "Dispersion-compensating single-mode fibers: efficient design for first and second-order compensation", *Opt. Lett.*, 1993, **18**, pp. 924-926.

[8]   A. Yariv, D. Fekete, D.M. Pepper, "Compensation for channel dispersion by nonlinear optical phase conjugation", *Opt. Lett.*, **4**, 1979, pp. 52-54.

[9]   J.-L. Auguste, R. Jindal, J.-M. Blondy, M. Clapeau, J. Marcou, B. Dussardier, G. Monnom, D.B. Ostrowsky, B.P. Pal, K. Thyagarajan, "-1800 ps/(nm.km) chromatic dispersion at 1.55 μm in dual concentric core fibre", *Electron. Lett.*, **36**, pp. 1689-1691

[10]   A.K. Sharma, R.K. Sinha, R.A. Agarwala, "Higher-order dispersion compensation by differential time delay", *Opt. Fiber Technol.*, **4**, 1998, pp. 135-143.

[11]   C. Lin, H. Kogelnik, L.G. Cohen, "Optical-pulse equalization of low-dispersion transmission in single-mode fibers in the 1.3-1.7 μm spectral region", *Opt. Lett.*, **5**, 1980.

[12]   F. Ouellette, "Dispersion cancellation using linearly chirped Bragg grating filters in optical waveguides", *Opt. Lett.*, **12**, 1987, pp. 847-849.

[13]   A. Sahara, T. Komukai, E. Yamada, M. Nakazawa, "40 Gbit/s return-to-zero transmission over 500 km of standard fibre using chirped fibre Bragg gratings with small group delay ripples", *Electron. Lett.*, **37**, 2001, pp. 8-9.

[14]   G.E. Kohnke, S.J. Spammer, M. Mlejnek, B. Agogliati, D. Caironi, L. Arcangeli, M. Belmonte, F. Garcia, A.D. Ellis "Fiber Bragg gratings for dispersion compensation" in proc. OFC 2002 (Anaheim, USA, 2002), *paper ThAA3*.

[15]   T. Okoshi, "Optical fibers", *Academic Press*, 1982.

[16]   K. Hinton, "Dispersion compensation using apodized Bragg fiber gratings in transmission", *J. Lightwave Technol.*, **16**, 1998, pp. 2336-2346.

[17]   L.G. Cohen, "Comparison of single-mode fiber dispersion measurement techniques", *J. Lightwave Technol.*, **LT-3**, 1985, pp. 958-966.

[18]   S. Barcelos, M.N. Zervas, R.I. Laming, D.N. Payne, L. Reekie, J.A. Tucknott, R. Kashyap, P.F. McKee, F. Sladen, B. Wojciechowicz, "High accuracy dispersion measurements of chirped fibre gratings", *Electron. Lett.*, **31**, 1995, pp.1280-1282.

[19] M. Volanthen, H. Geiger, M.J. Cole, R.I. Laming, J.P. Dakin, "Low coherence technique to characterise reflectivity and time delay as a function of wavelength within a long fibre grating", *Electron. Lett.*, **32**, 1996, pp. 757-758.

[20] S.D. Dyer, K.B. Rochford, "Low coherence interferometric measurements of fibre Bragg grating dispersion", *Electron. Lett.*, **35**, 1999, pp.1485-1486.

[21] S. Ryu, Y. Horiuchi, K. Mochizuki, " Novel chromatic dispersion measurement method over continuous Gigahertz tuning range", *J. Lightwave Technol.*, **7**, 1989, pp.1177-1180.

[22] G. Genty, T. Niemi, H. Ludvigsen, "New method to improve the accuracy of group delay measurements using the phase-shift technique", *Opt. Commun.*, **204**, 2002, pp. 119-126.

[23] B. Costa, D. Mazzoni, M. Puleo, E. Vezzoni, "Phase shift technique for the measuerement of chromatic dispersion in optical fibers using LED's", *IEEE J. Quantum Electron.*, **QE-18**, 1982, pp.1509-1515.

[24] K.O. Hill, S. Thériault, B. Malo, F. Bilodeau, T. Kitagawa, D.C. Johnson, J. Albert, K. Takiguchi, T. Kataoka, K. Hagimoto, "Chirped in-fibre Bragg grating dispersion compensators: linearisation of dispersion characteristic and dimostration of dispersion compensation in 100 km, 10 Gbit/s optical fibre link", *Electron. Lett.*, **30**, 1994, pp. 1755-1756.

[25] R. Kashyap, M. de Lacerda Rocha, "On the group delay characteristics of chirped fibre Bragg gratings", *Opt. Commun.*, **153**, 1998, pp. 19-22.

[26] J.D. Ania-Castañón, P. García Fernández, A. Sánchez-Díaz, J.M. Soto-Crespo, "Apodized chirped fibre Bragg gratings for dispersion compensation in a 10 Gbit/s IM-DD semiconductor laser system", *Opt. Commun.*, **170**, 1999, pp. 373-380.

[27] L. Quetel, L. Rivoallan, M. Morvan, M. Monerie, E. Delevaque, J.Y. Guilloux, J.F. Bayon, "Chromatic dispersion compensation by apodised Bragg gratings within controlled tapered fibers", *Opt. Fiber Technol.*, **3**, 1997, pp. 267-271.

[28] D. Garthe, G. Milner, Y. Cai, "System performance of broadband dispersion compensating gratings", *Electron. Lett.*, **34**, 1998, pp. 582-583.

[29] K. Ennser, M. Ibsen, M. Durkin, M.N. Zervas, R.I. Laming, "Influence of nonideal chirped fiber grating characteristics on dispersion cancellation", *IEEE Phot. Technol. Lett.*, **10**, 1998, pp.1476-1478.

[30] Y.H.C. Kwan, P.K.A. Wai, H.Y. Tam, "Effect of group-delay ripples on dispersion-managed soliton communication systems with chirped fiber gratings", *Opt. Lett.*, **26**, 2001, pp. 959-961.

[31] Q. Zeng, "Delay behaviours of phase-shifted Bragg grating filters", *Electron. Lett.*, **34**, 1998, pp. 1098-1099.

[32] T. Niemi, M. Uusimaa, H. Ludvigsen, "Limitations of phase-shift method in measuring dense group delay ripple of fiber Bragg gratings", *IEEE Photon. Technol. Lett.*, **13**, 2001, pp. 1334-1336.

[33] J.R. Taylor, "An introduction to error analysis", *University Science Books*, 1982.

[34] G.J. Borse, "Numerical methods with MATLAB", *PWS Publishing Company*, Boston, 1997.

[35] L.R. Mullin, S.G. Small, "Four easy ways to a faster FFT", *J. Mathemat. Modelling and Algorithms,* **1**, 2002, pp. 193-214.

[36] M.K. Durkin, M. Ibsen, R.I. Laming, V. Gusmeroli, "Equalisation of spectral non-uniformities in broad-band chirped fibre gratings", *Online paper*, ORC Southampton.

[37] L. Dong, L. Reekie, J.L. Cruz, J.E. Caplen, J.P. de Sandro, D.N. Payne, "Optical fibers with depressed claddings for suppression of coupling into cladding modes in fiber Bragg gratings", *IEEE Photon. Technol. Lett.*, **9**, 1997, pp. 64-66.

[38] J.T. Winthrop, C.R. Worthington, "Theory of Fresnel images. I. Plane periodic objects in monochromatic light," *J. Opt. Soc. Am.*, **55**, 1965, 373-381.

[39] T. Jannson, J. Jannson, "Temporal self-imaging effect in single-mode fibers", *J. Opt. Soc. Am.*, **71**, 1981, pp.1373-1376.

[40] M.A. Muriel, J. Azaña, A. Carballar, "Real-time Fourier transformer based on fibre gratings", *Opt. Lett.*, **24**, 1999, pp.1-3.

[41] J. Azaña, M.A. Muriel, "Temporal Talbot effect in fiber gratings and its applications", *Appl. Opt.*, **38**, 1999, pp.6700-6704.

[42] E.A. Swanson, S.R. Chinn, K. Hall, K. Rauschenbach, R.S. Bondurant, J.W. Miller, "100Ghz soliton pulse-train generation using soliton compression of 2 phase side bands from a single DFB laser", *IEEE Photon. Technol. Lett.*, **6**, 1994, pp. 1194-1196.

[43] Z. Ahmed, N. Onodera, "High repetition rate optical pulse generation by frequency multiplication in actively modelocked fibre ring lasers", *Electron. Lett.*, **32**, 1996, pp. 455-457.

[44] K.S. Abedin, N. Onodera, M. Hyodo, "Order of magnitude repetition rate multiplication in FM modelocked fibre laser by higher-order FM sideband generation and filtering", *Electron. Lett.*, **34**, 1998, pp. 1321-1322.

[45] I. Shake, H. Takara, S. Kawanishi, M. Saruwatari, "High-repetition-rate optical pulse generation by using chirped optical pulses", *Electron. Lett.*, **34**, 1998, pp. 792-793.

[46] J. Azaña, M.A. Muriel, "Technique for multiplying the repetition rates of periodic trains of pulses by means of a temporal self-imaging effect in chirped fiber gratings", *Opt. Lett.*, **24**, 1999, pp. 1672-1674.

Chapter **5**

TUNING OF DISPERSION AND OPTICAL FILTERING BY FBGs

5.1 Chapter Overview

This chapter deals with the subject of dynamic dispersion compensation and the possible ways of achieving it. We start our analysis by explaining the reasons why a method employing a tunable dispersion and slope compensation is often preferable to fixed dispersion compensation in real world optical transmission systems. We then overview the different methods that have been proposed so far for achieving the dispersion tuning of a FBG. We give a description of the working principle of the devices already commercialised (based on thermal or mechanical effects) and we compare these methods with the method that we propose here, i.e., the application of a distributed applied strain by a multipoint bending rig. A detailed description of the device and of its working principle is given. A theoretical model, enabling to calculate the chromatic dispersion and the dispersion slope that derives from the application of a given strain to a linearly chirped FBG, is developed. A set of measurements of the dispersion delivered by the device under different strain conditions, as well as the experimental results on pulse recompression,

showing the performance of the tunable dispersion compensator in real transmission systems, are included. The chapter ends with the results of spectral filtering performed by the same multipoint bending rig on the output of an overdriven pulsed laser diode. We demonstrate that the filtering provides a method to get more powerful and narrower pulses, by nearly complete suppression of the unwanted tail originated from the relaxation oscillations of the laser.

5.2 Why Tunable Dispersion Compensators Are Needed in Ultrafast Optical Transmission Systems

As we discussed in the previous chapter, the dispersion delivered by a linearly chirped FBG can compensate for the broadening induced by chromatic dispersion on an optical pulse data stream propagating through a span of SMF. Nevertheless, the compensation is exact only if the amount of chromatic dispersion in the system is not varying in time and has the same value as the grating dispersion. In many practical situations this is not true. Furthermore, there are other issues to be considered in order to make a FBG suitable for a realistic optical link. A linearly chirped FBG, for instance, can not compensate for high order dispersion (a nonlinearly chirped FBG is required for this purpose) and, in most of the practical cases, a variable dispersion device would be required. Two of the most troublesome issues in optical transmission systems, especially when operating at bit rates higher than 10 Gbit/s, are the accumulation of dispersion and nonlinearities. Dispersion-managed single channel or WDM systems have been demonstrated, where the dispersion accumulated in a span of fibre is cancelled by a dispersive element that provides an opposite sign dispersion. However, the accumulated dispersion for a given channel may vary in time due to the fact that a given channel can originate locally or far away in the optical network. On the other hand, it is often necessary in order to keep nonlinearities under control, to maintain a small non-zero dispersion at a given point along the fibre span. The case where the operating conditions are changed (including the dependence of the transmission path on temperature or stress), may equally affect the total amount of dispersion in the system. Unfortunately, the dispersion tolerance reduces quickly as the bit rate increases (and this is exacerbated by an uncompensated dispersion slope): as a consequence, variations in dispersion, which are usually negligible in slower systems, can severely affect the network performance at higher bit rates. Already at 40 Gbit/s, for instance, the dispersion map is required to be accurate to within less than 50 ps/nm, and at 160 Gb/s less than 5 ps/nm [1].

a)

b)
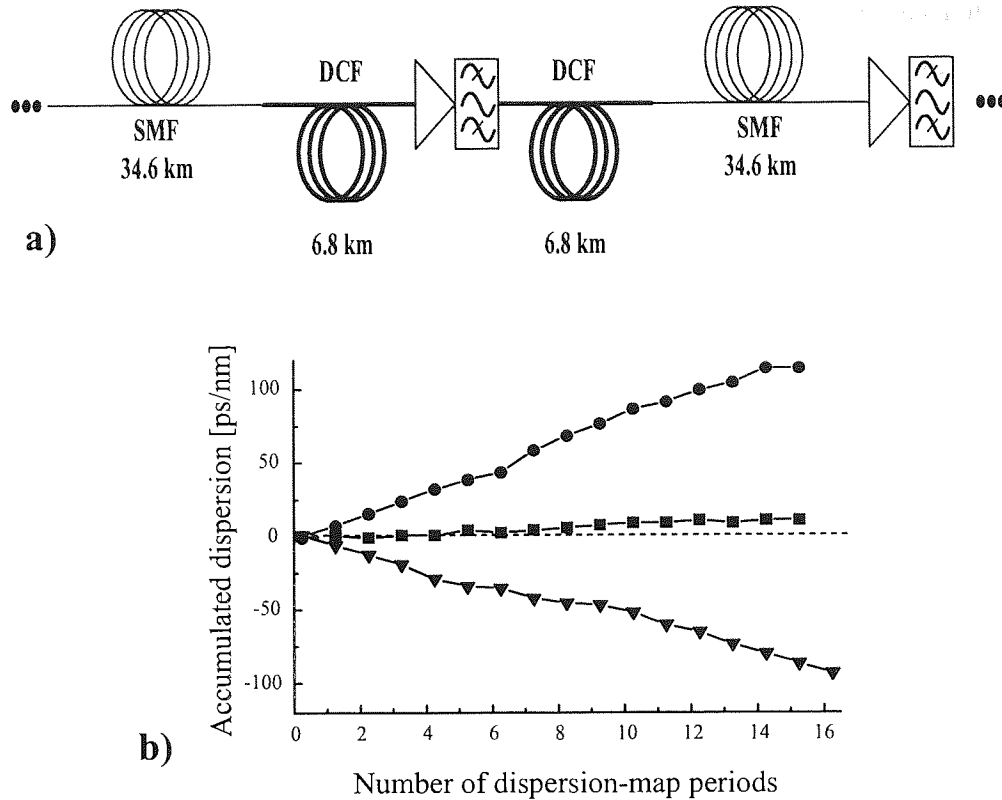
Figure 5.1 *Numerical optimisation of single channel transmission on 1000 km of SMF at 80 Gbit/s: a) Schema of the symmetric dispersion map used in the computation, b) Accumulated dispersion to be compensated as function of the number of dispersion map periods: (circles) −0.09 ps/nm, (squares) zero, and (triangles) 0.08 ps/nm average dispersion. From Ref. [2].*

Finally, in such a dispersion-managed optical transmission link it is very important to put a device, enabling dynamic dispersion compensation, at the end of the transmission line (post-compensator). This device would provide compensation against small dispersion variations and possibly against the action of high order dispersion as well. From these examples one may see that, in practice, for an accurate compensation, it would be more convenient to have a device delivering a variable amount of dispersion than a device with a fixed one. The necessity of a tunable dispersion post-compensator used complementary to the dispersion-map can be understood looking at the plot in Fig. 5.1.b. The dispersion map used to perform numerical simulation of a single channel transmission system operating at 80 Gbit/s over 1000 km together with the fibre parameters are shown in Fig. 5.1.a and in Table 5.1 respectively. The fibre length is balanced so that the system operates in the vicinity of zero average dispersion. Numerical computation shows that the best performance can be achieved at a slightly anomalous average dispersion. A plot of the accumulated dispersion compensation required after each period of the dispersion map is shown in Fig. 5.1.b. From the plot it can be seen that the accumulated dispersion, after just

few sections of the dispersion-map, is never exactly zero, then an accurate post compensation is required to limit the effect of distortion on the output optical signal.

FIBRE	SMF	DCF
Dispersion [ps/nm/km]	15.8 - 17.3	- 84
Dispersion slope [ps/nm ^{2}/km]	0.064	- 0.23
Effective area [μm^2]	80	25
Loss coefficient [dB/km]	0.22	0.65

Table 5.1 *Fibre parameters used for the simulation in Fig. 5.1. From Ref. [2].*

Clearly, the system is very sensitive to precise post-compensation. Although a span of post-compensating fibre could be used at the end of the map, to compensate for the residual dispersion, this solution would be unpractical and not very effective in the case where the dispersion varies in time. As a matter of fact, a tunable dispersion post-compensator, with a range of variability between −70 and 90 ps/nm is required. There is no method known at the moment for tuning the dispersion of a DCF. In the following sections, we will show that such a tunable dispersion compensator can be implemented by using FBGs.

5.3 Techniques for Tuning the FBG Dispersion

In recent years, several techniques to transform ordinary FBGs in tunable ones have been proposed. The working principles of such devices can be grouped in two different classes:

- the application of a gradient stretcher (strain, temperature, or other gradient field) to a uniform or linearly chirped FBG,
- the application of a linear stretcher to a nonlinearly chirped FBG.

In both cases, tuning of the grating dispersion is achieved, since the method affects the time delay in a "non-uniform" way. The reason why a non-uniform effect (temperature gradient or distributed strain) must be used for tuning the dispersion of a FBG will be clear in the following. At this stage, it is useful to overview the methods used to implement tunable dispersion FBGs. A general view of the topic will help the reader to understand why we choose one specific approach (i.e., tunable distributed strain) in conceiving and fabricating our tunable dispersion device.

Temperature and strain have been largely used to fabricate very accurate sensors because of the high sensitivity of FBGs to these physical quantities. The shift in the Bragg wavelength due to strain and temperature can be expressed as [3]

$$\Delta\lambda_B = 2n\Lambda\left(\left\{1-\left(\frac{n^2}{2}\right)\left[P_{12}-v\left(P_{11}+P_{12}\right)\right]\right\}\varepsilon+\left[\alpha+\frac{\left(\frac{dn}{dT}\right)}{n}\right]\Delta T\right) \qquad (5.3.1)$$

where ε is the applied strain, $P_{i,j}$ are the Pockel's (piezo) coefficients of the stress-optic tensor, v is the Poisson's ratio, α is the coefficient of thermal expansion of the fibre material (silica), and ΔT is the temperature change. We will give below a separate description of the dispersion compensator devices based on temperature and of those that use mechanical strain.

5.3.1 Thermal Tuning of a FBG

In silica fibres, the thermal response is dominated by the temperature dependence dn/dT of the material, which accounts for ~ 95% of the observed wavelength shift. The (normalised) thermal responsivity (at a constant strain) is given by [3]

$$\frac{1}{\lambda_B}\frac{\delta\lambda_B}{\delta T} = 6.67\times10^{-6}\ {}^{\circ}C^{-1} \qquad (5.3.2)$$

A wavelength resolution of 1 pm (0.001 nm) is required (at λ_B ~ 1.3µm) to resolve a temperature change of ~ 0.1 °C. The effect of tuning the Bragg wavelength of a FBG by temperature has been used to fabricate very precise optical filters (narrow- or pass-band). The application of a uniform temperature along the whole length of a linearly chirped FBG produces a shift in wavelength, proportional to the applied temperature, but fails in tuning the grating dispersion, as no differential effect on the different sections of the grating is involved. Devices based on non-uniform temperature distributions, in both chirped or uniform FBGs, have been demonstrated [4]. In thermally operating tunable devices, a gradient in temperature along the grating length causes a variation of the chirp of the grating, as a result of the temperature dependence of the silica refractive index. Typically this type of device is fabricated by using an heater (i.e., an oven) and a refrigerator (or heat sink) connected to the ends of a thermally conductive plate to which the fibre is bonded [5]. The linear temperature gradient established by thermal diffusion in the material supporting the fibre induces a similar gradient in the fibre, then a linear chirp in the FBG. Alternatively, a less bulky design has been proposed by Eggleton *et al.* [6-9] from Lucent

106

Technologies. This device works on a distributed on-fibre thin film heater, deposited onto the outer surface of a FBG, as shown in Fig. 5.2.
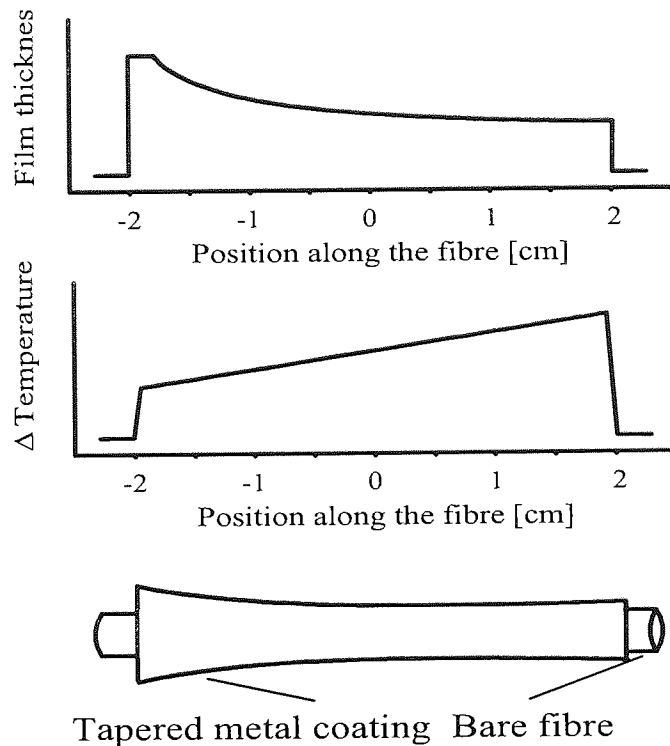
Figure 5.2 *Tapered metal coated FBG device for tunable chromatic dispersion, based on temperature gradient. From Ref. [6]*

The current, flowing through the thin film, generates resistive heating at rates that are governed by the thickness profile of the metal film. A chirp in the grating is obtained by using a thin film, whose thickness varies with position along the length of the grating. The chirp rate can be adjusted reversibly by varying the applied current to the metal coating. The device is meant for on a per-channel basis dispersion compensation. The use of a sampled grating enables to compensate for several different channels at once. Although the optical characteristics of these devices are generally good, they present some non-negligible disadvantages:

- The heat flow is notoriously a quite inertial process: the applied temperature gradient will take some time (some seconds at least) to be established or to react to a different voltage applied to the metal coating. This means that the device is necessarily slow and unsuitable for transmission systems where the dispersion is rapidly varying.

- The device is not passive and requires a very stable power supply in order to maintain the applied temperature gradient unchanged and to avoid unwanted drifts in the dispersion curve.

- A nonlinear chirp is difficult to achieve with such a device because of the thermalisation effect inside the coating. This means that the time delay delivered by the tunable FBG can only be linear, i.e., the device can not be used to compensate for high order dispersion.

- There is no way to avoid the wavelength shift produced by the change in temperature. This means that the reflection spectrum of the FBG will shift in wavelength and, for an excessive tuning, this could cause the operating wavelength to go outside the FBG bandwidth at some stage (this problem, however, can be solved by using a broadband grating).

Among the advantages of tapered metal coated thermally tuned FBGs we can mention: a small size that enables a compact packaging, and a large range of variability for the delivered chromatic dispersion, as shown in Fig. 5.3.

Aston University

Illustration removed for copyright restrictions
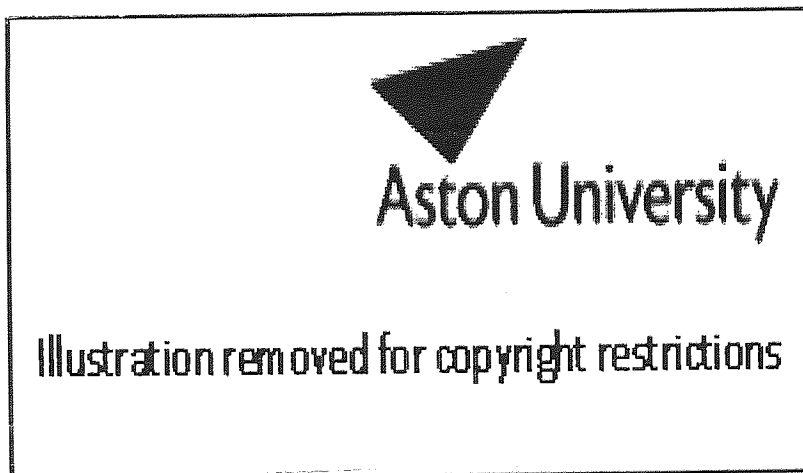
Figure 5.3 Measured dispersion as a function of the voltage applied to a temperature gradient tuned device. The inset shows the effect of the applied gradient on time delay curve. From Ref. [6]

To overcome the thermalisation effect and enable a nonlinear chirp to be established more easily, a tunable dispersion equaliser based on a divided thin film heater has been proposed [10]. The device has been realised by using a linearly chirped FBG and a divided thin film heater composed by 32 thin film heaters. The nonlinear chirp enables dispersion slope

compensation. The authors claim a chromatic dispersion change from –304 ps/nm to –196 ps/nm and a dispersion slope change from +100 ps/nm^2 to –300 ps/nm^2.

5.3.2 Mechanical Tuning of a FBG

We consider the effect of a strain applied to a FBG (at a constant temperature). The factor $\left\{(n^2/2)[P_{12} - v\,(P_{11} + P_{12})]\right\}$ in (5.3.1) has a value of ~ 0.22 and the measured strain response is found to be [3]

$$\frac{1}{\lambda_B}\frac{\delta\lambda_B}{\delta\varepsilon} = 0.78\times10^{-6}\,\mu\varepsilon^{-1} \tag{5.3.3}$$

This responsivity gives a "rule-of-thumb" measure of the grating wavelength shift with strain of 1nm per 1000 $\mu\varepsilon$ at $\lambda_B \sim$ 1300 nm.
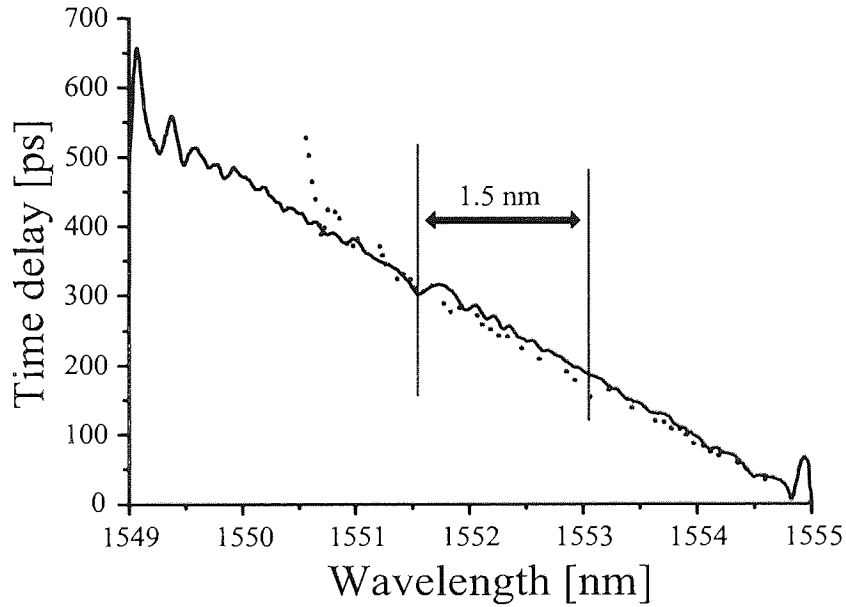
Figure 5.4 The effect of a uniform strain (3×10^{-3}) applied on a linearly chirped FBG.

As the experimental measurements in Fig. 5.4 show, the simple application of a uniform strain on a linearly chirped FBG can not change the slope of the linear time delay curve (i.e., its dispersion), but only produces a constant shift in wavelength, linearly proportional to the applied strain, in the resonant wavelength range (in Fig. 5.4, for instance, the application of a strain $\Delta\ell/\ell = 3\times10^{-3}$ would produce a linear wavelength shift of approximately 1.5 nm; here ℓ is the length of the grating in the absence of any strain, and $\Delta\ell$ is the elongation due to the applied strain). This is because all the different sections of the FBG are equally affected by the strain, as no differential effect acts between the grating different sections (i.e., the grating chirp remains linear also after the strain being applied).

In many respects, the application of a mechanical distributed (i.e., non-uniformly varying) strain on a uniform or chirped FBG can achieve tunable dispersion more easily and guarantee more stability, compared with a temperature gradient (as the induced chirp can be maintained indefinitely).

5.3.3 Overview on Mechanical Tuning Techniques

Techniques with various degree of complexity, have been proposed for tuning the chirp of a FBG. One of the first attempts to realise an adjustable chirp FBG by the use of mechanical strain was made by Hill *et al.* [11]. The proposed technique is, as matter of fact, bulky and not very practical, as masses of different weight and suspended on either side of a grating adherent to a plate with soft glue, must be used to obtain the tuning. Moreover, this method has the disadvantage that the exact strain profile applied to the fibre is hard to predict. A device easier to implement was proposed by Garthe *et al.* [12] who bounded the FBG to a cantilever beam: by deflecting one end of the beam, an almost linear strain gradient was established along the grating length. In a variation of this technique, Le Blanc *et al.* [13] used the strain gradient produced on the tapered section of an aluminium cantilever beam. The technique provides an adjustable grating chirp, but also an unpleasant shift in wavelength is produced in the reflection spectrum of the grating. The authors suggested to eliminate it by temperature control, but the thermal expansion of the beam poses a limit to the practical implementation of this idea. A technique based on a similar tuning principle, but implemented by using the strain gradient generated from a piezoelectric ceramic with tapered thickness, was suggested by Pacheco *et. al* [14], and improved in [15]. The use of a multilayer piezoelectric transducer to realize a low voltage and high tuning range efficiency was discussed by Inui *et. al* [16]. Several authors put their effort in the implementation of a bending beam technique enabling the tuning of the grating dispersion without wavelength shift [17], [18]. The authors were interested in the compensation of the chromatic dispersion only and the proposed technique is not intended for higher order dispersion compensation. A mechanical strain based method to achieve, positive or negative chirp in a FBG written in a tapered core fibre (used to generate a non uniform strain in alternative to a tapered beam) is described in [19]. The inconvenient of this technique is that the tapering of the core produces an higher loss and the risk of fibre breaking is higher. A "local" strain approach was proposed by Ohn *et al.* [20], [21]. The proposed tuning mechanism is based on the use of a piezoelectric stack with 21 individually controlled segments to control the local strain at different positions along the grating. By stepwise monotonic increase (or decrease) of the strain along the grating, a

110

linear group delay response was obtained. The main problem of this technique is that, because of the finite dimensions of each element in the piezoelectric stack, the strain is necessarily applied on finite segments of the FBG (discrete strain). The technique then produces a discontinuity (phase-shift) at the boundary between two consecutive elements. The discontinuity produces substantial ripples in the delay response of the device. Also in this case, the device is conceived as a compensator for the chromatic dispersion only. The use of a sampled chirped FBG, tuned by mechanical strain, was suggested to compensate the dispersion of several channels at once in a WDM transmission system [22], [23]. In this case the wavelength separation of the WDM channels is different from the wavelength separation between the sampled FBG wavelength bands. This means that each WDM channel experiences a slightly different dispersion compensation that can be tuned upon grating stretching. On the other hand, methods to fabricate nonlinearly chirped FBGs (suitable for higher order dispersion compensation), have been proposed already [24-26]. A technique based on the use of a (piezoelectric) tunable nonlinearly chirped FBG, to suppress channel degrading effects as well as to compensate for higher order dispersion, was reported by Willner et al. [27-29]. Similar techniques have been proposed to implement a strain-chirped FBG with an adjustable dispersion slope [30-32]. Various techniques, based on the use of double or twin FBGs, to achieve dispersion or slope compensation have been reported as well [33-36].

5.4 Tuning the FBG Dispersion by a Multipoint Bending Rig

From the previous overview on tunable dispersion FBG devices one may infer that no device works on a general principle enabling the compensation of both the chromatic dispersion and the dispersion slope. Clearly, the grating characteristics (such as the refractive index modulation period and the time delay) could be different for devices conceived as chromatic dispersion compensators and for those that deal with the dispersion slope (for instance, a nonlinear time delay is required for higher order dispersion). This means that, at least in principle, the same grating could not be used to compensate for dispersion of different orders. We describe a novel chirped FBG device that has a nonlinear tunable dispersion. The working principle of the device is based on the tuning of the group delay characteristic of an initially linearly chirped FBG. We show that the group delay of a linearly chirped FBG can be tuned to become nonlinear by the action of a distributed mechanical strain applied to the grating. In the absence of any strain applied, the FBG is linear, thus its dispersion is the same at any wavelength within the grating bandwidth. The device is engineered in such a way to apply a predetermined strain profile

111

to the FBG, inducing a controllable and reversible nonlinear grating chirp (which allows the compensation of higher order dispersion). This approach has many advantages with respect to other tunable dispersion compensators based on a similar working principle. Among them we mention

- The device can compensate for chromatic dispersion as well as for dispersion slope.

- It can be used to compensate for the optical transmission system dispersion in real time (a feedback mechanism can be easily implemented between the BER measurement and the rig that applies the strain to the grating, in such a way to compensate automatically for the necessary dispersion).

- It is a passive device (it does not require any power supply) and is stable (i.e., the delivered dispersion can be kept at a fixed value indefinitely without any of the drifts occurring in a temperature tunable device).

- The linearly chirped FBG has a large bandwidth, that can accommodate a 40 Gb/s channel, and that makes the device suitable for WDM applications. Moreover, such a large bandwidth makes the device more tolerant to the small wavelength shifts induced by the applied strain.

- A suitably chosen bending profile can be used to minimise (at least from one side of the FBG) the wavelength shift induced by the applied strain in the grating reflectivity.

- The strain applied to the FBG is continuous (no phase shifts are produced in the grating structure by the applied strain) and the disturbance to the group delay ripples is minimal.

- The device has a relatively small size that makes it compact.

- A simple theoretical model enables to predict the values of the chromatic dispersion and dispersion slope corresponding to a given applied strain, or inversely, to calculate the bending profile necessary to achieve a given dispersion.

In the device, a tunable dispersion is obtained via axial distributed strain applied to a (linearly) chirped FBG, by using a multipoint bending rig. The non-uniformly distributed strain modifies the core refractive index modulation period $\Lambda(z)$ along the grating length z. The use of a multipoint bending rig allows varying the strain applied to the grating in a predictable manner (the knowledge of the curvature radius of a metal beam is all we need to calculate the applied strain). This technique enables an accurate control of the strain applied along the grating length, thus allowing a very precise tuning of the "local" period $\Lambda(z)$ (or in other words of the time delay), and a fine tuning of the FBG dispersion. The multipoint bending rig is designed to apply a differential strain on each section of the FBG

in a very smooth way (no discontinuities are produced inside the grating structure as the strain is continuously varying). The exact design of a multipoint bending rig depends on the specific dispersion tunability required. The device that we used in our experiment, for instance, is the four point bending rig shown in Fig. 5.5. This bending rig had already been used in our laboratories, to test the behaviour of FBGs subjected to axial distributed strain for fibre sensing applications [37]. The work described here represents the first reported application to the tuning of the dispersion of a FBG.
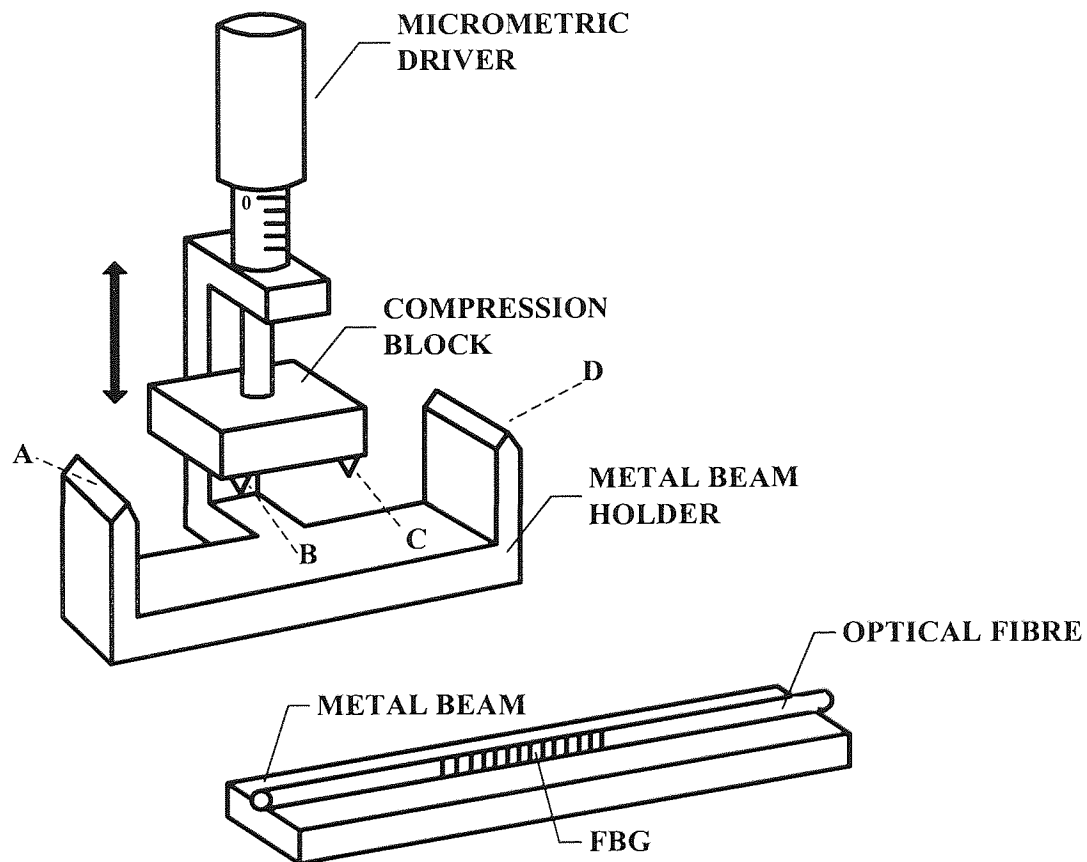
Figure 5.5 The four point bending rig used for tuning the chromatic dispersion and dispersion slope of a linearly chirped FBG.

The device in Fig. 5.5 consists of a metal holder with two wedges, one on each side (indicated with A and D), and of a compression block containing other two symmetrical wedges (indicated with B and C). The compression block can move up and down transversally (as shown by the left-right arrow) with a fine movement (1/20 mm) by using a micrometric driver. The FBG is embodied, using a special soft glue, to an elastic spring steel beam, into a V-groove (used to minimise the amount of non-axial strain applied to the FBG) in such a way that it can not slip away when the strain is applied. The beam including the FBG is put between the points A and D of the holder where the compression

113

block, controlled by the micrometer, pushes the beam down. Because of the action of the compression block, the originally straight beam becomes curve, and its curvature is directly controllable by the micrometer. As we will show, the amount of strain that is applied to the bar depends on the beam curvature radius. Because of the special material composing the beam, the original beam shape can be restored when the compression block moves up, releasing the beam (the deformation produced by the compression block is not permanent, because the device operates always within the elasticity limit of the material).

$$\Lambda_0 \qquad \Lambda_i = \alpha \, \Lambda_{i-1}$$

Linearly Chirped FBG (unstrained grating)

z

Nonlinearly Chirped FBG (strained grating)

$$\Lambda_i = \beta \, \Lambda_{i-1}^{n}$$
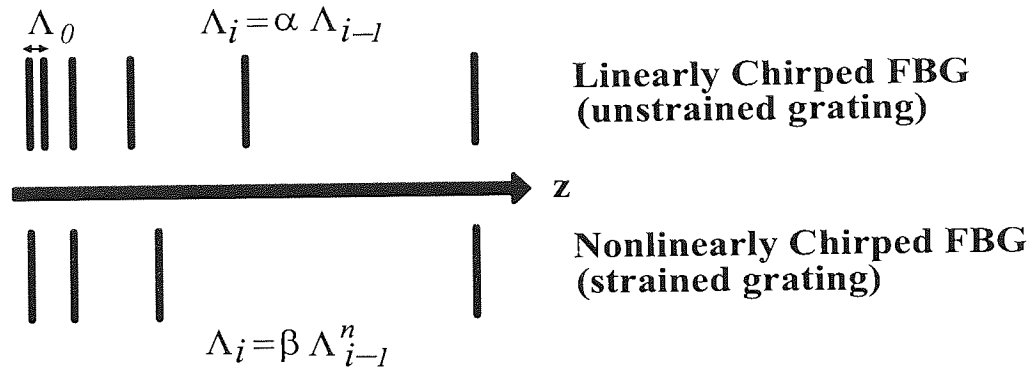
Figure 5.6 *Schematic representation of the effect of applying a controllable distributed mechanical strain to the refractive index modulation period Λ_0 of a linearly chirped FBG.*

The device applies a nearly linear strain to one region of the bar and a progressively nonlinear strain moving away from this region (the strain is symmetric with respect to the centre of the bending rig). The tuning action is optimised by translating the beam between the points A and D of the holder (i.e., placing the FBG asymmetrically with respect to the centre of the rig). This enables the application of the maximum strain allowed by the rig to a precisely chosen region of the grating. For our tunable dispersion experiment, we used a linearly chirped FBG, as the one shown in Fig. 4.9 (made by using the Lasiris Technology phase-mask). As we were interested in tuning the 1550 nm wavelength, for telecommunication purposes, the device was operated in such a way that the compression block acted approximately on a third of the grating length from the short wavelength region (maximum strain applied around 1550 nm).

5.5 Tuning of Chromatic Dispersion and Dispersion Slope of a Linearly Chirped FBG by Distributed Axial Strain

In this section we derive a model enabling the calculation of the dispersion changes induced by any axial distributed strain in a linearly chirped FBG. Let us suppose that the distributed strain is applied along the grating physical length by using a multipoint bending

rig as the one schematically shown in Fig. 5.7. Even if we consider here, for the sake of simplicity, a four point bending rig, the mathematical description can be extended to any case where the curvature radius ρ of the beam under strain is a function of the axial coordinate z along the FBG. The metal strip is supposed to be thinner than long, homogeneous and of a constant thickness 2w.
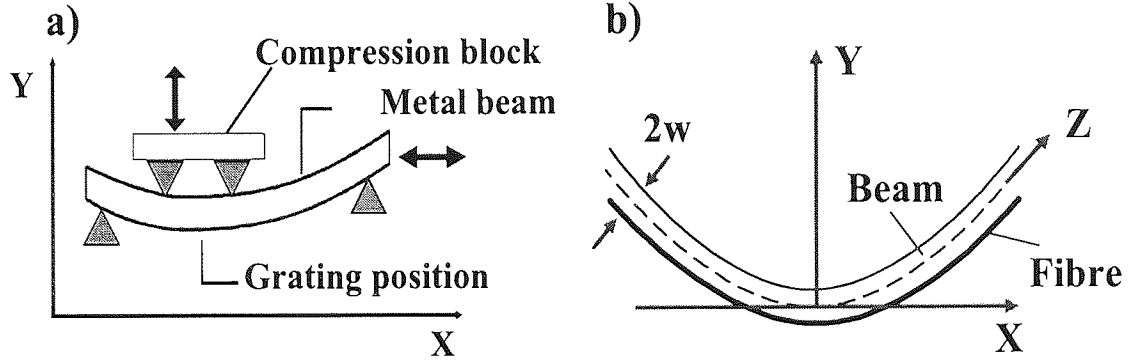
Figure 5.7 a) Schematic diagram of a four point bending rig and b) local geometry of a bended elastic beam of thickness 2w.

We consider a point-like interaction of the light with the FBG. This means that each wavelength component λ_B, within the propagating optical pulse bandwidth, is back-reflected by the FBG in the exact point of coordinate z where the grating Bragg period $\Lambda(z)$ is in resonance with that wavelength. The span of SMF travelled by the light in reaching the FBG is short enough to allow neglecting the fibre chromatic dispersion with respect to the grating dispersion. In the absence of any external perturbation (unbended beam), the linear period $\Lambda_u(z)$ of the linearly chirped FBG, as a function of the axial coordinate z along the fibre, is (see Eq. 4.2.2)

$$\Lambda_u(z) = \Lambda_0 + \alpha_0 \cdot z \qquad (5.5.1)$$

where the assigned index 'u' stays for 'unstrained' (in opposition to 's' that is used for all the quantities relative to a strained grating), and Λ_0 and α_0 are the grating refractive index modulation period and chirp rate respectively. The chromatic dispersion delivered by the linearly chirped FBG is estimated by

$$D_0 = \frac{\partial \tau(\lambda)}{\partial \lambda} \approx \frac{\beta_1}{n \dfrac{d \Lambda_u(z)}{dz}} = \frac{\beta_1}{n \alpha_0} = \text{const.} \qquad (5.5.2)$$

where n is the core effective refractive index.

Strictly speaking (5.5.2) is an approximation as we assume the core mode propagation coefficient β_1 to be independent of the wavelength. For the considered linearly chirped FBG (shown in Fig. 4.9), for instance, the estimated chromatic dispersion from (5.5.2), is

$D \approx 128.2$ ps/nm (the group velocity $v_g = 2.05 \times 10^5$ ps/nm is calculated as in Fig. 4.4, and $\alpha_0 = 0.26$ nm/cm is given by the phase-mask maker). This value of chromatic dispersion is in good agreement with the experimentally measured value. The bending of the metal beam, given by the multipoint bending rig, produces a perturbative axial distributed strain $\varepsilon(z) \ll 1$ in the linearly chirped FBG period according to

$$\Lambda_s(z) = \Lambda_u(z) \cdot (1 + \varepsilon(z)) \tag{5.5.3}$$

Now, we wish to derive a consistent system of equations relating all the relevant variables, such as the fibre strain and the dispersion delivered by the grating. For any multipoint beam bending device, including our special case of four point bending rig, the axial strain ε applied to the fibre depends on the curvature $\kappa(z)=1/\rho(z)$, where $\rho(z)$ is the local curvature radius and can be expressed as

$$\varepsilon(z) = \lim_{\ell \to 0} \frac{\Delta \ell}{\ell} = \frac{w}{\rho(z)} = w \, \kappa(z) \tag{5.5.4}$$

where ℓ represents the unstrained distance between two close points within the fibre, $\Delta \ell$ is the local elongation (or compression) after that the strain has been applied, and w is the half-thickness of the metal beam. For a given bending profile $y(x)$ the local curvature is conveniently expressed in Cartesian coordinates using the well-known formula

$$\kappa(x) = \frac{\dfrac{d^2 y(x)}{d x^2}}{\left(1 + \left(\dfrac{d y(x)}{d x}\right)^2\right)^{3/2}} \tag{5.5.5}$$

Therefore, the relation between the applied strain ε and the beam deflection $y(x)$ can be written in the form

$$\varepsilon(x) = \frac{w \dfrac{d^2 y(x)}{d x^2}}{\left(1 + \left(\dfrac{d y(x)}{d x}\right)^2\right)^{3/2}} \tag{5.5.6}$$

Finally, the coordinate z along the fibre length and the Cartesian coordinate x are related, as follows

$$\frac{d z}{d x} = \sqrt{1 + \left(\frac{d y(x)}{d x}\right)^2} \tag{5.5.7}$$

The above equations can be written in an invariant form, eliminating the Cartesian variable x. To do this, we introduce a deflection slope variable $\sigma = dy/dx$.

We then obtain

$$\frac{d\sigma}{dz} = w^{-1}(1 + \sigma(z)^2) \cdot \varepsilon(z) \qquad (5.5.8)$$

from (5.5.6) and (5.5.4). Another important, reasonably accurate simplification, can be made at this point. As it is clearly shown in Fig. 5.8, the real device always operates in the limit of small deflection, that means $\sigma \ll 1$, yielding $z = x$ instead of (5.5.7).

Using the small deviation approximation, (5.5.8) reduces to

$$\frac{d\sigma}{dz} = w^{-1}\varepsilon(z) \qquad (5.5.9)$$

Equations (5.5.3), (5.5.7) and (5.5.8) form a complete system, adequately describing the tuning of a linearly chirped FBG by axial distributed strain.
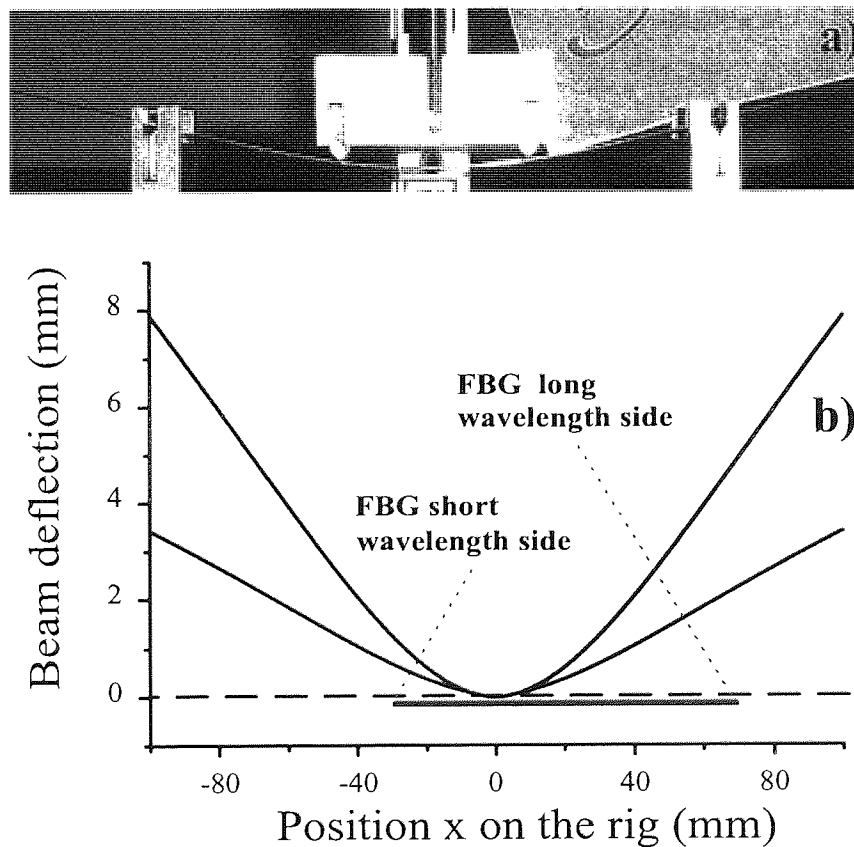
Figure 5.8 a) Photograph of the bending rig used for tuning the time delay delivered by a linearly chirped FBG by mechanical distributed strain, b) exact beam profile y(x) for two different bending conditions of the metal beam (corresponding to the full range of variability allowed by the device). The dashed line represents the unstrained beam profile, while the grey thick line on the bottom shows the position of the linearly chirped FBG within the metal beam in the actual device.

We now consider some simple specific cases where an analytic solution can be found. Either the full system or the one obtained for $\sigma \ll 1$ (small beam deviation approximation), can be considered in two opposite, but equally important situations. One may apply the above description to the calculation of the dispersion and dispersion slope in an arbitrarily strained linearly chirped FBG, once that the beam bending profile $y(x)$ is given. Alternatively, the required beam bending profile $y(x)$ can be found to provide a predetermined dispersion and dispersion slope. We refer to the two situations as the direct and the inverse problem, respectively.

5.5.1 The Direct Problem

By solving the direct problem, all the dispersion characteristics, such as the time delay, the chromatic dispersion, and the dispersion slope of the nonlinearly chirped FBG, are found as functions of the strain, which is in turn directly linked to the bending profile of the metal beam. The direct problem is straightforward and involves just a couple of simple steps, once that the bending beam profile $y(x)$ is explicitly given. The beam profile $y(x)$ can be obtained by direct scan of the photograph of the device and by subsequent numerical interpolation of the point read on the curve, as shown in Fig. 5.9.
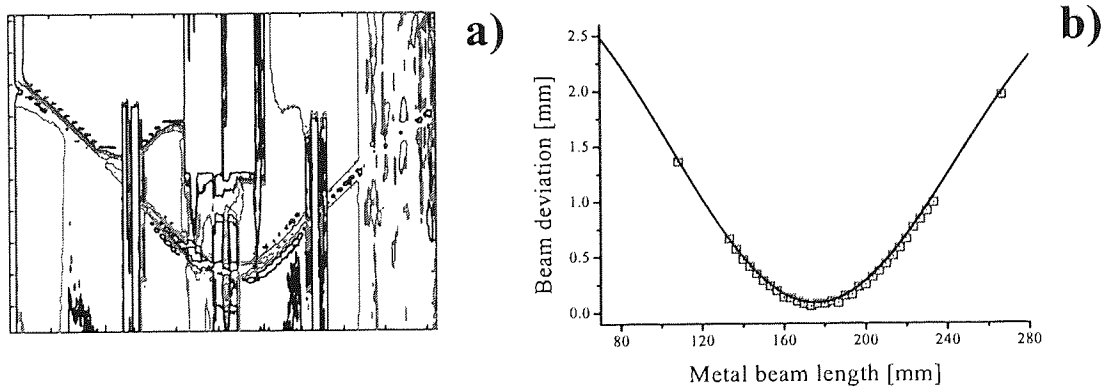
Figure 5.9 Examples of the method used to obtain the beam profile y(x) by photographic scan: a) photograph of the device in false colours, b) best-fit curve of the points (six-order polynomial).

In the specific case where the beam has been bended using the full range allowed by the device, the interpolating function (best-fit) of the beam profile $y(x)$ is a six-order polynomial of the general form $y(x) = A + B x^2 + C x^4 + D x^6$ (in the case of the maximum beam bending allowed by the rig, the coefficients are $A = -0.0032 \, \text{mm}$, $B = 0.00121 \, \text{mm}^{-1}$, $C = -5.29701 \times 10^{-8} \, \text{mm}^{-3}$, $D = 1.00709 \times 10^{-12} \, \text{mm}^{-5}$). Once that the beam profile has been found, the second step is to determine the axial strain $\varepsilon(x)$ and the

118

fibre length z(x) according to (5.5.8) and (5.5.7), respectively. These two relations provide a parametrically defined function $\varepsilon(z)$. Then, the time delay can be related to the wavelength by using the Bragg resonance condition. The chromatic dispersion D (in ps/nm) delivered by the strained chirped grating at each point of coordinate z is easily calculated by using

$$D(z) = \frac{\partial \tau(\lambda)}{\partial \lambda} = \frac{\beta_1}{n}\left[\frac{d\Lambda_s(z)}{dz}\right]^{-1} = \frac{\beta_1}{n}\frac{1}{\left[\alpha_0(1+\varepsilon(z)) + (\Lambda_0 + \alpha_0 z)\frac{d\varepsilon(z)}{dz}\right]} \tag{5.5.10}$$

One may notice that, in the case of unstrained grating (linearly chirped FBG), (5.5.10) yields a constant dispersion $D_0 = \beta_1 / n\alpha_0$. The numerically calculated value of the axial strain applied to the linearly chirped FBG by the bending of the beam, is never higher than 10^{-4}. On the other hand, the perturbative nature of the strain applied to the grating is clear from (5.5.10): as a consequence of the applied strain, the initial chirp rate α_0 of the grating becomes $\alpha_0 + \Delta\alpha$, where

$$\Delta\alpha = w\left(\alpha_0 \kappa(z) + \Lambda_u(z)\frac{d\kappa(z)}{dz}\right) \tag{5.5.11}$$

The controllable applied axial distributed strain transforms the chirping of the FBG from linear to nonlinear and the modulation refractive index period of the grating also becomes nonlinear function of the fibre length, as shown in Fig. 5.10.
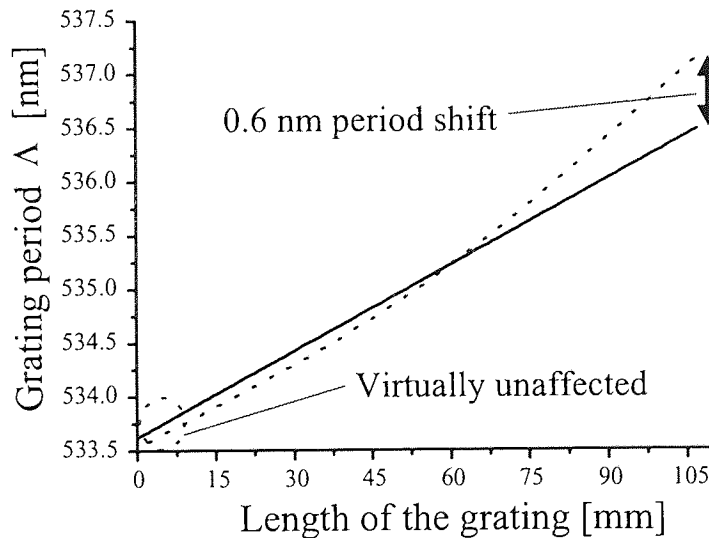
Figure 5.10 Deviation from linearity of the period $\Lambda(z)$ of an initially linearly chirped FBG subjected to axial distributed strain. Because of the special configuration chosen, the only wavelength shift induced by the strain is on the long wavelength side of the FBG, with the very short wavelengths being practically unaffected by the strain.

One last equation reflects the fact that both the chromatic dispersion D and the wavelength λ are parametrically defined via the position z along the grating

$$\lambda_s(z) = 2\,n\,(\Lambda_0 + \alpha_0\,z)\cdot(1 + \varepsilon(z)) \qquad (5.5.12)$$

The dispersion slope of the nonlinearly strained chirped FBG can be determined from

$$S(z) = \frac{\partial D}{\partial \lambda} = -\frac{\beta_1}{2\,n^2}\,\frac{2\,\alpha_0\,\dfrac{d\,\varepsilon(z)}{d\,z} + (\Lambda_0 + \alpha_0\,z)\,\dfrac{d^2\varepsilon(z)}{d\,z^2}}{\left[\alpha_0(1 + \varepsilon(z)) + (\Lambda_0 + \alpha_0\,z)\,\dfrac{d\,\varepsilon(z)}{d\,z}\right]^3} \qquad (5.5.13)$$

Figure 5.11 shows a comparison between the values of dispersion and slope predicted by the model and the experimentally determined ones. One can see, that the experimental and theoretical curves match with an accuracy of 10% for the dispersion and 15% for the slope. The data in Fig. 5.11 were obtained at the point of maximum strain of the grating, therefore the accuracy of the model at any other point is better than that shown here.
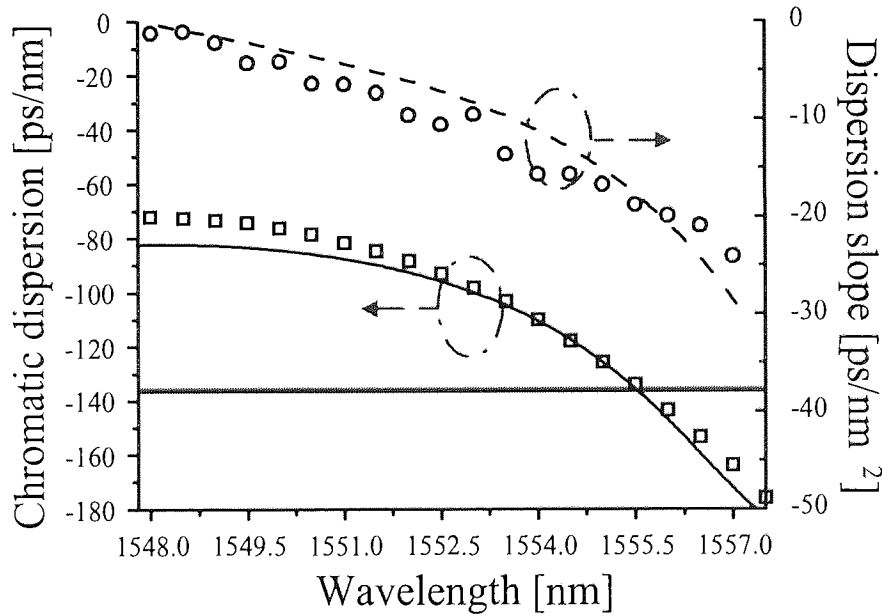
Figure 5.11 Comparison between the model prediction and the measurements in a nonlinearly strained FBG. Measured (squares) and calculated (solid line) chromatic dispersion D. Measured (circles) and calculated (dashed line) dispersion slope S. The straight horizontal line shows the dispersion of the unstrained (linearly chirped) FBG.

5.5.2 The Inverse Problem

By using the same model, it is also possible to solve the inverse problem, i.e. to calculate the beam bending profile y(x) required to obtain particular dispersion and slope. The multipoint bending rig can be easily modified in order to obtain the necessary strain. An

120

additional degree of tunability can be obtained by employing a varying beam thickness (tapered beam) or a material with a different elasticity, as well as changing the number and position of the supports in the bending rig with respect to the bar.

The inverse problem is solved assuming that the dispersion of the strained grating is given as a function of wavelength. Then the time delay can be elementary recovered, which gives a relation between the wavelength λ and the travelling distance z (i.e., the wavelength can be expressed as a function of z). By using (5.5.12), it is possible to write the strain ε as

$$\varepsilon(z) = \frac{\lambda(z)}{2n\,(\Lambda_0 + \alpha_0\,z)} - 1 = \frac{\lambda(z)}{\lambda_0 + 2n\,\alpha_0\,z} - 1 \qquad (5.5.14)$$

We can recover $z(x)$ and $y(x)$ by integrating (5.5.7) and (5.5.8). The small deviation approximation considerably simplifies this procedure, since it suffices to integrate (5.5.14) twice to obtain the beam profile $y(x)$. As an example, let us consider the practically important problem of providing the dispersion profile with given chromatic dispersion D_0 and slope S_0

$$D(\lambda) = D_0 + S_0\,(\lambda - \lambda_0) \qquad (5.5.15)$$

The relation between wavelength and travelling distance can be then written as

$$\tau(\lambda) = D_0(\lambda - \lambda_0) + \frac{1}{2}S_0\,(\lambda - \lambda_0)^2 = 2\beta_1 z \qquad (5.5.16)$$

Equation (5.5.16) enables to express the wavelength λ as a function of z

$$\lambda(z) = \lambda_0 - \frac{D_0}{S_0} + \sqrt{\frac{D_0^2}{S_0^2} + \frac{4\beta_1 z}{S_0}} \approx \lambda_0 + \frac{2\beta_1 z}{D_0} - \frac{2\,\beta_1^2\,S_0 z^2}{D_0^3} + \cdots \qquad (5.5.17)$$

where we have assumed $S_0\,(\lambda - \lambda_0) \ll D_0$ because of the smallness of the dispersion slope. Substituting (5.5.17) in (5.5.14) yields

$$\varepsilon(z) = -\frac{a+b}{1 + \dfrac{\alpha_0}{\Lambda_0}z} + a + 2b - b\left(1 + \frac{\alpha_0}{\Lambda_0}z\right) \qquad (5.5.18)$$

where $a = \dfrac{\beta_1}{n\,D_0\,\alpha_0} - 1$ and $b = \dfrac{\beta_1^2\,\Lambda_0\,S_0}{n\,D_0^3\,\alpha_0^2}$.

The required final expression for the beam bending profile $y(x)$ is then obtained from (5.5.9):

$$y(x) = w^{-1}\frac{\Lambda_0^2}{\alpha_0^2}\left\{-(a+b)\left(1 + \frac{\alpha_0}{\Lambda_0}x\right)\left[\ln\left(1 + \frac{\alpha_0}{\Lambda_0}x\right) - 1\right]\right.$$
$$\left. + \frac{1}{2}(a + 2b)\left(1 + \frac{\alpha_0}{\Lambda_0}x\right)^2 - \frac{b}{6}\left(1 + \frac{\alpha_0}{\Lambda_0}x\right)^3\right\} + c_1 x + c_0 \qquad (5.5.19)$$

The integration constant c_0 is irrelevant due to the translation invariance of the problem, whereas the integration constant c_1 should be determined from the boundary conditions corresponding to a particular implementation of the bending profile. For instance, for the bending rig described above: $\varepsilon(x = 0) = 0$, which implies that c_1 has to be set to zero. Notably, a zero strain corresponds to the dispersion D_0 resulting from a linear chirp.

5.6 Spectral and Temporal Measurements on Nonlinearly Strained FBG

Before testing the performance of the mechanical tunable FBG on a real dispersion-managed transmission system, we carried out a few measurements to understand how the applied strain could affect the dispersion and reflection characteristics of the grating. A first set of measurements is shown in Fig. 5.12.
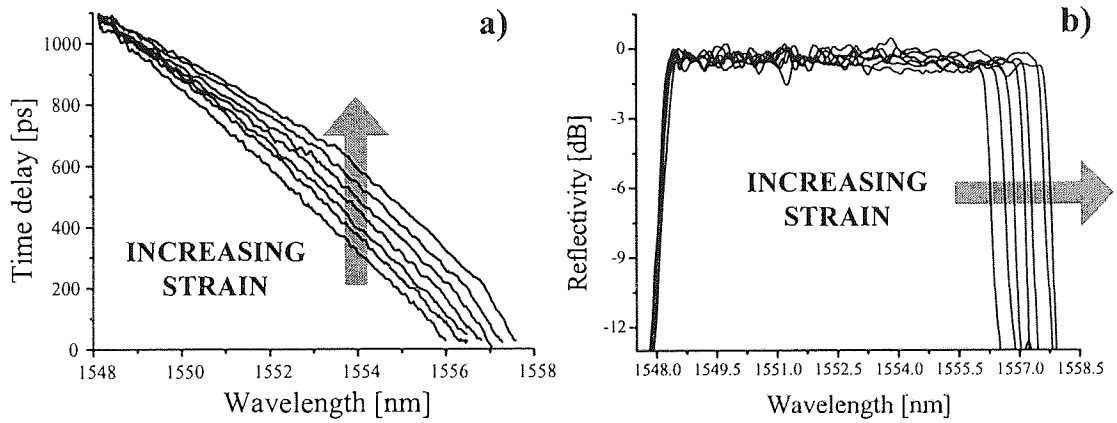
Figure 5.12 The effect of increasing distributed strain on a linearly chirped FBG: a) nonlinear tuning of the time delay and b) wavelength shift in the long wavelength region.

The linearly chirped FBG, glued to a thin spring steel beam, was subjected to an increasing curvature (i.e., an increasing nonlinear strain) by the multipoint bending rig. The transition from a linear time delay (constant chromatic dispersion) to a nonlinear one (where the chromatic dispersion depends on the wavelength), as a function of the distributed strain applied to the grating is shown in Fig. 5.12.a. A translation of the metal beam along z allows the application of the maximum strain on a precise region of the FBG. In the case considered here, the tuning of the chromatic dispersion and dispersion slope at 1550 nm was obtained by applying the maximum strain (asymmetrically) at approximately one third of the grating length starting from the short wavelength side. The special geometry of the bended beam enables to minimise the wavelength shift produced by the applied strain on the short wavelength region. Actually, as shown in Fig. 5.12.b, only the longer wavelengths within the grating bandwidth are shifted by the strain (by less than 2 nm).

122

This behaviour guarantees that the operating wavelength never leaves the grating band-gap and thus the device can work on the whole range of strain tunability. The tuning curves of the device, i.e., the measured chromatic dispersion and dispersion slope at 1550 nm, as functions of the distributed strain are shown in Fig. 5.13.
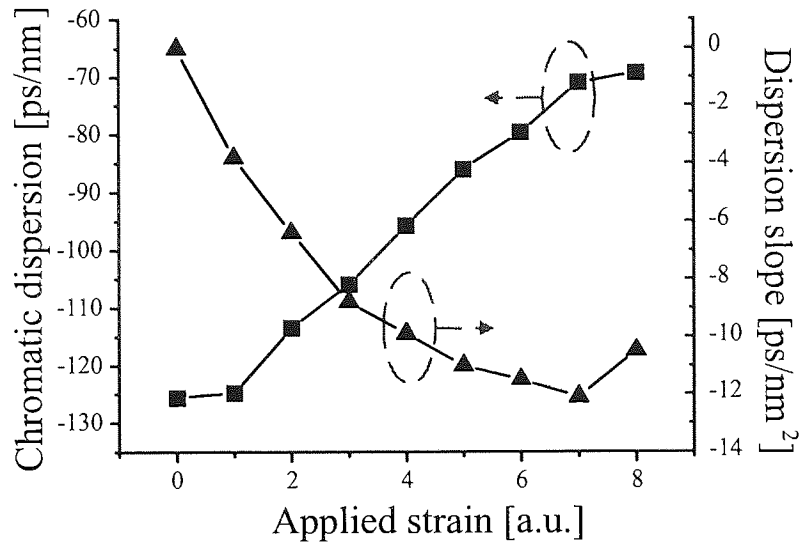
Figure 5.13 *Chromatic dispersion and dispersion slope versus applied strain, measured at 1550 nm.*

One may see that the chromatic dispersion is tuned in a range between –130 and –70 ps/nm by the applied strain. The dispersion slope (zero for a linearly chirped FBG) is tuned up to –13 ps/nm^2.
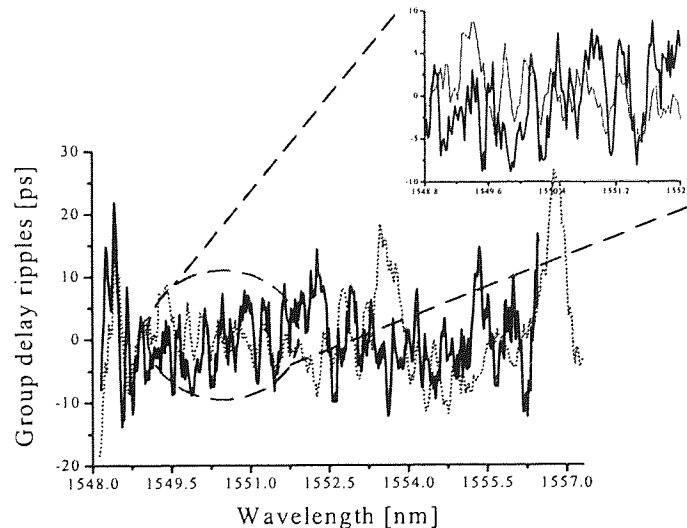
Figure 5.14 *Measured group delay ripples of a linearly chirped FBG under strain: (solid line) a moderate strain is applied, (dotted line) the maximum strain allowed by the device is applied. The inset shows the group delay ripples in the vicinity of 1550 nm, for the two different strains.*

We have also investigated the effect of the strain on the amplitude of the group delay ripples of the grating. From the data shown in Fig. 5.14 it can be seen that, for a grating subjected to a moderate strain, 68% of the group delay ripples has an amplitude of ± 5.8 ps or less. The corresponding average amplitude is estimated to be ± 4.7 ps (value slightly higher than for an unstrained apodised grating). When the maximum strain is applied, we have that 68% of the ripples has an amplitude of ± 7.3 ps or less (with an increase of ~ 25%), while the average amplitude is estimated to be ± 5.1 ps. Despite the strain produces an increase in the average value of the group delay ripples, in the region around the operating wavelength of 1550 nm the ripples are only slightly affected by the strain, and therefore the device can work very well at 1550 nm, as we show in the following section.

5.7 Pulse Recompression Experiments

We tested the performance of the mechanically tunable FBG by performing different pulse recompression experiments. A linearly chirped FBG, embedded within a V-groove of a 30 cm long and 1 mm thick spring steel beam, was used in all the experiments. This FBG has been fabricated by using the whole length of a 11 cm long holographic phase-mask (Lasiris Technology) and apodised (by the dithering phase-mask technique with a broad truncated cosine shaping function) to reduce the amplitude of the group delay ripples to less than 5 ps. The grating has a bandwidth of ~ 8nm and a linear chromatic dispersion of ~ 128.2 ps/nm (measured by the phase-shift modulation method). All the measurements were done in a linear regime, because the nonlinear effects in the fibre were minimised by keeping the optical power low. This because only the FBG should be responsible for the pulse recompression and no contribution should come from the nonlinearity.
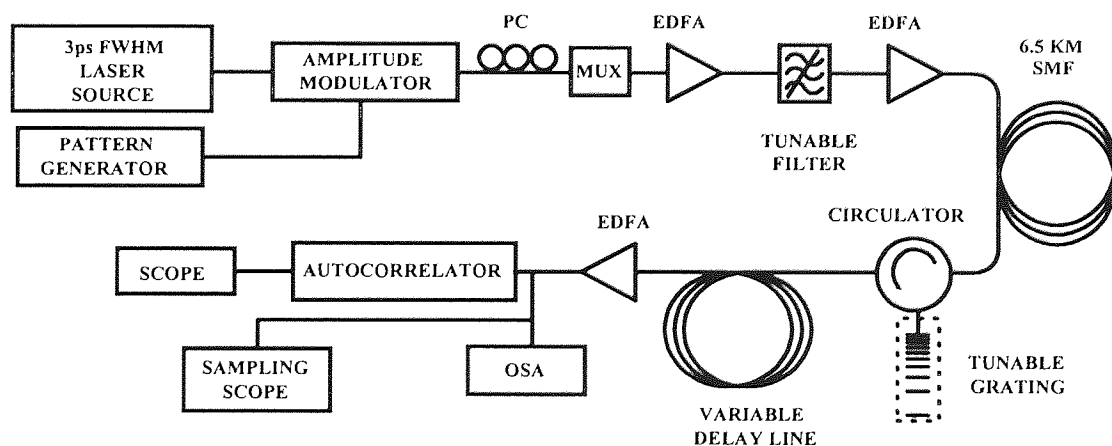
Figure 5.15 Experimental set-up used for testing the tunable FBG.

The fibre nonlinearity can be neglected whenever the condition

$$\frac{L_D}{L_{NL}} << 1 \qquad (5.7.1)$$

is satisfied, where L_D and L_{NL} are the characteristic dispersion and nonlinear lengths, respectively:

$$L_D = \frac{2\pi c \times 0.33 T_{FWHM}^2}{\lambda^2 |D|} \quad \text{and} \quad L_{NL} = \frac{1}{\gamma P_0} \qquad (5.7.2)$$

Here, P_0 is the pulse peak power and γ is the fibre nonlinear coefficient. P_0 can be recovered from the average power P_{avc} of a bit stream by using the relation

$$P_0 = 2 \times \frac{T}{T_{FWHM}} \times P_{avc} \qquad (5.7.3)$$

where T is the bit period.

We performed two experiments to test the ability of the mechanically tunable grating to recompress broadened optical pulses under different conditions of applied strain and/or for different repetition rates. The schema of the experimental set-up is shown in Fig. 5.15. A mode-locked fibre laser (PriTel UOC-3) was used, providing 2.7 ps FWHM pulses at the operating wavelength of 1550 nm. The time-bandwidth product was ~ 0.34, showing that the laser output pulses were a good approximation to transform limited and $sech^2(t)$ in profile. A 10 Gb/s pseudo-random binary sequence (PRBS) of length 2^{31}-1 is amplified by using an EDFA, then injected into a 6.5 km-long SMF. Because of the dispersion induced by the EDFA, the pulses at the output of the amplifier are slightly broader than at the output of the laser, with a measured FWHM of 3.04 ps. The measured average power at the beginning of the SMF is 16 mW, which gives a peak power of 1053 mW (see (5.7.3)). Using these values of peak power and FWHM, and $\gamma = 2.57$ (W km)$^{-1}$ in (5.7.2) we obtain L_D/L_{NL}~ 0.38, which shows that we are operating reasonably below the nonlinearity power threshold. The 6.5 km fibre acts as a dispersion reference, and intentionally broadens the laser pulses to ~ 90 ps. The broadened pulses are then injected into the tunable grating via a three-port optical circulator. As the measured chromatic dispersion of the unstrained grating is -128.2 ps/nm, the FBG clearly overcompensates for the dispersion imposed by the SMF. The pulses, detected at the grating output, are then ~ 40 ps in width.

The aim of the first experiment is the characterization of the dispersion delivered by the device under different conditions of applied strain. A variable delay line, delivering anomalous dispersion, was placed at the output of the circulator (after the grating). This variable delay line was essentially used for drawing the dispersion characteristic curves shown in Fig. 5.16.
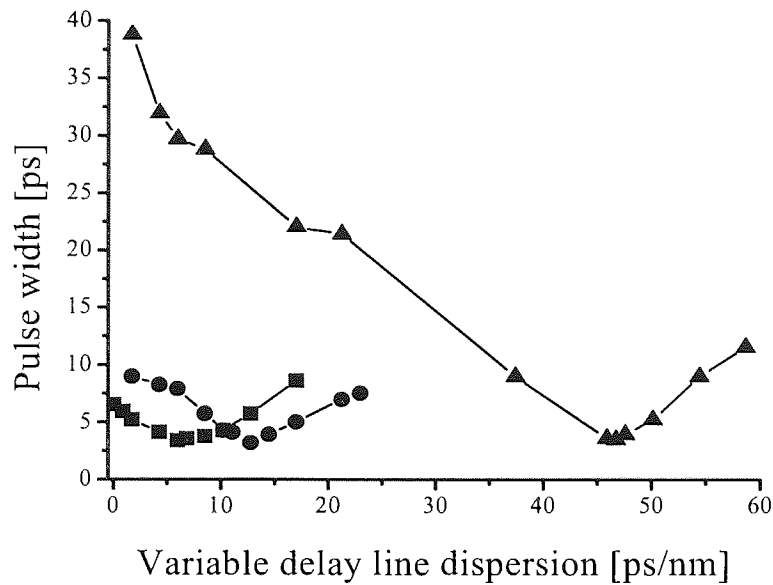
Figure 5.16 Experimental dispersion characteristic curves of the tunable FBG subjected to three different strain conditions: (triangles) flat unbended beam, (squares) maximum bending allowed by the rig, and (circles) intermediate bending.

The motivation for such measurements was to establish whether the application of a given strain can deteriorate in any way the compression capability of the grating. The curves in Fig. 5.16 refer to three different conditions of applied distributed strains. In each one of the cases considered here the grating was set in such a way to deliver a dispersion in excess (so that the pulses are broadened as a consequence of the unbalanced dispersion). Here the tunable FBG is maintained at a fixed position (either straight or bended beam) and the excess of dispersion is compensated by using the variable delay line only. It can be seen, from Fig. 5.16, that the minimum pulse-width has approximately the same value of 3.6 ps for all the strain conditions. We can then deduce that the strain does not affect the compression capability of the grating in any way (despite of an average 25% increase in the group delay ripples of the grating subjected to the maximum allowed strain with respect to the unstrained case). The good performance of the device is mostly due to the absence of phase-shifts within the grating structure because the strain applied is continuously varying along the grating length.

A second experiment was performed by using a variant of the set-up pictured in Fig. 5.15. This time we did not use the auxiliary delay line after the tunable FBG, but the recompression of the broadened pulses was directly obtained by tuning the grating dispersion. The same experiment was repeated at different pulse repetition rates (10 and 40 Gb/s). The 40 Gb/s pulse stream were obtained from the original 10 Gb/s stream by using a

technique of time division multiplexing, using a double Mach-Zehnder inter-leaver, including an adjustable fibre stretcher to give the required delay.
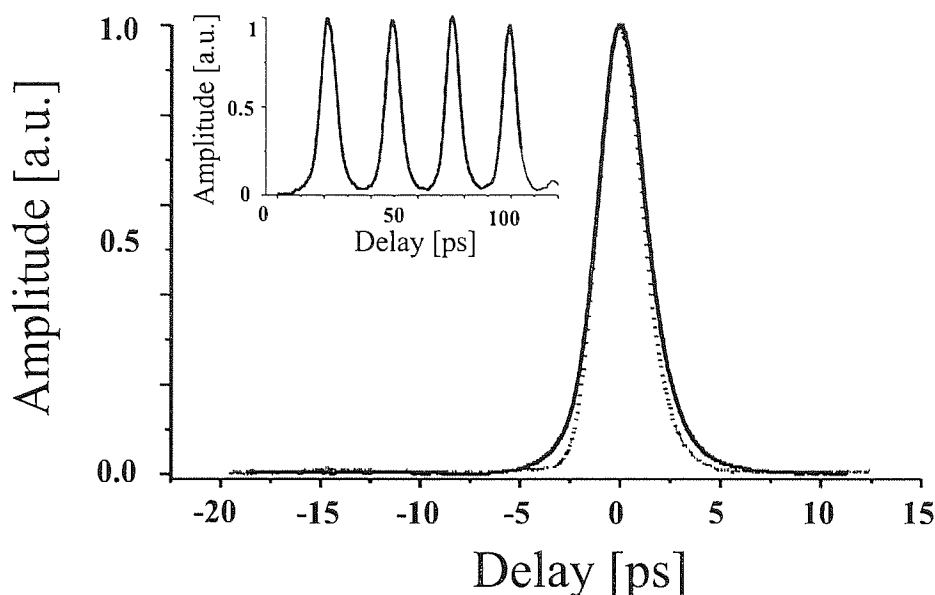
Figure 5.17 *Autocorrelation traces of the original pulses (dashed line) and of the recompressed pulses (solid line), showing high quality of the signal after dispersion compensation. Inset, the recompressed pulse stream at 40 Gbit/s.*

Figure 5.17 shows the high quality of the recompressed pulses: a clear return-to-zero recovered pulse stream can be seen. For what concerns the ability in recompressing broaden pulses, the device seems to be equally effective at 10 and 40 Gb/s. The pulse-width of the recompressed signal (measured by using an autocorrelator) is always very close to 3.6 ps (i.e., the grating has a recompression ratio of ~ 80%). From the above preliminary results we may infer that the device could be suitable for operation in high-bit rate optical transmission. Figure 5.18 shows the recovered eye-diagrams of a 10 Gb/s 2^{31}-1 PRBS data stream recompressed by the tunable grating, under different strain conditions, after travelling 6.5 km of SMF. The eye-diagrams at the output of the laser (back-to-back) and at the end of the span of fibre are also shown.
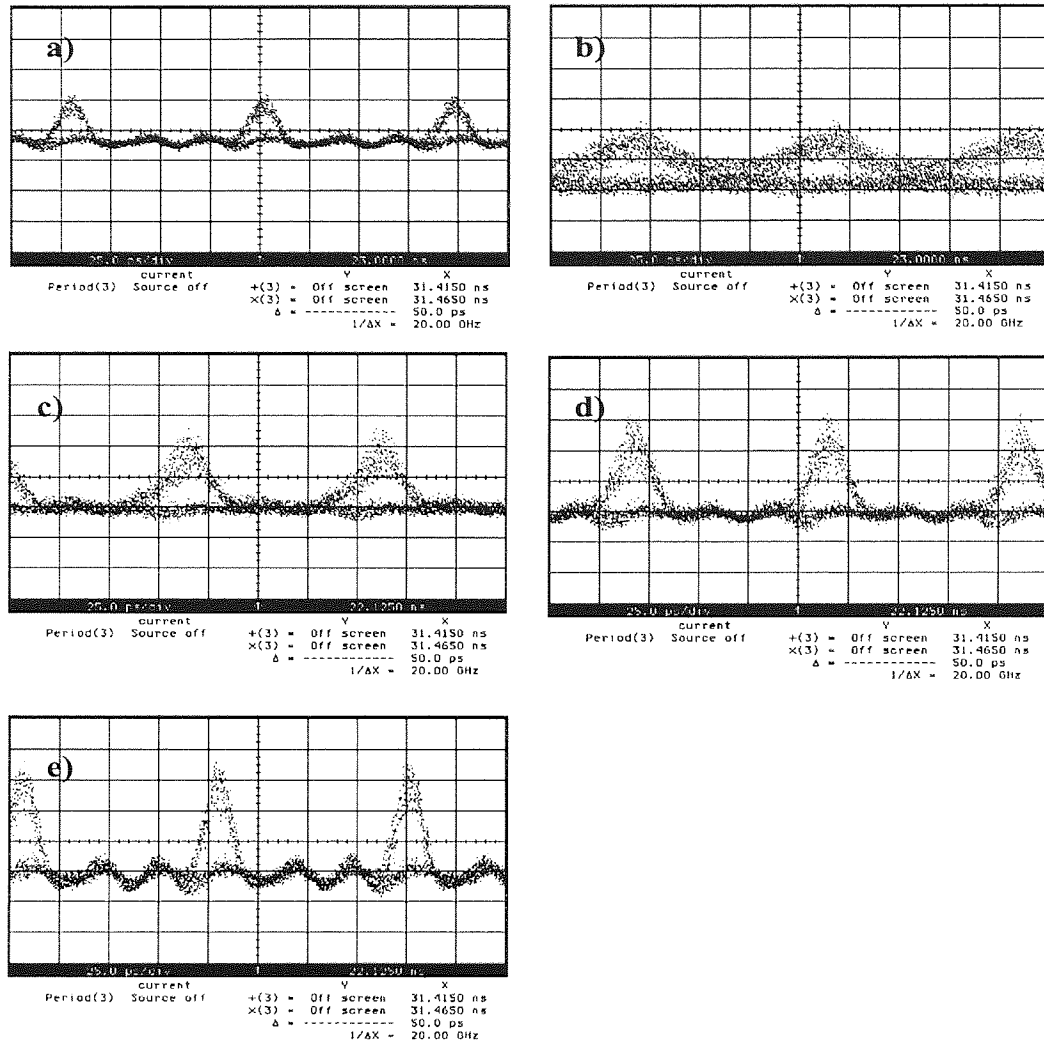
Figure 5.18 *Experimental eye diagrams of a 10 Gb/s pulse stream measured: (a) at the laser output, (b) at the end of 6.5 km SMF, and at the circulator output, (c) with unstrained grating, (d) with intermediate strain, (e) with optimal strain (3.6 ps pulse width).*

As a next step we performed an experiment to test the device as a dispersion post-compensator in a real dispersion-managed transmission line. The experimental set-up is schematically shown in Fig. 5.19, while the dispersion-map of the recirculating loop used for the experiment is detailed in Fig. 5.20.
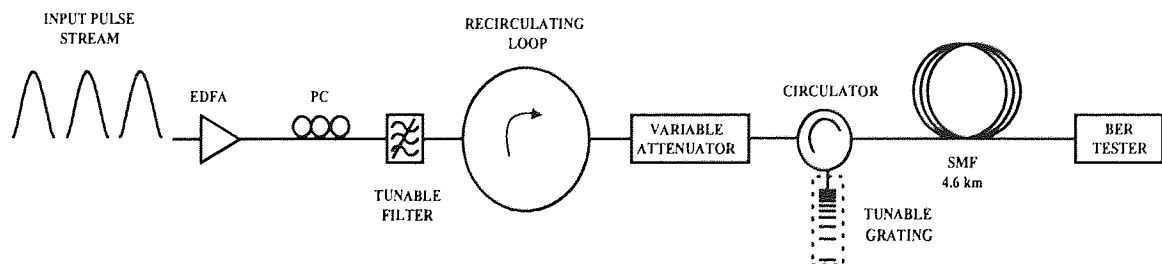
Figure 5.19 *Schema of the experimental set-up used to test the tunable FBG as a dispersion post-compensator.*
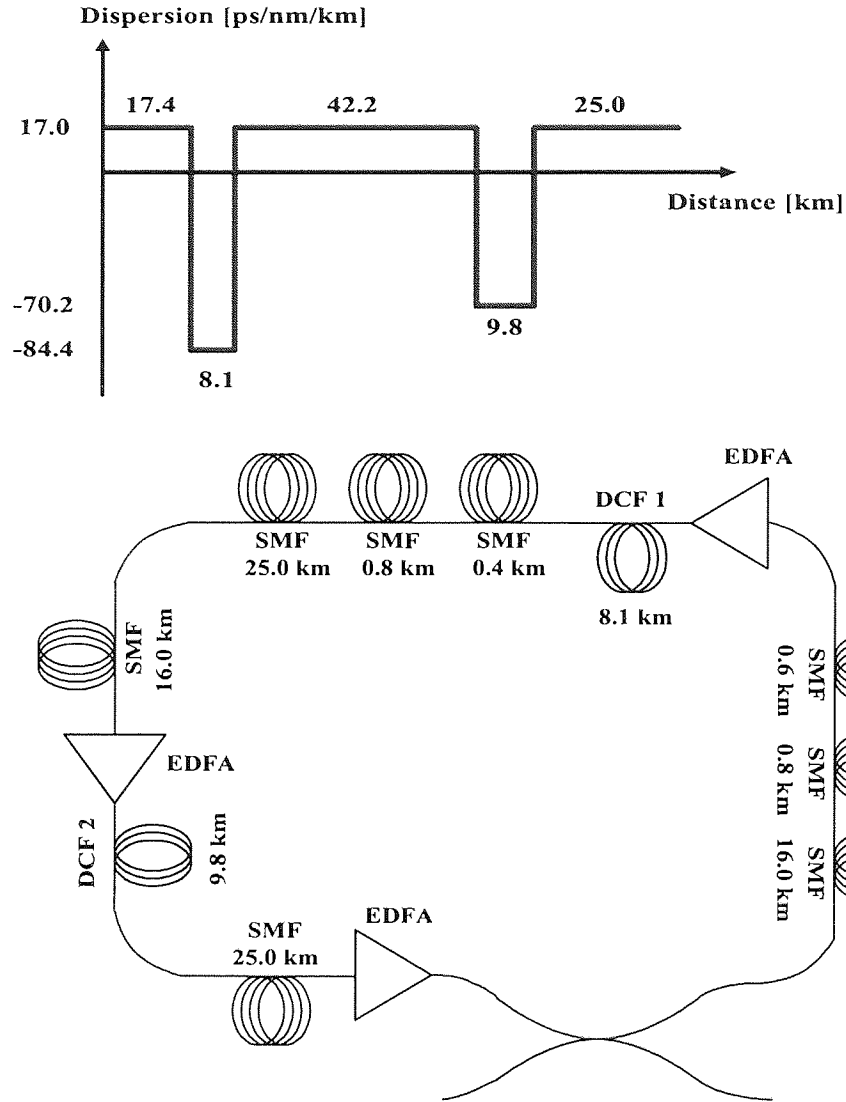
Figure 5.20 *Schematic diagram of the dispersion map and recirculating loop used in the dispersion post-compensation experiment.*

A first set of measurements were done by injecting a 10 Gb/s pulse stream into the recirculating loop. The 2^{31}-1 PRBS data stream propagates for the distance of one loop only (corresponding to 102.5 km propagation distance). Then the measurement of the Bit Error Rate (BER), to check the quality of the optical signal reaching the receiver, is effectuated as a function of the input optical power. The results of the measurement are shown in Fig. 5.21. From these results is clear that the use of the tunable dispersion post-compensator enables error-free transmission for a wider range of input powers. Specifically, we can see that without the use of the post-compensator, the BER drops to 2.93×10^{-7} when the optical power is lower than –6 dB, while with the use of the tunable FBG the region of free-error propagation becomes approximately three times larger (in such a case the BER drops to 1.88×10^{-8} for a power of –21.5 dB).
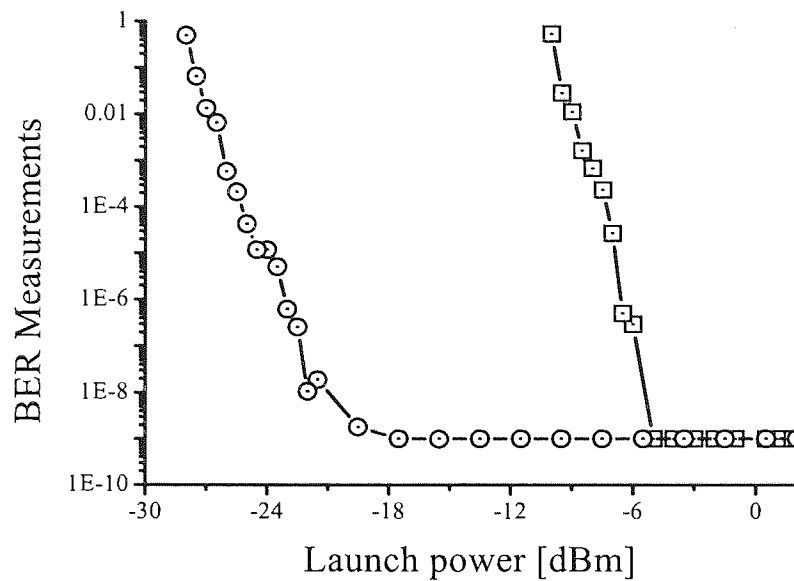
Figure 5.21 BER measurements versus input optical power: (circles) with tunable dispersion post-compensation device, and (squares) without tunable dispersion post-compensator.

One may also notice that the signal degradation is more gradual in the case where the tunable post-compensation is used than in the case where only the dispersion map is used. These measurements clearly demonstrate the effectiveness of the device.

Number of loops	BER Measurement (Without Tunable FBG)	BER Measurement (With Tunable FBG)
15	Error Free	Error Free
18	1.1×10^{-5}	Error Free
20	4.4×10^{-4}	Error Free
22	3.8×10^{-5}	5.2×10^{-8}
24	1.5×10^{-1}	5.8×10^{-4}

Table 5.2 Measured BER as a function of propagation distance with and without the tunable grating post-compensator.

A second set of measurements was carried out, again by using a 10 Gb/s pulse stream, but this time allowing propagation for more than one recirculating loop (i.e., the pulses are transmitted over a longer distance) and keeping the input optical power at a fixed value. The results of these measurements are summarised in Table 5.2. In this case also, the beneficial effect of the post-compensator is clearly visible as the error-free propagation

130

distance is increased by the device. The signal can propagate error free (BER<10^{-9}) over 1537.5 km (15 loops) when only the dispersion map is used to compensate for the chromatic dispersion. The use of the mechanical tunable grating, placed at the end of the recirculation loop, enables to extend the number of error free loops travelled by the signal to 20, which corresponds to a propagation distance of 2050 km. The same experiment was repeated by using a 40 Gb/s, 2^{31}-1 PRBS data stream and similar results were obtained (even if the error free propagation distance is shorter than in the case of 10 Gb/s similarly to what happens when the dispersion map only is used). We report below the recovered eye-diagrams for the propagation at 10 and 40 Gb/s.

	current
U p-p(1)	135.621 mU
U amptd(1)	135.383 mU
U max(1)	150.106 mU

	current
U p-p(1)	Source off
U amptd(1)	Source off
U max(1)	Source off
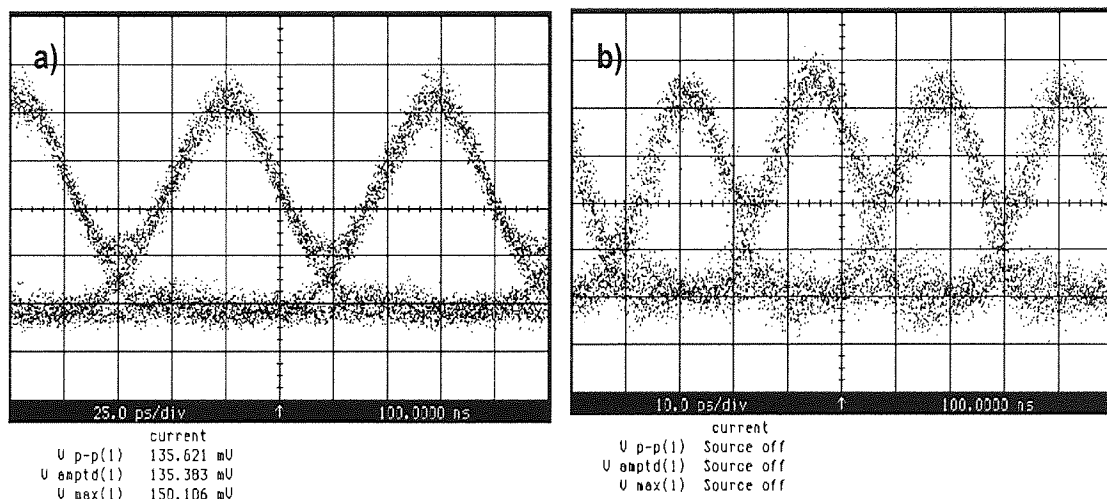
Figure 5.22 Back-to-back eye-diagrams for a 2^{31}-1 PRBS at: (a) 10 Gb/s (y scale: 25 mV/div) and (b) 40 Gb/s (y scale: 2 mV/div).

	current
U p-p(1)	153.135 mU
U amptd(1)	116.446 mU
U max(1)	167.915 mU

	current
U p-p(1)	Source off
U amptd(1)	Source off
U max(1)	Source off
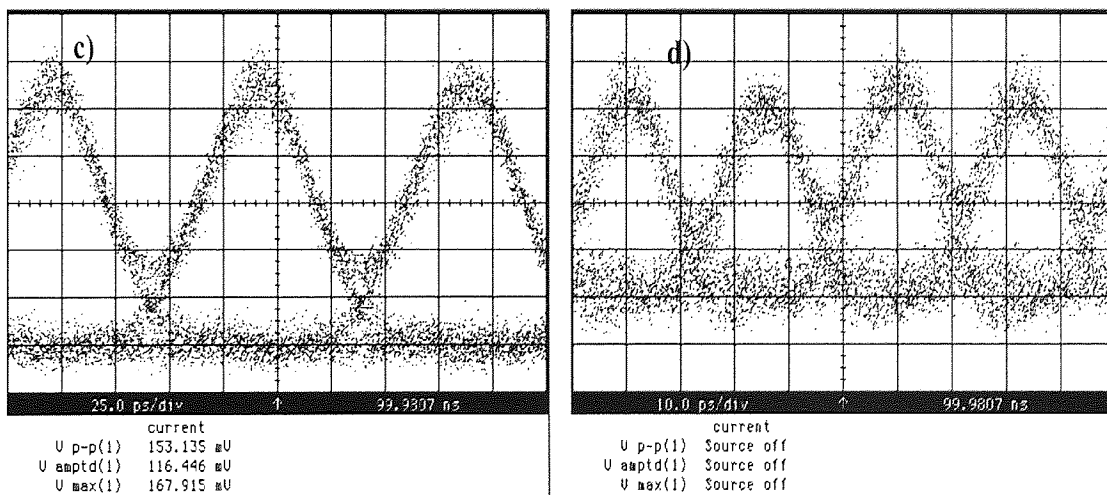
Figure 5.23 Recovered eye-diagrams of a 2^{31}-1 PRBS data stream propagating without dynamic dispersion compensation through 1 loop of the dispersion-map (102.5 km) at: (c) 10 Gb/s (y scale 20 mV/div) and (d) 40 Gb/s (y scale 2 mV/div).

131
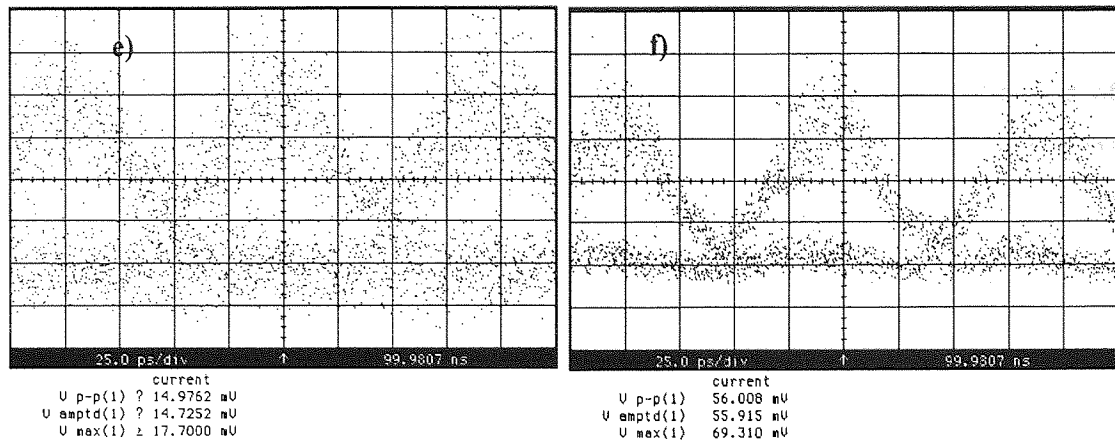
Figure 5.24 *Recovered eye-diagrams of a 10Gb/s, 2^{31}-1 PRBS data stream propagating over 1845 km (18 loops): (e) with fixed dispersion compensation delivered by the dispersion-map (y scale 10 mV/div), and (f) with dynamic compensation by tunable FBG (y scale 2 mV/div).*
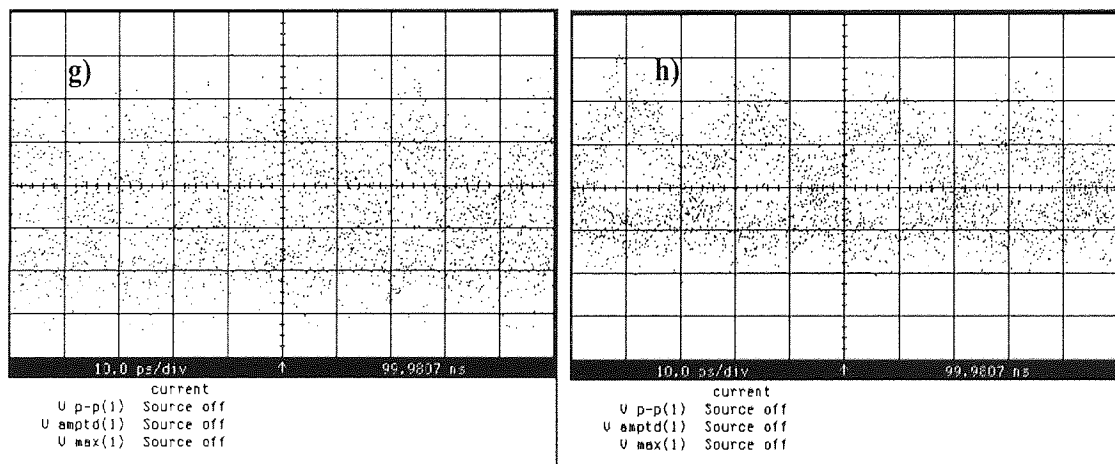
Figure 5.25 *Recovered eye-diagrams of a 40Gb/s, 2^{31}-1 PRBS data stream propagating over 1845 km (18 loops): (g) with fixed dispersion compensation delivered by the dispersion-map (y scale 1 mV/div), and (h) with dynamic compensation by tunable FBG (y scale 1 mV/div).*

Figure 5.24 shows the eye-diagram of the 10 Gb/s 2^{31}-1 PRBS, after 18 loops propagation, in the cases of tunable dispersion compensation and with fixed dispersion compensation only. It can be seen that, in the case where dynamic dispersion compensation is used, the eye-diagram results clearly open (error free propagation). From Fig. 5.25 we see that, for the same propagation distance, an equivalent optical stream at 40 Gb/s is more affected by errors. Nevertheless it is clear that the use of the tunable dispersion post-compensator device improves the quality of the signal reaching the receiver.

5.8 Pulse Tail Suppression by Tunable Filtering

The multipoint bending rig tuned FBGs have another useful application in the field of optical filtering. We demonstrate an efficient method to suppress the relaxation oscillations in the output signal of an overdriven gain-switched laser diode, based on spectral filtering by a non-uniformly strained FBG. We used the four point bending rig depicted in Fig. 5.5 to apply a distributed strain onto an apodised, unchirped, two centimetres long FBG that was glued on a side of a thin spring steel bar. The applied strain can provide adjustment of the peak wavelength and the bandwidth of the grating. As a result, the grating acts as a tunable notch filter that can be used to remove predefined components from the laser transmitted signal. The filtering is achieved without significant loss of the useful pulsed signal.
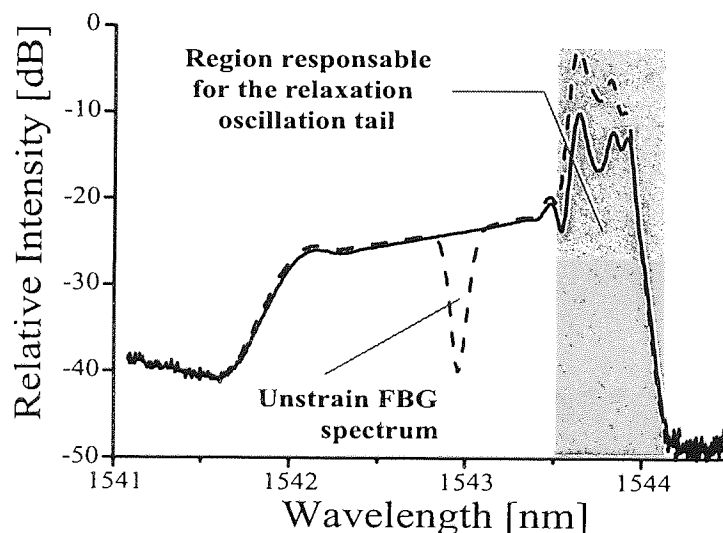
Figure 5.26 Spectra of the laser output (dashed line) without applied strain and (solid line) after filtering by using an optimised strain.

Pulsed operation of a laser diode in gain-switched or Q-switched regime is probably the simplest way to generate ultrashort optical pulses at an arbitrary repetition rate. However, the relatively low output power restricts the possible applications of pulsed laser diode sources. Increasing the signal power by driving the laser with higher current would result in a degradation of the pulse quality [38], as the useful laser signal carries only a small fraction of the total output power, the main contribution arising from the relaxation oscillation tail. In a gain-switched laser, the generation of an optical pulse starts at the point where the carrier density is high. Subsequently, the growing pulse causes substantial depletion of the carrier density. The relaxation oscillation sub-pulses, or tail, occur at the

next stage, where the carrier density oscillates above or around the threshold level. As a result, the spectral component corresponding to the tail is very similar to the continuous-wave (CW) spectrum of the same laser. The tail energy is confined in a narrow peak on the red side of the gain-switched laser spectrum, as shown in Fig. 5.26. The suppression of the pulse tail in the time domain is obtained by simply removing these spectral components from the laser spectrum. Nevertheless, such a filtering needs a very precise tuning since the spectral components involved are separated by a fraction of nanometer. In addition, the transmission function of the filter should have sharp edges to ensure the low-loss transmission of the useful signal and this can be done by suitable apodisation of the FBG. Figure 5.27 shows the results on the laser output of filtering by the use of a mechanically tunable FBG.
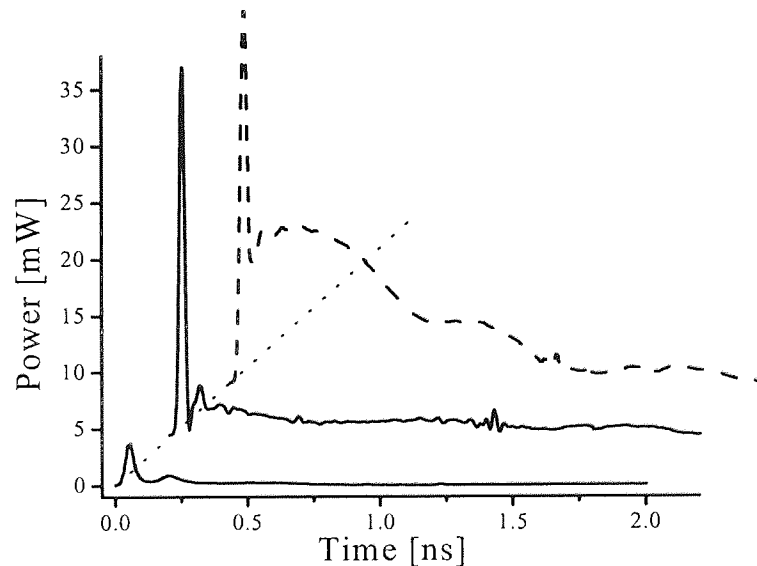
Figure 5.27 Oscilloscope traces of the laser signal: (dotted line) laser driven by low amplitude (0.5 A) electrical pulses, resulting in virtually tail-free output, (dashed line) overdriven laser (3 A electrical pulses), (solid line) spectrally filtered signal from an overdriven laser.

The experiment was performed by using a quantum-well DFB laser diode where the electrical signal is supplied by an avalanche pulse generator with repetition rate of 10 kHz and maximum current of 12 A. The electrical pulses have a rise-time of 150 ps and a fall-time of 650 ps. The pulse amplitude is adjusted by inserting a fixed electrical attenuator. No DC bias is used. When driven by electrical pulses, with a relatively low amplitude of 0.5 A, the laser produces single optical pulses with a duration between 30-40 ps and peak power up to 6 mW. Increasing the driving current produces a greater optical pulse

134

accompanied by the relaxation oscillation. At the pump level of 3 A, the peak optical power exceeds 30 mW but the pulse tail carries 90% of the total output power.

The effect of the spectral trimming on pulsed laser diode output have been studied earlier. For instance, the shaping of a gain-switched DFB laser pulse by means of the filtering has been demonstrated [39], [40]. The advantage of our approach is that we apply a notch filter instead of a bandpass filter, the signal then transmits through the filter with virtually zero loss, while the pulse tail is rejected. There is no need to use an optical circulator since the FBG operates in transmission regime. A grating with an arbitrary chirp could be used to affect the output pulse. From comparison on the curves of Fig. 5.27 it can be seen that the peak power of the tail-free pulse increases by a factor of 5 as a result of the spectral filtering. The relaxation oscillation suppression is further illustrated in Fig. 5.28.
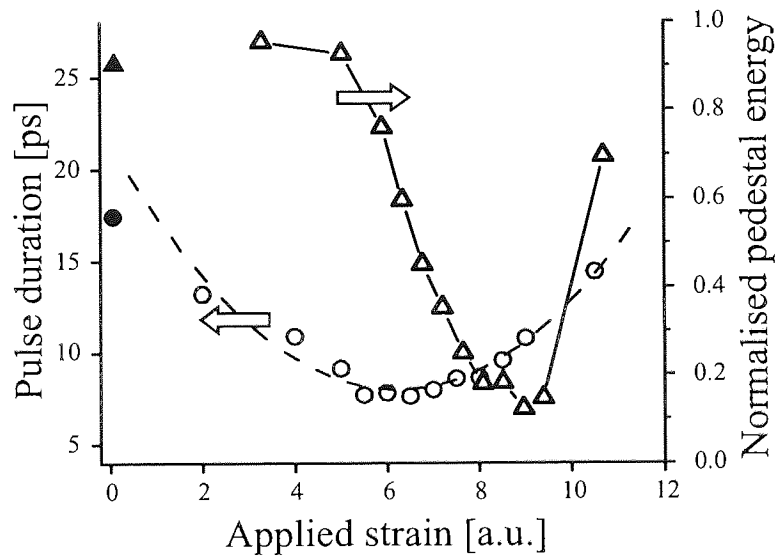
Figure 5.28 *Pulse-width and normalised relaxation tail energy E_{tail}/E_{total} against grating applied strain.*

Open triangle in Fig. 5.28 show the "normalised pedestal energy", i.e. the ratio of the energy contained in the pulse tail, to the total energy, as a function of the applied strain. The pedestal energy parameter changes from approximately 0.9, corresponding to the unfiltered signal, to a value around 0.1, when the filtering is optimised (i.e. the undesired spectral components are suppressed by approximately one order of magnitude). As well as suppressing the tail, the filtering affects the duration and chirp of the main optical pulse. It is well known that gain-switched laser diode pulses possess considerable chirp. Under the large-signal modulation the linewidth enhancement changes during the pulse, and the chirp is not linear. As a result, it is possible to obtain shorter pulses from the gain-switched laser output by selecting only the linearly chirped components. In our case, the result is achieved

135

by removing the long-wavelength components from the spectrum. The open circles in Fig. 5.28 show the output pulse-width as a function of the applied strain. As the nonlinearly chirped components are removed, the pulse experiences significant narrowing. For the optimal tuning, the output pulse is shortened to a duration of ~ 8 ps from the initial 25 ps. Unfortunately, the optimum point for the pulse shortening does not coincide with the best tail suppression, although the latter shorts the pulse-width to 10 ps. The loss experienced by the main pulse because of the filtering is very low (between 10% and 20%).

5.9 Chapter Conclusions

In the present chapter we discussed the reasons that make tunable dispersion compensation preferable to the fixed one (and even indispensable, in the case where the bit rate used is in excess of 40 Gb/s). After reviewing the state of the art on tunable dispersion compensators based on fibre grating technology (both thermally and mechanically tuned), we illustrated the working principle of a completely new device, conceived for using a distributed mechanical strain as tuning mechanism of the dispersion delivered by an initially linearly chirped FBG. The proposed device proves to be more flexible and reliable than other reported devices working on a similar principle. It clearly represents a step forward in the field of tunable dispersion compensation as allows the tuning of both chromatic and high-order dispersion. We formulated a detailed theoretical description that can be used to predict the dispersion and slope delivered by the device, once that the strain (bending) profile is given, or vice-versa, to calculate the beam bending profile to be used for a given dispersion pattern. A complete set of measurements, for the characterisation of the device, is reported: the effect of the distributed strain on time delay, reflectivity and group delay ripples of the FBG is investigated. Experiments for testing the performance of the dispersion compensator in a real optical transmission system were performed by using optical streams at different repetition rates. The device proves to be an useful tool for extending the propagation distance of an optical bit stream where the chromatic dispersion compensation is made by using a dispersion map. The use of the same rig, but this time used to apply the distributed strain on a uniform FBG, proves to be also suitable for realizing a tunable filter. The filter has a key role in the suppression of the pulse tails generated in an overdriven gain-switched laser diode. The novelty in this approach is that a notch filter, instead of a bandpass filter, is used that allows the useful part of signal to be transmitted through the filter with virtually zero loss. Using this technique we were able to generate short optical pulses and having higher power (with a power increase by a factor of 5 as a result of the spectral filtering).

References

[1] B.J. Eggleton, "Dynamic dispersion compensation devices for high speed transmission systems", in *proc. OFC 2001*, (Anaheim, USA, 2001), *paper WH1-1*.

[2] V.K. Mezentsev, S.K. Turitsyn, N.J. Doran, "System optimisation of 80 Gbit/s single channel transmission over 1000 km of standard fibre", *Electron. Lett.*, **36**, 2000, pp.

[3] A.D. Kersey, M.A. Davis, H.J. Patrick, M. LeBlanc, K.P. Koo, C.G. Askins, M.A. Putnam, E.J. Friebele, "Fiber grating sensors", *J. Lightwave Technol.*, **15**, 1997, pp.1442-1463.

[4] B.J. Eggleton, J.A. Rogers, P.S. Westbrook, T.A. Strasser, "Dual on-fiber thin film heater for fiber gratings with independently adjustable central wavelength and chirp", in *proc. Bragg Gratings, Photosensitivity, and Poling in Glass Waveguides*, 1999, *paper 6 /ThB3-1*.

[5] J. Lauzon, S. Thibault, M.J. Oullette, F. Oullette, "Implementation and characterisation of fiber Bragg gratings linearly chirped by temperature gradient", *Opt. Lett.*, **19**, 1994, pp. 2027-2029.

[6] B.J. Eggleton, A. Ahuja, P.S. Westbrook, J.A. Rogers, P. Kuo, T.N. Nielsen, B. Mikkelsen, "Integrated tunable fiber gratings for dispersion management in high-bit rate systems", *J. Lightwave Technol.*, **18**, 2000, pp.1418-1432.

[7] B.J. Eggleton, T.N. Nielsen, J.A. Rogers, P.S. Westbrook, T.A. Strasser, P.B. Hansen, K.F. Dreyer, "Dispersion compensation in 20 Gbit/s dynamic nonlinear lightwave systems using electrically tunable chirped fibre grating", *Electron. Lett.*, **30**, 1999, pp. 832-833.

[8] T.N. Nielsen, B.J. Eggleton, J.A. Rogers, P.S. Westbrook, P.B. Hansen, T.A. Strasser, "Dynamic post dispersion optimisation at 40 Gb/s using a tunable fiber Bragg grating", *IEEE Photon. Technol. Lett.*, **12**, 2000, pp. 173-175.

[9] J.A. Rogers, B.J. Eggleton, J.R. Pedrazzani, T.A. Strasser, "Distributed on-fiber thin film heaters for Bragg gratings with adjustable chirp", *Appl. Phys. Lett.*, **74**, 1999, pp. 3131-3133.

[10] S. Matsumoto, T. Ohira, M. Takabayashi, J. Hoshizaki, H. Takeya, "Tunable dispersion equalizer with a divided thin film heater", in *Proc. ECOC02*, (Copenhagen, Denmark, 2002), *paper TuS4-1*.

[11] P.C. Hill, B.J. Eggleton, "Strain gradient chirp of fibre Bragg gratings", *Electron. Lett.*, **30**, 1994, pp. 1172-1174.

[12] D. Garthe, R.E. Epworth, W.S. Lee, A. Hadjifotiou, C.P. Chew, T. Bricheno, A. Fielding, H.N. Rourke, S.R. Baker, K.C. Byron, R.S. Baulcom, S.M. Ohja, S: Clements, "Adjustable dispersion equaliser for 10 and 20 Gbit/s over distances up to 160 km", *Electron. Lett.*, **30**, 1994, pp. 2159-2160.

[13] M. Le Blanc, S.Y. Huang, M.M. Ohn, R.M. Measures, "Tunable chirping of a fibre Bragg grating using a tapered cantilever bed", *Electron. Lett*, **30**, 1994, pp. 2163-2165.

[14] M. Pacheco, A. Méndez, L.A. Zenteno, F. Mendoza-Santoyo, "Chirped optical fibre Bragg gratings using tapered-thickness piezoelectric ceramic", *Electron. Lett.*, **34**, 1998, pp. 2348-2350.

[15] M. Pacheco, A. Méndez, F. Mendoza-Santoyo, L.A. Zenteno, "Analysis of the spectral characteristics of piezoelectrically driven dual and triple-period optical fibre Bragg gratings", **167**, *Opt. Commun.*, 1999, pp. 89-94.

[16] T. Inui, T. Komukai, N. Nakazawa, "Highly efficient tunable fiber Bragg grating filters using multiplayer piezoelectric transducer", **190**, *Opt. Commun.*, 2001, pp. 1-4.

[17] T. Imai, T. Komukai, M. Nakazawa, "Dispersion tuning of a linearly chirped fiber Bragg grating without a center wavelength shift by applying a strain gradient", **10**, *IEEE Photon. Technol. Lett.*, 1998, pp. 845-847.

[18] X. Dong, B.-O. Guan, S. Yuan, X. Dong, H.-Y. Tam, "Strain gradient chirp of uniform fiber Bragg grating without shift of central Bragg wavelength", **202**, *Opt. Commun.*, 2002, pp. 91-95.

[19] J. Mora, J. Villatoro, A. Díez, J.L. Cruz, M.V. Andrés, "Tunable chirp in Bragg gratings written in tapered core fibers", *Opt. Commun., **210**, 2002, pp. 51-55.

[20] M.M. Ohn, A.T. Alavie, R. Maaskant, M.G. Xu, F. Bilodeau, K.O. Hill, "Dispersion variable fibre Bragg grating using a piezoelectric stack", *Electron. Lett.*, **32**, 1996, pp. 2000-2001

[21] A.T. Alavie *et al.*, "Method and apparatus of Bragg intra-grating strain control", US Patent application No. 2,134,958, November 1994s.

[22] J.-X. Cai, K.-M. Feng, A.E. Willner, V. Grubsky, D.S. Starodubov, J. Feinberg, "Simultaneous tunable dispersion compensation of many WDM channels using a sampled nonlinearly chirped fiber Bragg grating", *IEEE Photon. Techn. Lett.*, **11**, 1999, pp.1455-1457.

[23] Y. Xie, S. Lee, Z. Pan, J.-X. Cai, A.E. Willner, V. Grubsky, D.S. Starodubov, E. Salik, J. Feinberg, "Tunable compensation of the dispersion slope mismatch in dispersion-managed systems using a sampled nonlinearly chirped FBG", *IEEE Photon. Techn. Lett.*, **12**, 2000, pp. 1417-1419.

[24] J. Williams, I. Bennion, N. Doran, "The design of in-fibre Bragg gratings systems for cubic and quadratic dispersion compensation", *Opt. Comm.*, **116**, 1995, pp. 62-66.

[25] J.A.R. Williams, L.A. Everall, I. Bennion, N. Doran, "Fiber Bragg grating fabrication for dispersion slope compensation", *IEEE Photon. Technol. Lett.*, **8**, 1196, pp. 1187-1189.

[26] M. Ibsen, R. Feced, "Broadband fibre Bragg gratings for pure third-order dispersion compensation", Postdeadline OFC 2002 (Anaheim, USA, 2002), *paper FA7-1*.

[27] A.E. Willner, K.-M. Feng, J. Cai, S. Lee, J. Peng, H. Sun, "Tunable compensation of channel degrading effects using nonlinearly chirped passive fiber Bragg gratings", *IEEE J. Select. Topics Quant. Electron.*, **5**, 1999, pp.1298-1311.

[28] K.-M. Feng, J.-X. Cai, V. Grusbsky, D.S. Starodubov, M.I. Hayee, S. Lee, X. Jiang, A.E. Willner, J. Feinberg, "Dynamic dispersion compensation in a 10-Gb/s optical

system using a novel voltage tuned nonlinearly chirped fiber Bragg grating", *IEEE Photon. Technol. Lett.,* **11**, 1999, pp. 373-375.

[29] H. Sun, M.C. Cardakli, K.-M. Feng, J.-X. Cai, H. Long, M.I. Hayee, A.E. Willner, "Tunable RF-power-fading compensation of multiple-channel double-sideband SCM transmission using a nonlinearly chirped FBG", *IEEE Photon. Technol. Lett.,* **12**, 2000, pp. 546-548.

[30] S.S. Goh, S.Y. Set, K. Taira, S.K. Khijwania, K. Kikuchi, "An adjustable dispersion slope compensator based on nonlinearly strain-chirped fiber Bragg gratings", Postdeadline ECOC'01 (Amsterdam, The Netherlands, 2001).

[31] S.S. Goh, S.Y. Set, K. Taira, S.K. Khijwania, K. Kikuchi, "Nonlinearly strain-chirped fiber Bragg grating with an adjustable dispersion slope", *IEEE Photon. Technol. Lett.,* **14**, 2002, pp. 663-665.

[32] Y.W. Song, Z. Pan, C. Yu, Y. Wang, J. Popelek, H. Li, Y. Li, A.E. Willner, "Error-free tunable dispersion slope compensation for 40-Gb/s WDM systems using non-channelized 3rd-order chirped fiber Bragg gratings", *in proc. ECOC'02* (Copenhagen, Denmark, 2002), *paper 6.1.2.*

[33] A.J. Felis *et al.*, "Chromatic dispersion compensation", European Patent Application No. 00305007.7, June 2000.

[34] T. Inui, T. Komukai, M. Nakazawa, "A wavelength-tunable dispersion equaliser using a nonlinearly chirped fiber Bragg grating pair mounted on multilayer piezoelectric transducers", *IEEE Photon. Technol. Lett.,* **12**, 2000, pp. 1668-1670.

[35] T. Inui, T. Komukai, M. Nakazawa, K. Suzuki, K.R. Tamura, K. Uchiyama, T. Morioka, "Adaptive dispersion slope equalizer using a nonlinearly chirped fiber Bragg grating pair with a novel dispersion detection technique", *IEEE Photon. Technol. Lett.,* **14**, 2002, pp. 549-551.

[36] J.A.J. Fells, S.E. Kanellopoulos, P.J. Bennett, V. Baker, H.F.M. Priddle, W.S. Lee, A.J. Collar, C.B. Rogers, D.P. Goodchild, R. Feced, B.J. Pugh, S.J. Clements, A. Hadjifotiou, "Twin fiber grating tunable dispersion compensator", *IEEE Photon. Technol. Lett.,* **13**, 2001, pp. 984-986.

[37] B.A.L. Gwandu, L. Zhang, K. Chisholm, Y. Liu, I. Bennion, "Compact FBG grating array structure for high spatial resolution distributed strain sensing", in *proc. Optical Fibre Sensing 2000,* (Venice, Italy, 2000), *paper P 3-19.*

[38] P. Vasil'ev, "Ultrafast diode laser: fundamentals and applications", *Artech House, London,* 1995.

[39] T. Niemi, J. Zhang, H. Ludvigsen, "Effect of optical filtering on pulses generated with a gain-switched DFB laser", *Opt. Commun.,* **192**, 2001, pp. 339-345.

[40] T. Komukai, Y. Miyajima, M. Nakazawa, "An in-line optical bandpass filter with fiber grating and an optical circulator and its application to pulse compression", *Jpn. J. Appl. Phys.,* **34**, 1995, pp. L230-L232.

<div align="right">

Chapter **6**

</div>

METAL COATED FIBRE GRATING DEVICES

6.1 Chapter Overview

In this chapter the behaviour of fibre gratings coated with a metal is theoretically investigated and experimentally characterised. Metal coated fibre devices prove to be accurate sensors for detection of temperature, external medium refractive index and bending. For a suitably chosen metal coating (silver), we demonstrate that it is possible to write the grating directly through the metal, and this technique considerably simplifies the fabrication process of such devices. We fully characterize the behaviour of a partially silver coated double-section LPG sensor, having a period of 325 μm and recorded (through the metal coating) in a single-mode Boron/Germanium co-doped fibre. The structure generates two attenuation bands, associated with the 8th and 9th cladding modes, that can be used for sensing measurements as they are located spectrally close together. The attenuation band associated with the silvered section proves to be unaffected by changes in the surrounding medium refractive index and can be used to temperature compensate the bare fibre section. The sensing device possesses a resolution of $\pm 1.0 \times 10^{-3}$ for refractive index detection and $\pm 0.3\,^{\circ}C$ for temperature detection. The effect of bending on the

spectral characteristics of the two attenuation bands is found to be nonlinear, with the silver coated section having the greater sensitivity.

6.2 Three-Layer Cylindrical Optical Waveguides

Apart from their use in optical communications (where they have been employed as filters or dispersion compensators, just to give two examples), fibre gratings have been also widely used in the field of sensors as precise detectors of temperature, strain/bending and surrounding medium refractive index variations [1], [2]. In the usual fabrication process, any polymer coating, put around the fibre cladding to protect it from the mechanical stress and the attach of the air, must be stripped off and the fibre accurately cleaned with methanol (or a similar property chemical) and dried before the writing process can start. This is because the polymer absorbs the most part of the UV light focused on the fibre, making the process of writing in the core difficult. Once the grating has been written, the fibre is then recoated in order to preserve its mechanical strength. In recent years, special UV-transparent polymers have been developed in the attempt to simplify the writing process [3], which can be thus reduced to one single step. Also the use of a different writing wavelength, that is less absorbed by the fibre jacket, has been proposed [4], but this method is unpractical due to the fact that a specifically designed phase-mask is required in order to work at a wavelength different from 244 nm. On the other hand, adding a third layer to a conventional step index fibre, made of a material with a different refractive index, or having a interesting physical characteristic such as high thermal expansion or mechanical resistance, can be of advantage in some specific applications. Obvious advantages of using a metal coating, for instance, are an improved strength of the fibre and consequently a better long term resistance to the fatigue, or the ability to attach the fibre reliably to a connector, either by soldering, or by thermal compression bonding [5]. The disadvantage is an increased optical transmission loss due to the modified structure of the waveguide. Nevertheless, the interaction of the surface plasma mode of the metal film with the evanescent field of the mode guided by the core makes the metal coated waveguides a very interesting subject of studies, largely compensating for the disadvantage of an increased optical loss [6-8]. Recently, a variety of metal-coated fibre grating based devices have been proposed as filters or sensors [9-12]. Typically, first the grating is written in the core fibre (after stripping the fibre of its polymer coating), then the region containing the grating is recoated by using a thin evaporated layer of a metal (or alternatively, the coating layer is deposited by passing the fibre through a molten film of the liquid metal) [6], [10]. This simple technique produces a nonuniform metal coating on the fibre cladding, and can

be used for the fabrication of sensors, where the mesurand changes the external refractive index, tuneable spectral filters (e.g., for gain flattening or ASE removal in fibre amplifiers) [13], [14], or chemical sensors based on a narrow cladding-moded taper with a metal coating [15].
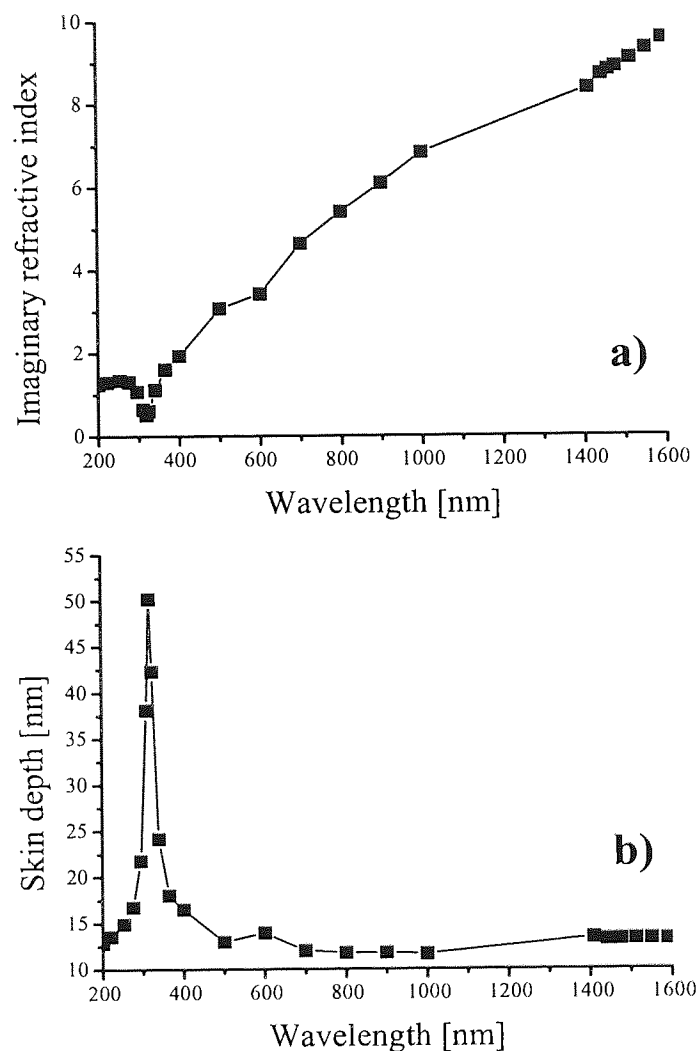
Figure 6.1 *Imaginary part of the refractive index and calculated skin depth of silver as functions of the wavelength. The high value of the skin depth in the near-UV region is responsible for the relative transparency of the metal at the wavelength used to write the fibre grating.*

A better accuracy in preserving the cylindrical geometry of the fibre (i.e., a symmetric radial coating) and uniform thickness of the metal coating along the fibre length is obtained by using a more sophisticated technique involving a DC magnetron-sputtering machine (the uniform thickness of the metal coating is achieved by a mechanical rotational rig placed within the sputtering machine). The devices used in our experiment were made in

two steps. First a section (approximately 4 cm long) of Borum/Germanium co-doped step index fibre is placed into the sputter machine. The section of fibre is uniformly coated with a silver layer having a thickness of 1 μm. The second step consists in writing the grating. The characterisation of the optical properties of metals has been the subject of extensive studies for more than a century, since the electromagnetic theory of light was developed [16]. Metals have a very high conductivity and for this reason they are practically opaque in the visible window of wavelengths. In spite of this, metals play an important part in optics, as the strong absorption is accompanied by a high reflectivity. The refractive index of a metal is expressed by a complex number, where the imaginary part accounts for the loss experienced by the electromagnetic wave that propagates inside the metallic medium. As illustrated in Fig. 6.1.a, silver is relatively transparent to the near-UV radiation [17]. The silver skin depth, a quantity that expresses the efficiency of the radiation at a given wavelength in penetrating the metal, and related to the imaginary part of the refractive index, has a pick around 300 nm, that implies a higher transparency of the metal at this specific wavelength. This special property of the silver allows to write a fibre grating directly in the core fibre through the metal coating, as shown in Fig. 6.2. However, as silver is not fully transparent to the 244 nm radiation, the inscription of the grating through the metal is generally difficult and requires a multiple scan when using a laser output average power of 110 mW (an higher power can not be used for not damaging the phase mask). The fabrication technique consists in a two steps inscription of the FBG in the bare fibre and in the metal coated section: the phase mask is positioned exactly in the middle of the region between the fibre coated and the bare sections.
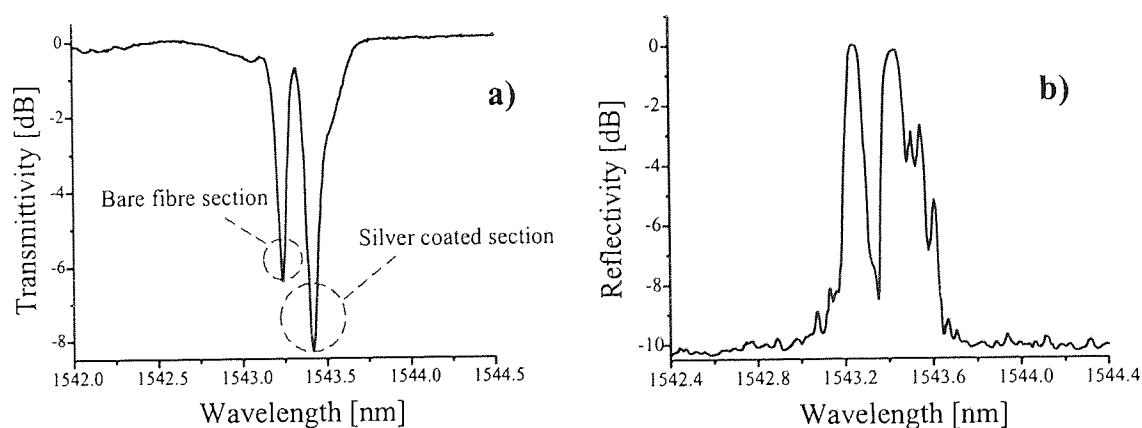
Figure 6.2 *Example of two-sections FBG device written partially through the silver metal coating and in the bare single mode Ge doped fibre: a) the transmission spectrum shows the appearance of a secondary peak with a shifted wavelength relative to the one written in the bare fibre, b) a refractive index sensitivity saturation effect can be deduced by looking at the reflectivity spectrum.*

The grating is first written by a single scan in the bare section of the fibre, then through the silver by using multiple scans. Looking at the reflection spectrum in Fig. 6.2.a, it is clear that the appearance of a secondary peak shifted in wavelength is due to a saturated index sensitivity produced by an overexposure to UV light because of the multiple scan technique used for the fabrication.

6.3 Component Fields of Normal Modes in a Three-Layer Waveguide

We analyse the behaviour of the normal modes in a cylindrical three layer waveguide, such as the one schematically illustrated in Fig. 6.3. We consider a generic two medium step-index dielectric waveguide surrounded by a third medium. The case where the third medium is air corresponds to the description already given in the second chapter of this thesis. We are interested now in studying the case where the external layer is a metal. In such a case, as we already told, the refractive index n_3 of the metal coating is taken to be complex. Because of the complex nature of the refractive index, the metal acts as a lossy medium. We want to investigate the properties of confinement of the modes propagating in the cladding, when a LPG has been written in the core of the metal coated waveguide. To do so we will follow the approach in [18-20], and we will not take in account the imaginary part of the refractive index. We omit the usual steps involving the solution of the Maxwell equations and we directly begin with the choice of cylindrical functions describing the dependencies of the longitudinal components of the field on the radial coordinate r. Since the fields on the waveguide axis ($r = 0$) should be finite, the cylindrical function in the first medium can be a Bessel function $J_n(k_1 r)$. For the second medium the cylindrical function can be in the form of a linear combination of a Bessel function $J_n(k_2 r)$ and a Neuman function $N_n(k_2 r)$. The wave field in the third medium is supposed to decrease monotonically with increasing r, therefore the cylindrical function for the third medium can be a MacDonald function $K_n(k_3 r)$. Thus, the expressions for the longitudinal components of the field in the three media of the dielectric waveguide are

$$E_{z1} = A_n J_n(k_1 r) F_c, \quad H_{z1} = B_n J_n(k_1 r) F_s,$$
$$E_{z2} = [C_n J_n(k_2 r) + T_n N_n(k_2 r)] F_c,$$
$$H_{z2} = [D_n J_n(k_2 r) + M_n N_n(k_2 r)] F_s, \qquad (6.3.1)$$
$$E_{z3} = \Phi_n K_n(k_3 r) F_c, \quad H_{z3} = P_n K_n(k_3 r) F_s,$$

where A_n, B_n, C_n, D_n, M_n, P_n, T_n, and Φ_n are the constants found from the boundary conditions; $F_c = \cos(n\varphi + \theta_n) \times \exp[i(\omega t - \beta z)]$, $F_s = \sin(n\varphi + \theta_n) \times \exp[i(\omega t - \beta z)]$; $k_{1,2,3}$ are the transverse wave numbers of the first, second and third medium of the waveguide,

respectively: $k_1^2 = k_0^2 n_1^2 - \beta^2$, $k_2^2 = k_0^2 n_2^2 - \beta^2$, $k_3^2 = \beta^2 - k_0^2 n_3^2$; $k_0 = 2\pi / \lambda$ is the wave number in free space; $\beta = 2\pi / \lambda_q = \omega / V_{ph}$ is the longitudinal wave number; ω is the angular frequency, n is an positive integer number.

We shall introduce dimensionless parameters p_1 and p_2, representing the relative magnitude of the fields E_z and H_z in a mode [19]. We shall do this using the expressions in the system (6.3.1) with $r = r_{co}$ and $r = r_{cl}$:

$$p_1 = \frac{W_0 k_0 B_n}{\beta A_n} = \frac{W_0 k_0}{\beta} \cdot \frac{D_n J_n(c x_2) + M_n N_n(c x_2)}{C_n J_n(c x_2) + T_n N_n(c x_2)} , \qquad (6.3.2)$$

$$p_2 = \frac{W_0 k_0 P_n}{\beta \Phi_n} = \frac{W_0 k_0}{\beta} \cdot \frac{D_n J_n(x_2) + M_n N_n(x_2)}{C_n J_n(x_2) + T_n N_n(x_2)} , \qquad (6.3.3)$$

where $x_2 = r_{cl} k_2$ is the dimensionless wave number of the second medium in the waveguide and $c = r_{co} / r_{cl}$ is the ratio of the core radius to the radius of the first cladding. The transverse components of the field can be expressed in terms of the longitudinal components using well known formulae [18].
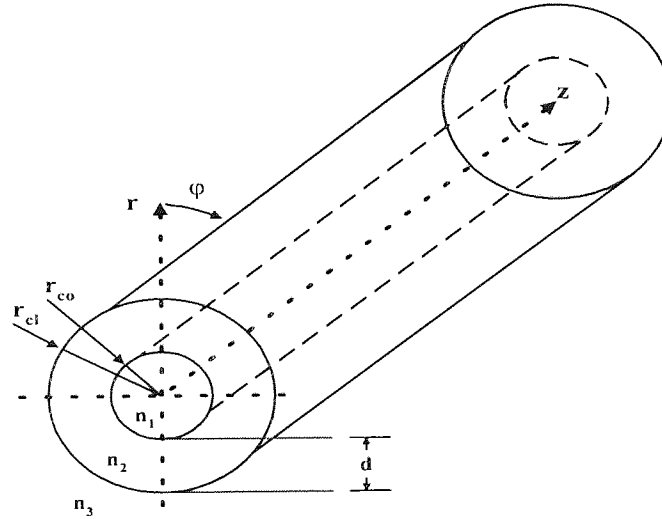
Figure 6.3 A generic three layers cylindrical waveguide as considered in the theoretical description.

By using Eqs. (6.3.1)-(6.3.3), it is possible to express the components of the field in the following form (after some simplification) [19]. In the first medium of the waveguide, we have

$$E_{r1} = \frac{A_n}{2}\left[(1+p_1)\,J_{n-1} - (1-p_1)\,J_{n+1}\right]F_c\,,$$

$$E_{\varphi 1} = -\frac{A_n}{2}\left[(1+p_1)\,J_{n-1} + (1-p_1)\,J_{n+1}\right]F_s\,,$$

$$E_{z1} = i\,A_n\,V\,J_n\,F_c\,,$$

$$H_{r1} = \frac{A_n\,U}{2\,W_2}\left[(\varepsilon_1\,U^{-2} + p_1)\,J_{n-1} + (\varepsilon_1\,U^{-2} - p_1)\,J_{n+1}\right]F_s\,, \qquad (6.3.4)$$

$$H_{\varphi 1} = \frac{A_n\,U}{2\,W_2}\left[(\varepsilon_1\,U^{-2} + p_1)\,J_{n-1} - (\varepsilon_1\,U^{-2} - p_1)\,J_{n+1}\right]F_c\,,$$

$$H_{z1} = i\,A_n\,V\,p_1\,\frac{U}{W_2}\,J_n\,F_s$$

In (6.3.4) the argument of the Bessel functions is $x_1\rho$, where $\rho = r/r_{co}$ is the dimensionless radial coordinate. For the second medium of the waveguide, we obtain

$$E_{r2} = \frac{x_1}{2\,x_2}\left\{C_n\left[(1+p')\,J_{n-1} - (1-p')\,J_{n+1}\right] + T_n\left[(1+p'')\,N_{n-1} - (1-p'')\,N_{n+1}\right]\right\}F_c\,,$$

$$E_{\varphi 2} = -\frac{x_1}{2\,x_2}\left\{C_n\left[(1+p')\,J_{n-1} + (1-p')\,J_{n+1}\right] + T_n\left[(1+p'')\,N_{n-1} + (1-p'')\,N_{n+1}\right]\right\}F_s\,,$$

$$E_{z2} = i\,V\left[C_n\,J_n(x_2\rho) + T_n\,N_n(x_2\rho)\right]F_c\,,$$

$$H_{r2} = \frac{U\,x_1}{2\,W_2\,x_2}\left\{C_n\left[(U^{-2} + p')\,J_{n-1} + (U^{-2} - p')\,J_{n+1}\right] + T_n\left[(U^{-2} + p'')\,N_{n-1} + (U^{-2} - p'')\,N_{n+1}\right]\right\}F_s\,,$$

$$H_{\varphi 2} = \frac{U\,x_1}{2\,W_2\,x_2}\left\{C_n\left[(U^{-2} + p')\,J_{n-1} - (U^{-2} - p')\,J_{n+1}\right] + T_n\left[(U^{-2} + p'')\,N_{n-1} - (U^{-2} - p'')\,N_{n+1}\right]\right\}F_c\,,$$

$$H_{z2} = i\,\frac{U\,V}{W_2}\left[C_n\,p'\,J_n(x_2\rho) + T_n\,p''\,N_n(x_2\rho)\right]F_s$$

$$(6.3.5)$$

where the argument of the function $J_{n\pm 1}$ and $N_{n\pm 1}$ is x_2. In the third medium of the waveguide, we find

$$E_{r3} = \frac{\Phi_n\,x_1}{2\,x_3}\left[(1+p_2)\,K_{n-1} + (1-p_2)\,K_{n+1}\right]F_c\,,$$

$$E_{\varphi 3} = -\frac{\Phi_n\,x_1}{2\,x_3}\left[(1+p_2)\,K_{n-1} - (1-p_2)\,K_{n+1}\right]F_s\,,$$

$$E_{z3} = i\,V\,\Phi_n\,K_n(x_3\rho)\,F_c\,,$$

$$H_{r3} = \frac{\Phi_n\,x_1\,U}{2\,W_2\,x_3}\left[(\varepsilon_3 U^{-2} + p_2)\,K_{n-1} - (\varepsilon_3 U^{-2} - p_2)\,K_{n+1}\right]F_s\,, \qquad (6.3.6)$$

$$H_{\varphi 3} = \frac{\Phi_n\,x_1\,U}{2\,W_2\,x_3}\left[(\varepsilon_3 U^{-2} + p_2)\,K_{n-1} + (\varepsilon_3 U^{-2} - p_2)\,K_{n+1}\right]F_c\,,$$

$$H_{z3} = i\,\Phi_n\,p_2\,V\,\frac{U}{W_2}\,K_n(x_3\rho)\,F_s$$

where the argument of the functions $K_{n\pm 1}$ is x_3. The following notation is adopted in the expressions for the fields components: $x_{1,2,3}$ are dimensionless wave numbers, defined by

146

$$x_1^2 = r_{cl}^2(k_0^2 n_1^2 - \beta^2), \quad x_2^2 = r_{cl}^2(k_0^2 n_2^2 - \beta^2), \quad x_3^2 = r_{cl}^2(\beta^2 - k_0^2 n_3^2), \quad (6.3.7)$$

$$V = \frac{x_1}{\beta r_{cl}} = \sqrt{\varepsilon_1 U^{-2} - 1}, \quad (6.3.8)$$

$$p' = \frac{p_1 F_1 - p_2 F_2}{F_1 - F_2}, \qquad p'' = \frac{p_2 F_1 - p_1 F_2}{F_1 - F_2}, \quad (6.3.9)$$

$$F_1 = J_n(c x_2)/J_n(x_2), \quad F_2 = N_n(c x_2)/N_n(x_2), \quad (6.3.10)$$

$$U^2 = \frac{x_1^2 - \varepsilon_1 x_2^2}{x_1^2 - x_2^2} = \frac{\varepsilon_3 x_1^2 + \varepsilon_1 x_3^2}{x_1^2 + x_3^2} = \frac{\varepsilon_3 x_2^2 + x_3^2}{x_2^2 + x_3^2}$$

$$\varepsilon_1 = n_1^2/n_2^2, \quad \varepsilon_3 = n_3^2/n_2^2, \quad W_2 = W_0/n_2, \quad W_0 = \sqrt{\mu_0/\varepsilon_0}, \quad c = r_{co}/r_{cl}$$

$$(6.3.11)$$

The component fields (6.3.4)-(6.3.6) are given for the positive values of x_1^2, x_2^2 and x_3^2. If

$x_1^2 < 0$ we have to make the following substitutions of the functions in Eqs. (6.3.3)-(6.3.6)

whose argument contains x_1:

$$J_n \text{ with } I_n; \quad J_{n\pm1} \text{ with } \mp I_{n\pm1}; \quad N_n \text{ with } K_n; \quad N_{n\pm1} \text{ with } \mp K_{n\pm1} \qquad (6.3.12)$$

The same substitution of the functions has to be made for $x_2^2 < 0$. If $x_3^2 < 0$, the following

substitutions of the functions whose argument contains x_3 have to be made:

$$K_n \text{ with } N_n, \quad K_{n\pm1} \text{ with } \mp N_{n\pm1} \qquad (6.3.13)$$

The expressions (6.3.4)-(6.3.6), subject to the substitutions (6.3.12), (6.3.13) describe the
components of the electromagnetic field of any normal mode. Note that in the case
discussed in chapter two, $n_3 < n_2 < n_1$. In the case under study, the refractive index of the
three media are related as $n_2 < n_1 < n_3$, condition that corresponds to four possible
situations:

a) $\beta > k_0 n_1, k_0 n_2, k_0 n_3$ which gives $x_1^2 < 0, x_2^2 < 0, x_3^2 > 0$

b) $k_0 n_1, k_0 n_2 < \beta < k_0 n_3$ which gives $x_1^2 < 0, x_2^2 < 0, x_3^2 < 0$

c) $k_0 n_2 < \beta < k_0 n_1, k_0 n_3$ which gives $x_1^2 > 0, x_2^2 < 0, x_3^2 < 0$

d) $\beta < k_0 n_1, k_0 n_2, k_0 n_3$ which gives $x_1^2 > 0, x_2^2 > 0, x_3^2 < 0$

Cases a) and b) should be discarded as the field components in the core (combinations of
I_n) and in the first cladding (combinations of I_n and K_n) would be monotonically increasing
functions of r. Case c) is also not acceptable because the fields in the cladding would
monotonically increase with r. The only remaining possible case is d). This case
corresponds to fields that are oscillating in the fibre core (combinations of J_n), the first

147

cladding (combinations of J_n and N_n) and the metallic coating (combinations of N_n). Dissimilarly to a step index fibre surrounded by air, case where the modes are confined in the fibre core or can be guided in the fibre cladding (for instance, when the light is diverted from the core to the cladding by a LPG written in the core fibre, as described in chapter two), in the case of a metal coated fibre no confinement is achieved neither in the core (as the condition $n_2 k_0 < \beta < n_1 k_0$ is not satisfied) nor in the cladding (as the condition $n_3 k_0 < \beta < n_2 k_0$ is also not satisfied). The physical interpretation of these results can be that the radiation, that is diverted to the cladding by the LPG, does not remain confined in the cladding, but propagates through the metal. Here it will be absorbed, because of the lossy nature of the material, therefore the waveguide is only suitable for all the purposes that do not involve transmission of the light on the long distance. A suitable application of such a metal coated waveguide is in the field of sensing as we want to show in the following section.

6.4 Spectral Characterisation of a Two Sections Silver Coated LPG Sensor

Fibre Long Period Gratings (LPGs) are axially periodic refractive index variations, typically with a period of a few hundreds of microns, photoinscribed directly in the core fibre. Over the last few years, LPGs have found numerous applications in the field of sensing through their sensitivity to strain, temperature and refractive index of the surrounding medium. The LPG sensitivity can manifest itself in two ways: firstly through the spectral shift in the attenuation band, which here we refer to as spectral sensitivity, and secondly through a change in the strength of the attenuation band. In general, problems can arise when using a LPG that is written into a conventional step-index fibre, due to its sensitivity to various external influences. One problem is that of distinguishing between individual mesurands, and several papers have been published addressing this problem [21-23]. Various discrimination schemes have been used to address this problem such as a pair of FBGs [24-27], a LPG working in series with a FBG [28], a FBG working in conjunction with a fibre Fabry-Perot device [29] or a sampled FBG [30].

Metal coated gratings show a higher temperature sensitivity because of the larger thermal expansion coefficient of the metal in comparison with a bare fibre. We report below the fabrication and characterisation of a new sensing device made by a two-sections LPG, that can be used to distinguish between spectral variations due to changes in temperature and those due to changes in the surrounding medium refractive index, using information from a limited spectral region. Therefore, this LPG based fibre sensor can be used for

simultaneous or separate measurements of temperature and refractive index by using a single optical source.
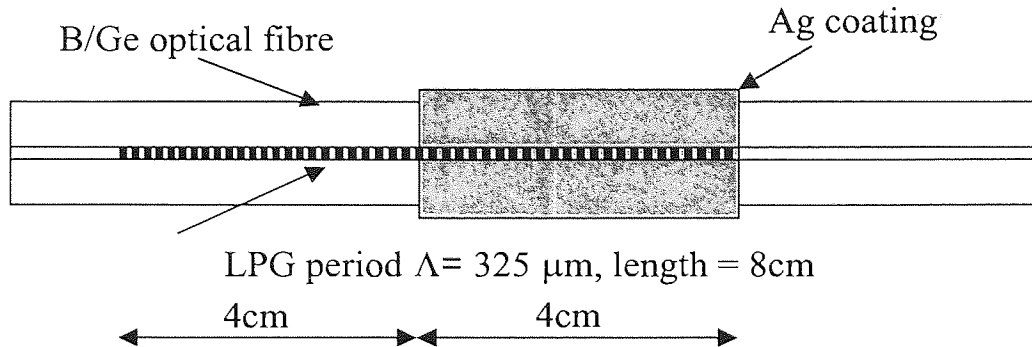
Figure 6.4 *Schematic of the two-sections LPG sensor for the simultaneous detection of temperature and surrounding medium refractive index.*

The LPGs were inscribed in the core of each of the 4 cm long section of the fibre, with a continuous multiple scan, using a point-by-point writing technique (a computer controlled shutter provides this facility). The grating period was set to 325 μm. The UV beam was generated from a frequency doubled argon ion laser (Coherent 300C FreD), which was focused to a size of approximately 10 μm. First, LPG in the Ag coated fibre was fabricated using a laser output power of 120 mW and a translation stage scan speed of 0.05 mm/s. For the bare fibre section a power of 90 mW and a scan speed of 0.27 mm/s were used. During the fabrication process the attenuation bands were monitored by using an internal broadband light source optical spectrum analyser (HP 71451A). Figure 6.5 illustrates the recording process in the coated section, with the strongest stop-band (~ 3 dB) occurring at a wavelength of 1540 nm, and the subsequent inscription in the bare fibre section. It can be seen from Fig. 6.5.b that, because of the different waveguide characteristics of the two sections, the attenuation band corresponding to the 8th cladding mode in the bare fibre section is spectrally located close to the 9th cladding mode attenuation band in the silver coated section (with a spectral separation of ~ 60 nm), which raises the interesting possibility of using a single light source to interrogate the device. The evolution of the attenuation bands in both sections during the fabrication shows a different behaviour as expected due to the fact that the presence of a third metallic layer modifies the structure of the optical waveguide (clearly the behaviour of the LPG cladding modes depend upon the material used, its refractive index, as well as the waveguide geometry) [31]. The sensor was subjected to three measurands: temperature, changes in the surrounding medium refractive index, and mechanical bending. In each of the three cases the measurements

149

were performed using an optical spectrum analyser with an internal broadband light source and with an accuracy of 0.04 nm.
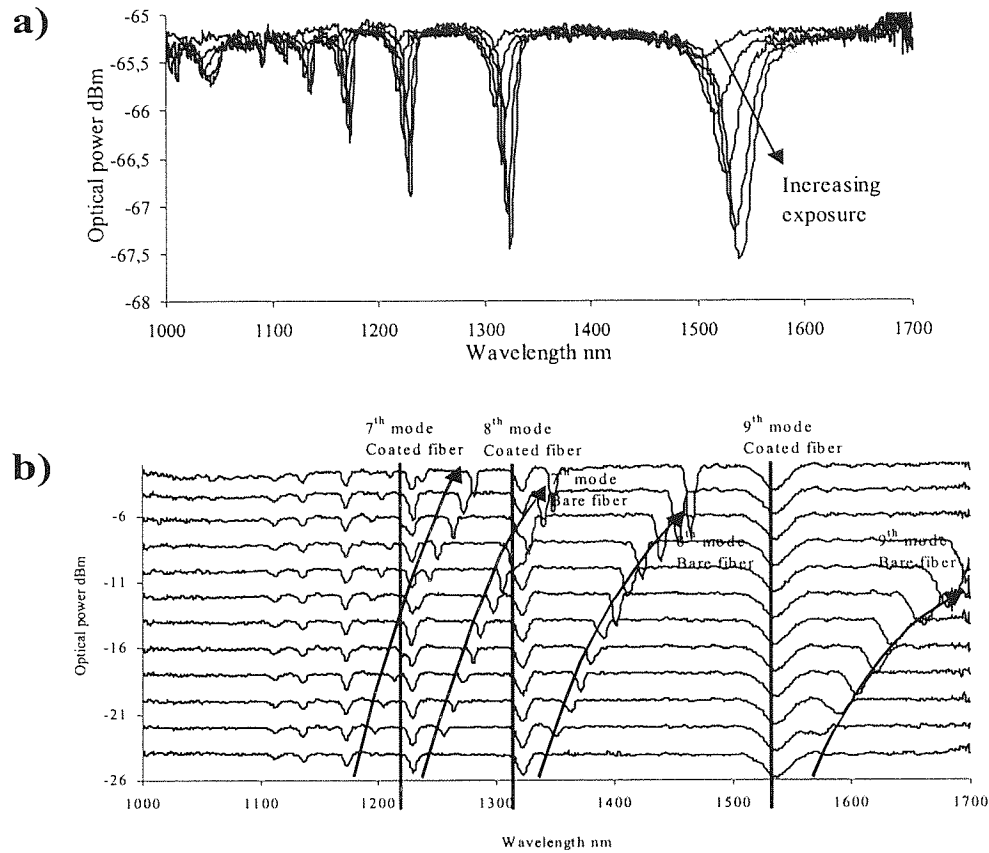
Figure 6.5 *Transmission spectra of the device recorded during fabrication: a) in the silver coated section only and b) after writing the LPG in the bare fibre section. Traces offset for clarity.*

6.4.1 Temperature Sensitivity Measurements

We investigated the temperature sensitivity of the device by placing the sensor on a hot-plate under a thermally insulating cover. The measurement of the temperature of the hot-plate was achieved by using a probe having an accuracy of 0.1°C. The spectral locations of the central wavelengths of the attenuation bands associated with the 8th cladding mode in the bare fibre section and the 9th cladding mode in the silver coated section were monitored as functions of the temperature.
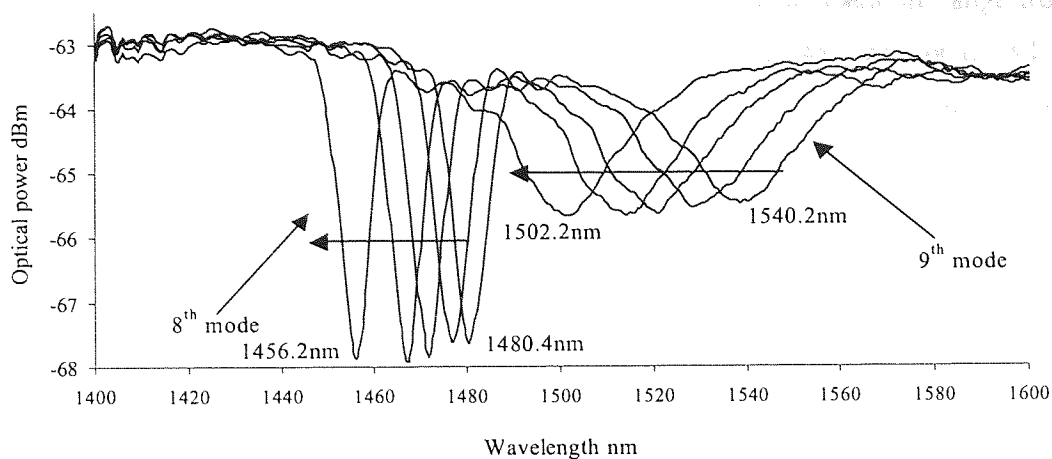
Figure 6.6 *The effect of temperature on the transmission spectrum of the double-section LPG fibre device over a range 20–80°C. The arrows show the direction of increasing temperature.*

Figure 6.6 shows the results of such measurements. It can be seen that the spectral sensitivities of the two attenuation bands are dissimilar from each other even though they are spectrally close. This is partly due to the fact that each attenuation band is associated with a different cladding mode and partly due to the fact that the thermal expansion coefficient of silver is higher than that of silica (which means that the coated section of the device is subjected to a temperature induced strain in addition to the temperature induced change of refractive index). Therefore the metal coated section proves to be more sensitive than the bare fibre in detecting a temperature change. The spectral shift of the central wavelength of the two attenuation bands as a function of the temperature change is illustrated in Fig. 6.7.
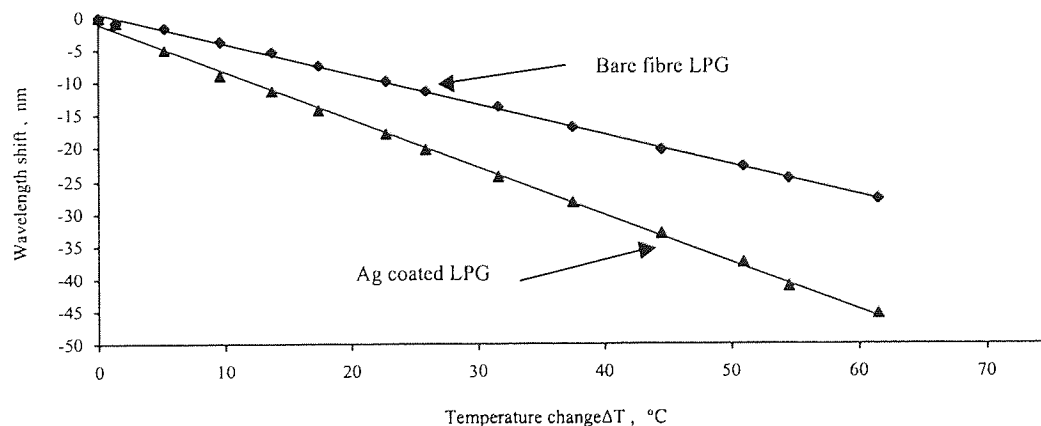
Figure 6.7 *Spectral sensitivity of the two attenuation bands associated with each section of the device as a function of the temperature change.*

151

As one may see from Fig. 6.7, the total wavelength shift over the temperature range from 20 °C to 80 °C is of –27.8 nm for the bare fibre section and of –45.4 nm for the silver coated section. This gives a temperature sensitivity of $d\lambda/dT = 0.458 \times 10^{-4}\,nm\,°C^{-1}$ for the first section and $d\lambda/dT = 0.728 \times 10^{-4}\,nm\,°C^{-1}$ for the second one. The temperature resolution of the device, defined as the root mean square deviation from linearity, is $\pm 0.4\,°C$ for the bare fibre attenuation band and $\pm 0.3\,°C$ for the silver coated one.

6.4.2 Surrounding Medium Refractive Index Sensitivity Measurements

We performed the measurements of the dependency of the spectral characteristics of the device on the external refractive index n_s by using the experimental set up described above. However, this time the LPG was placed into a V-groove and immersed in a certified refractive index liquid (supplied by Cargille Laboratories Inc.), which has a quoted accuracy of ± 0.0002. Both the LPG and the V-groove were carefully cleaned, washed in methanol, then in deionised water, and finally air dried before the immersion into a liquid with refractive index ranging from n_s=1.300 to n_s=1.452. The cleaning procedure was adopted to minimise the amount of salts being deposited on the fibre by the chemicals. The V-groove, made from an aluminium plate, was machined flat to reduce the bending on the fibre. During the measurements the plate was on direct contact with the optical table, which acted as a heat sink to maintain a constant temperature. The results of the measurements are shown in Fig. 6.8. Inspecting Fig. 6.8.a, it can be seen that the attenuation band associated with the silver coated section is essentially unaffected by the refractive index change. This was confirmed by immersing the LPG device into a liquid with a refractive index $n_s = 1.700$, when again no shift was discernible.

This behaviour was to be expected since the penetration depth of silver at a wavelength of 1550 nm is $\approx 10\,nm$, which implies that the electric field of the cladding mode associated with the attenuation band in the silver coated section is significantly attenuated in the 1 μm thickness of the metal coating, and therefore the change in refractive index has a negligible effect. The attenuation band associated with the bare fibre section demonstrates the usual spectral characteristics of a LPG with regards to the refractive index change, as shown in Fig. 6.8.b. Statistical techniques were employed on several sets of data for the spectral response of the LPG device to changes in the refractive index of the surrounding medium. The deviation in the experimental results yields a wavelength resolution of $\pm 0.066\,nm$ for the 8th mode around a refractive index of 1.375. This translates to an approximate refractive index resolution of $\pm 9.6 \times 10^{-4}$.

a)

b)
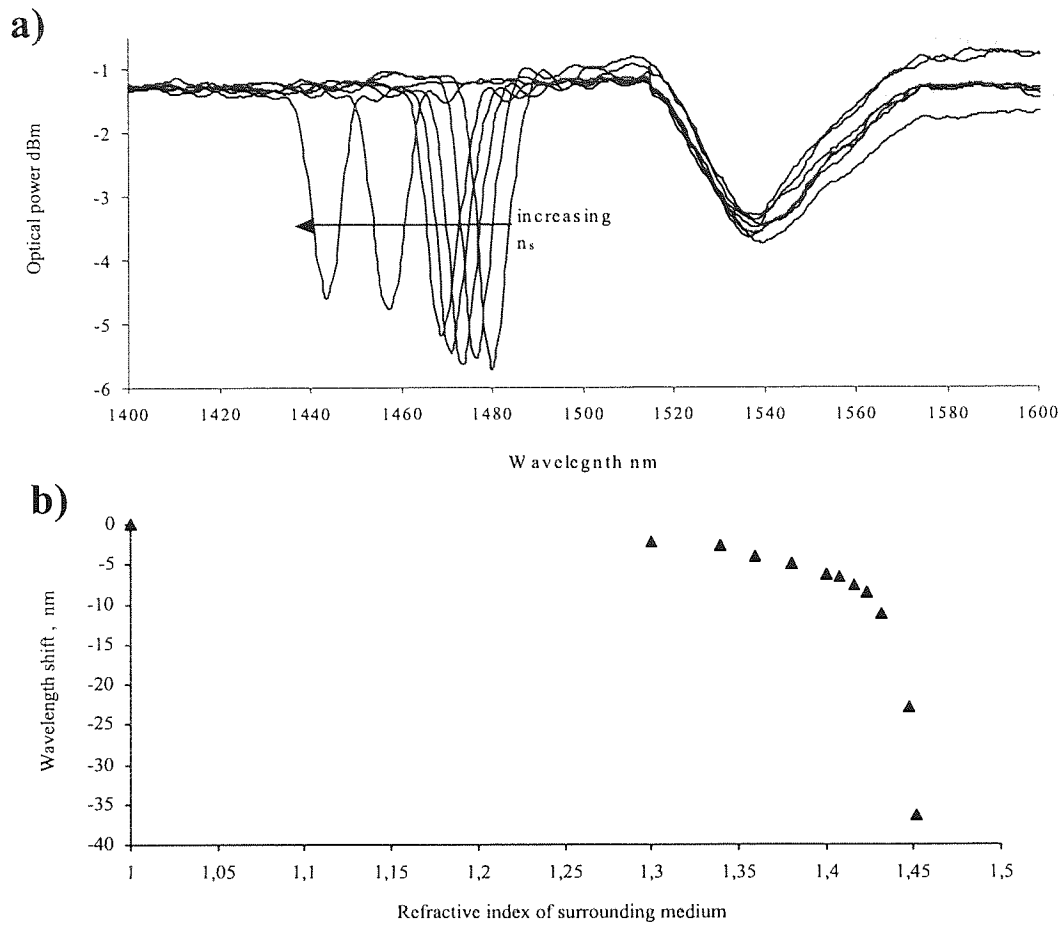
Figure 6.8 *Surrounding refractive index medium sensitivity of a two-section LPG device: a) the effect of an increasing refractive index on the transmission spectrum of both sections of the sensor, b) spectral sensitivity of the attenuation band associated with the bare fibre section of the device as a function of n_s.*

6.4.3 Bending Sensitivity Measurements

A final set of measurements was made to obtain the spectral sensitivity of the sensor to mechanical bending, by using the experimental set-up shown in Fig. 6.9.
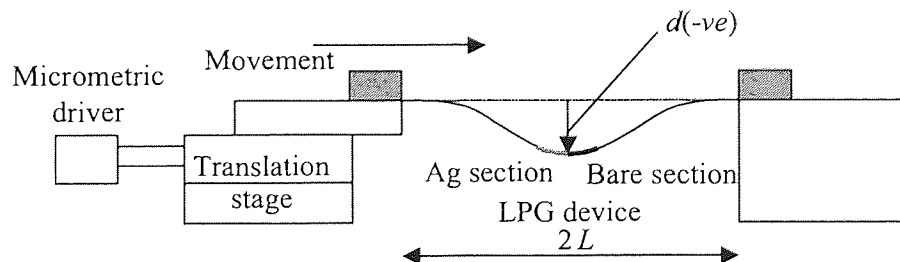
Figure 6.9 *Schematic of the experimental set-up used for testing the spectral sensitivity of the LPG device to bending.*

The device was clamped between two towers, one of which can be moved inward by a micrometer driver in such a way to induce a bend in the optical fibre. For such an arrangement, where the LPG sensor is placed mid-way between the clamps, the curvature ρ of the fibre is given by [32]

$$\rho = \frac{2d}{(d^2 + L^2)}$$

where L is the half-distance between the edges of the two towers and d is the bending displacement at the centre of the LPG. The central wavelength of the two attenuation bands was monitored as a function of the bending applied to the fibre. The results are reported in Fig. 6.9. The data reported in Fig. 6.10 show that the shift of the two attenuation bands is a nonlinear function of the curvature. We found that a quadratic polynomial produces a reasonable fit to the experimental data. The departure of the curves from the fitting polynomial corresponds to a wavelength resolution of $\pm 0.2\,nm$ for the 8th mode and $\pm 0.3\,nm$ for the 9th mode, which translates to an approximate curvature resolution of $\pm 0.037\,m^{-1}$ and $\pm 0.04\,m^{-1}$, respectively. It should be pointed out that the calculation of the curvature assumes that the fibre possesses a uniform cross-section. In our case, the silver coated section has a slightly higher rigidity than that of the bare fibre, and hence possesses a slightly lower curvature. The larger values of wavelength shift exhibited by the coated section are due to the fact that the attenuation band is associated with a higher order cladding mode, which leads to a greater sensitivity.
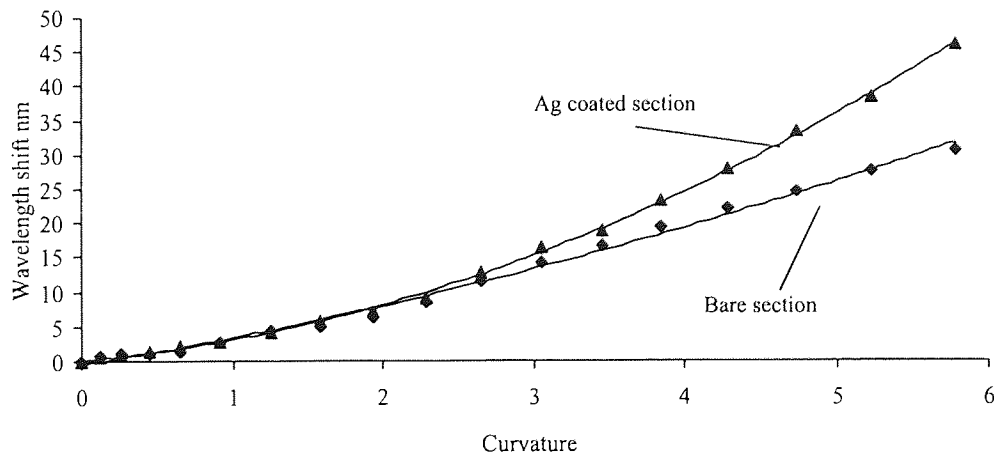
Figure 6.10 *Experimental wavelength shift of the attenuation bands for the silver coated and for the bare fibre section of the device as a function of the applied curvature.*

154

6.5 Chapter Conclusion

We investigated the behaviour of metal coated step index waveguides through a theoretical description based on propagation of normal modes. We also described and fully characterized a new two-sections silver coated LPG device. This type of device may be used to overcome the recoating problems associated with usual LPGs written in step-index fibre. Also as a sensor, it can be used for simultaneous measurements of temperature and surrounding medium refractive index. A clear advantage of such a device is that the it is possible to find two attenuation bands spectrally close to each other, allowing a single light source to be used to interrogate the device, thus reducing the cost.

References

[1]   H.J. Patrick, A.D. Kersey, F. Bucholtz, "Analysis of the response of long period fiber gratings to external index of refraction", *J. Lightwave Technol.*, **16**, 1998, pp. 1606-1612.

[2]   V. Bhatia, A.M. Vengsarkar, "Optical fibre long-period grating sensors", *Opt. Lett.*, **21**, 1996, pp. 692-694.

[3]   R.P. Espindola, R.M. Atkins, D.A. Simoff, K.T. Nelson, M.A. Paczkowski, "Fibre Bragg grating written through a fibre coating", in *proc. OFC 1997*, Postdeadline *paper PD-4*.

[4]   D.S. Starodubov, V. Grubsky, J. Feinberg, "Efficient Bragg grating fabrication in a fibre through its polymer jacket using near-UV ligth", *Electron. Lett.*, **33**, 1997, pp. 1331-1333.

[5]   P. Simpkins, C.R. Kurkjian, C.M. Schroeder, "Aluminium-coated silica fibres: strength and solderability", *Electron. Lett.*, **31**, 1995, pp. 747-749.

[6]   A. Diez, M.V. Andres, D.O. Culverhouse, T.A. Birks , "Cylindrical metal-coated optical fibre devices for filters and sensors", *Electron. Lett.*, **32**, 1996, pp. 1390-1392.

[7]   C.S. Lee, S.-W. Lee, S.-L. Chuang, "Normal modes in an overmoded circular waveguide coated with lossy material", *IEEE Transact. Microwave Theor. Techniques,* **MTT-34**, 1986, pp. 773-785.

[8]   S.J. Al-Bader, H.A. Jamid, "Comparison of absorbtion loss in metal-clad optical waveguides", *IEEE Transact. Microwave Theor. Techniques,* **MTT-34**, 1986, pp. 310-314.

[9]   D.M. Costantini, C.A.P. Muller, S.A. Vasiliev, H.G. Limberger, R.P. Salathé, "Tunable loss filter based on metal-coated long-period fiber grating", *IEEE Photon. Technol. Lett.*, **11**, 1999, pp.1458-1460.

[10] P.M. Cavaleiro, F.M. Araújo, A.B. Lobo Ribeiro, "Metal-coated fibre Bragg grating sensor for electric current metering", *Electron. Lett.*, **34**, 1998, pp. 1133-1135.

[11] G.-C. Lin, L. Wang, C.C. Yang, M.C. Shih, T.J. Chuang, "Thermal performance of metal-clad fibre Bragg grating sensors", *IEEE Photon. Technol. Lett.*, **10**, 1998, pp.406-408.

[12] O. Duhem, A. DaCosta, J.F. Henninot, M. Douay, "Long period copper-coated grating as an electrically tunable wavelength-selective filter", *Electron. Lett.*, **35**, 1999, pp. 1014-1016.

[13] R. Alonso, J. Subias, J. Pelayo, F. Villuendas, J. Tornos, "Single-mode, optical-fiber sensors and tunable wavelength filters based on the resonant excitation of metal-clad modes", *Appl. Opt.*, **33**, 1994, pp. 5197-5201.

[14] C.D. Su, L.A. Wang, "Linewidth broadening of Er-doped superfluorescent fiber source using long-period grating", *Electron. Lett.*, **35**, 1999, pp. 331-332.

[15] A.J.C. Tubb, F.P. Payne, R. Millington, C.R. Lowe, "Singlemode optical fibre surface plasma wave chemical sensor", *Electron. Lett.*, **31**, 1995, pp. 1770-1771.

[16] M. Born, E. Wolf, "Principles of optics", *Pergamon Press,* Oxford, 1959.

[17] E.D. Palik, "Handbook of optical constants of solids", 2nd ed., *Academic Press,* Boston, 1991.

[18] D. Marcuse, "Theory of dielectric optical waveguides", 2nd ed., *Academic Press*, New York, 1991.

[19] A.S. Belanov, E.M. Dianov, G.I. Ezhov, A.M. Prokhorov, "Propagation of normal modes in multilayer optical waveguides 1. Components fields and dispersion characteristics", *Sov. J. Quant. Electron.*, **6**, 1976, pp. 43-50.

[20] A.S. Belanov, E.M. Dianov, G.I. Ezhov, A.M. Prokhorov, "Propagation of normal modes in multilayer optical waveguides II. Energy characteristics", *Sov. J. Quant. Electron.*, **6**, 1976, pp. 915-920.

[21] V. Grubsky, J. Feinberg, "Long-period gratings with variable coupling for real-time sensing applications", *Opt. Lett.*, **25**, 2000, pp. 203-205.

[22] V. Bhatia, T. D'Alberto, N. Zabaronick, R. Claus, "Temperature-insensitive and strain-insensitive long-period gratings sensors for smart structures", *Opt. Eng.*, **36**, 1997, pp. 1872-1875.

[23] R.P. Espindola, R. Windeler, A. Abramov, B. Eggleton, T. Strasser, D. Di Giovanni, "External refractive index in sensitive air-clad long period fibre grating", *Electron. Lett.,* **35**, 1999, pp. 327-328.

[24] W. James, M.L. Dockney, R.P. Tatam, "Simultaneous independent temperature and strain measurements using in-fibre Bragg grating sensors", *Electron. Lett.,* **32**, 1996, pp. 1133-1134.

[25] M.G. Xu, J.-L. Archambault, L. Reekie, J.P. Dakin, "Discrimination between strain and temperature effects using dual-wavelength fibre grating sensors", *Electron. Lett.*, **30**, 1994, pp. 1085-1087.

[26] M. Song S. Lee, S. Choi, B. Lee, "Simultaneous temperature and strain measurement using two fiber Bragg gratings embedded in a glass tube", *Opt. Fiber Technol.*, **3**, 1997, pp. 194-196.

[27] B.-O. Guan, H.-Y. Tam, S.-L. Ho, W.-H. Chung, X.-Y. Dong, "Simultaneous strain and temperature measurement using a single fibre Bragg grating", *Electron. Lett.*, **36**, 2000, pp. 1018-1019.

[28] H. Patrick, G. Williams, A. Kersey, J. Pedrazzani, A. Vengsarkar, "Hybrid fiber Bragg grating/long period fiber grating sensor for strain/temperature discrimination", *Photon. Technol. Lett.*, **8**, 1996, pp. 1223-1225.

[29] Y.J. Rao, P.J. Henderson, D.A. Jackson, L. Zhang, I. Bennion *et al.*, "Simultaneous strain, temperature and vibration measurement using a multiplexed in-fibre Bragg grating/fibre-Fabry-Perot sensor system", *Electron. Lett.*, **33**, 1997, pp. 385-387.

[30] X. Shu, B. Gwandu, Y. Liu, L. Zhang, I. Bennion, "Sampled fibre Bragg grating for simultaneous refractive index and temperature measurement", *Opt. Lett.*, **26**, 2001, pp. 774-776.

[31] T. Allsop, L. Zhang, I. Bennion, "Detection of organic aromatic compounds in paraffin by a long period fibre grating optical sensor with optimised sensitivity", *Opt. Commun.*, **191**, 2001, pp. 181-190.

[32] W. Du, H. Tam, M. Liu, X. Tao, "Long-period fiber grating bending sensor in laminated composite structures", in *Sensory Phenomena and Measurements Instrumentation for Smart Structures and Materials,* Proc. SPIE **3330**, 1998, pp. 284-292.

Chapter 7

THESIS CONCLUSIONS

This thesis has investigated many different theoretical and experimental aspects related to the fibre grating technology with a special focus on the design, fabrication and experimental characterisation of tunable FBGs, that have been used as dispersion compensators or optical filters. A second issue was the fabrication and characterisation of gratings inscribed in the core of a metal coated fibre. We tried to keep a reasonable balance between experimental and theoretical investigation of the phenomena under study along the whole length of the thesis. Actually, our intention was to give wherever possible, a "physical" interpretation of the experimental results. In different occasions (as in the case of apodised gratings, or nonlinearly strained gratings, for instance), the numerical modelling took some efforts and a substantial number of pages in the thesis has been dedicated to the numerical results and their comparison with experiments. The reason of such a choice is that we strongly felt that the experimental results must find their "reason d'être" within the context of a more general theory. On the other hand, in some cases we obtained the right understanding of how to improve the experimental results just by comparing them with the theoretical predictions (a typical example is the simulation of

apodised gratings, from which we derived the values of the practical parameters used for the fabrication).

The first step in the formulation of any theory of fibre gratings is the coupled-mode theory, that has been presented in Chapter 2. This theory describes with a good accuracy the behaviour of modes propagating through the fibre core (or cladding) and being coupled each other by the action of a periodical modulation of the core refractive index (fibre grating). Our formulation of the theory describing the counter-directional coupling (FBGs) or the codirectional coupling (LPGs) is the most general possible. This formulation has some advantages as, for instance, the fact that it allows to calculate the coupling coefficient κ directly from the physical parameters of the real fibre (such as the core and cladding diameters, and the core-cladding refractive index difference). The theory proves to be a useful tool for the understanding of the features found in a real spectrum, and also enables to make predictions on the effect of changes of the fabrication parameters (the strength of the grating, its physical length and the shading apodisation function used, for instance). The coupled-mode theory, formulated for uniform gratings, can be easily adapted to the case of apodised gratings by using the transfer-matrix method (a numerical extension of the theory, that considers the contribution of each section of the non-uniform grating as locally uniform). The results of the numerical simulations, reported at the end of the third chapter, have been successfully used to predict the experimental spectrum and to optimise the experimental parameters in the fabrication of a real grating.

For many applications, it is important to spectrally shape the grating response and eliminate possible sources of noise. In the thesis we presented a number of results on this issue. A novel grating apodisation technique, working on a double exposure approach (with the speed of the translation stage varying with the amplitude of the shading function) has been detailed. The results obtained by use of this technique were compared to the results obtained from the phase mask dither technique. The optimisation of all the physical quantities (translation stage speed, laser average power, voltage applied to the piezoelectric oscillator, etc.) has been discussed in detail. A systematic comparison of the numerical with the experimental results enabled the production of apodised gratings of a very good quality (i.e., with an efficient side lobes suppression and a suitable reflection profile shaping). To find the dependence of the grating apodisation on the used parameters, we performed a full numerical investigation on six different shading functions, and we demonstrated that the kind of apodisation function to be used depends on the strength of

the grating. More precisely, a Gaussian shading function should be used in the case of a weak grating, whereas a Blackman function is more suitable for a strong grating.

Chirped FBGs have been widely used as dispersive elements, i.e., to contrast the pulse broadening induced by the dispersion occurring in optical fibres. Recently, the accurate measurement of the chromatic dispersion of each optical component has become a crucial issue, mostly because of the increased bit rate used to operate the new generation of optical transmission links. As a consequence of the high transmission speed, these transmission links have a lower tolerance to any dispersion fluctuations. It is clear that the measurement of the dispersion introduced by each optical component in the link should be evaluated with the minimum possible error. We detailed the modulation phase-shift method, that is one of the most reliable technique for the measurement of chromatic dispersion in both fibres and FBGs. The experimental "uncertainty" associated to the measurement was estimated and the effect produced by the modulation frequency on the measurement was discussed as well.

The impact of the apodisation on the reduction of the group delay ripples has been investigated by means of a statistical approach. By applying the apodisation techniques detailed in Chapter 3, we were able to reduce the amplitude of the group delay ripples in a chirped FBG, of 20% compared to the unapodised case. The magnitude of the group delay ripples is a particularly important issue as it can compromise the transmission capability of an optical link. A new characterisation of the group delay ripples, by a statistical approach based on Fast Fourier Transform method, has been developed. The statistical approach is especially useful for the detection of any hidden periodical regularity which may give information on the quality of the phase mask, or the presence of stitching errors, for instance. An investigation of the origin of two predominant imperfections in the spectrum of a linearly chirped FBG has been carried on and practical solutions, implemented at the time of the fabrication of the grating, have been detailed. Finally a method suitable for the generation of ultra-high repetition rate optical pulses, based on the spatial Talbot effect, has been reported. An experiment (performed with a linearly chirped FBG and an initial 10 Gb/s optical stream) demonstrated the possibility of multiplication of the bit rate of the optical stream up to ten times.

The main body of the thesis is about the dynamic dispersion compensation, that is essential when the transmission speed reaches or overcomes 40 Gb/s. An extensive theoretical and experimental study was made on a new tunable dispersion compensator device, designed to

work by application of a non-uniform strain onto a chirped FBG. A specially conceived multipoint bending rig was used to apply the strain. We employed a mechanical tuning of the grating dispersion because of the substantial advantages of this technique in comparison with a thermal tuning (such as the possibility to compensate for higher order dispersion, the passive nature of the technique, and the reduced impact on the group delay ripples). We developed a theoretical model enabling to calculate the chromatic dispersion and the dispersion slope delivered by the device as a consequence of the distributed strain applied to the chirped FBG and we made an experimental investigation of the effect produced by the non-uniform strain on the time delay, the reflectivity and the group delay ripples of the FBG. Also, the performance of the dispersion compensator in a real optical system, was tested by performing transmission experiments using optical streams at 10 and 40 Gb/s. The device proved to be a reliable, useful tool when used in combination with the well-known technique of dispersion-management. The various experiments performed showed that the device has a good recompression factor on broadened optical pulses, which leads to a significant extension of the error-free transmission distance.

Pulsed operation of a laser diode in gain-switched or Q-switched regime is probably the simplest way to generate ultrashort optical pulses at an arbitrary repetition rate. Unfortunately, the useful laser signal carries only a small fraction of the total output power, the main contribution arising from the relaxation oscillation tail. We developed a new technique of spectral filtering that uses a uniform FBG in transmission, tuned by the same multipoint rig used to implement the tunable dispersion compensator. The filtering, allowed us to achieve more powerful and narrower pulses with a nearly complete suppression of the unwanted relaxation tail (specifically the achieved increase in the optical power was of a factor of five).

We fabricated and fully characterised a new two-section silver coated LPG device. Because of its sensitivity this device has been used as strain, bending and external refractive index sensor. We demonstrated for the first time that, because of the high value of the skin depth of silver in the near UV region, it is possible to write the LPG directly through the metal coating, thus considerably simplifying the fabrication process. A set of measurements has been made to fully characterize the sensing behaviour, by using two attenuation bands located closely together. This has the advantage that a single light source can be used to interrogate the device. We proved that the attenuation band associated with the silvered section is unaffected by the changes in the surrounding medium refractive index and can be used to temperature compensate the bare fibre section. The sensing

device possesses a resolution of $\pm 1.0 \times 10^{-3}$ for refractive index detection and $\pm 0.3\,^{\circ}C$ for temperature detection. The effect of bending on the spectral characteristics of the two attenuation bands was found to be nonlinear, with the silver coated section having the greater sensitivity. Moreover, the device can be used as a sensor for simultaneous measurements of temperature and surrounding medium refractive index.

A number of issues remains still to be explored in future work. It would be interesting, for instance, to perform the recompression experiments by using simultaneously a couple of mechanical tunable dispersion compensators as the one described in Chapter 5. It is well known that chirped gratings exhibit opposite sign chromatic dispersion on the two sides (short and long wavelength sides). The use two tunable gratings could increase the range of variability of the dispersion and also, for a given configuration in the bending profile, compensate exactly for second order dispersion, thus allowing the tuning of a pure third order dispersion.

Publications

- T. Allsop, R. Neal, <u>D. Giannone</u>, D.J. Webb, D. Mapps, I. Bennion, "Sensing characteristics of a novel two-section long period grating", accepted for publication on *Appl. Opt.*

- <u>D. Giannone</u>, Y.W.A. Lee, I.Y. Khrushchev, V.K. Mezentsev, and I. Bennion, "Tunable dispersion and slope by distributed strain applied on a linearly chirped fibre Bragg garting", to be submitted to *Opt. Commun.*

- M.V. Dubov, <u>D. Giannone</u>, I.Y. Khrushchev, and I. Bennion, "Pulse tail suppression in laser diode output by tunable notch filter", *Electron. Lett.* **37** (23), pp. 1404-1405, (2001).

- D. Pudo, L.R. Chen, <u>D. Giannone</u>, L. Zhang, and I. Bennion, "Actively mode-locked, tunable dual-wavelength erbium-doped fiber laser with arbitrary wavelength spacing", *IEEE Photon. Technol. Lett.* **14** (2), pp. 143-145, (2002).

- <u>D. Giannone</u> and V.K. Mezentsev, "Implementation of a nonlinear tunable chirped fibre Bragg grating device as post compensator for high bit rate transmission in dispersion-managed systems", *Postgraduate Research in Electronics and Photonics Conference (PREP 2001)*, University of Keele, UK, pp. 99-100 (June 2001).

- M.V. Dubov, <u>D. Giannone</u>, I.Y. Khrushchev, and I. Bennion, "Tail-free operation of an overdriven gain-switched DFB laser by spectral filtering", *14th Annual Meeting of the IEEE Laser and Electro-Optics Society (LEOS 2001)*, **2**, San Diego, California, pp. 804-805 (November 2001).

- <u>D. Giannone</u>, Y.W.A. Lee, I.Y. Khrushchev, V.K. Mezentsev, and I. Bennion, "Tuneable compensator of dispersion and slope using non-uniformly strained chirped fibre grating", *Conference on Lasers and Electro-Optics (CLEO 2002)*, Long Beach, California (May 2002).

- <u>D. Giannone</u>, Y.W.A. Lee, I.Y. Khrushchev, V.K. Mezentsev, and I. Bennion, "Dispersion and slope compensation by mechanically tuned fibre Bragg gratings", *International Quantum Electronics Conference (IQEC/LAT 2002)*, Moscow, Russia (June 2002).

- <u>D. Giannone</u>, Y.W.A. Lee, I.Y. Khrushchev, V.K. Mezentsev, and I. Bennion, "Tuneable compensation of second and third order dispersion by non-uniformly strained chirped fibre Bragg gratings", *28th European Conference on Optical Communications (ECOC 2002)*, Copenhagen, Denmark (September 2002).

Europen Patent :

<u>D. Giannone</u>, Y.W.A. Lee, I.Y. Khrushchev, V.K. Mezentsev, and I. Bennion, "Nonlinear Tuneable Chirped Fibre Bragg Grating Device For Simultaneous Compensation Of Optical Chromatic Dispersion And Dispersion Slope", European Patent No: 01308203.7, (2001).